https://ntrs.nasa.gov/search.jsp?R=19970011008 2020-06-16T03:04:26+00:00Z

IN-34
013193

NASA Contractor Report 198530

Flow in Rotating Serpentine Coolant Passages With Skewed Trip Strips

David G.N. Tse
Scientific Research Associates, Inc.
Glastonbury, Connecticut

and

Gary Steuber
Pratt and Whitney
North Haven, Connecticut

October 1996

Prepared for
Lewis Research Center
Under Contract NAS3–27378

National Aeronautics and
Space Administration

Scientific Research Associates, inc.

50 Nye Road, P.O. Box 1058
Glastonbury, CT 06033
(860) 659-0333 FAX (860) 633-0676

NAS3-27378

FLOW IN ROTATING SERPENTINE COOLANT PASSAGES WITH SKEWED TRIP STRIPS

R95-9089F

Final Report

David G.N. Tse (SRA)

Gary Steuber (P&W)

May 1996

Prepared for

NASA Lewis Research Center

Cleveland, OH 44135

ABSTRACT

Laser velocimetry was utilized to map the velocity field in serpentine turbine blade cooling passages with skewed trip strips. The measurements were obtained at Reynolds and Rotation numbers of 25,000 and 0.24 to assess the influence of trips, passage curvature and Coriolis force on the flow field.

The interaction of the secondary flows induced by skewed trips with the passage rotation produces a swirling vortex and a corner recirculation zone. With trips skewed at +45°, the secondary flows remain unaltered as the cross-flow proceeds from the passage to the turn. However, the flow characteristics at these locations differ when trips are skewed at -45°. Changes in the flow structure are expected to augment heat transfer, in agreement with the heat transfer measurements of Johnson, et al. (1994). The present results show that trips skewed at -45° in the outward flow passage and trips skewed at +45° in the inward flow passage maximize heat transfer. Details of the present measurements were related to the heat transfer measurements of Johnson, et al. to relate fluid flow and heat transfer measurements.

1. INTRODUCTION

In advanced gas turbine engines increased temperatures, stage pressure ratios and rotor speeds are used to increase thrust/weight ratios and reduce specific fuel consumption. Consequently, the turbine is subjected to increased heat load and stress and efficient internal cooling is essential to maintain turbine blade structural integrity. Blade rotation gives rise to Coriolis and buoyancy forces which can significantly alter the heat transfer in coolant passages due to development of tangential (Coriolis) and radial (buoyant) secondary flows. The process is further complicated by the presence of secondary flows arising from the sharp turns in the cooling passage. A better understanding of Coriolis and buoyancy effects and the capability to predict their influence on heat transfer is necessary for efficient management of cooling air.

The complex coupling of Coriolis and buoyancy forces has prompted many investigators to study the heat transfer characteristics of rotating cooling passages. Guidez (1989), Hajek, et al. (1991), Wagner, et al. (1991), Yang, et al. (1992) and Mochizuki, et al. (1994) conducted experimental studies on heat transfer perfomance in rotating serpentine passages of square cross section with smooth walls. These results revealed a significant increase in heat transfer at the turns and showed considerable differences between straight passages having radially inward and outward flows. These references focused only on heat transfer measurements and did not include the velocity field which drives convective heat transfer. A study which focused on the velocity field was reported by Tse, et al. (1994), McGrath and Tse (1995) and Tse and McGrath (1995) for flow in smooth wall turbine cooling passages. These velocity field results explained many of the heat transfer results noted by previous investigators.

In practice, cooling passages contain trips, which create secondary flow to augment heat transfer. The heat transfer results of Taslim, et al. (1991a, 1991b), Johnson, et al. (1993, 1994) and Wagner, et al. (1992) indicate that the secondary flow produced by trips and trip orientation have large effects on heat transfer. The large decrease in heat transfer in the inlet region measured in models with smooth walls does not occur in models with trips. The effect of density ratio upon the resulting heat transfer is less for skewed trips than for trips normal to

the cross-flow. The effect of flow direction on heat transfer is less for models with trips than for models with smooth walls.

As part of the Integrated High Performance Turbine Engine Technology (IHPTET) goals, turbines would operate at near stoichiometric, i.e., 2200-2500 K, inlet temperatures, maintain efficiencies in the 88-94% range, and require total coolant flows of only 5% of the engine air flow rate. To attain these goals, a thorough understanding of the effect of rotation upon heat transfer and flow in turbine blade coolant passages is mandatory. Further advancement of blade cooling schemes beyond the current state-of-art requires an advance in the knowledge base of convective heat transfer in rotating ribbed channels. The objective of the experimental portion of the current program was to acquire benchmark quality velocity data in rotating coolant passages with ribbed walls. The results were used to quantify the influence of Coriolis effects and to explain the heat transfer phenomena observed by Johnson, et al. (1993, 1994).

Streamwise (radial), tangential and cross-stream velocities were obtained in rotating serpentine passages representative of internal cooling passages in modern gas turbine engines. Mean and rms quantities of these velocity components were obtained by laser-Doppler velocimetry (LDV). The measurements were obtained with a refractive-index-matching (RIM) experimental approach. Since the experimental program is isothermal and incompressible, it isolates the effect of Coriolis forces. The effects of buoyancy are addressed in the computational portion of the program, Steuber (1995).

Flow configuration, instrumentation and its associated uncertainties are described in Section 2. Results and their implications on heat transfer for two inlet conditions are presented and discussed in Sections 3 and 4. Conclusions are stated in Section 5.

2. FLOW CONFIGURATION AND INSTRUMENTATION

Figure 2.1 shows the flow circuit for the rotating turbine blade rig. Fluid was delivered to the cooling passage by a pump at a flow rate of 8.8 gpm and was monitored by a turbine meter to a precision of ±3%. The temperature was monitored downstream of the pump and was maintained at 26°C, ±0.2°C, by a temperature controller. The fluid was a

mixture of 70% turpentine and 30% Tetralin (by volume), which had a refractive index of 1.49 at 26°C for green light at 514.5 nm. This refractive index was identical to that of the acrylic model and allowed the beam to pass from one medium to the other without any distortion.

A shaft encoder was fitted at one end of the shaft to monitor the angular position and rotational speed of 617 rpm to precision of ±0.018° and ±1%, respectively. The fluid had a density of 894 kg m^{-3} and a kinematic viscosity of 1.74 x 10^{-6} $m^{-1}s$. The flow rate and rotational speed corresponded to a Reynolds number of 25,000 and a Rotation number of 0.24. Stationary experiments were conducted to provide reference conditions to quantify the effect of rotation. The Reynolds and Rotation numbers are of direct practical relevance to modern turbines.

The two inlet configurations of the turbine blade passage model are given in Figures 2.2 and 2.3, and the measuring plane locations are given in Tables 2.1 and 2.2. The model has a four-pass passage with three 180° turns and is similar to that of Wagner, et al. (1994). This geometry was chosen to allow analysis of the velocity measurements corresponding to the heat transfer results obtained by Wagner, et al. (1994). The differences between UTRC and SRA rigs are shown in Figure 2.4. The first two passes of the passage have a rectangular cross-section of 1.0" x 0.5". The last two passes have a square cross-section of 0.5" x 0.5". Trips with a streamwise pitch to trip height (P/e) = 5 and trip height to coolant passage width (e/2Z) = 0.1, were machined along the leading and trailing walls. These geometries are typical of those used in turbine blade coolant passages. The trips on the walls are staggered by the half-pitch. The trips are skewed at ±45° to the cross-flow, as shown in the figure, and this allows the effect of trip orientation to be examined. Experiments were conducted with flow entering the model through the 0.5" x 0.5" square passage (Passage 1) and the 1.0" x 0.5" rectangular passage (Passage 2) to examine the effect of passage configuration.

The streamwise and tangential velocity components were obtained by the laser-Doppler velocimeter set-up shown in Figure 2.5. It made use of diffraction grating optics, together with an Argon ion laser operating at 200mW and 514.5nm. The measurement volume was projected into the rotating passage by a mirror at 45° with respect to the laser axis. The optical characteristics of the velocimeter are given in Table 2.3.1. The cross-stream velocity component was obtained by the laser-Doppler velocimeter set-up shown in

Figure 2.6. It made use of the same optics with the Argon ion laser operating at 400mW and 514.5nm. The optical characteristics of the velocimeter are given in Table 2.3.2. The optics were mounted on a mechanism that traversed the measurement volume in three orthogonal directions with a maximum uncertainty of 0.02mm. The output of the photomultiplier was processed by a TSI 1990C counter. The counter and the shaft encoder were interfaced to a microcomputer, which recorded the angular position for every validated Doppler burst. The results at each angular position were then ensemble-averaged to yield mean and rms velocity profiles as a function of passage angle. The processing software continuously displayed the sample size curve during the data acquisition process and allowed the user to terminate the procedure after a statistically meaningful sample was attained. The mean and rms velocities in each ensemble-average was evaluated with statistical uncertainties of less than 2% and 5%, respectively.

Figures 2.2 and 2.3 show the measurement locations for both inlet configurations. Details of these locations are given in Tables 2.4 and 2.5. Measurements were obtained at Reynolds (Re) and Rotation (Ro) numbers of 25,000 and 0.24. The Reynolds number was based on the hydraulic diameter and the bulk mean velocity of the half-inch square passage. The mean and rms velocities were ensemble-averaged over pre-selected angle windows of $0.036° \pm 2\%$ by means of an index and a TTL pulse train from an encoder with 5000 pulses per revolution and external quadrupling. This angular resolution corresponds to a spatial resolution of roughly 0.40 mm ± 2% at radial positions between 0.557 and 0.738m. Stationary measurements were obtained with approximately 100 grid points. Rotating measurements were obtained with over 200 grid points. Details of each measurement plane are given on the data files submitted to NASA.

Streamwise distance (x) from the entrance is normalized by the hydraulic diameter (D). Vertical (y) and tangential (z) distances are normalized by the half passage height (H) and width (Z), respectively. For the x coordinate and U component, streamwise is positive. In the straight passage, the y coordinate and V component are positive against gravity. At the turn, the concave side is positive. The z coordinate and W component are positive in the direction of rotation. The velocities are normalized by the bulk mean velocity (U_b) of 3.44 ms^{-1}, based on the half-inch square passage.

NOMENCLATURE - CHAPTERS 3 AND 4

D	Hydraulic diameter
e	Trip height
H	Half passage height
P	Trip spacing
Nu	Nusselt number
Nu_∞	Reference Nusselt number
R	Average model radius
Re	Reynolds number
Ro	Rotation number
U	Streamwise (radial) velocity
U_b	Bulk mean velocity
U_p	Passage mean velocity
V	Vertical or cross-stream velocity
W	Tangential velocity
x	Streamwise coordinate
y	Vertical or cross-stream velocity coordinate
z	Tangential coordinate
Z	Half passage width

3. RESULTS AND DISCUSSION - PASSAGE 1.

3.1 Stationary measurements

Figures 3.1 to 3.3 show the velocities in the first passage. At 1 D downstream of the inlet, Figure 3.1.1, the streamwise velocities show an almost uniform distribution. The high velocity region, 1.1 U_b, is close to the lower wall. The vertical and tangential velocities, Figure 3.1.2, in the lower half of the passage are close to zero. The maximum cross-flow plane velocities are 0.18 U_b and -0.15 U_b. They occur in the upper half of the passage where the streamwise velocities are approximately 0.9 U_b. The velocity characteristics are consistent with the flow exiting an S-bend; the bend upstream of the inlet is an S-bend. Figs. 3.1.3 and 3.1.4 show rms velocities and will be discussed later.

At 7 D downstream of the inlet, Figure 3.2.1, the high velocity region (~1.65 U_b) has shifted to the upper wall. The streamwise flow development is large (>0.65 U_b within 6 D) and this is attributed to strong secondary flow due to the trips. The vector plot, Figure 3.3.2, shows a two-vortex structure with downward velocity reaching 0.95 U_b near the two walls and upward velocity of around 0.6 U_b in the center of the passage. Re-attachment of the cross-flow can be seen at y/H = 0.6 and 0.8.

At 1 D upstream of the first turn, Figure 3.3.1, there are two high velocity regions (both reaching 1.50 U_b) close to the side walls. Large streamwise flow development is also present in the last 6 D of the first passage. Comparison of Figures 3.3.2 and 3.2.2 indicates the strength of the vortices are equal. The trips lead to the development of asymptotic secondary flows.

Figure 3.4 shows the velocities in the first turn. The streamwise velocity contours, Figure 3.4.1, show that the high velocity region is close to the convex (suction) side of the turn. It achieves a maximum value 1.65 U_b. Qualitatively, the flow in the first turn exhibits inviscid behavior. The cross-stream velocity contours of Figure 3.4.2 are consistent with the flow visualization of Mochizuki, et al. (1994). Their results show that flow progresses from the first passage to the second passage as two separate streams. The first stream is close to the lower wall. It bifurcates into another two streams on impact with the concave wall. These streams separately propagate toward the side walls, then along the walls and to the second passage through the inside of the turn. Their signatures are evident in the negative

cross-stream velocities of Figure 3.4.2. The second stream is located above the center of the passage. It sweeps along the concave surface and continues to the second passage along the outside of the turn. The signature of this stream is evident in the positive cross-stream velocities of Figure 3.4.2.

Figures 3.5 to 3.6 show the velocities in the second passage. At 1 D downstream of the first turn, Figure 3.5.1, the high velocity region (1.55 U_b) is close to the upper wall. The convection of the high velocity region to the upper wall at the exit of the first turn is attributed to the secondary flow generated by the turn. Figure 3.5.2 shows that the two-vortex structure at the exit of the turn is considerably weakened. The maximum magnitude of the upward velocity at the center of the passage is reduced from 0.60 U_b to 0.25 U_b. The maximum downward velocity near the walls is reduced from -0.85 U_b to -0.70 U_b. The secondary flow induced by the turn opposes the vortices generated in the first passage.

At 1 D upstream of the second turn, Figure 3.6.1, the high velocity regions (1.55 U_b) are close to the side walls. The velocity characteristics are similar to those at the end of the first passage, Figure 3.3.1. The flow at the end of both passages is fully developed. The convection of the high velocity region from the upper wall at the beginning of the second passage to the side walls towards the end of the second passage stems from the two-vortex structure. Figures 3.3.2 and 3.6.2 show that the two-vortex structures in the first and second passages circulate in the same direction with similar strength.

Figure 3.7 shows the velocities in the second turn. The streamwise velocity contours, Figure 3.7.1 show that the high velocity region (1.0 U_b) is close to the convex (suction) side of the turn. The maximum velocity is much lower than that observed in the first turn, 1.65 U_b, because of the streamwise recirculation bubble at the exit of the turn, Figure 3.8.1. The recirculation bubble at the exit of the turn induces a more gradual flow turning. In addition, it directs the cross-flow toward the concave side of the bend. The cross-stream velocities shown in Figure 3.7.2 are all positive. In the first turn, Figure 3.4.2, the cross-stream velocities near the convex surface are negative. Thus, the differences between the flow in the first and second turns are attributed to sudden expansion from the second to the third passage.

Figures 3.8 and 3.9 show the velocities in the third passage. At 1 D downstream of the second turn, Figure 3.8.1, the high velocity region (1.4 U_b) is close to the upper wall. The

passage mean velocity, U_p, is 0.5 U_b because of the expansion in flow area. The flow velocity near the upper wall is almost 3.0 U_p. The sharp turning, coupled with the expansion in flow area, gives rise to the reverse flow which occurs near the lower wall. It reaches a maximum value of -0.25 U_b and extends to the 0.4 H location. The vertical velocities, Figure 3.8.2, are approximately 0.2 U_b and are mainly downward.

At 1 D upstream of the third turn, Figure 3.9.1, the high velocity region remains close to the upper wall. However, the maximum velocity has been reduced from 1.4 U_b to 0.8 U_b. The vertical convection in the third passage is substantial. Figure 3.9.2 shows the downward velocity reaching 0.35 U_b near the side walls and the upward velocity reaching 0.25 U_b in the center, indicating the presence of a two-vortex flow pattern. The two-vortex pattern circulates in the same direction as that in the first passage.

Figures 3.10 and 3.11 show the velocities obtained in the fourth passage. At 1 D downstream of the third turn, Figure 3.10.1, there is a high velocity region of magnitude 1.25 U_b close to the upper wall. Reverse flow occurs close to the lower wall. It reaches a maximum value of -0.35 U_b and extends to the 0.25 H location. Figure 3.10.2 shows upward velocity of 0.5 U_b near the side walls. The downward velocity is of the order of -0.4 U_b in the upper half of the passage but it is close to the trailing wall. This indicates separation of cross-flow in the inter-ribbed region on the leading side and re-attachment of cross-flow in the inter-ribbed region on the trailing side.

At 1 D upstream of the exit, Figure 3.11.1, the high velocity region (0.8 U_b) is close to the lower wall. The convection of the high velocity region from the upper wall at the beginning of the passage to the lower wall at the end of the passage is due to the two-vortex structure, Figure 3.11.2. The direction of the vortex is reversed from that found in the first passage. The near wall vertical velocity is upward and that in the middle of the passage is downward. The reversal in the recirculation direction is assocated with the reversal of the flow direction. The double vortex generated by the ribs redistributes the cross-flow to the lower wall. This leads to a more drastic change in the primary flow characteristics.

The rms velocities of the streamwise and vertical components are of the order of 10 to 20% in the straight passages (Figures 3.x.3 and 3.x.4 of Figures 3.1, 3.2, 3.3, 3.6, 3.9 and 3.11). They rise to 15 to 25% in the first and second turns (Figures 3.x.3 and 3.x.4 of Figures

3.4, 3.7). The rms velocities are highest at 1 D downstream of turns (Figures 3.x.3 and 3.x.4 of Figures 3.5, 3.8 3.10). They reach a maximum value of 35%.

The velocity measurements will be further analyzed in relation to the heat transfer results obtained by Wagner, et al. (1992) and Johnson, et al. (1994) in Section 3.3.

3.2 Rotating measurements

Figures 3.12 to 3.16 show the velocities in the first passage. At x/D = 1, Figure 3.12.1, the high velocity region occurs on the leading side of the passage near the upper wall. The maximum streamwise velocity reaches 1.35 U_b. Stationary measurements, Figure 3.1.1, indicate that the high velocity region is near the lower wall. Rotation alters the inlet condition.

Figures 3.13.1, 3.14.1, 3.15.1 and 3.16.1 show that the maximum streamwise velocity between x/D = 4 and x/D = 12 is within ± 5% of 1.6 U_b. The results of Tse, et al. (1994) show that the maximum streamwise velocity reaches 1.2 U_b at the end of the passage in a 0.5" x 0.5" square passage with smooth walls. The present results show that the maximum streamwise velocity reaches its asymptotic value after 4 D.

The streamwise velocities at x/D = 4 with rotation, Figures 3.13.1, are similar to those obtained at x/D = 7 without rotation, Figure 3.2.1. The upward convection of cross-flow induced by trips skewed at -45° is not significantly affected by rotation in the first 4 D. A comparison of Figures 3.14.1 and 3.2.1 shows that model rotation shifts the high velocity region from the upper wall to the trailing surface. As expected, rotation induces a net tangential convection from the leading (low pressure) to (high pressure) trailing side. Figures 3.15.1 and 3.16.1 show the development of streamwise velocity in the last 4 D of the first passage associated with secondary flows induced by trips skewed at -45° and rotation. The cross-flow continues to shift toward the high pressure side. Comparison of Figures 3.15.1, 3.16.1, 3.15.2 and 3.16.2 shows that the high velocity regions occur at the eye of the swirling vortex.

Figure 3.12.2 shows positive tangential velocity near the upper and lower wall and negative tangential velocity at the center of the passage. The two-vortex structure associated with rotation has been established at x/D = 1. The maximum positive and negative velocities

reach $\pm 0.18\ U_b$. The lower vortex extends above the center of the passage. This is consistent with convection of the cross-flow to the upper half of the passage observed in the streamwise velocity measurements, Figure 3.12.1. Figure 3.13.2 shows positive tangential velocity near the lower wall and negative tangential velocity above the center of the passage. The negative velocity extends to the upper wall, indicating further expansion of the lower vortex at x/D = 4.

Figures 3.14.2, 3.15.2 and 3.16.2 show the secondary flows at x/D = 7, 10 and 12. With clockwise rotation of the rig (viewed from the top), the combination of outward flow and trips skewed at -45° generates counter-clockwise swirl (viewed radially outward) and a corner recirculation zone. The stationary measurements show that the secondary flow in the first passage is characterized by the two-vortex structure of Figure 3.14.3. Rotation induces a second two-vortex structure, Figure 3.14.4. Each structure in Figures 3.14.3 and 3.14.4 has a clockwise circulating vortex and a counter-clockwise circulating vortex. The two counter-clockwise vortices reinforce each other and give rise to the counter-clockwise swirl observed in Figures 3.14.2, 3.15.2 and 3.16.2. The vortices circulating in the clockwise direction are compressed to form a corner recirculation. The maximum tangential velocities at x/D = 4, 7, 10, and 12 are respectively 0.48, 0.65, 0.71, and $0.72\ U_b$. The secondary flow becomes asymptotic by the end of the first passage.

The study of Prakash and Zerkle (1993) shows that flow in a rectangular duct with normal trip strips and an aspect ratio (H/Z) of 0.5 is characterized by a two-vortex structure for Ro = 0.12. Coriolis effects are less pronounced in a ribbed passage compared to a smooth wall passage. Separation and re-attachment of the cross-flow in the inter-rib region prevents Coriolis effects from reaching the walls. Separation and re-attachment of the cross-flow occur on both the leading surface and the trailing surface at alternate intervals. Augmentation of heat transfer stems from re-attachment of the cross-flow, which brings the cool cross-flow to the surface.

However, the flow in a square duct with skewed trip strips is characterized by a large counter-clockwise swirl bubble and a small corner recirculation for Ro = 0.24, Figures 3.14.2, 3.15.2 and 3.16.2. The counter-clockwise swirl and corner recirculation flow structure leads to re-attachment of the cross-flow in the upper and lower corners of the leading surface and separation of the cross-flow in the center region of the leading surface. Separation and re-

attachment of the cross-flow on the trailing surface is less noticeable because of the high vertical velocity associated with the strong swirl. The difference between the secondary flow characteristics observed here and those evaluated from the theoretical analysis of Prakash and Zerkle (1993) stems from differences in trip orientation and passage configuration.

Figure 3.17 shows the velocities in the first turn. Rotation reduces the maximum velocity at the turn from 1.65 U_b, Figure 3.4.1, to 0.9 U_b, Figure 3.17.1. In addition, it shifts the high velocity region from the convex side to the trailing side. The ring structure associated with swirl is less noticeable in Passage 1 than in Passage 2, Figure 4.21.1. The flow in the first turn of Passage 1 is less sensitive to secondary flow than that in Passage 2 because of the increase in velocity associated with the reduction in flow area. Figure 3.17.2 shows that clockwise swirl (viewed from the downstream direction) is present at the turn. The swirl in the first passage and the first turn are in the same direction (counter-clockwise) when they are viewed from the upstream direction. The swirl level at the turn is higher than that in the first passage. The outward flow on the trailing side is reinforced by centrifugal force. The momentum is transferred to the inward flow on the leading side by convection.

The swirl at the first turn is much stronger than that in Tse, et al. (1994) and McGrath and Tse (1995) in a turn with a square cross-section. This is partly attributed to the difference between the aspect ratio of the turn and partly to the presence of swirl before the turn. The tangential velocities in the present and the previous investigations are of similar magnitudes. The maximum cross-stream velocity (1.4 Up) is 200% higher in the present case because of a 50% increase in the aspect ratio of the turn. In the present case, swirl already exists in the first passage, but in Tse, et al. (1994) and McGrath and Tse (1995) the flow is characterized by the two-vortex structure induced by Coriolis effects. The velocity vector in y/H = -0.8 of Figure 3.17.2 shows that, for a turn with a radius of 3.05 mm, some flow propagates to the second passage along the leading side of the turn. Tse, et al. (1994) and McGrath and Tse (1995) show that, for a turn with a radius of 15 mm, the flow on the leading side of the turn is convected back to the trailing wall along the convex wall.

The corner recirculation zone in the first passage, Figures 3.14.2, 3.15.2, 3.16.2, is eliminated by the expansion of the swirl bubble, Figure 3.17.2. The strong inward velocity on the leading side acts as a blockage to the flow discharging from the first passage. It induces a

contraction and forces the cross-flow to propagate to the second passage along the trailing side. Consequently, the streamwise velocities on the trailing side of the turn are greater than those on the leading side, Figure 3.16.1.

Figures 3.18 to 3.21 show the velocities in the second passage. At 1 D downstream of the first turn, Figure 3.18.1, the maximum streamwise velocity reaches a value of 1.55 U_b and is located close to the lower wall. This is consistent with the flow visualization obtained in the sharp turn of a stationary passage with small radius of curvature, Mochizuki, et al. (1994). The present results show that the high velocity region is shifted laterally to the trailing side because of rotation.

Figures 3.19.1, 3.20.1 and 3.21.1 show that the maximum velocity in all of these locations remains within ±5% of the maximum velocity existing in the first turn (1.55 U_b). Tse, et al. (1994) show that in a 0.5" x 0.5" square passage with smooth walls, the maximum streamwise velocity reaches 1.5 U_b at the exit of the first turn and decays to 1.2 U_b towards the end of the passage. The secondary flows induced by trips skewed at +45° and rotation in the second passage are as strong as those induced by the first turn and rotation. This is evident in the secondary flow characteristics shown in Figures 3.17.2, 3.20.2 and 3.21.2.

Figures 3.18.1 and 3.19.1 show that rotation shifts the high velocity region from the trailing side toward the leading side. Rotation induces a net tangential convection from the low pressure surface to the high pressure surface and the effect is noticeable within 3 D downstream of the turn. The redistribution of the cross-flow is consistent with the secondary flow characteristics described in Figure 3.19.2. Figures 3.20.1 and 3.21.1 show the development of streamwise velocity in the last 2 D of the second passage associated with secondary flows induced by trips skewed at +45° and rotation. The cross-flow continues to shift toward the high pressure side. Comparison of Figures 3.20.1, 3.21.1, 3.20.2 and 3.21.2 shows that, similar to the first passage, the high velocity regions in the second passage occur at the eye of the swirling vortex.

Figures 3.18.2 and 3.19.2 show the secondary flow characteristics at 1 and 3 D downstream of the first turn. The cross-stream component can not be obtained at y/H = +0.8 for x/D = 17.5 and at y/H = +0.6 and 0.8 for x/D = 19.5. At these locations only the tangential components are plotted so vectors do not include the vertical flow component.

They only present tangential velocity component information. The flow in the second passage is characterized by a clockwise swirl (viewed radially outward) and a corner recirculation. The second passage is an inward flow passage with trips skewed at +45°. Stationary measurements show that inward flow and trips skewed at +45° generate the two-vortex structure of Figure 3.19.3. The direction of Coriolis force is reversed, Figure 3.19.4. In the second passage, the two clockwise vortices reinforce each other and give rise to the clockwise swirl, Figure 3.19.2. The vortices circulating in the counter-clockwise direction are compressed to form a corner recirculation. The mean tangential velocity contours at locations D9 and D10, Figures 3.20.2 and 3.21.2, are consistent with those associated with the vectors of Figures 3.18.2 and 3.19.2. Thus, the entire second passage is characterized by a clockwise swirl and a corner recirculation.

Figure 3.22 shows the secondary flow in the second turn. A large counter-clockwise swirl (viewed from the downstream direction) on the trailing side and a corner recirculation on the leading side near the concave wall are evident. The swirl in the second passage and the second turn are in the same direction (clockwise) when they are viewed from the upstream direction. However, the corner recirculation in the passage is on the trailing side and that in the turn is on the leading side. The corner recirculation induced by the trips collapses at the turn. The inward flow on the leading side of the second turn is retarded by centrifugal force. This induces a new corner recirculation zone close to the concave surface of the turn.

The corner recirculation in the second turn is much stronger than that in the first. Centrifugal force directs flow to the concave surface in the first turn and weakens the corner recirculation. It directs flow away from the concave surface in the second turn and strengthens the corner recirculation. The level of swirl in the first turn is higher than that in the second. This partly stems from retardation of the flow on the leading side by centrifugal force and from reduction of Coriolis effects. In the second turn, Coriolis forces are weaker than those at the first because it has a smaller radius.

Figures 3.23 and 3.24 show the streamwise velocities in the third passage. At 1 D downstream of the second turn, Figures 3.23, the maximum velocity reaches 0.8 U_b and occurs on the trailing side of the passage. Tse, et al. (1994) show that the high velocity at the exit of the second turn is on the leading (low pressure) side because of the Coriolis effect

associated with the upstream inward flow passage. In the present investigation, the cross-flow on the trailing side of the turn propagates to the third passage because of lack of confinement associated with the sharp turn. In Tse, et al. (1994), the cross-flow on the trailing side of the turn is convected back to the leading side along the convex surface before it can proceed to the third passage because of the confinement induced by the gradual turn. The distortions of the high velocity region on the trailing side stem from separation and re-attachment of cross-flow associated with the trips. The signature of the corner recirculation on the concave side of the second turn is evident in the high velocity pocket on the upper corner of the leading side.

At 6 D downstream of the second turn, Figure 3.24, the maximum streamwise velocity reaches 0.7 U_b and occurs on the leading side of the passage near the lower wall. The general characteristics of swirl and corner recirculation structure observed in the first passage (0.5" x 0.5") is also present in the third passage (1.0" x 0.5"); the interaction of secondary flows induced by trips skewed at -45° (Figure 3.24.2) and rotation (Figure 3.24.3) leads to expansion of the counter-clockwise vortex and compression of the clockwise vortex (Figure 3.24.4).

3.3 Relationship with heat transfer results

This section analyzes the velocity measurements in relation to the heat transfer results of Johnson, et al. (1994). The increases and decreases in heat transfer quoted in this section are relative to the stationary reference Nusselt number, Nu_∞. Both the velocity and heat transfer experiments were conducted with Reynolds and Rotation numbers of 25,000 and 0.24, respectively.

The heat transfer results of Johnson, et al. (1994) were obtained in a 0.5" x 0.5" square duct with trips skewed at -45° in the first passage and +45° in the second. The trip streamwise pitch to trip height (P/e), trip height to coolant passage width (e/2Z) and a radius ratio at the average model radius (R/D) were 10, 0.1 and 49, respectively. Their first turn has a radius of 15.0 mm. In the present experiment, velocity measurements were obtained in a

0.5" x 0.5" passage with trips skewed at +45°. The ratios of P/e, e/2Z and R/D were 5, 0.1 and 53, respectively. The first turn had a radius of 3.05 mm.

3.3.1 Stationary ribbed-wall heat transfer in relation to reference

Johnson, et al. (1994), show that the heat transfer from surfaces with skewed trips is 100 to 200% higher than that with smooth surfaces, even in the absence of rotation. The increase in surface area (5% according to Johnson, et al. (1994)) associated with the trips, and the increase in flow velocity (3%), due to the blockage of the trips, will contribute to the increase in heat transfer. However, their contributions are expected to be small and can not account for the 100 to 200% increase in the heat transfer observed by Johnson, et al. (1994).

The stationary results show very strong secondary flow being generated by the trips in the absence of rotation. The trips generate a two-vortex structure, for which the circulation direction is dependent on flow direction and trip orientation. In the first straight passage of Passage 1, the flow direction and trip orientation give rise to a double vortex, with upward velocity of 0.60 U_b in the center and downward velocity of -0.95 U_b (obtained at 0.09 D from the walls) near the leading and trailing walls. The two-vortex structure induced by the trips is similar to the Coriolis-induced two-vortex structure observed in Tse, et al. (1994). The relative tangential velocity measurements in Tse, et al. (1994) show that near-wall secondary flow of the order of 0.1 U_b (obtained at 0.1 D from the walls) is present near the upper and lower walls. The incompressible flow simulations in Tse, et al. (1994) and McGrath and Tse (1995) show that near-wall secondary flow is of the order of 0.3 U_b (leading to a 24% increase in heat transfer) at a location closer than 0.1 D from the walls. The effect of near-wall secondary flow of the order of 0.95 U_b on heat transfer can be potentially large.

The stationary measurements further show that, for a passage with trips, the development of streamwise flow in the first two passages is very significant, as a consequence of the strong secondary flow. The trips generate two high velocity regions (both reaching 1.50 U_b) close to the leading and trailing walls. The velocity measurements of Tse, et al. (1994) show that, for the model with smooth walls, the high velocity region (1.2 U_b) is close to the center of the passage and the velocity at the boundary layer near the walls is below 0.8 U_b. Based upon the $Nu\text{-}Re^{0.8}$ relationship, the change in flow characteristics leads to a

66% increase in heat transfer. Therefore, most of the increase in heat transfer (100 to 200%), observed by Johnson, et al. (1994) with skewed trips, is attributed to the changes in flow characteristics and to the strong secondary flow induced by the two-vortex structure.

3.3.2 Rotating ribbed-wall heat transfer in relation to reference heat transfer

Johnson, et al. (1994) show that with skewed trips there are no significant differences in the heat transfer characteristics between stationary and rotating measurements after the first few hydraulic diameters in the second passage. The analysis in this section will focus on the first passage. The increase in heat transfer from the high pressure surface in the first passage and in the first few hydraulic diameters in the second passage reach 300 and 266%. The corresponding increase in the first turn is of the order of 100%.

Coriolis effects increase the streamwise velocity on the high pressure side of the first passage by $0.6\,U_p$, Figure 3.14.1. Based upon the $Nu\text{-}Re^{0.8}$ correlation, the increase in convective heat transfer is of the order of 48 %. The results of Johnson, et al. (1994) show that the buoyancy increases heat transfer on the trailing side of first passage by 25%. The combined effect of the increase in streamwise velocity and buoyancy is less than 75%. Swirl and the re-attachment of cross-flow in the inter-ribbed region account for over 200% of the 300% increase in heat transfer observed by Johnson, et al. (1994).

Johnson, et al. (1994) show an increase in heat transfer of 100% in the first turn. The overall swirl level at the first turn is higher than that in the first passage, Figures 3.14.2, 3.15.2, 3.16.2 and 3.17.2. The increase in swirl level at the turn stems from increases in velocities near the eye of the vortex. The swirl levels close to the wall are of similar magnitude in the turn and the passage. The increase in turbulence intensity at the turn contributes to the increase of 100%, Tse, et al. (1994). The increase in heat transfer associated with swirl in the first passage is expected to be less than 100%.

Johnson, et al. (1994) showed increases in heat transfer of up to 300% from the pressure surface of the first passage. The above discussion shows that the increase in heat transfer associated with increase in streamwise velocity (~48%), swirl (<100%) and buoyancy (~25%) is of the order of 175%. Thus, it appears that re-attachment of cross-flow in the inter-ribbed region increases the heat transfer by over 125%.

3.3.3 Rotating ribbed-wall in relation to stationary ribbed-wall measurements

Johnson, et al. (1994) show that, in the first passage, rotation increases the heat transfer from the trailing (high pressure) surface by 25 to 30%. The heat transfer from the leading (low pressure) surface of the first passage decreases by 50%. In the second passage, rotation increases the heat transfer from the leading (high pressure) surface by 5 to 11.5%. The decrease in heat transfer from the trailing (low pressure) surface of the second passage is close to zero.

Figure 3.3.1 shows that, in the first passage, the trips generate two high velocity regions close to the walls (both reaching 1.50 U_b) in the absence of rotation. Figures 3.14.1, 3.15.1 and 3.16.1 show that, with rotation, the maximum streamwise velocity on the trailing (high pressure) side reaches 1.60 U_b. Based upon the $Nu\text{-}Re^{0.8}$ correlation, this leads to a 5% increases in convective heat transfer. Johnson, et al. (1994) show that rotation increases the heat transfer from the trailing surface by 30%. Their results further show that buoyancy increases the heat transfer from the trailing surface by 25%. Re-attachment of cross-flow in the inter-ribbed region increases the heat transfer from the trailing (high pressure) side by the same magnitude in both stationary and rotating cases. The two-vortex structure of Figure 3.14.2 and the swirl and corner recirculation structure of Figure 3.2.2 induce the same degree of heat transfer from the surface.

Figures 3.3.1 and 3.14.1 show that rotation induces a large velocity deficit on the leading (low pressure) side. With rotation, the streamwise velocity at the location corresponding to high velocity (1.5 U_b) under stationary conditions is of the order of 0.9 U_b. Based upon the $Nu\text{-}Re^{0.8}$ correlation, this leads to a 50% decrease in convective heat transfer. The results of Johnson, et al. (1994) show that rotation decreases the heat transfer from the leading surface of the first passage by 50%. Their results further show that buoyancy increases the heat transfer from the leading surface by 20 %. With rotation, the influence of re-attachment of the cross-flow in the inter-ribbed region on the leading (low pressure) surface is reduced by 20 %. This is expected because rotation increases the separation of the cross-flow in the inter-ribbed region on the low pressure surface. The heat transfer from the surface induced by the swirl and corner recirculation structure of Figure 3.14.2 is 20% less than that induced by the two-vortex structure of Figure 3.2.2.

Figures 3.23.1 and 3.24.1 show that, in the second passage, rotation increases the streamwise velocity on the leading (high pressure) side from 1.50 U_b to 1.55 U_b. Based upon the $Nu\text{-}Re^{0.8}$ correlation, this leads to a 2.5 % increase in convective heat transfer. The results of Johnson et al. (1994) show that rotation increases the heat transfer from the leading (high pressure) surface by 5 to 11.5%. Since Johnson, et al. (1994) do not assess the effect of buoyancy in this region, the individual effect of buoyancy and re-attachment of cross-flow in the inter-ribbed region is unknown. These effects account for the difference between the heat transfer characteristics observed in Johnson, et al. (1994) and those estimated from the $Nu\text{-}Re^{0.8}$ correlation.

Figures 3.23.1 and 3.24.1 show that, in the second passage, rotation decreases streamwise velocity on the trailing (low pressure) side from 1.50 U_b to 1.0 U_b. Based upon the $Nu\text{-}Re^{0.8}$ correlation, this leads to a 40% decrease in convective heat transfer. Johnson, et al. (1994) show that rotation does not affect the overall heat transfer from the trailing (low pressure) surface. Their results further show that buoyancy increases the heat transfer from the trailing (low pressure) surface by 60 %. Similar to the situation in the first passage, rotation reduces the influence of re-attachment of cross-flow in the inter-ribbed region on the leading (low pressure) side in the second passage by 20%. The heat transfer from the surface induced swirl and corner recirculation structure of Figure 3.22.2 is 20% less than that induced by the two-vortex structure of Figure 3.2.2.

The relative increase in heat transfer between the ribbed wall passages and the smooth wall passage (100 to 200%) is much greater than the relative increases and decreases in heat transfer between stationary and rotating ribbed wall passages. Thus, the skewed trips have a much stronger influence on heat transfer than rotation. In the first passage, the reduction in heat transfer from the low pressure wall is greater than the increase from the high pressure wall. Rotation leads to an overall decrease in heat transfer. The reduction in heat transfer stems mainly from the large velocity deficit on the low pressure side.

4. RESULTS AND DISCUSSION - PASSAGE 2.

4.1 Stationary measurement

Figures 4.1 to 4.3 show the velocities in the first passage. At x/D = 1, Figure 4.1.1, the high velocity region is close to the lower wall. This is consistent with the flow exiting an S-bend. The maximum streamwise velocity reaches 0.65 U_b, 30% higher than U_p; U_p is 0.5 U_b because of the expansion in flow area. The vertical velocities, Figure 4.1.2, indicate that the S-bend directs the center flow downward and the near-wall flow upward. The maximum positive and negative velocities reach values of ±0.15 U_b, 0.3 U_p. The results in Section 3.1 show that the streamwise flow non-uniformity and vertical velocity in Passage 1 are of the order of 0.1 U_p. The increase in streamwise flow non-uniformity and vertical velocity in Passage 2 is attributed to the increase in flow area. The flow is more sensitive to secondary flow as a result of the reduced momentum.

At x/D = 7, Figure 4.2.1, the high velocity region remains close to the lower wall and the maximum velocity has increased to 0.80 U_b within 6 D. There is a convection from the upper to lower wall between x/D = 1 and 7. This is attributed to the two-vortex structure, Figure 4.2.2. These vortices have upward velocity reaching 0.95 U_b near the side walls and downward velocity of around 0.6 U_b in the center. Figures 4.2.2 and 3.2.2 show that the strength of the vortices at x/D = 7 are almost equal for Passages 1 and 2. However, the vortices in Passage 2 circulate in the opposite direction. The circulation of the vortices generated by the trips is dependent on trip orientation.

At x/D = 12, Figure 4.3.1, the maximum velocity remains at 0.8 U_b and is located close to the lower wall. The streamwise flow development between x/D = 7 and 12 is reduced. This is consistent with a substantial reduction in the strength of the vortices, Figure 4.3.2. Flow entering a turn usually peaks on the convex side. Figure 4.3.1 shows that the flow entering the turn peaks on the concave side. This is attributed to convection associated with the two-vortex structure induced by the outward flow and the trips skewed at +45°.

Figure 4.4 shows the velocities in the first turn. Figure 4.4.1 shows that, similar to Passage 1, the high velocity region is close to the convex (suction) side of the turn. It achieves a maximum value of 0.8 U_b. The flow in the first turn exhibits inviscid behavior for Passages 1 and 2. The division of the cross-flow into two separate streams at the first turn

observed in Passage 1, Section 3, is also evident in Passage 2. The stream that is close to the lower wall is more noticeable in Passage 2 because the combination of outward flow and trips skewed at +45° induces a high velocity region close to that wall. The bifurcation on this stream into two streams on impact with the concave wall and its subsequent entry into the second passage along the side walls can be seen in the bifurcation of the high velocity region, Figure 4.4.1. The stream that propagates to the second passage by sweeping along the concave side is evident in the increase in streamwise velocity near the concave wall. The signatures of these two streams are evident in the positive and negative cross-stream velocities of Figure 4.4.2.

Figures 4.5 and 4.6 show the velocities in the second passage. At 1 D downstream of the first turn, Figure 4.5.1, streamwise recirculation with negative velocity of -0.25 U_b (50% of U_p) occurs near the lower wall. The sharp turning of the cross-flow induces streamwise recirculation which extends to 0.3 H. As expected, the high velocity region at the exit of the first turn is on the concave (pressure) side. The high velocity region increases in size and its maximum velocity increases from 0.8 U_b, Figure 4.3.1, to 1.0 U_b, Figure 4.5.1; indicating further convection from the suction to the pressure side of the turn. The vertical velocity contours, Figure 4.5.2, show maximum upward velocity of 0.25 U_b in the center and maximum downward velocity of 0.6 U_b near the side walls. The circulation direction of the two-vortex structure is opposite to that in the first passage. The circulation of the vortices generated by the trips is dependent on flow direction.

At 1 D upstream of the third turn, Figure 4.6.1, the high velocity is close to the lower wall. The redistribution of the high velocity from the upper to the lower wall in the third pasasge is consistent with the circulation direction of the two-vortex structure, Figure 4.6.2. Figures 4.6.1 and 4.3.1 show that the streamwise velocity characteristics at the end of the first and second passages are inverted. This inversion is due to the change in circulation direction of the two-vortex structure associated with change in flow direction. In contrast to Passage 1, Figures 3.6.1 and 3.3.1, the streamwise velocity characteristics at the end of the first and second passages are the same. Reversing the trip orientation or the flow direction reverses the circulation of the vortices. However, reversing the trip orientation and the flow direction do

not alter the circulation of the vortices (see Figures 2.1 and 2.2 for trip orientation and flow direction).

At 1 D downstream of the second turn, Figure 4.7.1, the maximum streamwise velocity increases to 1.65 U_b (from 0.8 U_b at 1 D upstream of the second turn) as a result of further convection from the suction to the pressure side and the reduction of flow area. Separation does not occur at the exit of the second turn for Passage 2 because of the contraction. Figures 4.7.1 and 4.6.1 show that the high velocity region enters the second turn on the convex (suction) side and exits it on the concave (pressure) side. This is expected because flow entering a turn peaks on the convex side and flow exiting a turn peaks on the concave side. The vertical velocity contours, Figure 4.7.2, show the expected two-vortex structure. The negative velocities are close to the side walls and reach a maximum value of -0.80 U_b. The positive velocities are in the center and reach a maximum value of 0.60 U_b. The vortices circulate in the same direction as those in the second passage (both trip orientation and flow direction are reversed) but opposite to those in the first passage (only trip orientation is reversed).

The velocity characteristics at locations B9, B11 and B12 are similar to those at locations A3, A5 and A6. This is expected because both trip orientation and flow direction are reversed. The resulting two-vortex structures which determine the flow characteristics in the passage are the same for both Passages 1 and 2.

4.2 Rotating measurement

Figures 4.11 to 4.15 show the velocities of the first passage. At x/D = 1 and 4, Figures 4.11.1 and 4.12.1 show the maximum streamwise velocity reaches 0.85U_b (70% above U_p). The high velocity region occurs on the leading side of the passage near the upper wall. Stationary measurements, Figure 4.1.1, indicate that the high velocity region is near the lower wall. The differences between stationary and rotating measurements stems from rotation induced secondary flow.

At x/D = 1, the tangential velocities within the region y/H = ±0.8 are all negative, Figure 4.11.2. The maximum negative velocity reaches -0.1 U_b and occurs near the center of

the passage. The results are consistent with the characteristics of a two-vortex structure induced by rotation. The positive velocities are expected to occur within 0.1 D from the upper and lower walls.

Figures 4.12.2, 4.13.2, 4.14.2 and 4.15.2 show the tangential and vertical velocity components at x/D = 4, 7, 10 and 12 in vector form. After 4 D, the first pasasge is characterized by counter-clockwise swirl and a corner recirculation. With outward flow and the trips skewed at +45°, the swirl is located on the leading side of the passage. The corner recirculation is on the trailing side and it is compressed to the lower half of the passage. In the absence of rotation the trip strips generated the two-vortex structure shown in Figure 4.12.3. Figure 4.12.4 shows the two-vortex structure expected from rotation. The interaction of these two-vortex structures produces the swirl and corner recirculation characteristics.

At x/D = 7, Figure 4.13.1, the maximum velocity remains at $0.85U_b$. However, the high velocities have divided into two regions. The first region remains in the upper half of the passage, but it has shifted to the trailing surface. This is consistent with the vectors of Figures 4.12.2 and 4.13.2, which indicate tangential convection from the leading to trailing surface along the upper wall. The second pocket is in the lower half of the passage near the leading surface. It is induced by convection from the upper half of the trailing wall to the lower half of the trailing wall, indicated by the vectors.

At x/D = 10, Figure 4.14.1, the maximum velocity remains at 0.85 U_b. The high velocity region at x/D = 10 is more compressed and is closer to the trailing surface than that at x/D = 7. This indicates a net tangential convection from leading to trailing surface.

At x/D = 12 (1 D upstream of the first turn), Figure 4.15.1, the maximum velocity reduces to 0.8 U_b. The high velocity region remains close to the trailing surface and the velocity gradient in the tangential direction has been reduced relative to that at x/D = 10. This is attributed to the aerodynamic contraction induced by the turn and is evident in the results presented below. Acceleration through a contraction reduces asymmetry in the flow.

Figure 4.16 shows the velocities in the first turn. The streamwise velocities, Figure 4.16.1, show that the high velocity region is in the form of a ring. This is attributed to swirl. Figure 4.16.2 shows the tangential and cross-stream velocity components in vector form.

Clockwise swirl (viewed from the downstream direction) is present at the turn. The swirl in the first passage and the first turn are in the same direction (counter-clockwise) when they are viewed from the upstream direction. The swirl level at the turn is higher than that in the first passage. The outward flow on the trailing side is reinforced by the centrifugal force. The momentum is transferred to the inward flow on the leading side by convection.

The swirl at the first turn is much stronger than that in Tse, et al. (1994) and McGrath and Tse (1995) in a turn with a square cross-section. This is partly attributed to the difference between the aspect ratio of the turn and partly to the presence of swirl before the turn. The tangential velocities in the present and the previous investigations are of similar magnitudes. The maximum cross-stream velocities (1.7 U_p) is 260% higher in the present case because of a 100% increase in the aspect ratio of the turn. In the present case, swirl already exists in the first passage, but in Tse, et al. (1994) and McGrath and Tse (1995) the flow is characterized by the two-vortex structure induced by the Coriolis effect. The velocity vector in y/H = -0.8 of Figure 4.16.2 shows that, for a turn with a radius of 3.05 mm, some flow proceeds to the second passage along the leading side of the turn. Tse, et al. (1994) and McGrath and Tse (1995) show that, for a turn with a radius of 15 mm, the flow on the leading side of the turn is convected back to the trailing side along the convex wall.

The corner recirculation zone in the first passage, Figures 4.14.2, 4.14.2, 4.15.2, is compressed to a small region by the expansion of the swirl region, Figure 4.16.2. The strong inward velocity on the leading side acts as a blockage to the flow discharging from the first passage. It induces a contraction and forces the cross-flow to proceed to the second passage along the trailing side. Consequently, the streamwise velocities on the trailing side of the turn are greater than those on the leading side. This is evident in the contours of Figure 4.16.1.

Figures 4.17 to 4.20 show the velocities in the second passage (inward flow passage). At 1 D downstream of the first turn, Figure 4.17.1, the maximum streamwise velocity reaches 0.95U_b (90% above U_p). The high velocity region is located on the trailing side of the passage. The ring structure observed at the turn is also evident at 1 D downstream of the turn. The absence of streamwise recirculation is a striking feature of Figure 4.17.1. The stationary results, Figure 4.5.1, show a strong recirculation region which extends to 0.35 H in the lower half of the passage at this location. Inward flow of the order of the bulk mean

velocity on the leading side of the turn, Figure 4.16.2, fills the velocity deficit and eliminates the recirculation zone.

Figure 4.17.2 shows the tangential and cross-stream velocity components obtained at x/D = 18 in vector form. The vertical components can not be obtained at y/H = +0.8 and only the tangential components are plotted at this location. The secondary flow at 1 D downstream of the first turn is characterized by a clockwise swirl (viewed against the flow). The maximum absolute tangential and vertical velocities reach 0.35 and 0.55 U_b. The swirl is considerably weakened at the exit. The downward force induced by the turn has prevented the swirl from reaching the upper wall.

Figures 4.18.1, 4.19.1 and 4.20.1 show the streamwise velocities at x/D = 20, 25.5 and 27.5. The high velocity region in the second passage is close to the leading (pressure) surface after the 3 D location. This streamwise velocity distribution is consistent with the Coriolis-induced secondary flow. The maximum velocity is reduced from 0.85 U_b at x/D = 20 to 0.80 U_b at x/D = 25.5 and 27.5. The distortions of the high velocity region on the leading side at x/D = 20 stem from separation and re-attachment of cross-flow associated with the trips. The stationary measurements, Figures 4.5.1 and 4.6.1, show that the trips induce a vertical convection from the upper to lower wall. The vertical convection can be seen in the velocity contours between x/D = 20 and 25.5, Figures 4.18.1 and 4.19.1. Comparison of Figures 4.19.1, 4.20.1 and 4.6.1 shows that, with rotation, the contours are distorted in the tangential direction because of the Coriolis effect. The bifurcation of the high velocity region between x/D = 25.5 and 27.5, Figures 4.19.1 and 4.20.1, stems from the upstream effect of the turn. The cross-flow is expected to peak on the convex (low pressure) side before entering a turn.

Figure 4.18.2 shows the tangential and vertical velocity components at x/D = 20 in vector form. The vertical components can not be obtained at y/H = +0.8. Only the tangential components are plotted at this location. In a 1.0" x 0.5" passage with inward flow and trips skewed at +45°, the secondary flow is characterized by a large clockwise swirl on the leading side and a corner recirculation on the upper half of the trailing side. In the absence of rotation the trip strips generate the two-vortex structure shown in Figure 4.18.3. Figure 4.18.4 shows the two-vortex structure expected from rotation. The interaction of these two-vortex structures produces the velocity vectors of Figure 4.18.2. The corner recirculation zone is re-

established within 3 D downstream of the turn. The secondary flow characteristics in a 1.0" x 0.5" passage are consistent with those observed in a 0.5" x 0.5" passage under the same trip orientation and flow direction, Figure 3.19.2. The aspect ratio of the passage does not affect the general nature of the secondary flow.

At x/D = 25.5 and 27.5, Figures 4.19.2 and 4.20.2, the tangential velocity contours are consistent with the clockwise swirl and corner recirculation flow structure described in Figure 4.18.2. The secondary flow in the second passage is characterized by a large clockwise swirl on the leading side and a corner recirculation on the upper half of the trailing side. The results of Tse, et al. (1994) show that, in a 0.5" x 0.5" passage with smooth walls, the swirl induced by the first turn dissipates within 4 D downstream of the turn. Trips skewed at +45° preserve the swirl in the inward flow passage to the end of the passage.

Figure 4.21 shows the tangential and cross-stream velocity components obtained in the second turn in vector form. The secondary flow at the turn is characterized by a large counter-clockwise swirl (viewed against the flow) on the trailing side and a corner recirculation on the leading side near the concave wall. The swirl in the second passage and the second turn are in the same direction (clockwise) when they are viewed from the upstream direction. However, the corner recirculation in the second passage is on the trailing side and that in the second turn is on the leading side. The corner recirculation in the second passage is induced by the trips and it collapses at the turn. The inward flow on the leading side of the second turn is retarded by centrifugal force. This induces a new corner recirculation zone close to the concave surface of the turn.

The corner recirculation in the second turn is much stronger than that in the first turn. Centrifugal force directs flow to the concave surface in the first turn and weakens the corner recirculation. It directs flow away from the concave surface in the second turn and strengthens the corner recirculation. The level of swirl in the first turn is higher than that in the second. This partly stems from retardation of the flow on the leading side by centrifugal force and from the reduction of the Coriolis effect. In the second turn, Coriolis forces are weaker than those in the first turn because the second turn is located at a smaller radial distance from the axis of rotation.

Figures 4.22 and 4.23 show the streamwise velocity contours in the third passage. At x/D = 31.5 and 36.5 (1 and 6 D downstream of the second turn), the high velocity regions reach 1.55 U_b and occur on the trailing side. However, previous results with smooth walls, (Tse, et al. (1994)) have shown rotation increases the maximum streamwise velocity to 1.2 U_b. The results of Tse, et al. (1994) further show that the high velocity region at the exit of a gradual turn with a large radius of curvature is located close to the upper wall. Figure 4.22 shows that the high velocity region is near the lower wall in the ribbed wall passage. This is consistent with the flow visualization obtained in the sharp turn of a stationary passage with a small radius of curvature, Mochizuki, et al. (1994). The present results show that rotation does not alter the vertical distribution of the flow. The high velocity region is shifted laterally to the trailing side, because of rotation. The contours of Figure 4.23 are consistent with those of Figure 3.14.1. The flow characteristics in the third passage of Passage 2 are similar to those in the first passage of Passage 1. This is expected because the trip orientation and flow direction are the same for both of these passages.

4.3 Relationship with heat transfer

No heat transfer measurements in the configuration of Passage 2 are available in the open literature. The velocity measurements presented in the previous subsections will be analyzed in relation to the heat transfer results reported in Wagner, et al. (1991) and Johnson, et al. (1994). Details of each configuration are available in the corresponding publication and the brief summary in Section 3.3. The increase and decrease in heat transfer quoted in sebsequent discussions are relative to the stationary reference Nusselt number, Nu_∞, used in both Wagner, et al. (1991) and Johnson, et al. (1994).

Passages 1 and 2 allow a comparison of using trips skewed at -45° and +45° in the first passage. Skewed trips and rotation induce swirl in the passage and separation and re-attachment of cross-flow in the inter-ribbed region. Figures 4.13.2, 4.14.2 and 4.15.2 show that, for trips skewed at +45°, separation occurs at the upper half of the leading side and at the center of the trailing side. Re-attachment occurs at the lower half of the leading side and at the upper and lower corner at the trailing side. Figures 3.13.2, 3.14.2 and 3.15.2 show

that, for trips skewed at -45°, separation occurs at the center of the leading side and the lower corner of the trailing side. Re-attachment occurs at the upper and lower corner of the leading side. On the trailing side, re-attachment occurs at the upper corner and the center.

The upper half of the leading surface can be a local hot spot with trips skewed at +45°. The center of the leading surface can be a local hot spot with trips skewed at -45°. The streamwise velocities in those regions are low because of the associated secondary flows. In addition, they are regions with separation of cross-flow, which further inhibits surface heat transfer.

Figures 4.15.2 and 4.16.2 show that, with trips skewed at +45°, the secondary flow characteristics remain the same as the flow propagates from the first passage to the first turn. Figures 3.16.2 and 3.17.2 show that, with trips skewed at -45°, the secondary flow characteristics in the first passage and the first turn are different. The corner recirculation zone in the first passage is on the leading side and that in the first turn is on the trailing side. Changes in the secondary flow structure enhance mixing. Trips skewed at -45° induce more effective mixing in the vicinity of the first turn than trips skewed at +45°. The heat transfer results of Johnson, et al. (1994) are obtained with trips skewed at -45°. Their results show that, on the leading side of the first passage, the heat transfer in the last few hydraulic diameters is 20% higher than that in the remaining passage. Based upon these results, the use of trips skewed at -45° in the first passage (outward flow passage) is to be preferred.

Figures 3.16.2, 3.17.2, 4.15.2 and 4.16.2 show that, with trips skewed at +45°, the secondary flow characteristics in the second passage are different from those at the second turn. The corner recirculation zone in the second passage is on the trailing side and that in the second turn is on the leading side. The mixing induced by trips skewed at +45° to the cross-flow is more effective in the vicinity of the second turn than that induced by trips skewed at -45°. The use of trips skewed at +45° is to be preferred in the second passage, the inward flow pasasge.

For Passage 2, Coriolis effects increase the streamwise velocity on the high pressure side of the first and second passages by 10% of the passage mean velocity, Figures 4.14.1 and 4.19.1. They decrease the streamwise velocity on the low pressure side of the first and second

passages by 100 %. Based upon the $Nu\text{-}Re^{0.8}$ correlation, the increase in convective heat transfer from the high pressure surface in the first and second passages is of the order of 8%. The corresponding decrease in convective heat transfer from the low pressure surface in the first and second passages is of the order of 70 %. The relative increase in heat transfer from the high pressure surface associated with convection in Passage 2 is larger than that in Passage 1 (5%), Section 3.3. However, the relative decrease in heat transfer from the low pressure surface associated with convection in Passage 2 is larger than that in Passage 1 (40 to 50%). Rotation induced a steeper streamwise velocity gradient in the tangential direction in Passage 2 than that in Passage 1 because of the reduction in velocity associated with the increase in flow area. The influence of rotation on heat transfer for rectangular passages with an aspect ratio of above unity is higher than that for square passages.

Similar to Passage 1, the overall swirl level at the first turn of Passage 2 is higher than that in the first passage, where the trips are skewed at +45°, Figures 4.13.2, 4.14.2, 4.15.2 and 4.16.2. The increase in swirl level at the turn stems from increases in velocity at the eye of the vortex for both passages. The swirl levels close to the wall are of similar magnitude in the turn and the straight passage. Comparison of the results of Passage 1 and Johnson, et al. (1994), both obtained in 0.5" x 0.5" square passages with trips skewed in the same orientation, shows that augmentation of heat transfer by the re-attachment of cross-flow in the inter-ribbed region is greater than that by swirl. Similar results can be expected with 1.0" x 0.5" passages.

The results of Wagner, et al. (1991) show that, in a square passage with smooth walls, rotation leads to an increase in heat transfer of over 150% in the first turn but an increase of 15% at the second turn. The discussions in Sections 3.2 and 4.2 show that the level of swirl in the second turn is lower than that in the first, Figures 3.16.2, 3.21.2, 4.16.2 and 4.21.2. In addition, the corner recirculation in the second turn is stronger than that in the first. The present results show that there are differences between the secondary flow characteristics in the first and second turn. The differences between the heat transfer in the first and second turns observed by Wagner, et al. (1991) are partly attributed to differences in secondary flow characteristics.

Johnson, et al. (1994) show that, in the first turn, the heat transfer in the smooth wall passage is higher than that in the passage with skewed trips. However, in the second turn, the heat transfer in the smooth wall passage is lower than that in the passage with skewed trips. The cross-stream velocities in the first turn are different from those in Tse, et al. (1994) and McGrath and Tse (1995). The turn configuration and turning radius in both cases are different. However, the results can be analyzed in a qualitative manner. The present results show that the velocities near the eye of the vortex are higher than those Tse et al. (1994) and McGrath and Tse (1995). For flow over ribbed walls, the velocity in the center of the channel can be expected to increase due to momentum losses at each trip. For the smooth wall case, the velocities near the wall are expected to be higher than that with ribbed walls. The decrease in heat transfer (relative to the smooth wall case) in the first turn of a ribbed wall passage is attributed to decreases in velocity near the wall. No data is available from the investigations of Tse, et al. (1994) and McGrath and Tse (1995) in the second turn for comparison.

NOMENCLATURE - CHAPTER 5

A	Wall surface area, ft (m^2)
–A	Pressure drop parameter
B	Temperature increase parameter
D_h	Channel hydraulic diameter, in (cm)
e	Trip strip height, in (cm)
f	Channel friction factor
f_{corr}	Channel friction factor (corrected to 14 trip strip pitches)
f_{pipe}	Turbulent pipe flow friction factor (smooth pipe)
f_{ratio}	Fricton factor ratio
$f_{ratio\ corr}$	Fricton factor ratio (corrected)
h	Heat transfer coefficient, Btu/(hrft^{2}F) W/(m^{2}C)
H	Channel height, spacing between trip strip walls, in (cm)
i	Y–axis grid plane direction for CFD simulations
j	Z–axis grid plane direction for CFD simulations
k	X–axis grid plane direction for CFD simulations
k_{air}	Thermal conductivity of air, Btu/(hrftF) W/(mC)
k	Turbulent kinetic energy
L	Channel length, in (cm)
Nu	Nusselt number
Nu_{pipe}	Turbulent pipe flow Nusselt number (smooth pipe)
Nu_{ratio}	Nusselt number ratio
P	Pressure field
p(x, y, z)	3–d Pressure field
P_{exit}	Channel exit plane pressure, psia (N/m^2)

P_{inlet}	Channel inlet plane pressure, psia (N/m^2)
Pr	Prandtl number
P_{static}	Static pressure, psia (N/m^2)
ΔP	Channel pressure drop, psia (N/m^2)
$\Delta P_{pumping}$	Channel pressure increase from rotation pumping, psia (N/m^2)
p	Trip strip pitch, in (cm)
q	Wall surface heat rate, Btu/hr (W)
R	Ideal gas constant, ft–lbf/(lbm°R) J/(Kmol°K)
Re	Reynolds number
rms	Root mean square component of the channel streamwise velocity
Ro	Rotation number
r_{exit}	Channel exit plane radius (from axis of rotation), in (cm)
r_{inlet}	Channel inlet plane radius (from axis of rotation), in (cm)
rpm	Revolutions per minute
St	Stanton number
St_{ribbed}	Stanton number on (ribbed) trip strip surface
St_{smooth}	Stanton number from smooth wall channel simulation
T	Temperature Field
t(x, y, z)	3–d dimensional temperature field
$T_{air\ inlet}$	Channel inlet plane temperatue, °R (°C)
T_{bulk}	Channel bulk (mass averaged) temperature, °R (°C)
T/c	Thermocouple
tds	Turbulent energy dissipation
TDS	NASTAR non–dimentionalized turbulent energy dissipation

tke	Turbulent kinetic energy
TKE	NASTAR non–dimentionalized turbulent kinetic energy
T_{film}	Fluid film tempertature, $^{\circ}R$ ($^{\circ}C$)
T_{wall}	Channel wall temperatue, $^{\circ}R$ ($^{\circ}C$)
u	Channel x–axis velocity for CFD simulations, ft/sec (m/sec)
U	Channel streamwise bulk velocity, ft/sec (m/sec)
U_{bulk}	Channel streamwise bulk velocity, ft/sec (m/sec)
uinpav	NASTAR reference velocity, ft/sec (m/sec)
V	Channel streamwise bulk velocity, ft/sec (m/sec)
v	Channel y–axis velocity for CFD simulations, ft/sec (m/sec)
W	Channel width, in (cm)
w	Channel z–axis velocity for CFD simulations, ft/sec (m/sec)
x	Channel x–axis direction
ΔX	Channel length, in (cm)
y	Channel y–axis direction
y^+	Dimensionless distance to solid surface
z	Channel z–axis direction

Greek Character

α	Trip strip skew angle, degrees
ε	Turbulent energy dissipation
ω	Rotational speed, radians/sec
ρ	Fluid density, lbm/ft^3 (kg/m^3)

$\Delta \rho$	Difference between fluid bulk and wall densities, lbm/ft^3 (kg/m^3)
ρ_{bulk}	Fluid bulk density, lbm/ft^3 (kg/m^3)
ρ_{wall}	Fluid wall density, lbm/ft^3 (kg/m^3)
μ	Absolute viscosity, lbm/ftsec (kg/msec)

Subscripts

CFD	Computational fluid dynamics
SRA	Scientific Research Associates
UTRC	United Technologies Research Center

5.0 NUMERICAL SIMULATIONS

5.1 OVERVIEW

The objective of this subcontract was to perform benchmark numerical simulations of a rotating (and stationary) internal cooling channel with skewed trip strips and compare them to the experimental velocity field data obtained by the contractor, Scientific Research Associates (SRA) under Task 4 of NAS3–27378. In addition, calculations were run to simulate selected heat transfer data (acquired by the United Technologies Research Center (UTRC) under Task 30 of NAS3–26618).

The computational effort under this task was broken down into two phases. In the first phase, a grid sensitivity study was performed (assuming periodically fully developed flow) on a cooling channel computational domain limited to the region between two adjacent trip strips. The use of this limited domain allowed the grid studies to be performed relatively quickly (compared to full channel simulations). The results from four separate grid–study simulations are presented evaluating the effects of rotation, grid density, and two near–wall treatments of the two–equation k–ϵ turbulence model (ie., wall functions and a two–layer wall integration model).

In the second phase, based on the results from the grid sensitivity study, four trip strip channel simulations (all utilizing the same channel geometry and computational grid) are presented for; 1) a stationary channel with incompressible flow, 2) a stationary channel with compressible flow, 3) a rotating channel with incompressible flow, and 4) a rotating channel with compressible flow. These four simulations allow for comparison to both the incompressible–fluid velocity field data of SRA, and the compressible–flow heat transfer data acquired by UTRC.

5.2 FLOW FIELD INITIALIZATION

One of the major objectives of the numerical simulations was to be able to compare the four trip strip channel simulations to each other, in addition to the velocity field data of SRA and the heat transfer data acquired by UTRC. The velocity field measurements at SRA were performed with an incompressible, isothermal, refractive–index–matching (RIM) fluid, whereas the the UTRC heat transfer experiments were performed using heated air as the working fluid. In order to model all these effects, it was necessary to develop a set of consistent CFD simulation

conditions that were close (but not identical) to either the experimental test conditions of SRA or that of UTRC.

The experimental test rigs used by UTRC and SRA were originally intended to be geometrically identical. However, differences between the rigs were inadvertently created during the rig construction process (see Section 5.3). It was therefore necessary to select one of the rig geometries over the other, in order to create the CFD simulation geometry. Since the velocity flow field initialization conditions were coming from the SRA rig and comparisons to the CFD simulations at exact geometry locations were planned, it was decided to use the SRA rig as the simulation geometry.

Preliminary discussions between NASA Lewis, SRA, UTRC, and P&W had established the experimental flow field conditions would be incompressible (for SRA's RIM fluid) and near incompressible flow for the UTRC heat transfer experiments. However, previous experimental heat transfer studies (Hajek et al., 1991, and Johnson et al., 1993), had shown that centrifugal buoyancy forces (compressible flow density ratio effects) were important factors in rotating channel internal heat transfer flows. With this in mind, and since the convective heat transfer effects could not be simulated using the isothermal SRA fluid test conditions, it was decided to use air as the CFD simulation fluid.

With the choice of the CFD geometry coming from the SRA tests, and the simulation fluid from the UTRC experiments, it was necessary to selectively match the Reynolds number, rotation number, and density ratio for the CFD simulation cases. If the Reynolds numbers conditions for the SRA, UTRC and CFD simulations were identical ie., ($Re_{SRA} = Re_{UTRC} = Re_{CFD}$) then,

$$\left(\frac{\rho U D_h}{\mu}\right)_{SRA} = \left(\frac{\rho U D_h}{\mu}\right)_{UTRC} = \left(\frac{\rho U D_h}{\mu}\right)_{CFD} \quad (1)$$

$$\text{Therefore,} \quad \left(\frac{\rho U}{\mu}\right)_{SRA} = \left(\frac{\rho U}{\mu}\right)_{UTRC} = \left(\frac{\rho U}{\mu}\right)_{CFD} \quad (2)$$

Since all three have the same hydraulic diameter. If it is further assumed that the CFD simulation uses air properties and that only $Re_{CFD} = Re_{SRA}$ then,

$$U_{CFD} = \frac{\rho_{SRA}}{\rho_{CFD}}\left(\frac{\mu_{CFD}}{\mu_{SRA}}\right) U_{SRA} \tag{3}$$

The u, v, w, and streamwise rms values from the SRA data sets are given in terms of,

$$\left(\frac{u}{U_{bulk}}\right)_{SRA} , \left(\frac{v}{U_{bulk}}\right)_{SRA} , \left(\frac{w}{U_{bulk}}\right)_{SRA} , \left(\frac{rms}{U_{bulk}}\right)_{SRA} \tag{4}$$

If we assume the non–dimensionalized velocity and rms ratios of equation (4) are independent of the experimental fluid used, and multiply each by equation (3), the channel inlet plane local grid point initialization values of u, v, w & rms for the CFD simulation become,

$$u_{CFD} = \frac{\rho_{SRA}}{\rho_{CFD}}\left(\frac{\mu_{CFD}}{\mu_{SRA}}\right) U_{SRA}\left(\frac{u}{U_{SRA}}\right) \tag{5}$$

$$v_{CFD} = \frac{\rho_{SRA}}{\rho_{CFD}}\left(\frac{\mu_{CFD}}{\mu_{SRA}}\right) U_{SRA}\left(\frac{v}{U_{SRA}}\right) \tag{6}$$

$$w_{CFD} = \frac{\rho_{SRA}}{\rho_{CFD}}\left(\frac{\mu_{CFD}}{\mu_{SRA}}\right) U_{SRA}\left(\frac{w}{U_{SRA}}\right) \tag{7}$$

$$rms_{CFD} = \frac{\rho_{SRA}}{\rho_{CFD}}\left(\frac{\mu_{CFD}}{\mu_{SRA}}\right) U_{SRA}\left(\frac{rms}{U_{SRA}}\right) \tag{8}$$

where $U_{SRA} = (U_{bulk})_{SRA}$. Now, if the Rotation numbers for the SRA, UTRC and CFD simulations were identical ie., ($Ro_{SRA} = Ro_{UTRC} = Ro_{CFD}$), where H is the spacing between the trip strip walls then,

$$\left(\frac{\omega H}{U}\right)_{SRA} = \left(\frac{\omega H}{U}\right)_{UTRC} = \left(\frac{\omega H}{U}\right)_{CFD} \tag{9}$$

where,

$$\omega = \frac{2\pi \text{ rpm}}{60}$$

Assuming for the CFD simulation that only $Ro_{CFD} = Ro_{SRA}$ and solving equation (9) for U_{CFD} then,

$$U_{CFD} = \left(\frac{rpm_{CFD}}{rpm_{SRA}}\right) U_{SRA} \tag{10}$$

Finally, using the definition of the density ratio from Hajek et al., 1991,

$$\frac{\Delta \rho}{\rho} = \left(\frac{\rho_{bulk} - \rho_{wall}}{\rho_{bulk}}\right) = \left(\frac{T_{wall} - T_{bulk}}{T_{wall}}\right) \tag{11}$$

Assuming for the CFD simulation that only $(\Delta\rho/\rho)_{CFD} = (\Delta\rho/\rho)_{UTRC}$ then,

$$\left(\frac{\Delta \rho}{\rho}\right)_{CFD} = \left(\frac{T_{wall} - T_{bulk}}{T_{wall}}\right)_{UTRC} \tag{12}$$

The following table summarizes the dimensional and non–dimensional parameters used for all the skewed trip strip 3–d channel (and channel segment) flowfield CFD simulations.

Table 5.1 Dimensional & Non–Dimensional CFD Simulation Flow Parameters

	SRA	UTRC	CFD Simulations
mass flowrate lbm/sec (kg/sec)	1.0932 (0.4958)	0.01308 (0.00593)	0.01259 (0.00571)
rpm rev/min	–617	–600	–555
P_{static} psia ($N/m^2 x 10^{-6}$)	—	145.18 (1.001)	133.42 (0.920)
T_{bulk} ^oR (^oC)	538.49 (26.0)	504.64 (7.19)	504.64 (7.19)
T_{wall} ^oR (^oC)	538.49 (26.0)	532.98 (22.94)	532.98 (22.94)
T_{film} ^oR (^oC)	538.49 (26.0)	518.81 (15.07)	518.81 (15.07)
ρ_{bulk} $slug/ft^3$ (kg/m^3)	1.7328 (893.0)	0.02414 (12.44)	0.022184 (11.43)
U_{bulk} ft/sec (m/sec)	11.295 (3.443)	9.700 (2.956)	10.1602 (3.097)
Ro	0.2384	0.2699	0.2384
μ lbm/ftsec (kg/msec)	0.001044 (0.00155)	$1.203x10^{-5}$ ($1.79x10^{-5}$)	$1.203x10^{-5}$ ($1.79x10^{-5}$)
Re	25,125.4	26,096.9	25,125.4
$\frac{\Delta \rho}{\rho}$	—	0.0532	0.0532

5.3 EXPERIMENTAL RIG GEOMETRY DIFFERENCES

The experimental test rigs used by UTRC and SRA were originally intended to be geometrically identical. However, differences between the rigs were inadvertently created during the rig construction process. Figure 5.1 shows the original rig design drawings from UTRC. The views shown of the leading and trailing sides of the model (for this and the following figures) are what one would see from the outside of the rig looking through the clear model walls to the inside surface.

Figure 5.2 shows photographs of the leading and trailing sides of UTRC heat transfer rig that was constructed. Also shown are the the UTRC wall thermocouple locations 7, 8, 9, & 10. Figure 5.3 shows photographs of the leading and trailing sides of SRA rig that was constructed, along with an overlay of the SRA experimental velocity plane locations for the stationary (A1 & A2), and rotating (D1, D2, & D3) test cases that fall within the CFD simulation computational domain. Figure 5.4 shows the differences between the UTRC and SRA experimental rigs.

5.4 COMPUTATIONAL PROCEDURES

The governing equations of continuity, momentum, and energy were solved using the Pratt & Whitney Navier–Stokes code, NASTAR (Rhie, 1986). This is a pressure–based implicit procedure which solves the full Navier–Stokes equations in general coordinates, thus allowing the use of body–fitted coordinate systems. In Rhie's approach, the preliminary velocity field is first obtained from the momentum equations with a preliminary pressure field. Since this preliminary velocity field does not satisfy the continuity equation, pressure correction equations are solved to establish a new velocity field which does satisfy the continuity equation. The momentum and continuity equations are coupled through this pressure correction procedure. Then, the energy and turbulent scalar equations are solved in turn. Two near–wall shear–stress treatments were evaluated (during the grid sensitivity study) in conjunction with the two–equation k–ϵ formulation of turbulence. In one case, the governing equations near the wall were solved by employing generalized wall functions which assume that the boundary layer velocity profile has a universal "law–of–the–wall" profile (Launder and Spaulding, 1974). In the other case, the two–layer wall integration method was used in which the governing equations are solved to the wall

(Dash et al., 1983). Near the wall, the classical Van–Driest mixing length formulation was used. This region was patched with the two–equation k–ε turbulence model at $y^+ = 50$.

In the initial phase of this project, some numerical convergence difficulties were experienced due to the severely skewed grid topology which is natural to the skewed trip strips. The original version of NASTAR used a three step pressure correction procedure, where the skewed grid effect on the Poisson–like pressure equation was lagged as a explicit source term. One pressure correction step was devoted to treat this lagging explicit source term. To fix the convergence problem, the skewed grid effect was solved implicitly so that there was no lagging effect during the iterations. The pressure correction procedure was thus modified into a two step procedure, but the skewed grid effect was solved implicitly during each step to determine the local 19–point finite volume relationship.

5.5 GRID SENSITIVITY STUDY

One of the obstacles to the use of CFD for airfoil internal cooling design (with the current generation of computer resources) is the large amount of computational grid required in order to model the entire highly complex 3–dimensional flow path, at a sufficient resolution to obtain a grid independent solution. However, internal cooling schemes often make use of geometries that contain streamwise repeating geometric patterns (like trip strips). In an effort to take advantage this "repeating" geometry, the grid sensitivity study was performed by assuming periodically fully developed flow on a cooling channel computational domain limited to the region between two adjacent trip strips (see Figure 5.10). The use of this limited domain allowed the grid sensitivity studies to be performed relatively quickly (compared to full channel simulations).

First, a general discussion of the periodically fully developed "conveyor–belt" boundary condition logic is presented. Next, results are presented from a 2–d channel simulation study used to evaluate the "conveyor–belt" type boundary condition capabilities of NASTAR. Finally, four separate (compressible flow) 3–d skewed trip strip grid–study simulations are presented, evaluating the effects of rotation, grid density, and two near–wall treatments of the two–equation k–ε turbulence model (ie., wall functions and a two–layer wall integration model).

5.51 Periodically Fully Developed "Conveyor–belt" Boundary Conditions

As part of a separately funded P&W effort, NASTAR was modified to allow for periodically fully developed type inlet and exit plane boundary conditions. The general idea behind this boundary condition logic is that the flow, temperature, and pressure fields are assumed to be periodic over a streamwise repeating geometric pattern. Boundary condition information at the exit plane of the computational domain is used to create the inlet plane conditions (as though the boundary conditions were being passed upstream on a conveyor belt). This approach described by (Liou and Chen 1995), presents a relationship for the pressure and temperature field as,

$$P = -Ax + p(x, y, z) \tag{13}$$

$$T = Bx + t(x, y, z) \tag{14}$$

Where the pressure drop parameter A and the temperature increase parameter B are constants. The term –Ax is related to the global mass flow (or Reynolds number) and represents the general decrease in pressure in the streamwise direction. For the case of heating, it can be shown that the term Bx is related to the rate of heat addition (per unit span) to the fluid in one streamwise repeating geometry pitch. The functions P and T repeat themselves identically from pitch to pitch and indicate the local departure from linear pressure decay given by –Ax, and linear temperature increase given by Bx.

In the present calculation, the –Ax and Bx terms are iterated on to satisfy the global mass and heat balances. The exit plane static pressure and static temperature profiles, as functions of the exit plane coordinates (y, z) are injected back to the inlet plane as boundary conditions with the corrections to the –Ax and Bx terms respectively.

5.52 2–d Channel "Conveyor–belt" Boundary Condition Evaluation Study

In order to evaluate the "conveyor–belt" boundary condition capabilities of NASTAR, (prior to its application for the grid sensitivity study), a simplified 2–dimensional, square trip strip profile, non–rotating, version of the 0.5 inch (1.27 cm) high trip strip channel geometry was created (see Figure 5.5). This figure shows two views of the same computational grid. The simulated channel is 3.5 inches (8.89 cm) long by 0.5 inches (1.27 cm) high (H), and has 8 trip strips in

an alternating pattern on the upper and lower walls. The trip strip pitch (p) is 0.25 inches (0.635 cm), and the square trip height (e) is equal to 0.05 inches (0.127 cm). This yields a value of p/e = 5 and e/h = 0.1. The incompressible flow conditions are presented in the following table.

Table 5.2 2–d Channel (Conveyor–belt BC) Evaluation Study Parameters

$\mu = 3.9533 \times 10^{-7}$ slug/ftsec $(5.8824 \times 10^{-7}$ kg/msec)	Re =16,600.
$\rho = 0.027429$ slugs/ft^3 (14.14 kg/m^3)	$T_{air\ inlet} = 450^{\circ}$R $(-10^{\circ}$F) $(-23.3^{\circ}$C)
$U_{bulk} = 4.3078$ ft/sec (1.313 m/sec)	$T_{wall} = 661^{\circ}$R $(201^{\circ}$F) $(93.9^{\circ}$C)

These parameters correspond to test condition (402) of UTRC's contract NAS3–26618 Task 30 (Wagner 1994). For the purposes of this simulation, a dense rectangular grid (1400x99 with 30 grids over the trip height) was used. No attempt was made to control y^+ values evenly along the wall and trip surface. The purpose here, was to define a "fully developed" flow field solution for a fixed grid, that could be used to compare results generated from a separate "conveyor–belt" boundary condition simulation of a local section of the same trip strip geometry.

Figure 5.6a shows the streamwise component velocity contours generated by NASTAR for this 2–d grid. Figure 5.6b shows the same contours with the height of the channel expanded in order to show the details of the flow field near the trip strip surfaces.

Figure 5.7 shows the 2–d channel velocity contours near trip strips 5, 6, and 7, compared to those resulting from the "conveyor–belt" logic applied to a single trip strip pitch segment of the same geometry. Results from both a 2–d segment (and a center spanwise slice of a 3–d segment) are shown. Excellent agreement in the near wall velocity contours patterns is seen between these three cases. The differences in the channel midspan contours are attributed to different iteration counts (and therefore slightly different global mass balances) between the runs, which were not held strictly constant for these proof–of–concept simulations.

Figure 5.8 shows a comparison of the static pressure contours. The absolute level of the static reference pressure was set differently for the 2–d channel simulation (set at the channel exit), and the conveyor–belt simulations (set at the segment inlet). However, the contour patterns and relative high to low contour pressure delta's are very consistent. A small discontinuity

observed in the 2–d "conveyor–belt" simulation velocity and pressure contours (at an internal streamwise parallel–process break–up plane), was eliminated in the 3–d simulation. Figure 5.9 shows a similar comparison of the static temperature contours. Once again, excellent agreement in the temperature contour patterns is seen between these cases.

5.53 3–d Skewed Trip Strip Grid Sensitivity Study

Based on the successful results obtained from the 2–d channel evaluation study, efforts were then shifted to the application of the NASTAR "conveyor–belt" logic for the grid sensitivity study. Four separate 3–d skewed trip strip (compressible flow) grid–study simulations are presented evaluating the effects of rotation, grid density, and two near–wall treatments of the two–equation k–ε turbulence model (ie., wall functions and a two–layer wall integration model).

Figure 5.10 shows a plan view of one side of the 4–leg test rig geometry, and a 3–d orientation view of the (single trip strip pitch) channel segment grid for the conveyor–belt simulation. The grid segment shown has i, j, k, dimensions of 66x39x39. Also shown is a detail view of the grid geometry near the trip strip (as seen from inside the channel segment). A number of different grid density schemes were considered for the conveyor–belt segment domain based on an initial review of two previous internal cooling channel heat transfer studies.

In the first study (by Tse et al., 1994) a smooth square channel geometry (with no trip strips) was simulated using a two–equation k–ε turbulence model with wall integration and a jxk grid dimension of 59x59. The distance between the wall and the first grid point off the wall was 0.0002 inch which corresponded to a y^+ of approximately 0.5. In the second study, (Stephens et al., 1995) used a low Reynolds number k–ω turbulence model formulation for a skewed trip strip channel geometry; p/e = 5, e/H = 0.1, H/W = 1.0, α = 45 degrees, (identical to the current study) containing an alternating pattern of 5 skewed trip strips on the top and bottom channel walls. That simulation had a jxk grid dimension of 65x65 and y^+ values at the wall of less than 1.0.

The grid densities that were indicated by the two studies above, had to be weighed against the need in the current contract effort, to be able to compare to as many SRA velocity field data planes (downstream of the channel inlet) as was feasible for the four subsequent channel simulations (see discussion in Section 5.6). It was decided that a practical upper limit for the i, j, k, conveyor–belt segment domain (that could be duplicated for the 15 trip strip channel simulation

geometries) was 66x39x39. A denser conveyor–belt grid domain of 92x49x49 was also selected for evaluation as part of the grid sensitivity study.

Figure 5.11 shows secondary flow velocity field results (looking downstream along the positive y–axis at i–plane = 1) for the four separate (compressible flow) conveyor–belt simulations. The dimensional and non–dimensional flow parameters for these CFD simulations were previously presented in Table 5.1. View (a) shows the results obtained from a stationary channel segment using wall integration and a grid density of 92x49x49. Two clearly defined major vortices are observed. The upper vortex rotates in the counter–clockwise direction, whereas the lower vortex rotates clockwise. These vortices are created by the alternating skewed trip strip pattern on the channel segment's upper and lower wall surfaces. View (b) shows the effect of rotation. The upper vortex is moved down and the the left and the lower vortex is moved both down and to the right. The displacement of the vortices is a consequence of the addition of the Coriolis forces acting on the flow field that were induced by rotation.

Figure 5.11 view (c) shows the same simulation conditions as view (b) except that the channel segment grid density has been reduced to 66x39x39. The secondary flow patterns are very similar to that shown view (b), with the vortex relative position and size being nearly identical. View (d) shows the effect of using wall functions compared to wall integration (in view (c)) for a the same rotating flow conditions and a similar 67x31x31 size grid. The relative placement, size, and strength of the vortices is completely different for the wall function case. In addition, the secondary flow vortices are rotating in the opposite directions.

The y^+ values on the upper and lower surfaces of the wall function simulation view (d), ranged mostly between 30 and 60, with some small localized regions going as low as 10. The y^+ values for the wall integration case view (c), were almost all less than one except for a extremely small region on the top of one side of the trip strip (where the values increased to 1.5). Based on these results, and those that are presented in Section 5.65 (showing good agreement between view (c) and the rotating compressible flow channel simulations), the following conclusions were reached.

It appears that the use of wall functions for this trip strip geometry produces entirely un–reliable secondary flow velocity field results, and it was recommended that they not be used for

the full channel simulations. The wall integration grid 66x39x39 of Figure 5.11 view (c) appeared to produce results very similar to that of view (b). Although the grids of both views (c & b) were less dense than that recommended by (Tse et al., 1994 and Stephens et al., 1995), it was felt that for practical considerations that the upper limit for jxk that could be duplicated (and run in a reasonable time frame) for the four 15 trip strip channel simulation geometries was 39x39.

5.6 SKEWED TRIP STRIP CHANNEL SIMULATIONS

Based on the results from the grid sensitivity study presented in the previous section, four skewed trip strip channel CFD simulations (all utilizing the same channel geometry and computational grid) are presented for: 1) a stationary channel with incompressible flow, 2) a stationary channel with compressible flow, 3) a rotating channel with incompressible flow, and 4) a rotating channel with compressible flow. These four simulations are then compared to both the incompressible–fluid velocity field data of SRA, and the available compressible–flow heat transfer data acquired by UTRC.

5.61 Channel Geometry and Data Comparison Format

Figure 5.12 shows a 3–dimensional outline view of the skewed trip strip channel geometry. This view shows the locations of the SRA stationary (A1 & A2), and rotating (D1, D2, & D3) velocity field data planes (shown previously in Figure 5.3). Note that locations A1 & D1 are at the same relative channel location (as are A2 & D3). It also shows the (relative) wall–thermocouple locations T/c 7, 8, 9, & 10 from the UTRC test geometry. The thermocouple locations are relative to the channel trip strips that they are nearest to in the figure. The actual locations of the thermocouples (shown previously in Figure 5.2) could not be depicted in Figure 5.12 due to the differences in the SRA and UTRC test rig geometries. In addition, Figure 5.12 shows that the simulation geometry contains 15 trip strips on the lower (or rotating leading) side surface, and 14 trip strips on the upper (or rotating trailing) side surface. The location of i–plane 760 is also shown (and will be discussed in connection with Figure 5.27 later).

Figure 5.13 shows a 3–dimensional view of the skewed trip strip channel geometry grid. The channel has a i, j, k, grid domain of 1123x39x39 for a total of 1,708,083 grid points. The channel height (H) is 0.5 inches (1.27 cm), the channel width (W) is 0.5 inches (1.27 cm), the channel length (L) is 4.79 inches (12.17cm), the trip strip pitch (p) is 0.25 inches (0.635 cm), and

the trip strip height (e) is 0.05 inches (0.127 cm). This yields a value of p/e = 5, e/h = 0.1, H/W = 1.0 and a trip strip skew angle (α) equal to 45 degrees. In Figure 5.13, only every 4th i–plane is shown (presenting all the i–planes would make the geometry grid look almost black at this scale).

Figure 5.14 shows a view of the computational grid looking along the streamwise (positive y–axis) direction at (a) the channel "inlet" locations (A1 & D1), and (b) at the downstream data comparison plane locations (A2, D2, and D3). These views represents the readers orientation in Figures 5.15 thru 5.25 where the channel simulations will be compared to the SRA velocity field data. Note, view (b) is an interpolated "slice" of the channel grid at a constant y–axis location, and has had selected i and k–plane grid locations removed for the sake of clarity.

Each of the four 1,708,083 grid point channel simulations was broken into 18 separate calculation domains, and run simultaneously (for a total of 72 workstation slaves) on a Sparc–20 workstation parallel–process network at P&W. The calculations were run off–shift at night and on weekends for a total of 15 calender days to an average of 9,200 iterations. The relatively high iteration count was used to ensure the flow and thermal fields were converged for these benchmark simulations.

The dimensional and non–dimensional flow parameters for all four channel CFD simulations were previously presented in Table 5.1. It should be re–iterated here that it was necessary to develop a set of consistent CFD simulation conditions that were close (but not identical) to either the experimental test conditions of SRA or that of UTRC (see the discussion in Section 5.2). All the non–dimensional velocity field data sets provided by SRA,

$$\left(\frac{u}{U_{bulk}}\right)_{SRA} , \left(\frac{v}{U_{bulk}}\right)_{SRA} , \left(\frac{w}{U_{bulk}}\right)_{SRA} \tag{15}$$

Where $(U_{bulk})_{SRA} = U_{SRA}$, were multiplied by the constant value of,

$$U_{CFD} = \frac{\rho_{SRA}}{\rho_{CFD}}\left(\frac{\mu_{CFD}}{\mu_{SRA}}\right) U_{SRA} = 0.89953\, U_{SRA} \tag{16}$$

in order to obtain the local velocity field values of u_{CFD}, v_{CFD}, and w_{CFD}. Therefore the magnitude of the SRA data sets shown in this section will be ~10% smaller than that presented in the other sections of this final report.

The reference velocity used in the NASTAR non–dimensionalization process (uinpav) was required to be set to $10U_{CFD}$ (in order to maintain the accuracy of the other NASTAR non–dimensional terms). Since the SRA reference velocity U_{SRA} and the NASTAR reference velocity $10U_{CFD}$ were not consistent, it was decided to present all the velocity field results as a consistent set of dimensional (ft/sec) values. This was done in order to avoid both the time and complexity required in post processing all the information into a common non–dimensional form (as an additional step following the completion of the channel calculation effort).

The non–dimensional rms data set values provided by SRA in equation (4), are presented as NASTAR non–dimensionalized values of turbulent kinetic energy (TKE) and turbulent dissipation (TDS) by using the following equations,

$$\text{tke} = 1.5\left(\frac{\rho_{SRA}}{\rho_{CFD}}\left(\frac{\mu_{CFD}}{\mu_{SRA}}\right) U_{SRA}\left(\frac{\text{rms}}{U_{SRA}}\right)\right)^2 \tag{17}$$

$$\text{tds} = \frac{0.09\,\text{tke}^{1.5}}{0.03\,D_h} \tag{18}$$

$$\text{TKE} = \frac{\text{tke}}{\text{uinpav}^2} \tag{19}$$

$$\text{TDS} = \frac{12.0\,\text{tds}}{\text{uinpav}^3} \tag{20}$$

Where,

$\text{uinpav} = 10.0\,U_{CFD}$

D_h = channel hydraulic diameter

5.62 (Stationary Channel) Simulations Compared to SRA Data

Figures 5.15 thru 5.18 present the CFD calculated (incompressible and compressible) flow field values of u, v, w, (in the x, y, z directions) and NASTAR non–dimensional TKE & TDS, compared to the SRA stationary channel data at locations A1 & A2. Figure 5.15 shows the three components of velocity (u, v, w), the secondary flow velocity vector field, and TKE & TDS

at location A1. The SRA data sets and the CFD simulations are identical at this location, since the data (interpolated to the CFD grid) was used as the simulation inlet plane boundary conditions.

Figure 5.16 shows a comparison of the secondary flow velocity vector fields and the u–component of velocity at location A2. The SRA velocity vector field shows two clearly defined major vortices. The upper vortex rotates in the counter–clockwise direction, whereas the lower vortex rotates clockwise. These vortices are created by the alternating skewed trip strip pattern on the channel segment's upper and lower wall surfaces. The calculated incompressible (and nearly identical) compressible velocity vector fields also show the same two major vortices. The direction of vortices' rotation is the same as the data. However, the center of the upper vortex has been shifted to the left and upwards, and the lower vortex has been shifted to the left and downwards. The motion along the channel walls is similar, however the calculations show higher values at the wall surfaces in many locations.

This difference at the walls, could be in part due to the sparse nature of the SRA data sets (near the walls). In order to interpolate the SRA data to the much denser CFD grid, values of the SRA velocity components had to be linearly interpolated between the closest data plane and the wall (where the value was set to zero). Unfortunately, this also appears to be a location where there is a high gradient in the calculated flow field. These differences are probably un–avoidable in the near wall region (for the calculations presented in this report) and reflect the need (in future efforts) for more data in the near–wall region.

It should be noted that the "wavey" nature of the calculated velocity vectors fields (is in part) due to the grid structure at the interpolated grid "slice" location (see Figure 5.14b). One has to be careful to separate out this "wavey" grid effect from the size and direction of the vectors when interpreting the results. In hindsight, it would probably have been better not to let the trip strip surface shape propagate beyond the channel midplane location during the grid generation process.

Figure 5.16 also shows a comparison of the u–component of velocity at location A2 (that along with w–component, makes the velocity vector plots that were just described). The u–components are all plotted to the same velocity scale, and show very similar patterns. The data shows a region of high +u velocity just left of the center of the channel. For the calculations, this value is

reduced slightly and shifted to the left. The –u velocities are more pronounced for the calculations in the near wall region. However, the overall agreement between data and the calculations is very good.

The incompressible and compressible calculated velocity component results are virtually identical for this (and the other following stationary channel comparisons). This result (of the calculations being independent of the density variation) is expected for non–rotating flows dominated by forced convection (see Hajek et al., 1991). Therefore, for the stationary channel comparisons, no further comment will be made between the two calculated results.

Figure 5.17 shows a comparison of the v–component and w–component velocities at location A2. The SRA data shows a region of high v velocity along the right hand side of the channel. This is consistent with the two counter–rotating secondary flow vortices (described in Figure 5.16) forcing the streamwise flow to the right and piling it up along the right hand side wall. The calculations also show this effect, at a slight lower level of velocity. The overall velocity levels are quite comparable, however the horseshoe (on its side) pattern of the v–component data is more pronounced than the calculated results. The w–component of velocities agree quite well in the location of high and low velocity regions. However, the gradients are more pronounced in the data than in the calculations.

Figure 5.18 shows a comparison of the TKE and TDS values at location A2. The SRA data shows high values of TKE and TDS along the trips strip wall surfaces with medium to low regions spanning across the channel mid–section. The simulations also show high regions near the trip strip surfaces with low values dominating the mid–channel core area. In general, the simulations appear to underpredict TKE and TDS in the channel mid–section core area.

5.63 (Rotating Channel) Simulations Compared to SRA Data

Figures 5.19 thru 5.25 present the CFD calculated (incompressible and compressible) flow field values of u, v, w, (in the x, y, z directions) and NASTAR non–dimensional TKE & TDS, compared to the SRA rotating channel data at locations D1, D2 & D3. Figure 5.19 shows two (v & w) of the three components of velocity, (the w–component of) the secondary flow velocity vector field, and TKE & TDS at location D1. The SRA data sets and the CFD simulations are identical at this location, since the data (interpolated to the CFD grid) was used as the simula-

tion inlet plane boundary conditions. Unfortunately, SRA was not able to experimentally acquire the u–component of velocity at this data plane. Therefore, the inlet boundary conditions reflect arbitrarily setting the u–component equal to zero everywhere at location D1.

Figure 5.20 shows a comparison of the secondary flow velocity vector fields and the u–component of velocity at location D2. Unfortunately, the SRA velocity vector field reflects only w–component (SRA was not able to experimentally acquire the u–component of velocity). The calculated incompressible (and nearly identical) compressible velocity vector fields show three major vortices. A large counter–clockwise rotating vortex dominates the channel mid–section region. Beneath this vortex are two smaller clockwise–rotating vortices that fall in the near wall region between the trip strips.

Figure 5.20 also shows a comparison of the u–component of velocity at location D2. The calculations show a region of high +u velocity in the lower left hand side of the channel, with high values of –u along the trip strip wall regions. There are only very minor differences observed between the incompressible and compressible flow simulations.

Figure 5.21 shows a comparison of the v–component and w–component velocities at location D2. The SRA data shows a region of high v–component velocity extending along the upper and right hand sides of the channel (and reaching a maximum value along the lower right side). This is consistent with a large counter–clockwise rotating secondary flow vortex forcing the streamwise flow to the right and piling it up along the upper and right hand side walls. The calculations also show these effects, with the compressible flow simulation reaching slightly higher levels. The w–component of velocities agree quite well in the location of high and low velocity regions, except along the upper right side wall. The calculations indicate a region of high +w that is not observed in the data.

Figure 5.22 shows a comparison of the TKE and TDS values at location D2. The SRA data shows high values of TKE and TDS along the trips strip wall surfaces with a medium level region spanning along the left hand side of the channel. The simulations also show high regions near the trip strip surfaces, low values dominating the mid–channel core area, and sightly elevated values along the left hand side wall. In general, the simulations appear to underpredict TKE and TDS in the channel mid–section core area.

Figure 5.23 shows a comparison of the secondary flow velocity vector fields and the u–component of velocity at location D3. The SRA velocity vector field data shows two clearly defined major vortices. The large upper vortex rotates in the counter–clockwise direction, whereas the smaller vortex rotates clockwise in the lower wall region between the middle and right hand side trip strips. These vortices are created by the alternating skewed trip strip pattern on the channel segment's upper and lower wall surfaces, interacting with the Coriolis forces that were induced by rotation. The calculated incompressible (and nearly identical) compressible velocity vector fields also show the same two major vortices, plus an third clockwise rotating vortex located in the lower channel region between the left side and middle trip strips. The direction of the first two vortices' rotation is the same as the data. However, the center of the upper vortex has been shifted to the left and upwards, and the second vortex has been shifted to the left and downwards. The motion along the channel walls is similar, however the calculations show higher values at the wall surfaces in many locations (see the previous discussion of Figure 5.16 about the problems in interpolating the SRA data between the wall and the nearest channel data plane).

Figure 5.23 also shows a comparison of the u–component of velocity at location D3. The data shows a region of high +u velocity in the lower left hand region of the channel. For the calculations, this value is reduced slightly. The –u velocities are more pronounced for the calculations in the trip strip wall regions. However, the overall agreement between data and the calculations is very good. It is also interesting to note that the calculated u–component values (and secondary flow velocity vector fields) at locations D2 and D3 are almost identical.

Figure 5.24 shows a comparison of the v–component and w–component velocities at location D3. The SRA data shows a region of high v–component velocity extending along the upper mid–portion of the channel (with two distinct local maximum regions). The calculations also show this overall pattern, with the compressible flow simulation reaching slightly higher levels of velocity. The w–component of velocities agree fairly well in the overall location of high and low velocity regions. However, the region of +w velocity seems to be underpredicted in the calculations.

Figure 5.25 shows a comparison of the TKE and TDS values at location D3. The SRA data shows high values of TKE and TDS along the trips strip wall surfaces with a medium level region spanning along the upper and left hand sides of the channel. The simulations also show high regions near the trip strip surfaces, low values dominating the mid–channel core area, and sightly elevated values along the left hand side wall. In general, the simulations appear to under-predict TKE and TDS in the channel mid–section core area.

5.64 3–dimensional Streakline Particle Trace Comparisons

In order to gain additional insight into the velocity flow fields calculated by the channel simulations, Figure 5.26 shows 3–d streakline particle trace comparisons for both the stationary and rotating incompressible flow simulations. The traces, which are represented as ribbons (in order to show the local "twisting" nature of the flow) are introduced at the inlet plane (i = 1).

Four different color traces are presented at the following (j, k) grid point locations. Blue; at 10,30 20,30 and 30,30. Pink; at 10,20 20,20 and 30,20. Green; at 10,10 20,10 and 30,10. And finally Purple; at 15,15 15,25 25,15 and 25,25. There are a lot of interesting detail features shown by the traces. Two general observations are noted here. First, there are dramatic differences caused by rotation (as should be expected by the discussion of the previous section). Secondly, its interesting to note that the particle motions do not appear to "repeat" their pattern over the length of the channel. This indicates that the single trip strip pitch "conveyor–belt" assumption, although very useful for the grid sensitivity study, does not completely capture the full channel trip strip flow field effects.

5.65 "Conveyor–belt" Segment Versus Channel Simulations

It is of interest to compare the "conveyor–belt" simulation grid study results of Figure 5.11 view (c), to that of the rotating compressible flow channel simulation. Figure 5.27, view (a) shows the secondary flow velocity fields for the rotating channel compressible flow simulation at i–plane = 760 (see Figure 5.12), compared to view (b) which shows the "conveyor–belt" rotating channel segment simulation, which had the same compressible flow conditions, wall integration scheme, and grid geometry. Both views show two clearly defined vortices, that are in similar channel locations and rotating in the same fashion. The upper vortex appears to be almost the same relative location, whereas the lower vortex for the channel simulation view (a), is shifted

slightly down and toward the lower left hand side of the channel. It should also be noted that the small differences between views (a & b), could in part be related to the fact that the radial (y–axis location) for the "conveyor–belt" simulation inlet i–plane, was at y = 26.314 inches (66.83 cm) versus 24.5475 inches (62.35 cm) for channel simulation. This difference occurred due to the fact that the "conveyor–belt" segment location was determined prior to the point where it was decided that the channel simulations would not extend to that radial location (due to the additional computational grid required). Due to the difference in the radial locations, the flow field will be modified slightly by a change in the induced centrifugal acceleration.

However, that being said, the agreement between these two simulations is excellent, especially when you consider that the "conveyor–belt" simulation had a computational domain of 100,386 grid points (less than 6%) of the 1,708,083 grid points required for the full channel simulation. Clearly, the "conveyor–belt" boundary condition logic worked well, and has the potential for providing insight to streamwise repeating geometry flows well beyond the scope of the grid sensitivity results presented here.

5.66 Heat Transfer Results

Once the four channel simulations had been completed, the resulting NASTAR output files were post–processed in order to acquire heat transfer information. A local channel heat transfer coefficient was defined as,

$$h = \frac{q}{A\,(T_{wall} - T_{air\ inlet})} \tag{21}$$

Where T_{wall} was set to a constant value of wall temperature (see Table 5.1), and $T_{air\ inlet}$ was defined as the integrated average inlet plane static temperature. The heat transfer coefficient can be written in a non–dimensionalized Nusselt number form as,

$$Nu = \frac{h\,D_h}{k_{air}} \tag{22}$$

Where, D_h is the channel hydraulic diameter, and where the air properties are based on the average of the wall and air–inlet temperatures. The Nusselt number can be represented as non–dimensionalized Nusselt number ratio by using the fully developed turbulent pipe flow equation,

$$Nu_{pipe} = 0.021\,Re^{0.8}\,Pr^{0.6} \tag{23}$$

$$Nu_{ratio} = \frac{Nu}{Nu_{pipe}} \tag{24}$$

The heat transfer results are presented in terms of this Nusselt number ratio.

Figure 5.28 shows a comparison of the stationary (and rotating channel) Nusselt number ratios for the incompressible flow simulations. Results are presented for the upper (trailing side) and lower (leading side) channel surfaces. View (a) shows for the upper stationary channel surface, and the decay in Nusselt number ratio just downstream of the channel inlet plane. This effect is caused as the thermal boundary layer grows from its initial starting point at the channel inlet. The secondary flow induced by the skewed trip strip pattern, then creates the classical "high h" regions downstream of each of the trip strips. These patterns are caused as the upper channel counter–clockwise secondary flow vortex (see Figure 5.16) is driven into the upper wall surface and thins the local thermal boundary layer. Nusselt number ratio patterns observed in views (b), (c), and (d), are the result of similar interactions between the induced secondary flow vortices and the trip strip wall surfaces.

Figure 5.28 view (c) show the effect of rotation for the trailing side channel surface. Nusselt ratios are increased over that of the stationary case . View (d) shows a decrease in the Nusselt ratios relative to the stationary channel (a quantitative comparison of these effects is presented later in the discussion of Figures 5.30 thru 5.35). This increase on the trailing side trip strip surface, and decrease on the leading side surface is consistent with the trends shown in the experimental results of Johnson et al., 1993.

Figure 5.29 shows a comparison of the stationary (and rotating channel) Nusselt number ratios for the compressible flow simulations. Results are presented for the upper (trailing side) and lower (leading side) channel surfaces. The compressible flow results are nearly identical to

the incompressible results presented in Figure 5.28. It is expected that the density variations (that compressible flow allows for) should have an impact on both the velocity field and the wall surface heat transfer (see Johnson et al., 1993). However, at the low (0.053) $\Delta\rho/\rho$ ratio that the CFD simulations were run at (required in order to match the UTRC experiments), the differences are very small.

Figure 5.30 shows a comparison of the stationary (and rotating channel) Nusselt ratios, along the channel centerline, for the incompressible flow simulations. Results are presented for the upper (trailing side) and lower (leading side) channel surfaces. View (a) shows that the rotating trailing side Nusselt ratios are higher (in most locations) than those for the stationary upper side channel surface. View (b) shows the reverse trend, where the rotating leading side Nusselt ratios are lower than those for the stationary lower side channel surface. Figure 5.31 presents the same information as Figure 5.30 over a limited y–axis range of 24 to 25 inches (60.96 to 63.50 cm), in order more easily show the rotational effects on Nusselt ratio for this incompressible flow case.

Also shown in Figure 5.30 is the available wall–T/c (wall thermocouple) data from NASA contact NAS3–26618 Task 30 (currently in progress at UTRC), which correspond to the four channel simulation conditions. The symbols shown in view (a) correspond to T/c 10, and those in view (b) correspond to T/c 7 (see also Figures 5.2 & 5.12). Data from T/c locations 8 & 9 were not considered reliable (based on discussions with UTRC), and are not presented here. Unfortunately, at the time this report was written, liquid–crystal (surface contour) test results were not yet available from UTRC.

Figure 5.30 view (b) shows four UTRC data points at wall–T/c 7 for the lower channel surface. This location is in the channel entrance region upstream of the first trip strip. Three data points are presented for the stationary channel test case at 13k, 26k, and 55k Reynolds number, and one data point is presented at Re equal to 26k for the rotating channel case. For Re equal to 26k (closest to the CFD simulation conditions), the data like the simulations indicate that Nu_{ratio} is decreased due to rotation. The stationary channel data points at 13k & 55k Re show a consistent trend in that they are higher than the rotating case.

Horizontal lines have been drawn through the data points in order to to extend the trends to just upstream of the first trip strip. This was done in order to better compare the test points to the channel simulations. The UTRC channel entrance extends further upstream than the CFD channel simulations (whose entrance location was set by the SRA planes A1 & D1). The Nu_{ratio} level from the UTRC test conditions (ranging between 1.0 & 2.0) reflect being at a "decayed" level of turbulent pipe flow downstream of a typical channel entrance location. This would be consistent with the channel simulations at a point just upstream of the first trip strip where the Nu_{ratio} values have decayed to their lowest level downstream of the channel entrance plane. At this location the simulations compare within 15% of the data for the stationary channel test case, and within 30% for the rotating channel conditions.

Figure 5.30 view (a) shows four UTRC data points at wall–T/c 10 for the upper channel surface. Three data points are presented for the stationary channel test case at 13k, 26k, and 55k Reynolds number, and one data point is presented at Re equal to 26k for the rotating channel test case. For Re equal to 26k, the data and the channel simulations both indicate that Nu_{ratio} is relatively unaffected by rotation at this location. The stationary channel Nu_{ratio} at 13k Re is nearly identical to the 26k case. However, the 55k Re case indicates a higher level of augmentation. Although the overall trends between the data and the simulations are consistent at this location, the absolute level of Nu_{ratio} is overpredicted by approximately 80%.

Figure 5.32 shows a comparison of the stationary (and rotating channel) Nusselt ratios, along the channel centerline, for the compressible flow simulations. Results are presented for the upper (trailing side) and lower (leading side) channel surfaces. View (a) shows that the rotating trailing side Nusselt ratios are higher than those for the stationary upper side channel surface. View (b) shows the reverse trend, where the rotating leading side Nusselt ratios are lower than those for the stationary lower side channel surface. Figure 5.33 presents the same information as Figure 5.32 over a limited y–axis range, in order more easily show the rotational effects on Nusselt ratio for this compressible flow case. Also shown in Figure 5.32 (for reference) are the same UTRC data points previously discussed in connection with Figure 5.30.

Figure 5.34 shows Nusselt number ratios, along the stationary channel centerline, for the incompressible and compressible flow simulations. View (a) and (b) both show that the calcula-

tions are essentially independent of density variation effects, as expected for non–rotating flows dominated by forced convection (see Hajek et al., 1991). Figure 5.35 shows Nusselt number ratios, along the rotating channel centerline, for the incompressible and compressible flow simulations. Both view (a) and (b) indicate slightly higher Nusselt ratios for the compressible flow simulations.

One final Nusselt number ratio comparison is made (in Figure 5.36) between the stationary channel compressible flow simulation results, and the CFD solution from Case 1 of Stephens et al., 1995. As was previously discussed in Section 5.53, Stephens numerically simulated a stationary channel geometry containing an alternating pattern of 5 skewed trip strips on the top and bottom walls with; p/e = 5, e/H = 0.1, H/W = 1.0, α = 45 degrees, Re = 25,000, (an identical geometry to the current study, except for the total number of trip strips and channel entrance and exit lengths). Stephens' results, were presented as a Stanton number ratio St_{ribbed}/St_{smooth}. In general, Stanton number ratio's are numerically identical to Nusselt number ratio's. However, St_{smooth} was based on a calculated smooth channel simulation vs the current study, where Nu_{pipe} was based on a (constant) value from equation (23). Unfortunately, the 3–dimensional variation in St_{smooth} along the channel surface was not reported. Therefore, there was no way to "back calculate" in order to put the the heat transfer ratios on an "exact" equal footing.

Figure 5.36 shows Stephens' results in view (a) compared to a similar wall section in view (b) from the lower side stationary channel compressible flow simulation. The channel entrance region for Stephens' calculation (not shown here) extends 5.75 trip strip pitches (along the lower edge of the figure) before the flow reaches the first trip strip. In contrast, the left hand side of view (b) shows the inlet plane for the current study. Both views show similar regions of high heat transfer downstream of each trip strip (along the bottom edge of the figures). These regions are caused as the lower channel secondary flow vortex is driven into the trip strip wall surface and thins the local thermal boundary layer.

In general, the results presented in the current study are about 250% (2.5x) higher than those predicted by Stephens. Differences in the entrance region (upstream of the 1st trip strip) would be expected due to the different channel inlet lengths, and the relative rates of Nu_{ratio} decay due to the thermal boundary layer growth from the inlet plane. However, once the flow has

entered the trip trip region these differences should diminish. The channel inlet $\Delta\rho/\rho$ density ratio for Stephens was 0.143 versus 0.053 for the current study. However, the differences in density (or wall to bulk fluid temperature driving potential) should not matter for this stationary channel simulation which is dominated by forced convection effects. It should be noted however that Stephens assumed the two sooth side walls were insulated versus the current study where the side walls were held to the same constant wall temperature as the trip strip surfaces. Unfortunately, at the time that this report was written, all of the issues relating to the relative differences in heat transfer level observed in Figure 5.36 had not been resolved.

5.67 Pressure Loss Results

At the same time that the NASTAR output files were post–processed to acquire heat transfer information, channel static pressure loss and non–dimensionalized friction factor quantities were also calculated. A channel friction factor can be defined as,

$$f = \left(\frac{\Delta P}{\Delta X}\right)\frac{D_h}{2\rho V^2} \tag{25}$$

Where ΔP is the difference between inlet and exit plane integrated average static pressures, over the channel length ΔX. For this particular simulation geometry it was assumed that the calculated ΔP_{static} would be essentially equal to ΔP_{total}. This assumption was based on the fact that the inlet & exit plane locations have the the same smooth wall cross–sectional shape, the exit plane pressures were calculated far downstream of the last trip strip, and the inlet plane pressures were held at a uniform value at the inlet. The hydraulic diameter, density and velocity were determined at the channel inlet location. The friction factor can be represented as non–dimensionalized friction factor ratio by using the turbulent pipe flow friction coefficient equation,

$$f_{pipe} = 0.046\,Re^{-0.2} \tag{26}$$

$$f_{ratio} = \frac{f}{f_{pipe}} \tag{27}$$

The ΔP quantities determined for the rotating channel simulations had the rotating pressure "pumping" effects removed. This was done by subtracting the channel ΔP by,

$$\Delta P_{pumping} = P_{exit} - P_{inlet} e^{\left(\frac{\omega^2}{2RT}\left(r_{exit}^2 - r_{inlet}^2\right)\right)} \tag{28}$$

Using this procedure, the following values were calculated from the four channel simulations,

Table 5.3 Calulated Channel Pressure Loss & Friction Factor Quantities

	Stationary Incompr	Stationary Compr	Rotating Incompr	Rotating Compr
ΔP psia	0.0170	0.0182	0.0151	0.0244
(N/m^2)	(117.22)	(125.49)	(104.11)	(168.24)
f	0.0551	0.0588	0.0488	0.0789
f_{ratio}	9.0561	9.6734	8.0334	12.9779

In order to compare these results to a similar channel geometry from the P&W data base, the friction factors were recalculated using ΔX equal to exactly 14 trip strip pitches. In addition, the channel ΔP was modified by subtracting the channel pressure loss do to the smooth channel entrance and exit lengths. The friction factor quantities then become,

Table 5.4 Corrected Channel Friction Factor Quantities

	Stationary Incompr	Stationary Compr	Rotating Incompr	Rotating Compr
f_{corr}	0.0730	0.0781	0.0645	0.1056
$f_{ratio\ corr}$	12.005	12.848	10.608	17.363

The corrected friction factor ratio values compare to a value of ~9.4 from the P&W data base for a; p/e = 5, e/H = 0.081, H/W = 1.0, and α = 45 degrees. Unfortunately, an exact case with a e/H of 0.01 was not available. However, other P&W data points where e/H was matched (but H/W was not), indicated that the friction factor ratio was probably not affected significantly by the 20% difference in e/H level.

A review of the results presented in Table 5.4 show that these benchmark simulations appear to overpredict the level of channel friction factor. The average f_{ratio} value for the stationary channel simulations is about 30% higher than the P&W data base. The rotating channel f_{ratio} averages about 50% higher, with a incompressible vs compressible flow range of (13% to 85% higher) than the stationary channel P&W data base.

6. CONCLUSIONS - EXPERIMENTAL PROGRAM

Velocity measurements were obtained in passages having skewed trip strips with cross sections of 0.5" x 0.5" and 1.0" x 0.5". The passage is representative of internal cooling passages used in turbine blades. The measurements were obtained at Reynolds number of 25,000 (based on the hydraulic diameter of the square passage) and Rotation numbers of 0.0 and 0.24. The following conclusions are the main findings of this investigation.

6.1 Stationary measurements (Rotation number = 0.0)

1. The combination of outward flow and trips skewed at -45° in the first passage leads to a two-vortex structure with upward velocity of 0.6 U_b in the center and a downward velocity of -0.95 U_b at 0.09 D from the wall. The development of secondary flows in the straight passages is very significant as a consequence of the strong secondary flow generated by the skewed trips. Skewed trips generate two high velocity regions of magnitude 1.50 U_b close to the side walls. Tse, et al. (1994) show that, for a smooth wall passage, the velocity near the walls is less then 0.8 U_b. Based upon the $Nu\text{-}Re^{0.8}$ relationship, this change in flow characteristics leads to a 66 % increase in heat transfer. The increase in heat transfer (100 to 200 %), observed by Johnson, et al. (1994) is attributed to the changes in streamwise velocities and strong secondary flow induced by trips.

2. The combination of outward flow and trips skewed at -45° leads to a two-vortex structure with upward velocity in the center and downward velocity near the wall. When both trip orientation and flow direction are reversed, i.e., inward flow and trips skewed at +45°, the vortices circulate in the same direction. When either trip orientation or flow direction alone is reversed, the vortices circulate in the opposite direction.

3. Streamwise recirculation occurs at the exit of a turn in the 1.0" x 0.5" passage. The negative velocity reaches a maximum value of -0.25 U_b and the recirculation zone extends to the 0.4 H location. Rotation induces strong inward flow, of the order of the bulk mean velocity, on the leading side of the turn. This flow fills the velocity deficit and eliminates the recirculation zone.

6.2 Rotating measurements (Rotation number = 0.24)

4. The interaction of the secondary flows induced by skewed trips and by rotation produces a swirling vortex and a corner recirculation zone. With the passage rotating in a clockwise direction, the combination of outward flow and trips skewed at -45° generates counter-clockwise swirl and a corner recirculation zone at the upper corner of the leading side. The combination of inward flow and trips skewed at +45° generates clockwise swirl and a corner recirculation zone at the upper corner of the trailing side. The combination of outward flow and trips skewed at +45° generates clockwise swirl and a corner recirculation zone at the lower corner of the trailing side.

5. With trips skewed at +45°, the secondary flow characteristics remain the same as the flow propagates from the first passage to the first turn. With trips skewed at -45°, the corner recirculation zone in the first passage is on the leading side and that in the first turn is on the trailing side. Changes in the secondary flow structure enhance mixing and this is evident in a 20% increase in heat transfer in Johnson, et al. (1994). With trips skewed at +45°, the corner recirculation zone in the second passage is on the trailing side and that in the second turn is on the leading side. Therefore, the use of trips skewed at -45° is to be preferred in the outward flow passage. The use of trips skewed at +45° is to be preferred in the inward flow passage.

6. With trips skewed at -45° in the outward flow passage and trips skewed at +45° in the inward flow passage, the swirl and corner recirculation flow structure induced by skewed trips leads to re-attachment of the cross-flow in the upper and lower corners and separation of the cross-flow in the center on the low pressure side. Separation and re-attachment of the cross-flow on the high pressure side is less noticeable because of the high cross-stream velocity associated with the strong swirl. The secondary flow characteristics for stationary and rotating cases are different on the low pressure side, but are similar on the high pressure side.

7. The secondary flows in the first and second turns are characterized by swirl and corner recirculation. The swirl level in the first turn is higher than the swirl level in the second. In

the first turn, outward flow on the high pressure side is reinforced by centrifugal force. The momentum is transferred to the inward flow on the low pressure side by convection. In the second turn, the flow on the low pressure side is retarded by centrifugal force. In addition, Coriolis forces are weakened in the second turn because it has a smaller radius than the first. The corner recirculations are located near the concave side in both turns. The corner recirculation in the first turn is weaker than that in the second. Centrifugal force directs flow toward the concave side in the first turn and away from it in the second. The large difference in heat transfer at the turns observed in Johnson et al. (1994) is partly attributed to these flow effects.

8. Johnson, et al. (1994) show that, relative to the stationary smooth wall reference flow, rotation increases the heat transfer from the pressure surface of the first passage in a passage with skewed trips by up to 300%. In addition, their results show that buoyancy accounts for an increase in heat transfer of 25%. The velocity measurements show that the increase in heat transfer associated with the increase in streamwise velocity, swirl and re-attachment of cross-flow in the inter-ribbed region are, respectively, 48%, <100% and >125%.

9. Rotation induces a marginal velocity increase on the high pressure side. Based upon the $Nu\text{-}Re^{0.8}$ correlation, the increase leads to a 5% increase in convective heat transfer. The results of Johnson, et al. (1994) show that rotation increases the heat transfer from the trailing surface by 30%. They further show that buoyancy increases the heat transfer from that surface by 25%. Re-attachment of cross-flow in the inter-ribbed region increases the heat transfer from the high pressure side by the same magnitude in both stationary and rotating cases. This is consistent with the observations in Conclusion 6.

10. Rotation induces a large velocity deficity on the low pressure side. Based upon the $Nu\text{-}Re^{0.8}$ correlation, the deficit leads to a 50% decrease in convective heat transfer. The results of Johnson, et al. (1994) show that rotation decreases the heat transfer from the low pressure surface by 50%. They further show that buoyancy increases the heat transfer from that surface by 20%. The influence of re-attachment of cross-flow in the inter-ribbed region

on the low pressure surface is reduced by 20% with rotation. This is consistent with the observations in Conclusion 6.

7.0 CONCLUSIONS – NUMERICAL SIMULATIONS

Benchmark numerical simulations for both stationary and rotating internal cooling channels with skewed trip strips were performed. The computational effort was broken down into two phases. In the first phase, a grid sensitivity study was performed (assuming periodically fully developed flow) on a cooling channel computational domain limited to the region between two adjacent trip strips. In the second phase, based on the results from the grid sensitivity study, four trip strip channel simulations all utilizing the same channel geometry and computational grid were presented. These simulations were then compared to experimental velocity field data obtained by Scientific Research Associates, and selected heat transfer data acquired by the United Technologies Research Center. A more detailed discussion of the conclusions presented here can be found in Sections 5.2 thru 5.6 of this report.

7.1 Conclusions – Flow Field Initialization

1. One of the major objectives of the computational effort was to be able to compare all the channel simulations to each other, in addition to the velocity field data of SRA and the heat transfer data acquired by UTRC. Due to the differences between the experimental methods (and working fluids) used by SRA and UTRC, it was necessary to develop a set of consistent CFD simulation conditions that were close (but not identical) to either the experimental test conditions of SRA or that of UTRC (see Table 5.1)

7.2 Conclusions – Grid Sensitivity Study

1. Excellent agreement was found between the velocity, pressure, and temperature contours calculated by NASTAR for the single trip strip pitch (channel segment) using the "conveyor–belt" boundary condition logic, and the 2–d full length channel evaluation geometry.
2. It appears that the use of wall functions for this skewed trip strip channel geometry, produces entirely un–reliable secondary flow velocity field results. It was recommended that wall functions not be used for the full channel simulations.
3. The baseline wall integration grid (i, j, k) of 66x39x39 produces results very similar to the denser grid domain of 92x49x49 selected for the grid evaluation study.

4. Although the two grids (discussed above) were less dense than that recommended by (Tse et al., 1994 and Stephens et al., 1995), it was felt that for practical considerations that the upper limit for jxk that could be duplicated (and run in a reasonable time frame) for the four 15 trip strip channel simulation geometries was 39x39.

7.3 Conclusions – Stationary Channel Simulations Compared to SRA Data

1. The calculated incompressible (and nearly identical) compressible velocity vector fields at channel location A2 show very good agreement with the SRA data in the channel core flow region.
2. The predicted velocity field along the channel walls is similar to the data. However, the calculations show higher values at the wall surfaces in many locations.
3. The differences between the calculated flow field and the data at the walls, could be in part due to the sparse nature of the SRA data sets near the wall, and the process used to interpolate the data to the much denser CFD grid in the wall region.
4. The overall agreement between the SRA data and the CFD calculations is (very good) for the u, v, and w velocity field components.
5. In general, the simulations appear to underpredict TKE and TDS in the channel mid–section core area, but have reasonable agreement near the wall surfaces.
6. The incompressible and compressible calculated velocity component results were virtually identical for the stationary channel simulations.

7.4 Conclusions – Rotating Channel Simulations Compared to SRA Data

1. The general conclusions for the rotating channel simulations (compared to the SRA data at locations D2 & D3), are the same as 1 thru 5 presented above for the stationary channel.
2. Only very minor differences were observed between the incompressible and compressible flow simulations (see heat transfer conclusions below).

7.5 Conclusions – "Conveyor–belt" Segment Versus Channel Simulations

1. Based on the streakline particle trace comparisons shown in (Figure 5.26), the particle motions do not appear to "repeat" their pattern over the length of the channel. This indicates that

the single trip strip pitch "conveyor–belt" assumption, although very useful for the grid sensitivity study, does not completely capture the full channel trip strip flow field effects.

2. However, the overall agreement between the "conveyor–belt' segment and the skewed trip strip channel simulation was excellent, especially when you consider that the "conveyor–belt" simulation had a computational domain of 100,386 grid points (less than 6%) of the 1,708,083 grid points required for the full channel simulation.

7.6 Conclusions – Heat Transfer Results

1. The rotating channel (trailing side) Nusselt ratios were increased relative to the stationary channel surface. The rotating channel (leading side) Nusselt ratios were decreased relative to the stationary channel surface. These trends are consistent with the experimental observations of (Johnson et al., 1993) for rotating channel flows.
2. There are only very minor differences observed between the incompressible and compressible flow simulations. It was expected that the density variations (that compressible flow allows for) should have an impact on both the velocity field and the wall surface heat transfer. However, at the low (0.053) $\Delta\rho/\rho$ ratio that the CFD simulations were run at (required in order to also match the UTRC experiments), the differences were very small.
3. In the channel entrance region upstream of the first trip strip (at UTRC wall–T/c 7) CFD simulations compare within 15% of the UTRC data for the stationary channel test case, and within 30% for the rotating channel conditions for the lower channel surface.
4. At the downstream channel location (UTRC wall–T/c 10, on the upper wall), the overall trends between the data and the simulations are consistent. However the absolute level of Nu_{ratio} is overpredicted by approximately 80%.
5. Unfortunately, at the time this report was written, liquid–crystal (surface contour) test results were not yet available from UTRC, so these comparisons could not be made for this report.
6. The results presented in the current study are about 250% (2.5x) higher than those predicted by (Stephens et al., 1995) for a stationary channel geometry identical to the current study, except for the total number of trip strips and channel entrance and exit lengths.

7.7 Conclusions – Pressure Loss Results

1. The average f_{ratio} value for the stationary channel simulations is about 30% higher than the P&W data base value for this channel geometry.
2. The rotating channel f_{ratio} averages about 50% higher, with a incompressible vs compressible flow range of (13% to 85% higher) than the stationary channel P&W data base value.

ACKNOWLEDGMENTS

The authors are pleased to acknowledge the financial support from NASA/Lewis Research Center under SBIR Contract No. NAS3-27378. They thank Dr. J. Wagner of UTRC for his assistance in providing heat transfer data and rig geometry information from the NAS3-26618 Task 30 contract. Thanks are due to Dr. S. Tanrikut and Mr. C. Rhie, R. Zacharias, W. Siddons and R. Malecki of P&W for their efforts and insight in using NASTAR for the CFD simulation efforts. Thanks are also due to Dr. Wagner, Drs. P. Poinsatte, R. Simoneau, K. Civinskas, D. Rigby and L. Tran of NASA Lewis Research Center for their many discussions providing important insight and suggestions during this program.

REFERENCES

Dash, S.M., Beddini, R.A., Wolf, D.E., and Sinha, N. (1983), "Viscous/Inviscid Analysis of Curved Sub- or Supersonic Wall Jets", AIAA Paper 83-1679.

Guidez, J., (1989), "Study of the Convective Heat Transfer in Rotating Coolant Channel," ASME Journal of Turbomachinery, Vol. 111, pp -43-50.

Hajek, T.J., Wagner, J.H., Johnson, B.V. Higgens, A.W., and Steuber, G.D.,. (1991), "Effects of Rotations on Coolant Passage Heat Transfer: Volume I - Coolant Passages With Smooth Walls," NASA Contractor Report 4396, Vol. I.

Johnson, B.V. Wagner, J.H., and Steuber, G.D., (1993), "Effects of Rotations on Coolant Passage Heat Transfer: Volume II - Coolant Passages With Trips Normal ans Skew to the Flow," NASA Contractor Report 4396, Vol. II.

Johnson, B.V. Wagner, J.H., Steuber, G.D., and Yeh, F.C., (1994), "Heat Transfer in Rotating Serpentine Passages with Trips Skewed to the Flow," ASME Journal of Turbomachinery, Vol. 116, pp -113-123.

Launder, B.E., and Spaulding, D.B. (1974), "The Numerical Computation of Turbulent Flows", Computer Methods in Applied Mechanics and Engineering, 3: 269-289.

Liou, T-M., and Chen, S-H. (1995), "Computation of Spatially Periodic Turbulent Fluid Flow and Heat Transfer in a Channel with Various Rib Shapes", ASME Paper 95-GT-23.

McGrath, D.B., and Tse, D.G.N., (1995), "A Combined Experimental/Computational Study of Flow in Turbine Blade Passage: Part II - Computational Investigation", ASME Paper 95-GT-149.

Mochizuki, S., Takamura, J, Ymamwaki, S., and Yang, W-J., (1994), "Heat Transfer in Rotating Serpentine Passages with Rotation," ASME Journal of Turbomachinery, Vol. 116, pp -133-140.

Prakash, C., and Zerkle, R., (1993), 'Prediction of Turbulent Flow and Heat Transfer in a Ribbed Rectangular Duct with and without Rotation," Paper presented at the Cincinnati, Ohio May 24-27, 1993.

Rhie, C.M. (1986), "A Pressure Based Navier-Stokes Solver Using the Multigrid Method", AIAA Paper 86-0207.

Stephens, M.A., Shih, T.I-P., Civinskas, K.C. (1995), 'Effects of Inclined Rounded Ribs on Flow and Heat Transfer in a Square Duct", AIAA Paper 95-2115.

Taslim, M.E., Rahman, A., and Spring, S.D., (1991a), "An Experimental Investigation of Heat Transfer Coefficients in Spanwise Rotating Channels With Two Opposite Rib-Roughened Walls," ASME Journal of Turbomachinery, Vol. 113, pp 75-82.

Taslim, M.E., Bondi, L.A., and Kercher, D.M., (1991b), "An Experimental Investigation of Heat Transfer Coefficients in Spanwise Rotating Channels With Two Opposite Rib-Roughened Walls," ASME Journal of Turbomachinery, Vol. 113, pp 346-353.

Tse, D.G.N., Kreskovsky, J.P., Shamroth, S.J., and McGrath, D.B., (1994), "A Combined Experimental/Computational Study of Flow in Turbine Blade Passage", NASA CR 4584.

Tse, D.G.N. and McGrath, D.B., (1995), "A Combined Experimental/Computational Study of Flow in Turbine Blade Passage: Part I - Experimental Study", ASME Paper 95-GT-355.

Wagner, J.H., Johnson, B.V., and Kopper, F.C., (1991), "Heat Transfer in Rotating Serpentine Passages with Smooth Walls," ASME Journal of Turbomachinery, Vol. 113, pp 321-330.

Wagner, J.H., Johnson, B.V., Graziani, R.A., and Yeh, F.C., (1992), "Heat Transfer in Rotating Serpentine Passages with Trips Normal to the Flow," ASME Journal of Turbomachinery, Vol. 114, pp 847-857.

Wagner, J.H, (1994), Personal communication.

Wagner, J.H. (1994), NASA Contract NAS3-26618, 'Monthly Technical Progress Report for November 1994; Task 30 - Heat Transfer in the Turn Regions of Serpentine Coolant Passages".

Yang, W-J., Zhang, N., and Chiou, J., (1992), "Local Heat Transfer in a Rotating Serpentine Flow Passage," ASME J. Heat Transfer, Vol. 114, pp 354-361.

TABLE 2.1

Location	
A1	1 D downstream of inlet
A2	7 D downstream of inlet
A3	1 D upstream of the first turn
A4	First turn
A5	1 D downstream of the first turn
A6	1 D upstream of the second turn
A7	Second turn
A8	1 D downstream of the second turn
A9	1 D upstream of the third turn
A10	1 D downstream of the third turn
A11	1 D upstream of exit

TABLE 2.2

Location	
B1	1 D downstream of inlet
B2	7 D downstream of inlet
B3	1 D upstream of the first turn
B4	First turn
B5	1 D downstream of the first turn
B6	1 D upstream of the second turn
B7	1 D downstream of the second turn
B8	1 D upstream of the third turn
B9	1 D downstream of the third turn
B10	1 D upstream of exit

TABLE 2.3.1

Optical characteristics of the laser-Doppler Velocimeter employing forward scattering

Half angle of the beam interaction (°)	4.85
Fringe spacing (μm)	3.04
Number of fringes without frequency shift	14
Diameter of control volume at $1/e^2$ intensity (μm)	42.0
Length of control volume at $1/e^2$ intensity (μm)	738
Maximum frequency shift (Mhz)	9.0
Frequency to velocity conversion (ms^{-1}/Mhz)	3.04

TABLE 2.3.2

Optical characteristics of the laser-Doppler Velocimeter employing back scattering

Half angle of the beam interaction (°)	2.43
Fringe spacing (μm)	6.06
Number of fringes without frequency shift	14
Diameter of control volume at $1/e^2$ intensity (μm)	84.0
Length of control volume at $1/e^2$ intensity (μm)	2944
Maximum frequency shift (Mhz)	9.0
Frequency to velocity conversion (ms^{-1}/Mhz)	6.06

TABLE 2.4

Location	
C1	x/D = 1, 1 D downstream of the inlet
C2	x/D = 4, 4 D downstream of the inlet
C3	x/D = 7, 7 D downstream of the inlet
C4	x/D = 10, 10 D downstream of the inlet
C5	x/D = 12, 12 D downstream of the inlet
C6	x/D = 15, First turn
C7	x/D = 18, 1 D downstream of the first turn
C8	x/D = 20, 3 D downstream of the first turn
C9	x/D = 25.5, 8.5 D downstream of the first turn
C10	x/D = 27.5, 10.5 D downstream of the first turn
C11	x/D = 29.5, Second turn
C12	x/D = 31.5, 1 D downstream of the second turn
C13	x/D = 36.5, 6 D downstream of the second turn

TABLE 2.5

Location	
D1	x/D = 1, 1 D downstream of the inlet
D2	x/D = 4, 4 D downstream of the inlet
D3	x/D = 7, 7 D downstream of the inlet
D4	x/D = 10, 10 D downstream of the inlet
D5	x/D = 12, 12 D downstream of the inlet
D6	x/D = 15, First turn
D7	x/D = 17.5, 1 D downstream of the first turn
D8	x/D = 19.5, 3 D downstream of the first turn
D9	x/D = 25.5, 9 D downstream of the first turn
D10	x/D = 27.5, 11 D downstream of the first turn
D11	x/D = 29.5, Second turn
D12	x/D = 31.5, 1 D downstream of the second turn
D13	x/D = 36.5, 6 D downstream of the second turn

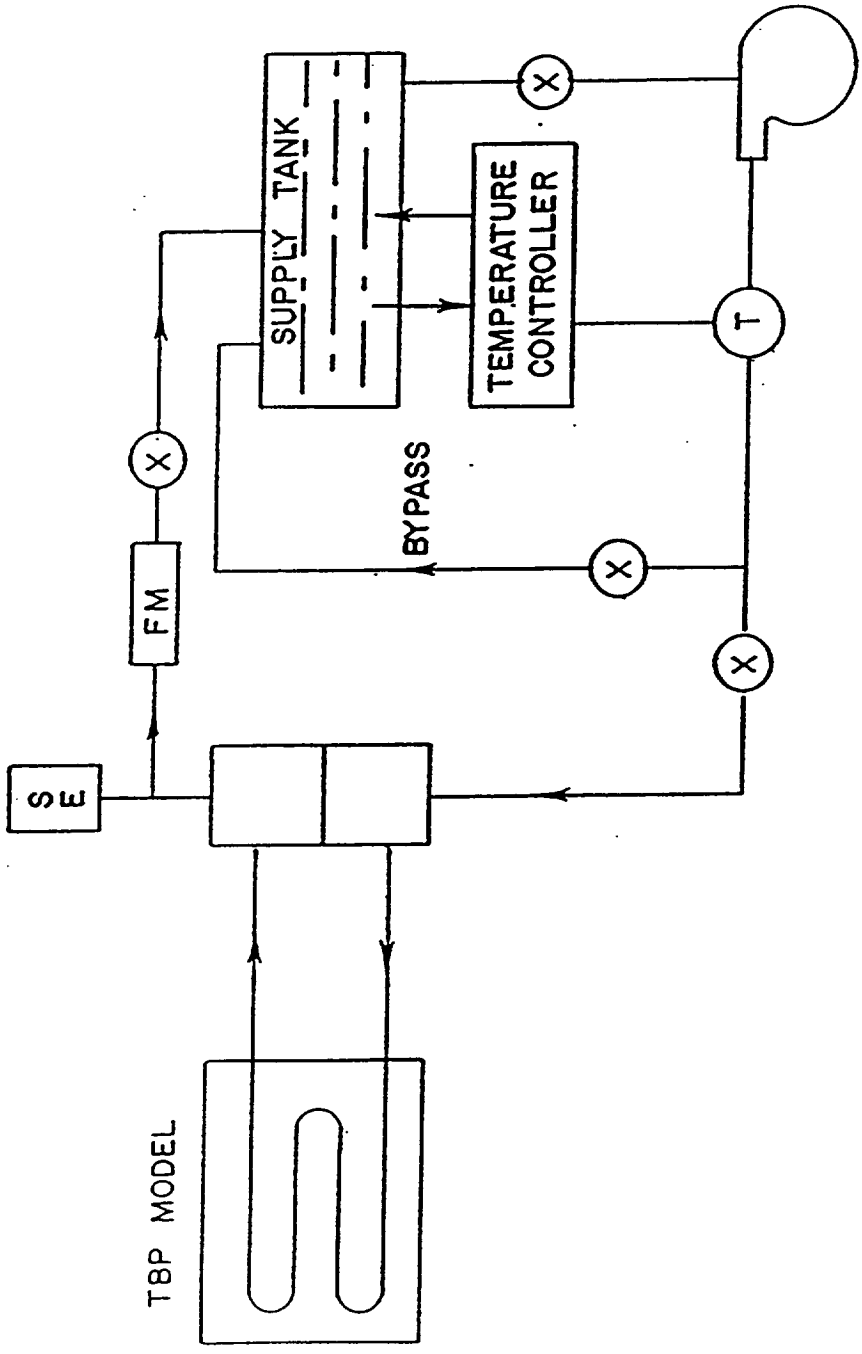

Figure 2.1 - Flow circuit of the turbine-blade cooling passage rig.

SRA Rig View from outside of model "looking in"

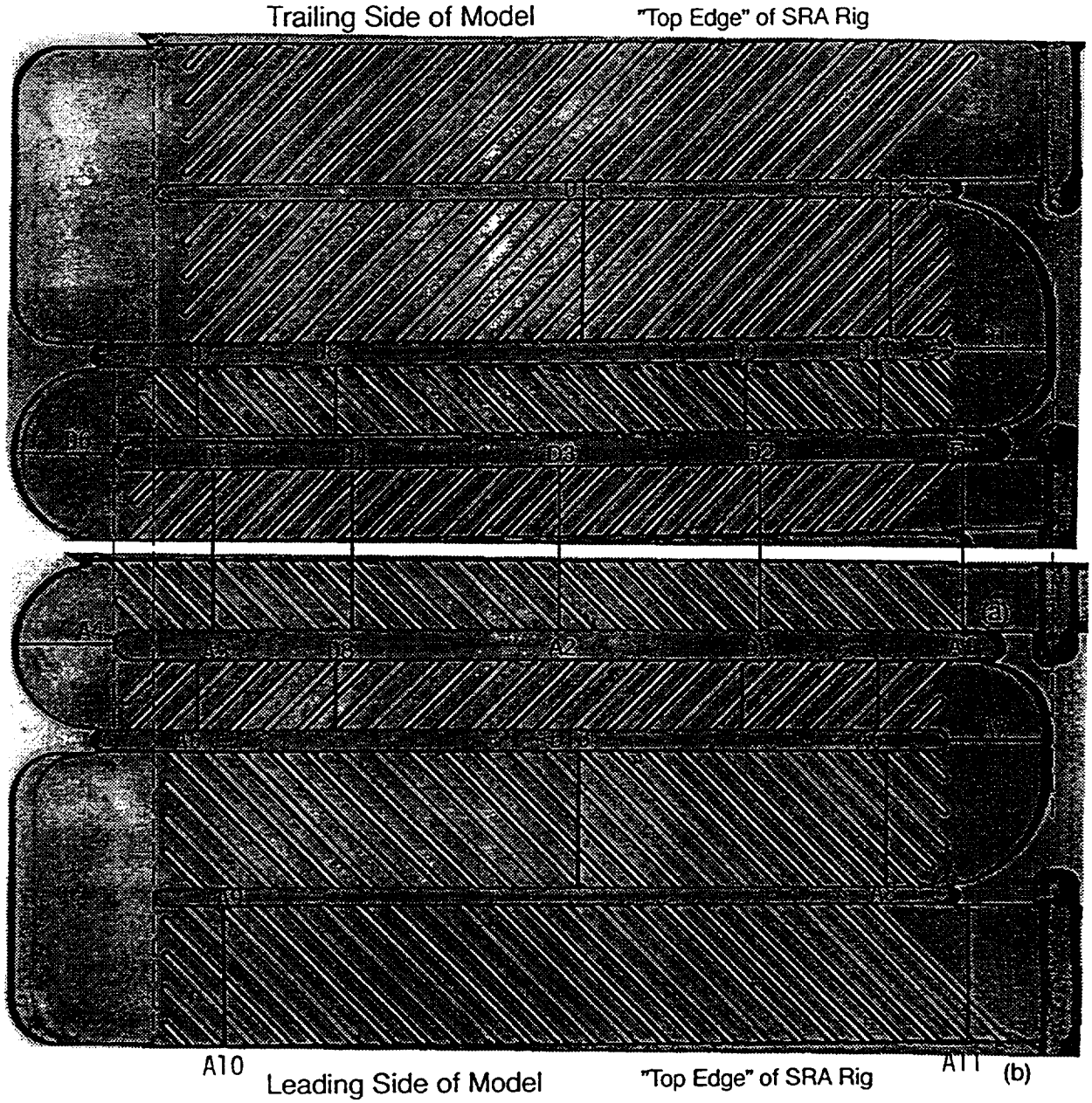

Figure 2.2 - Measuring Locations of Passage 1.

SRA Rig View from outside of model "looking in"

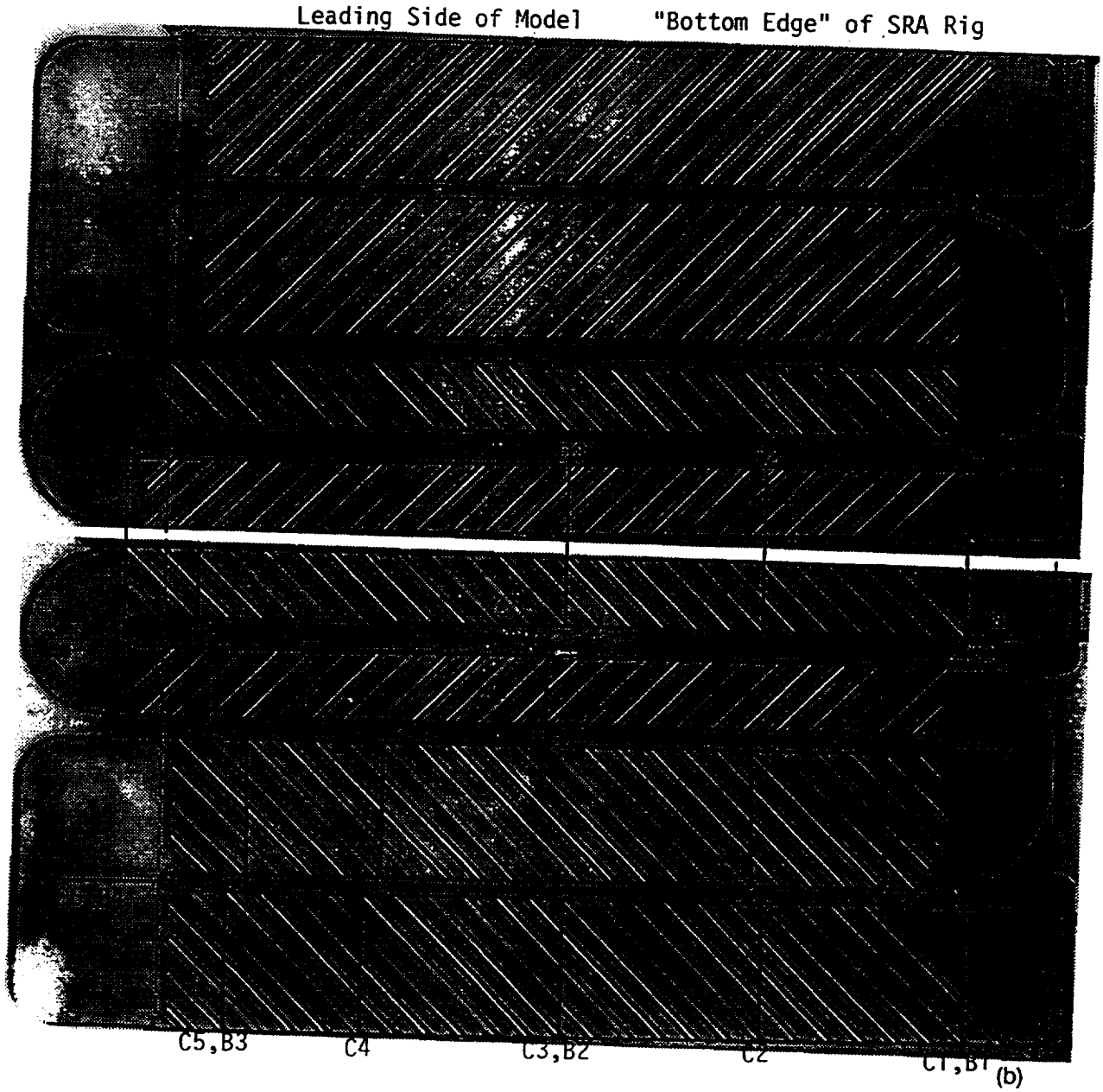

Figure 2.3 - Measuring Locations of Passage 2.

Differences Between UTRC & SRA Rigs

SRA Rig View from outside of model "looking in"

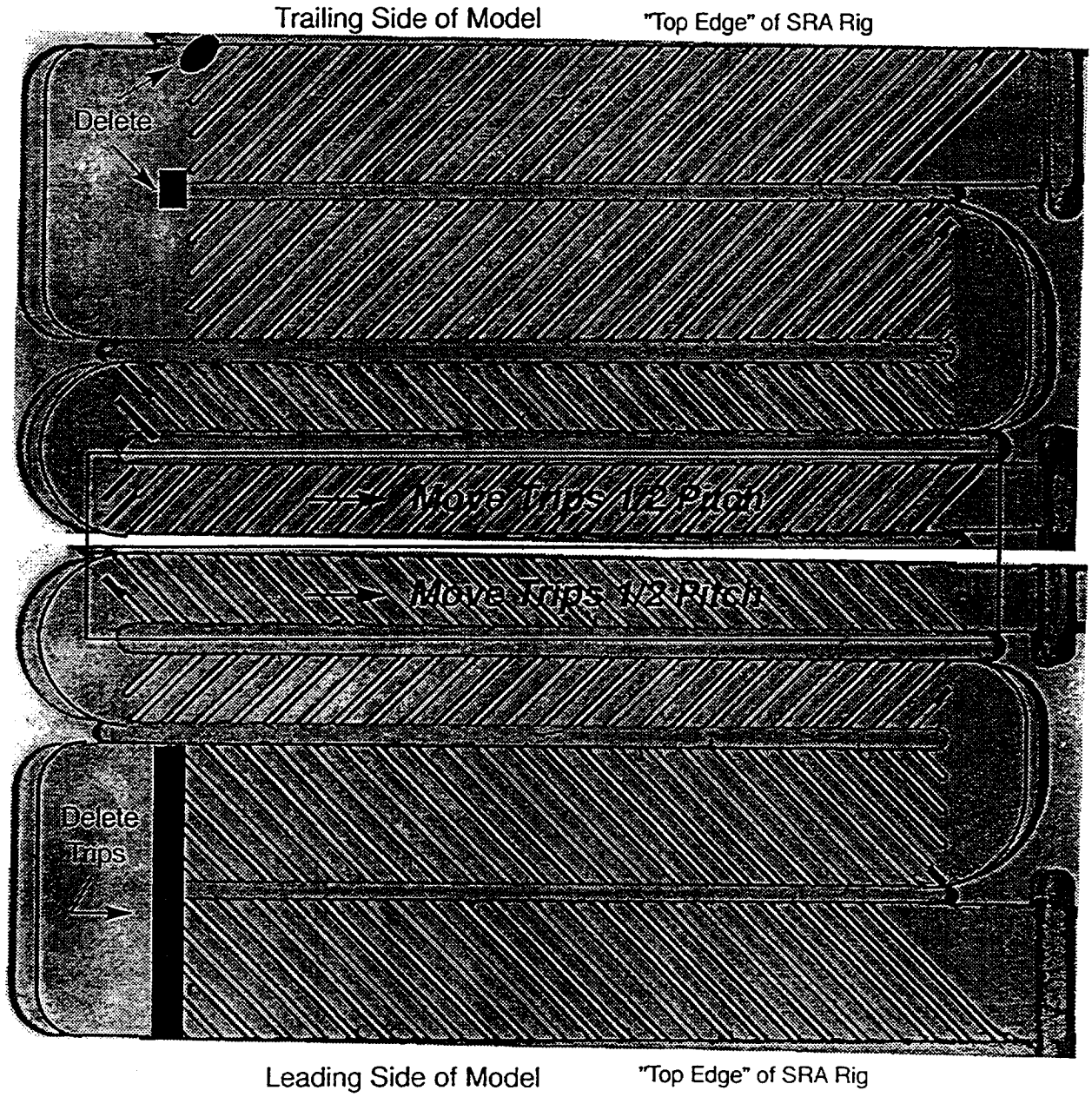

Figure 2.4 - Differences between UTRC & SRA rigs.

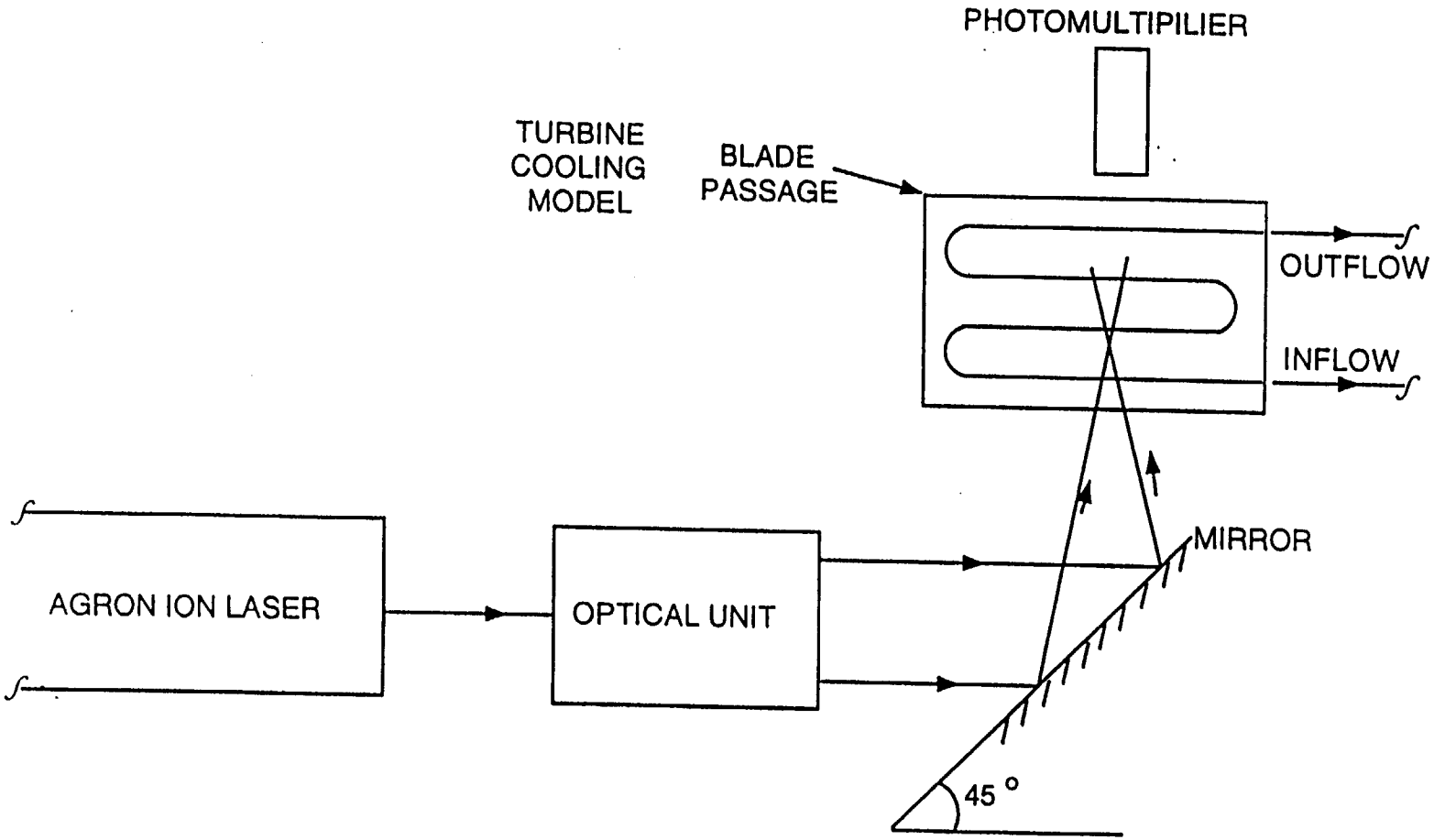

Figure 2.5 - Laser-Doppler Velocimeter set-up - forward scattering.

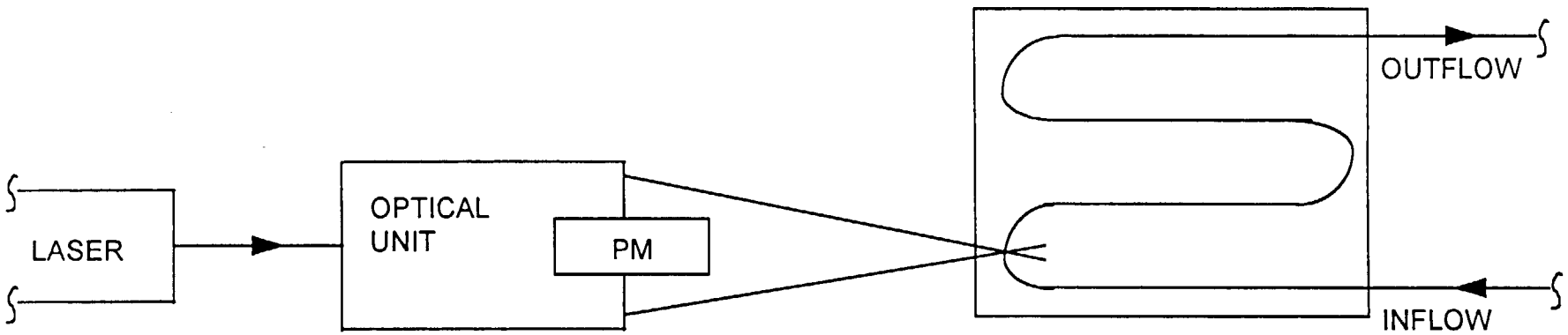

Figure 2.6 - Laser-Doppler Velocimeter Set-up - Back Scattering

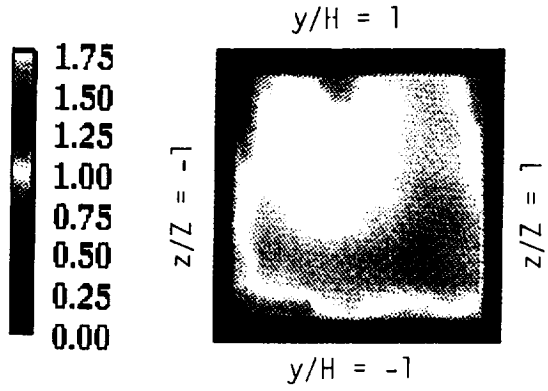

3.1.1

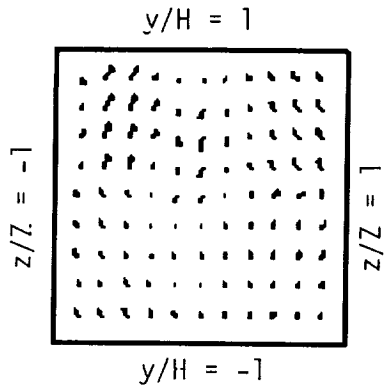

3.1.2

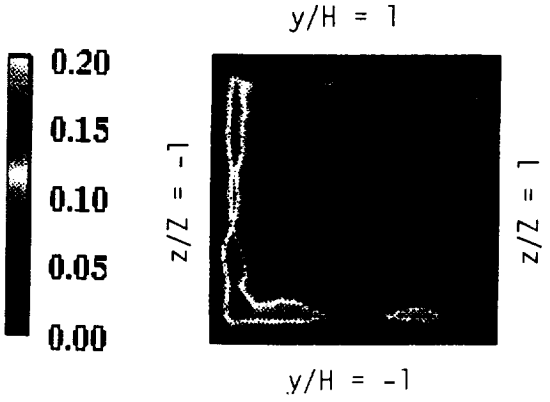

3.1.3

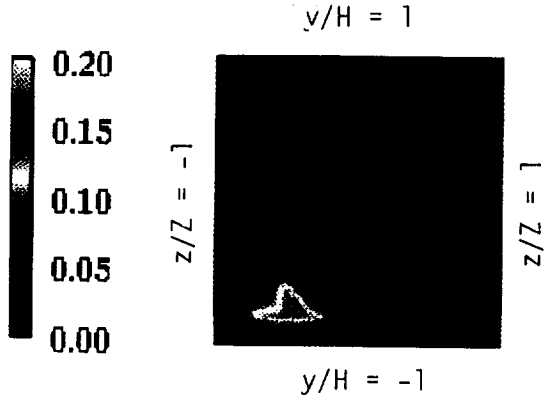

3.1.4

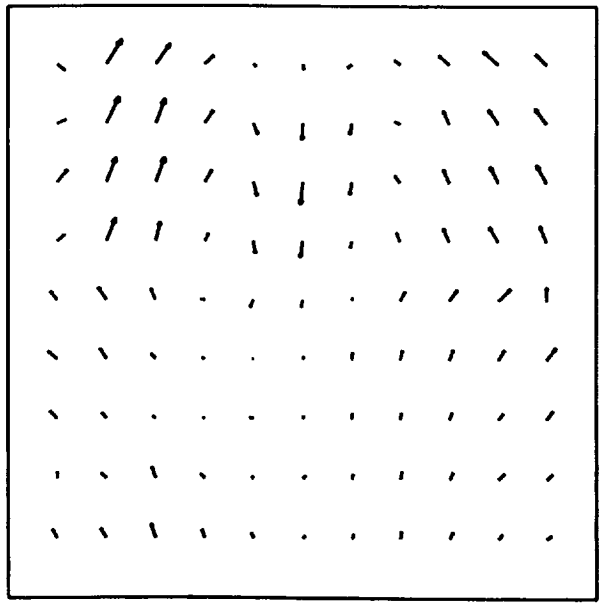

Enlargement of 3.1.2

Figure 3.1 - Velocities at location A1, 1 D downstream of the inlet.

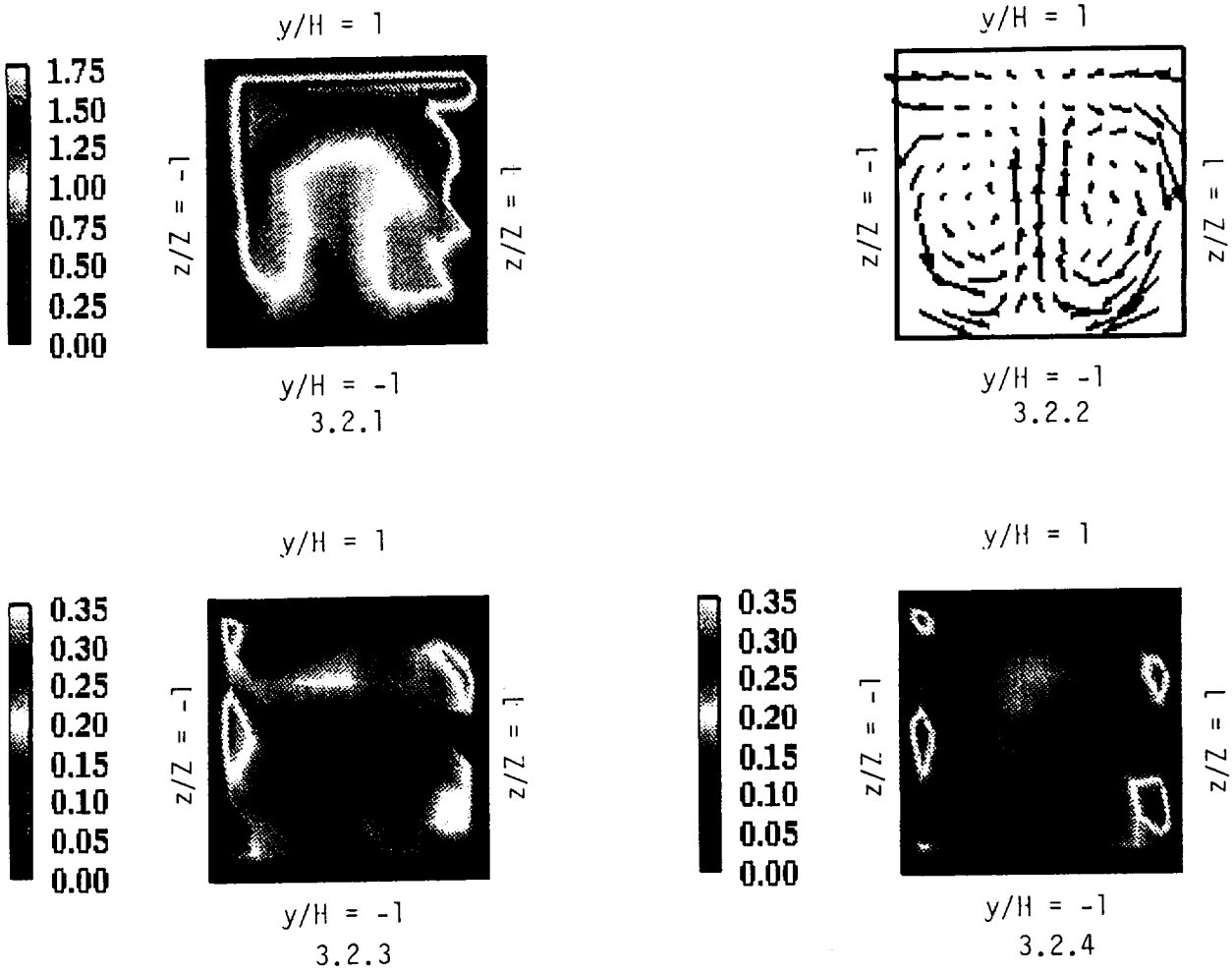

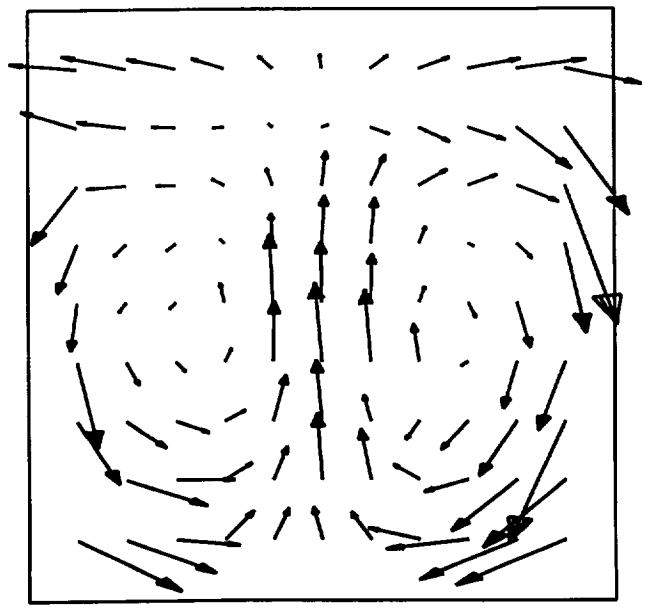

Enlargement of 3.2.2

Figure 3.2 - Velocities at location A2, 7 D downstream of the inlet.

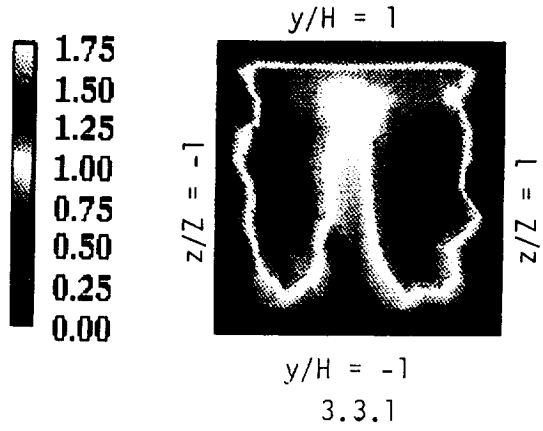

3.3.1

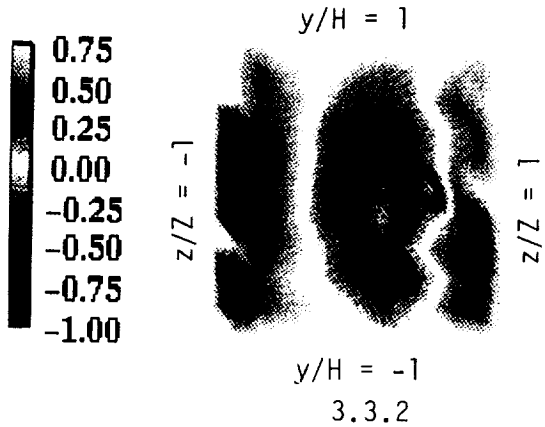

3.3.2

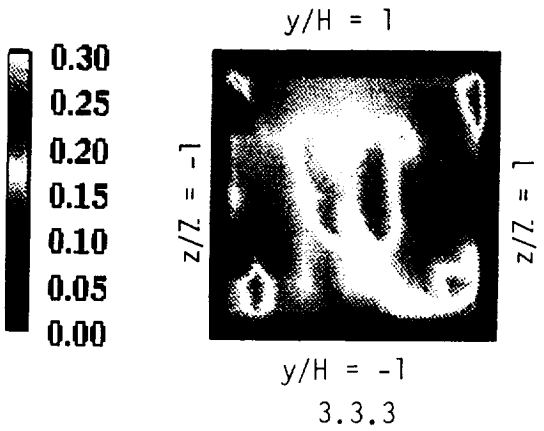

3.3.3

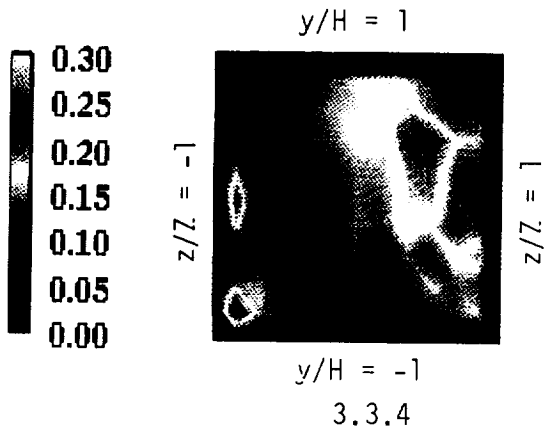

3.3.4

Figure 3.3 - Velocities at location A3, 1 D upstream of the first turn.

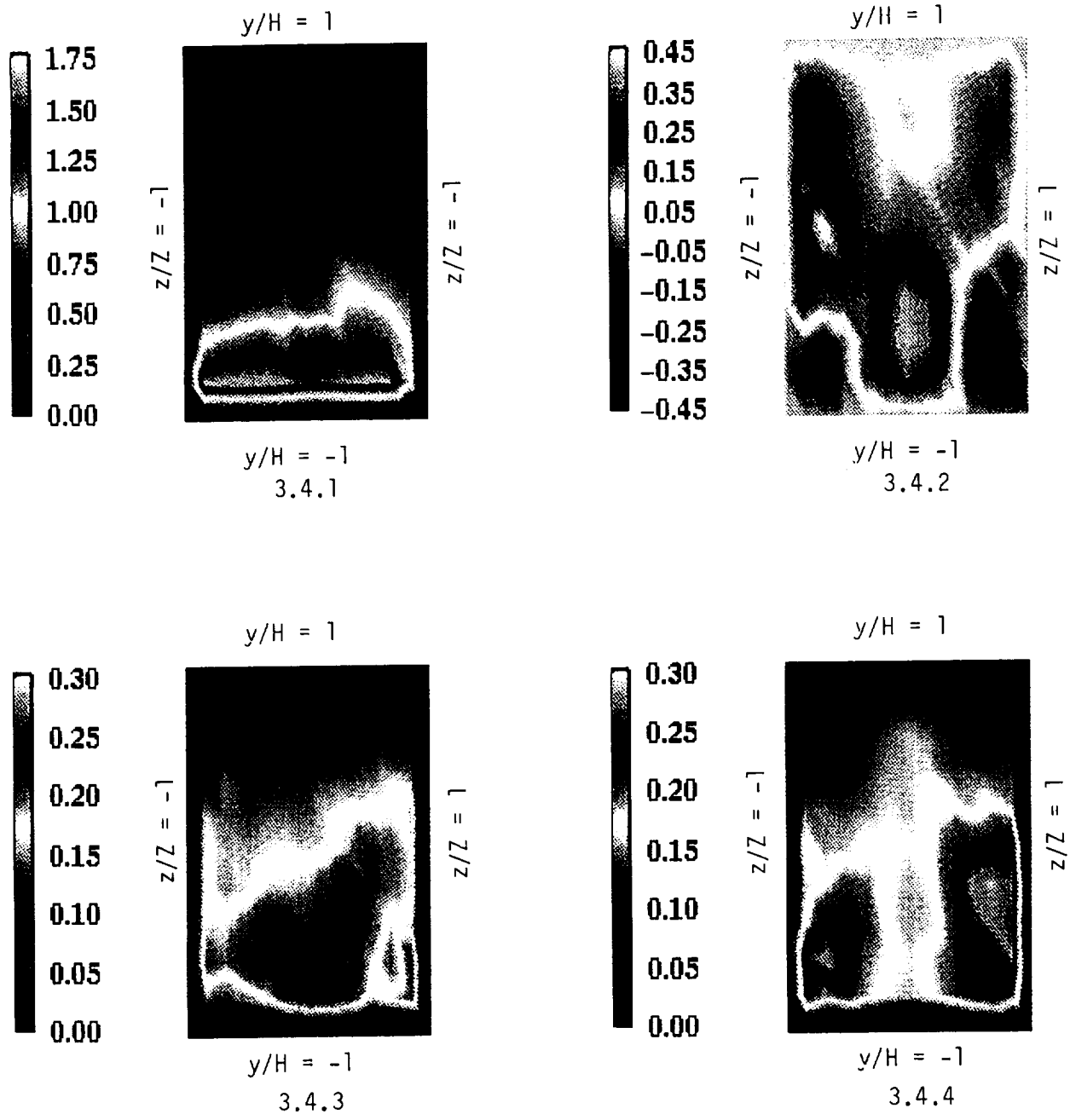

Figure 3.4 - Velocities at location A4, the first turn.

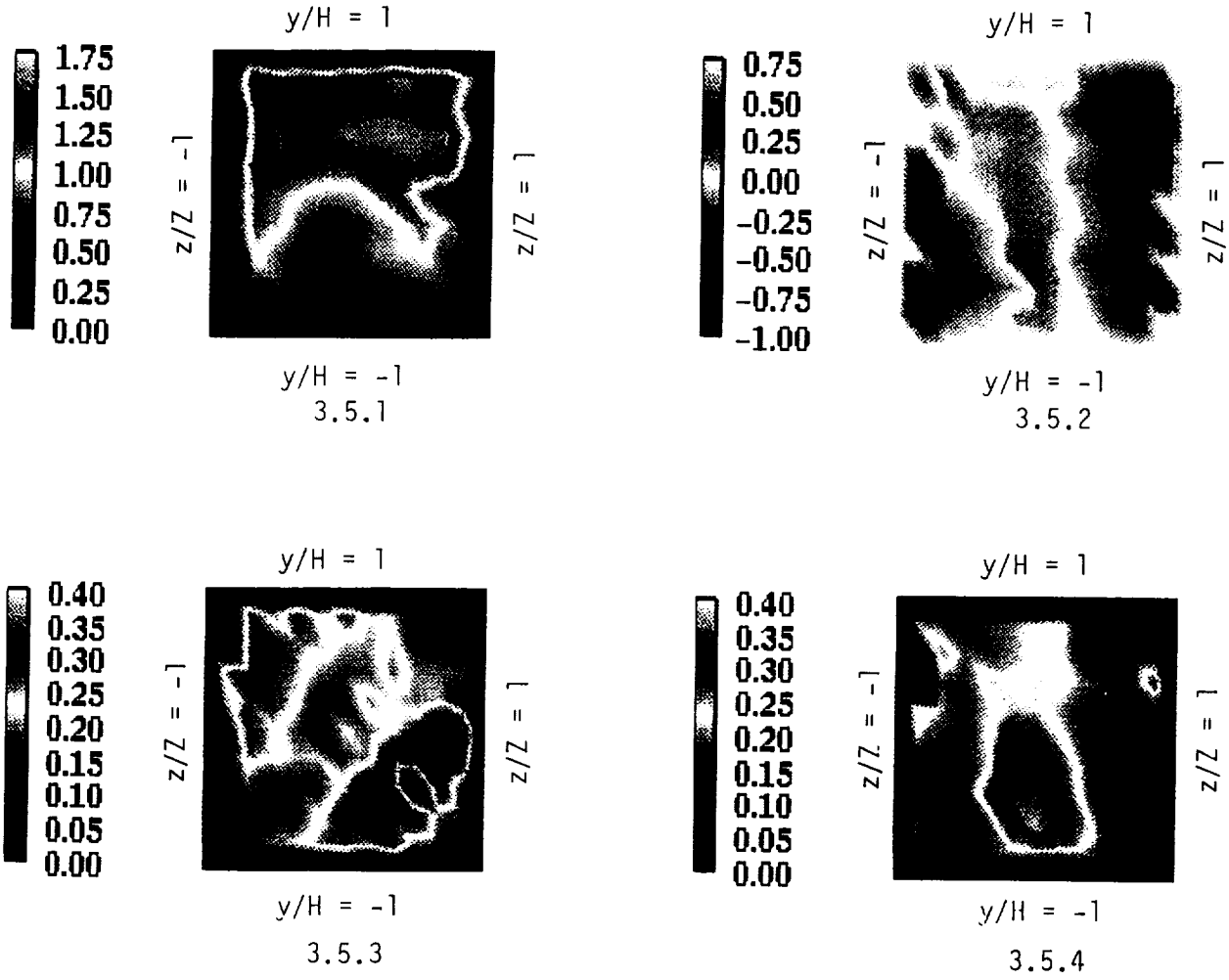

Figure 3.5 - Velocities at location A5, 1 D downstream of the first turn.

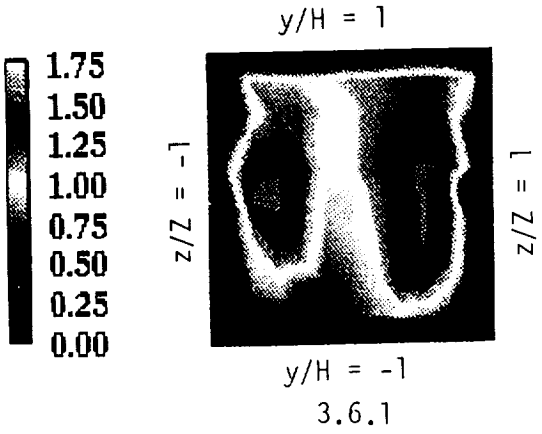

3.6.1

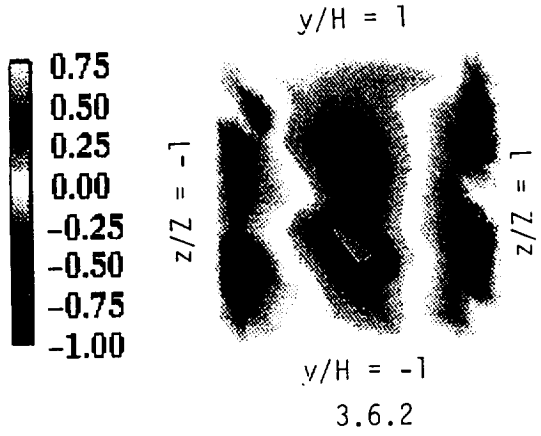

3.6.2

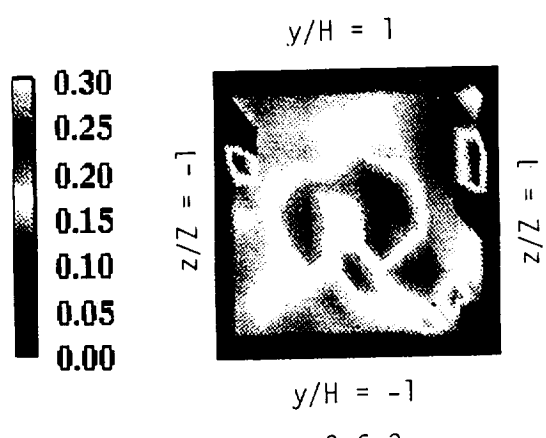

3.6.3

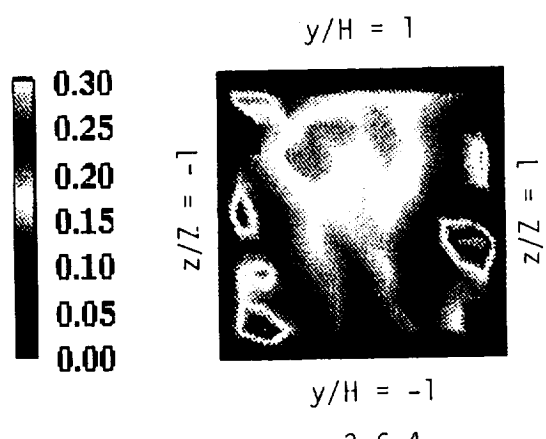

3.6.4

Figure 3.6 - Velocities at location A6, 1 D upstream of the second turn.

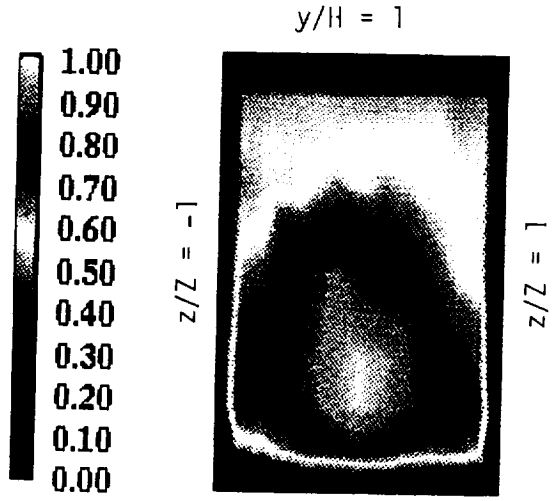

3.7.1

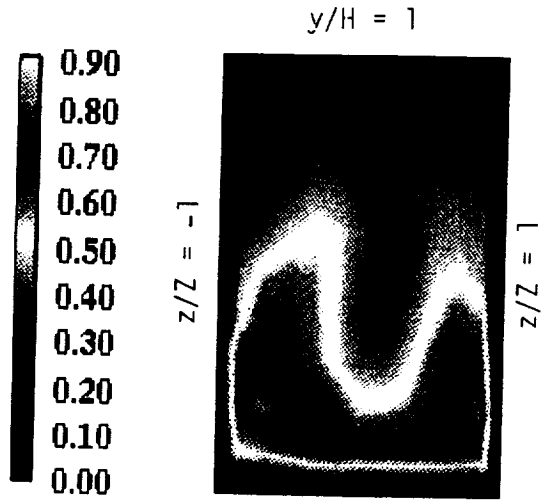

3.7.2

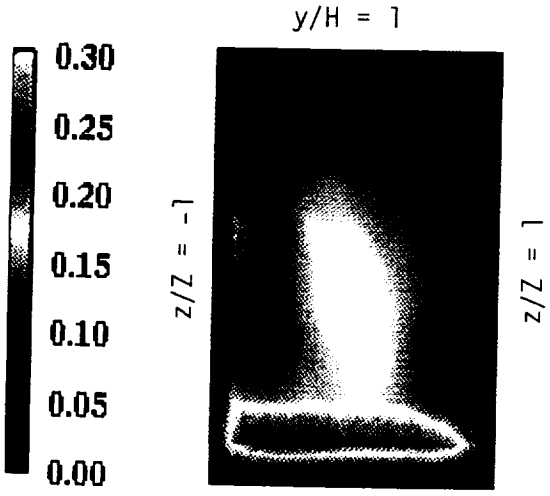

3.7.3

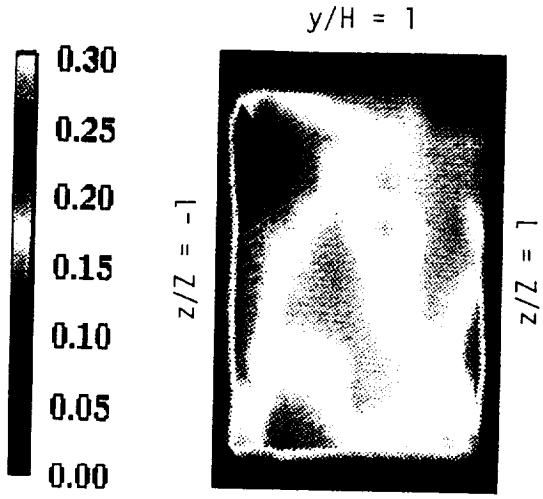

3.7.4

Figure 3.7 - Velocities at location A7, the second turn.

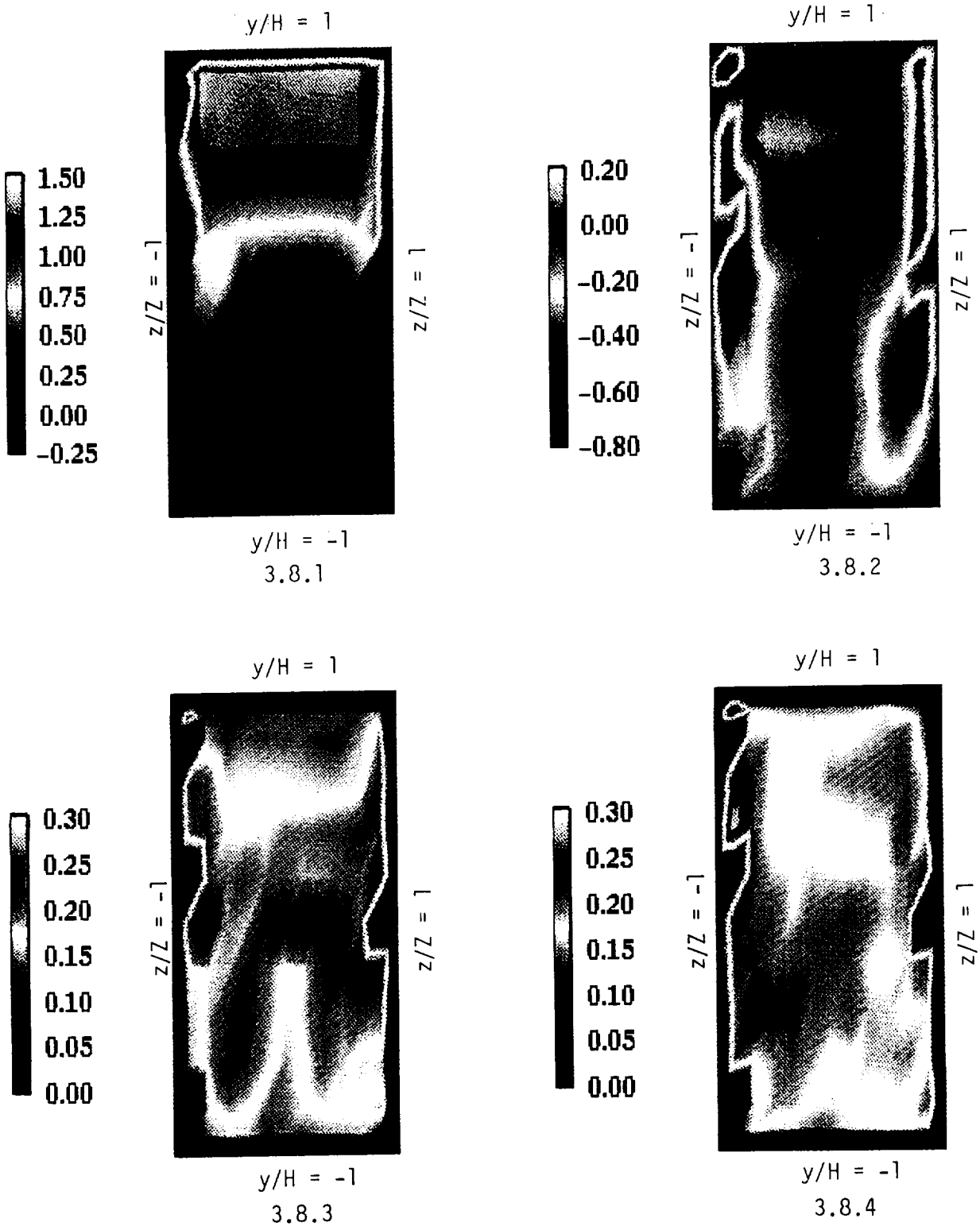

Figure 3.8 - Velocities at location A8, 1 D downstream of the second turn.

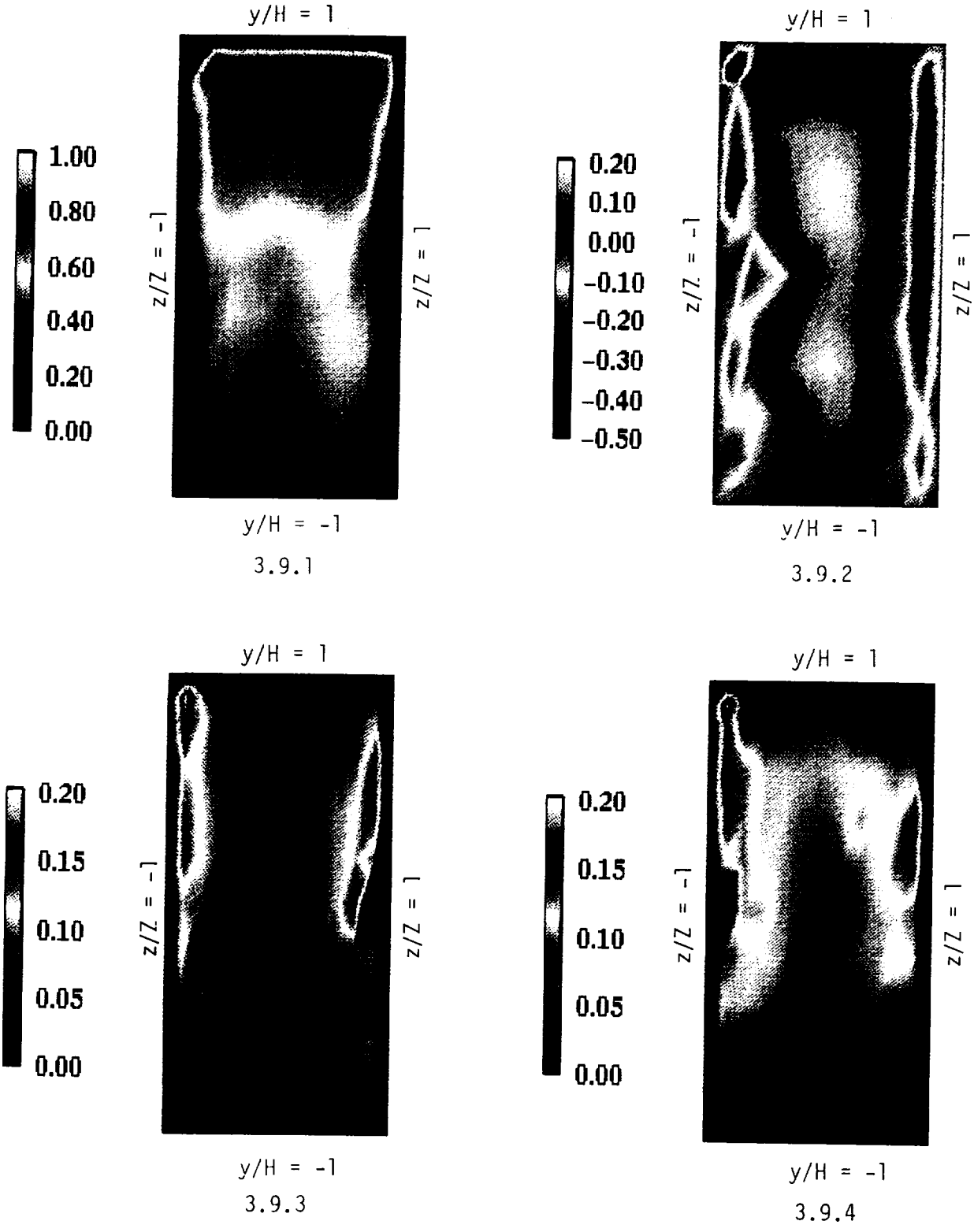

Figure 3.9 - Velocities at location A9, 1 D upstream of the third turn.

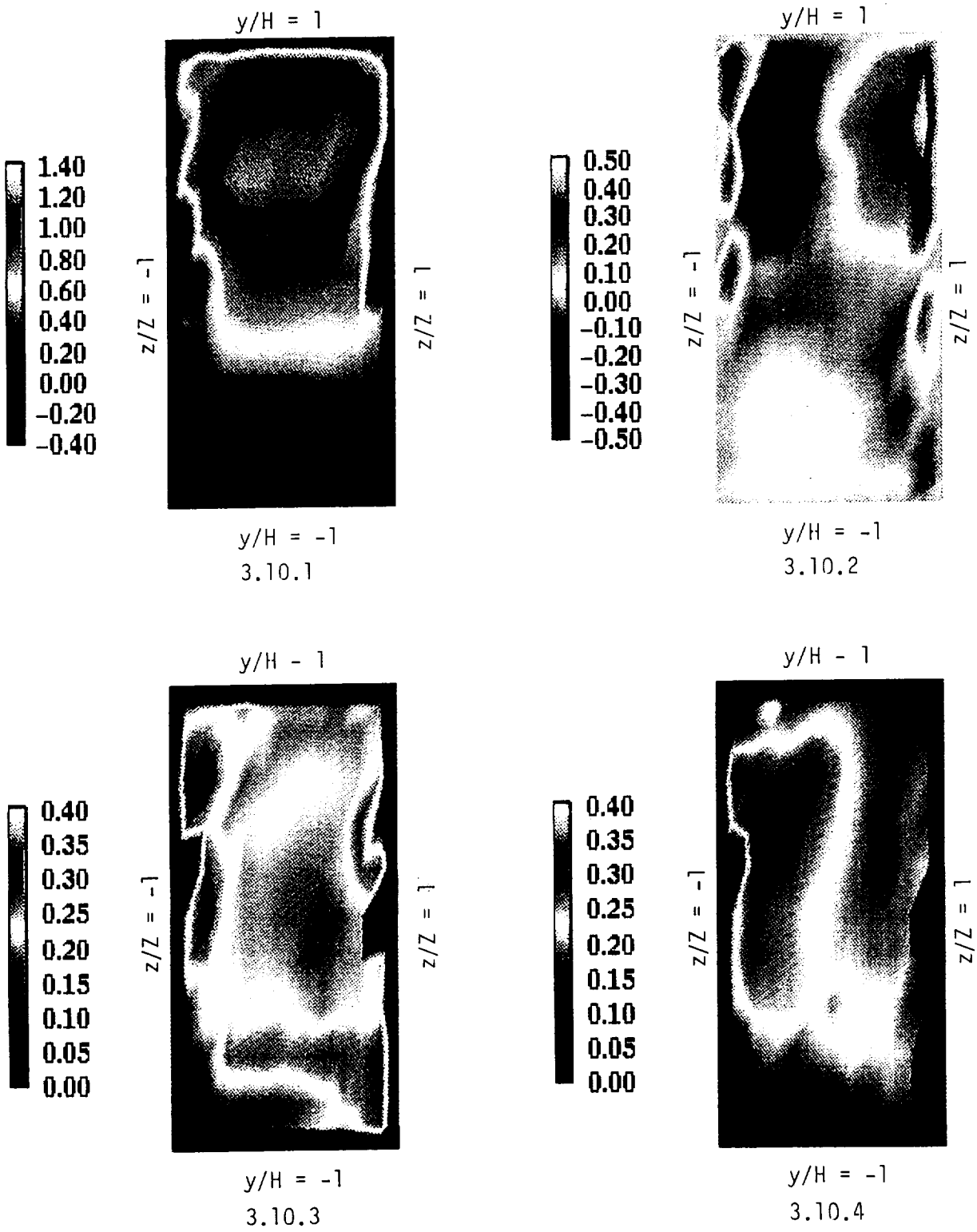

Figure 3.10 - Velocities at location A10, 1 D downstream of the third turn.

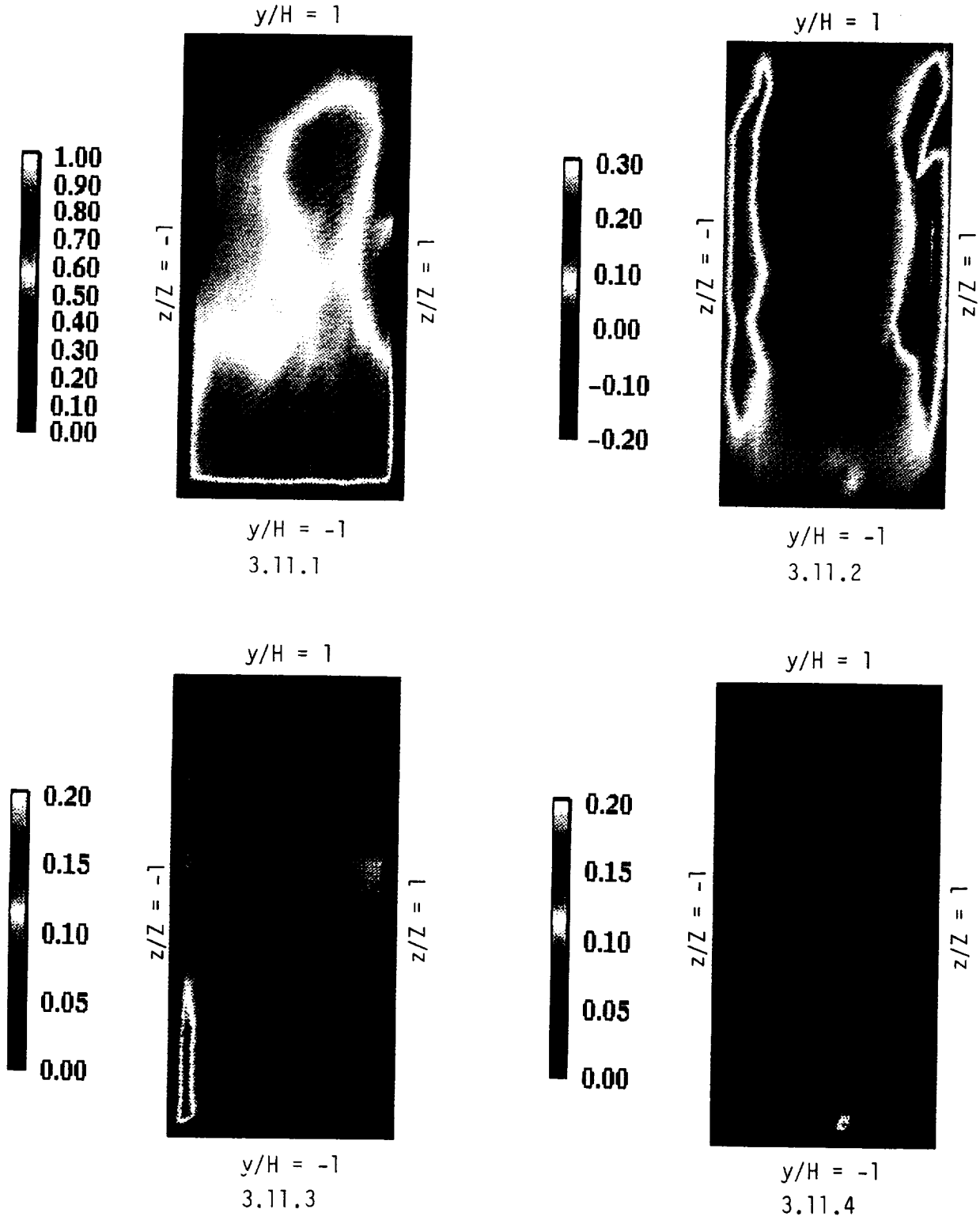

Figure 3.11 - Velocities at location A11, 1 D upstream of the exit.

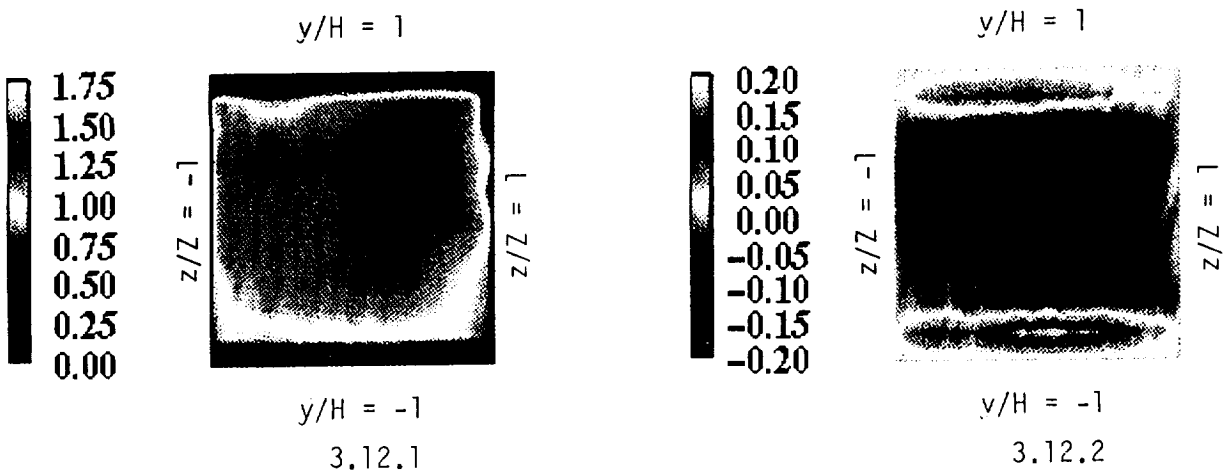

Figure 3.12 - Velocities at location D1, 1 D downstream of the inlet.

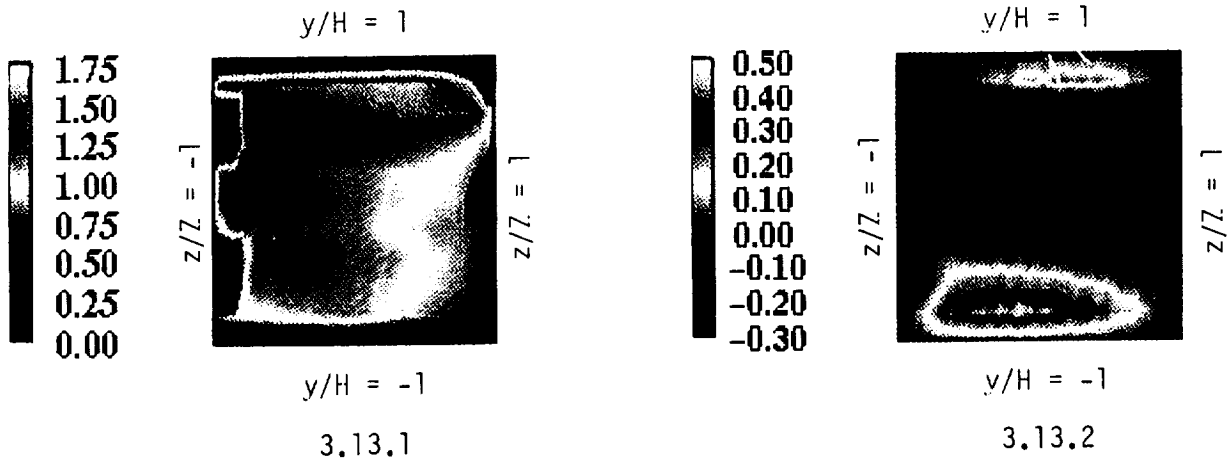

Figure 3.13 - Velocities at location D2, 4 D downstream of the inlet.

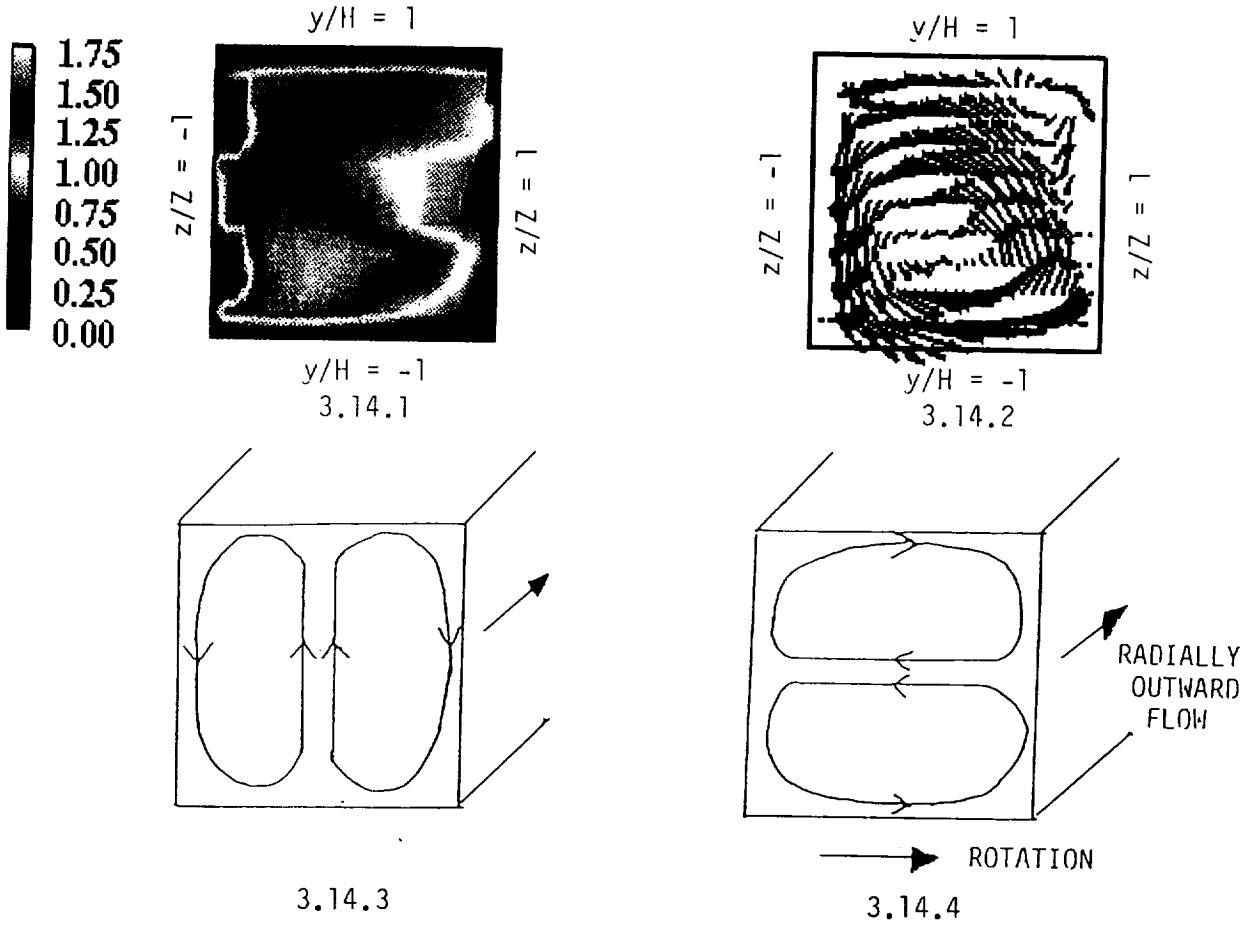

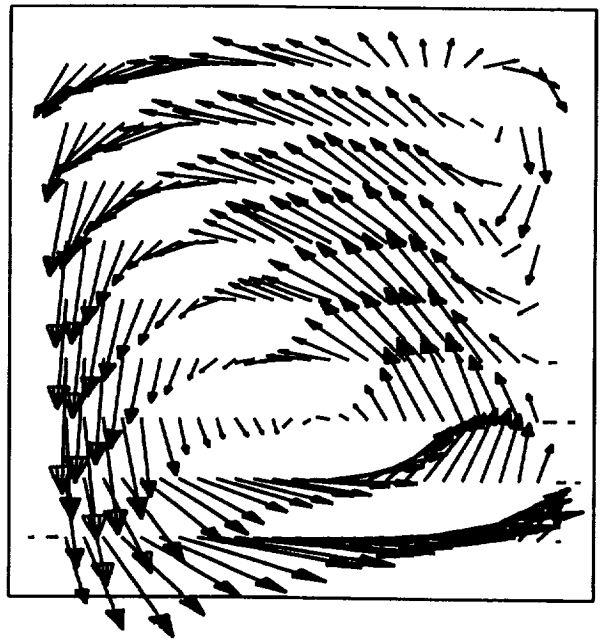

Enlargement of 3.14.2

Figure 3.14 - Velocities at location D3, 7 D downstream of the inlet.

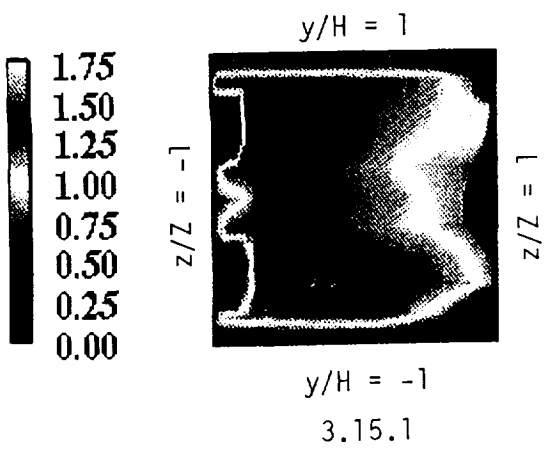

3.15.1

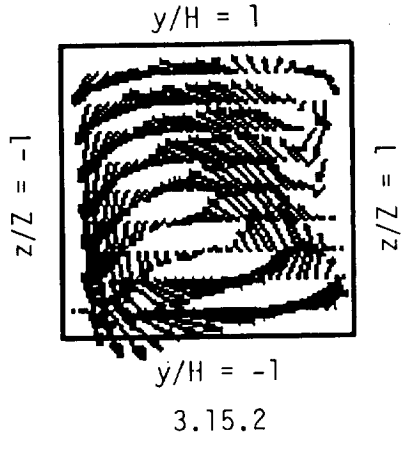

3.15.2

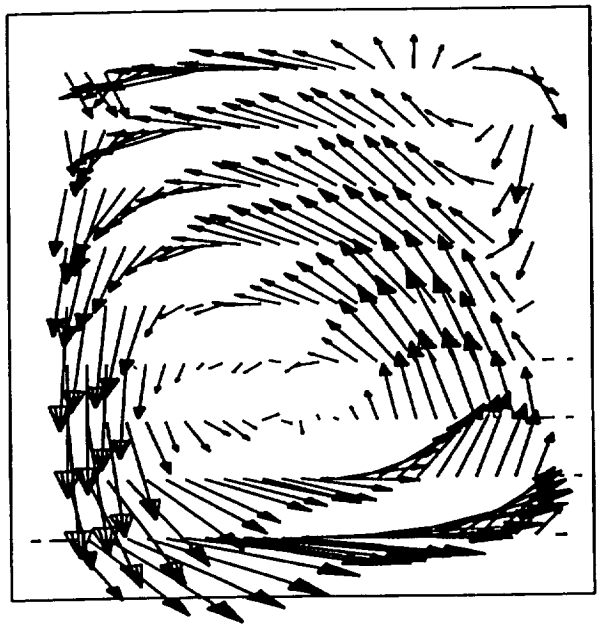

Enlargement of 3.15.2

Figure 3.15 - Velocities at location D4, 10 D downstream of the inlet.

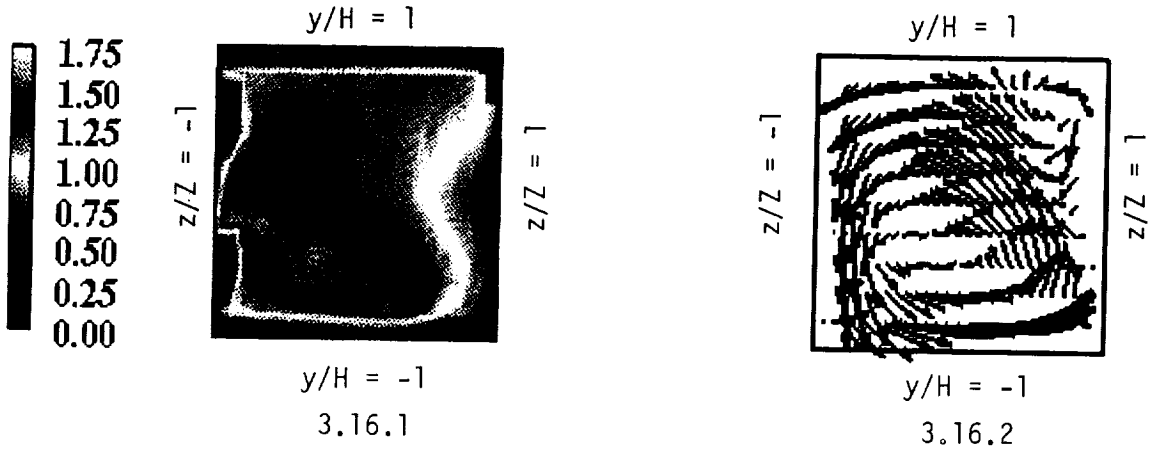

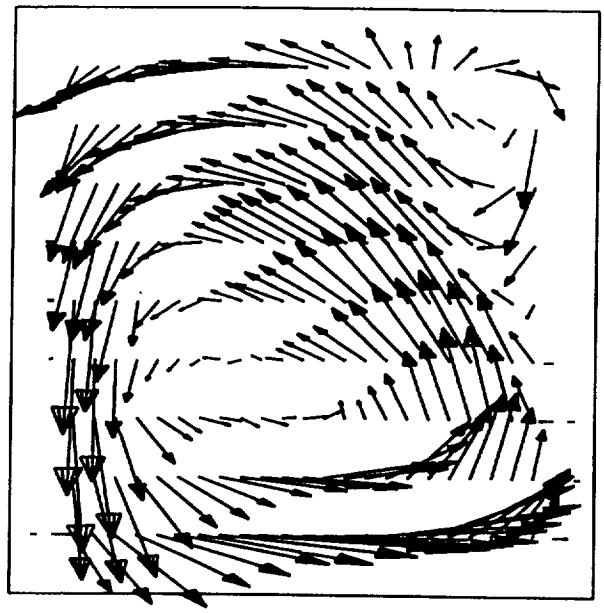

Enlargement of 3.16.2

Figure 3.16 - Velocities at location D5, 12 D downstream of the inlet.

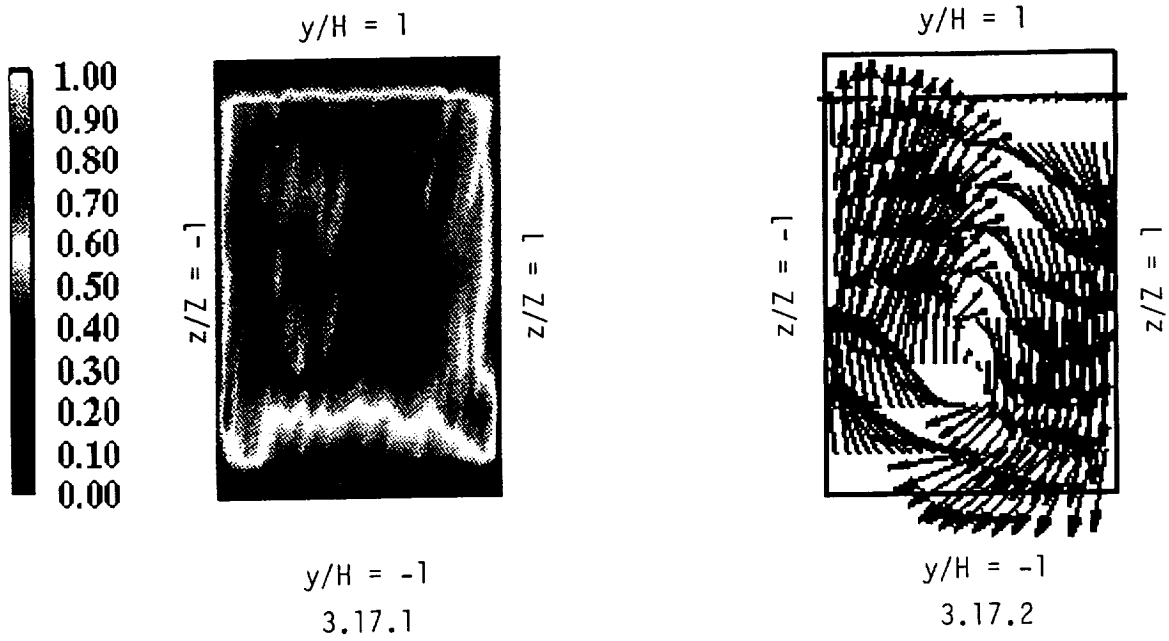

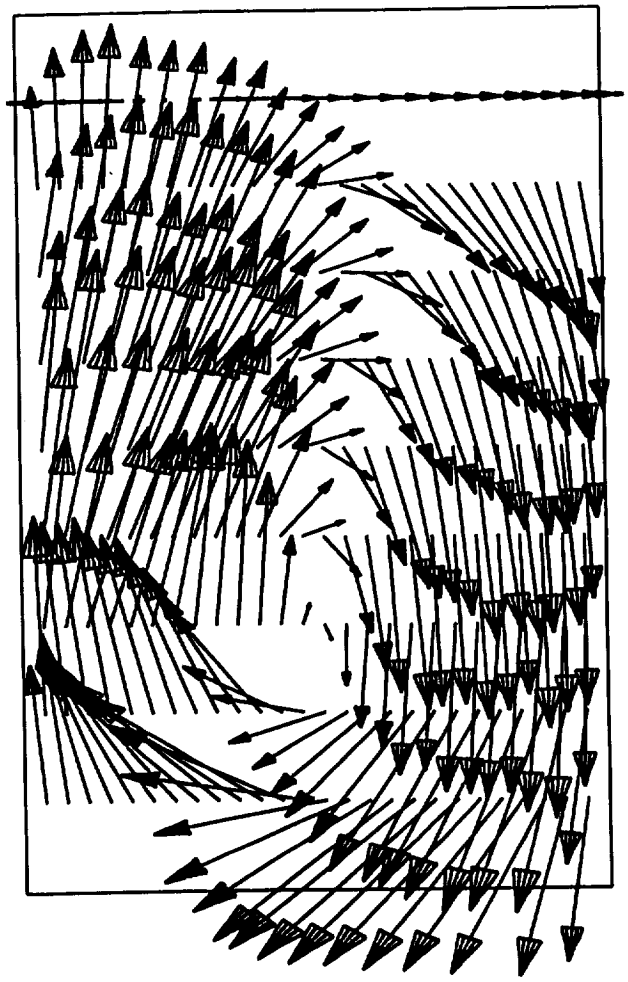

Enlargement of 3.17.2

Figure 3.17 - Velocities at location D6, the first turn.

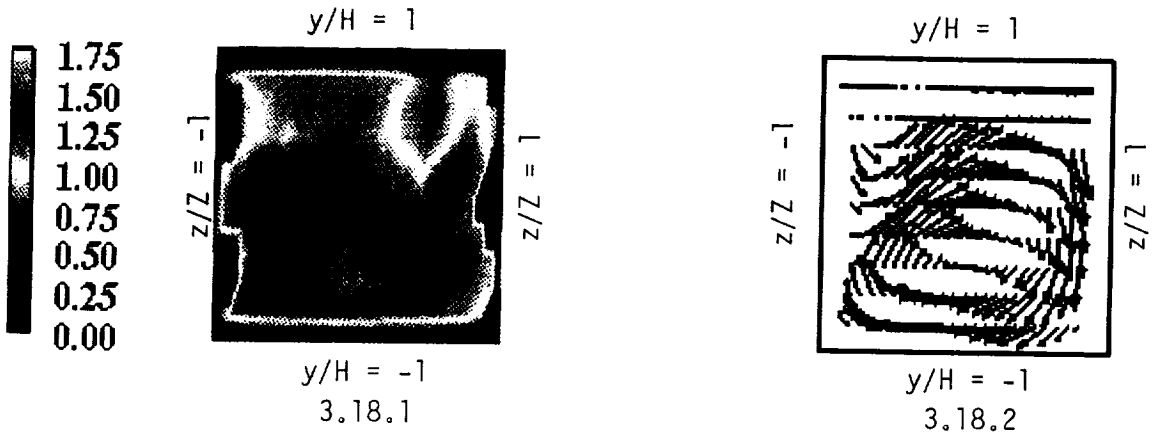

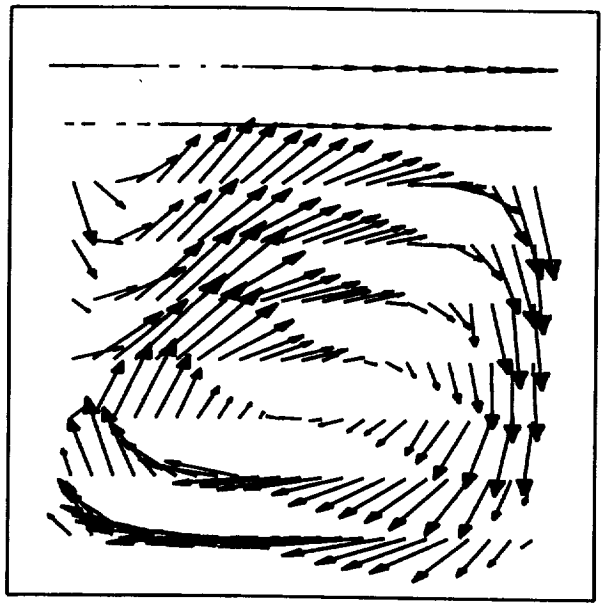

Enlargement of 3.18.2

Figure 3.18 - Velocities at location D7, 1 D downstream of the first turn.

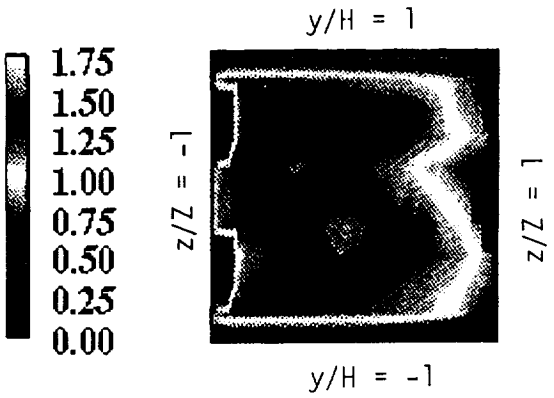

3.19.1

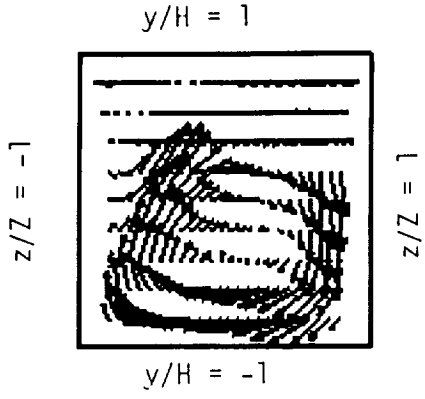

3.19.2

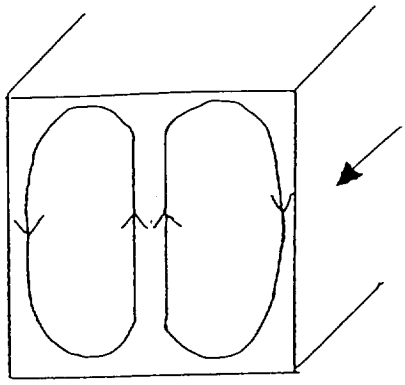

3.19.3

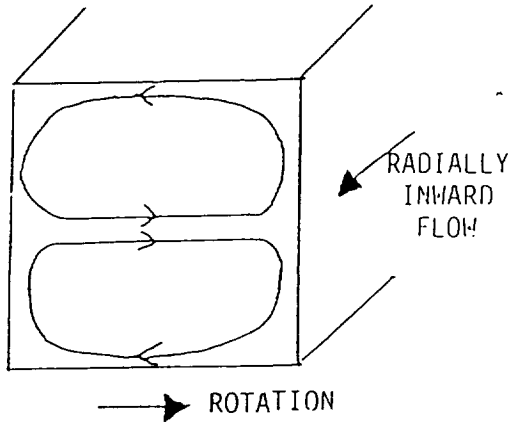

3.19.4

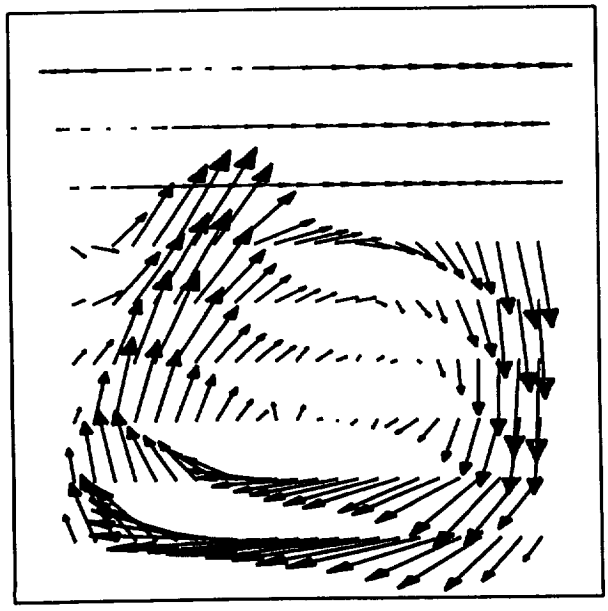

Enlargement of 3.19.2

Figure 3.19 - Velocities at location D8, 3 D downstream of the first turn.

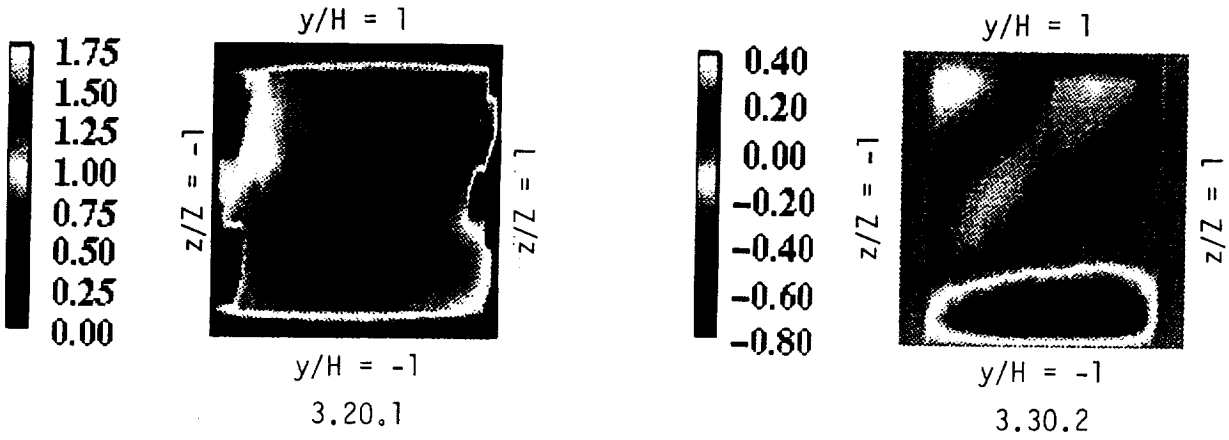

Figure 3.20 - Velocities at location D9, 9 D downstream of the first turn.

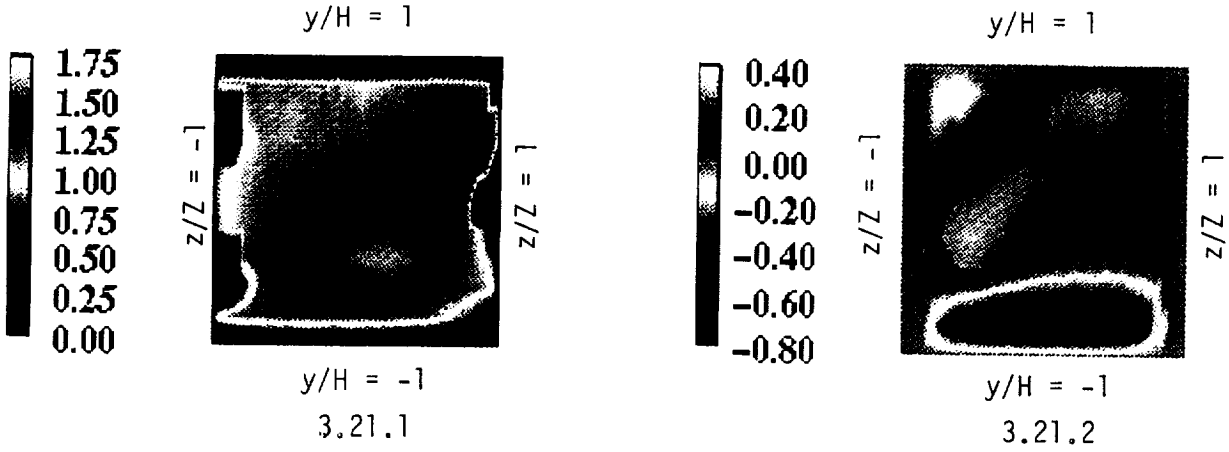

Figure 3.21 - Velocities at location D10, 11 D downstream of the first turn.

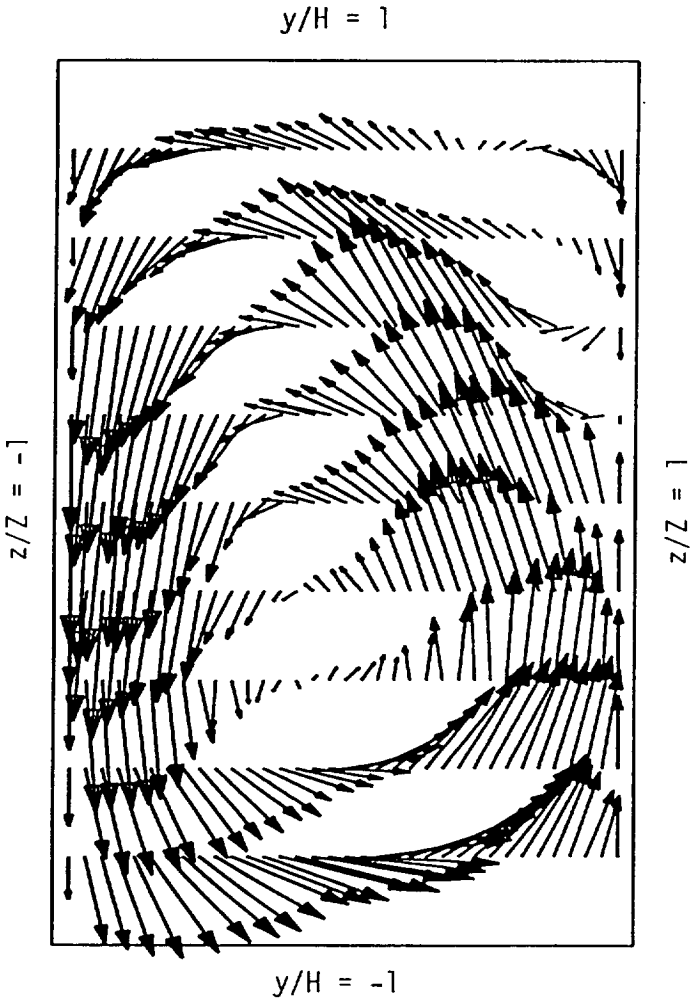

Figure 3.22 - Velocities at location D11, the second turn.

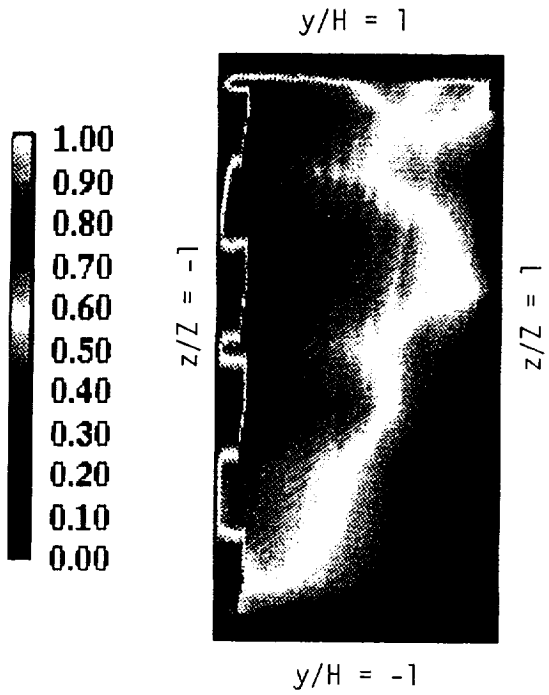

Figure 3.23 - Velocities at location D12, 1 D downstream of the second turn.

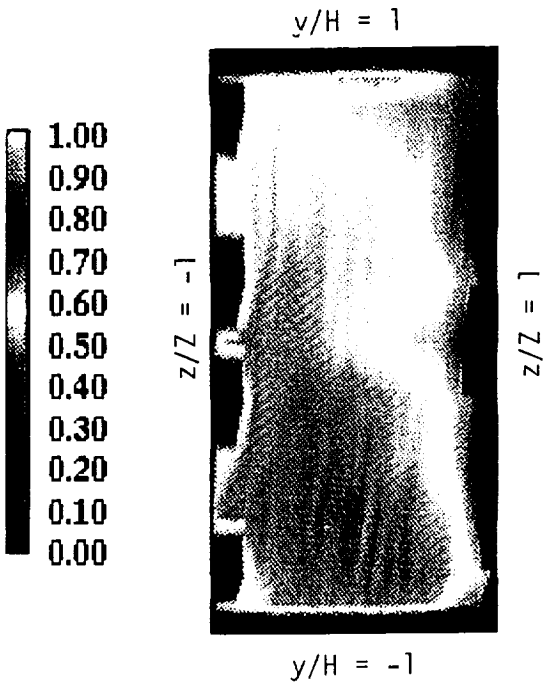

3.24.1

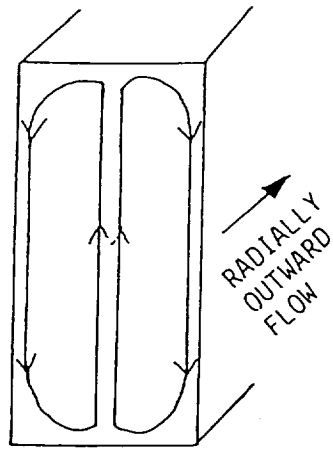

3.24.2

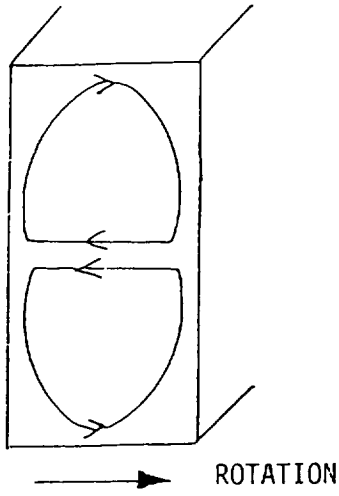

3.24.3

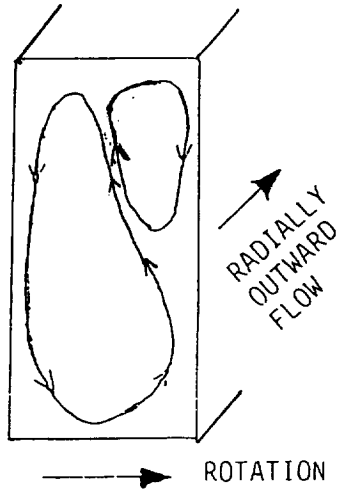

3.24.4

Figure 3.24 - Velocities at location D13, 6 D downstream of the second turn.

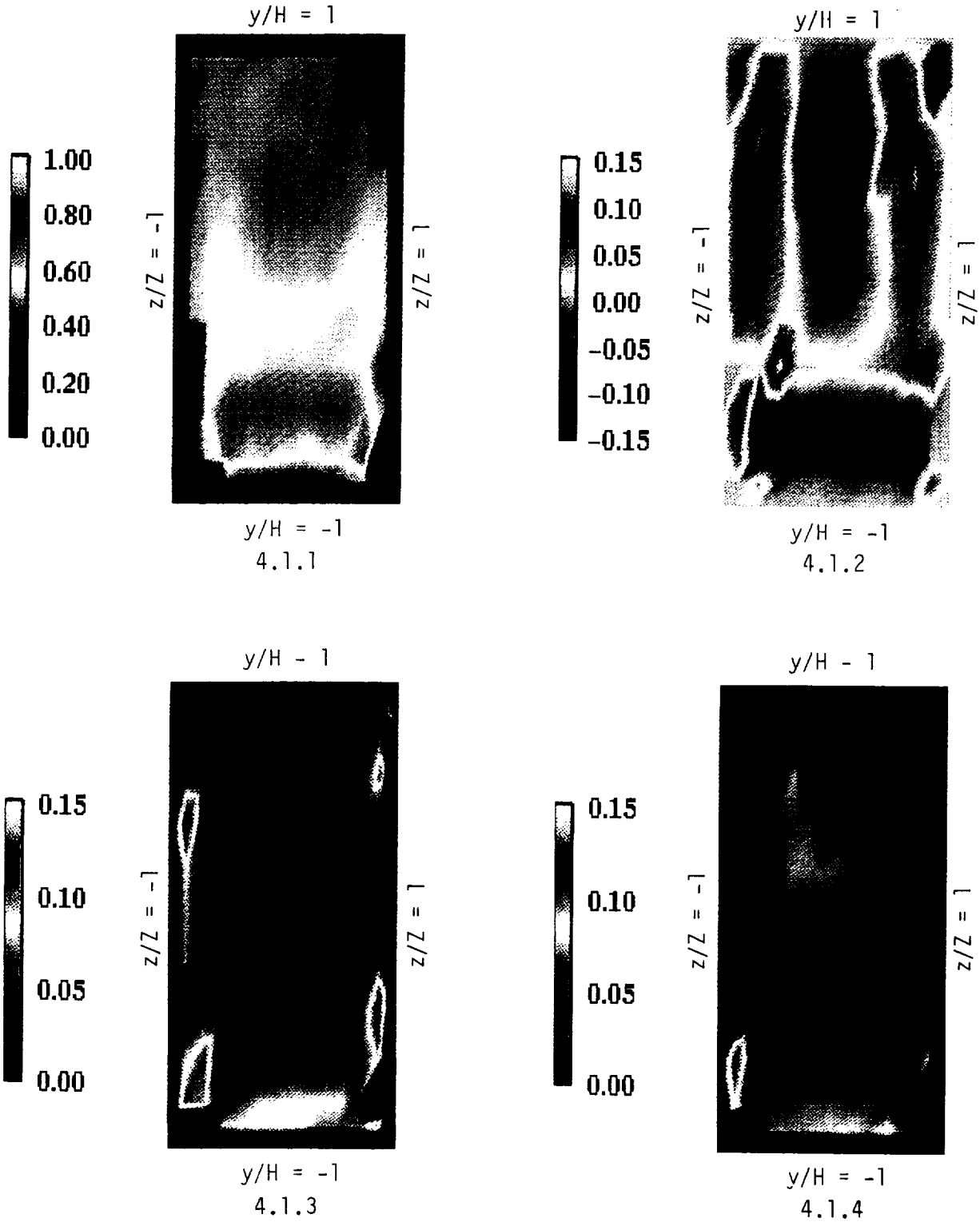

Figure 4.1 - Velocities at location B1, 1 D downstream of the inlet.

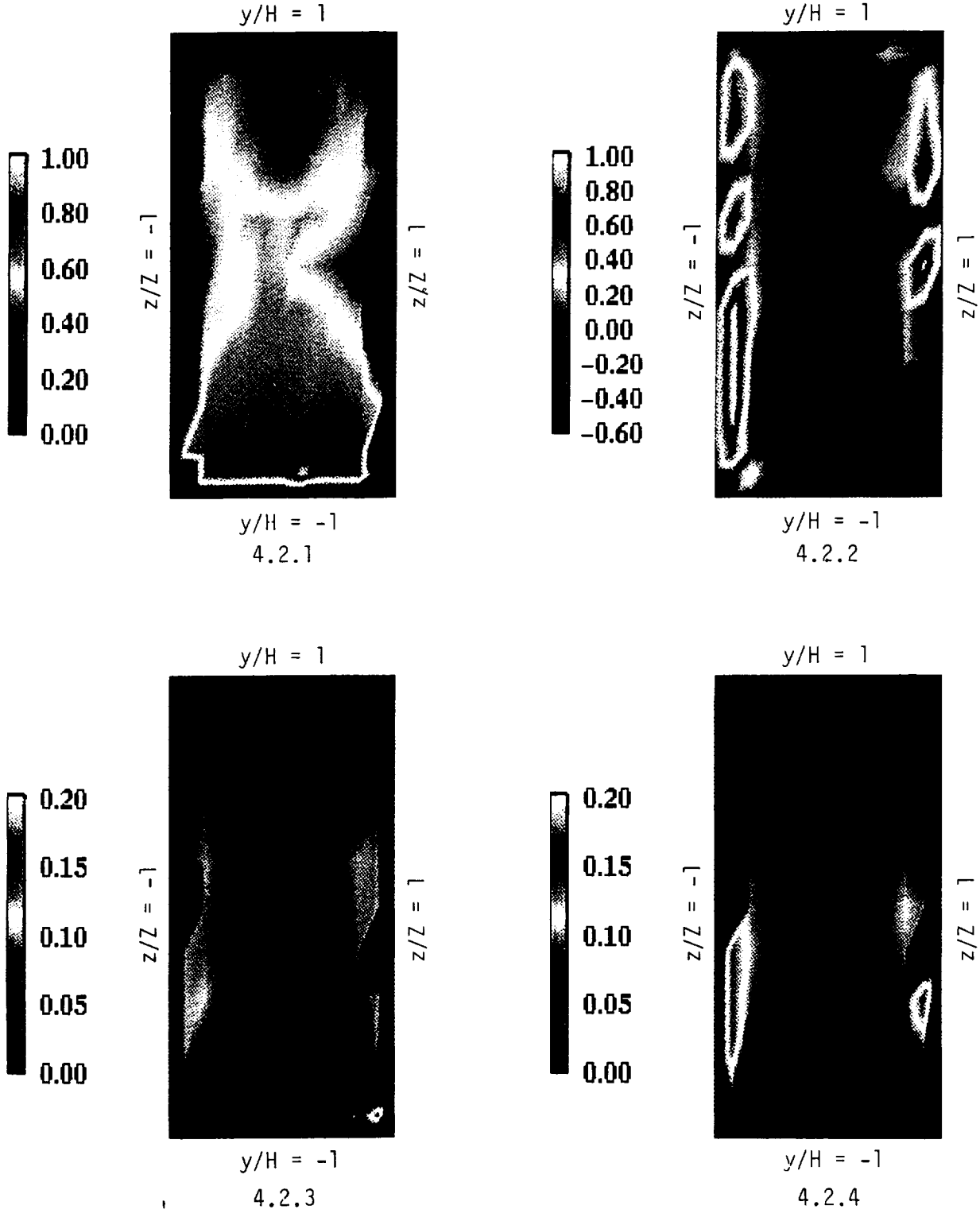

Figure 4.2 - Velocities at location B2, 7 D downstream of the inlet.

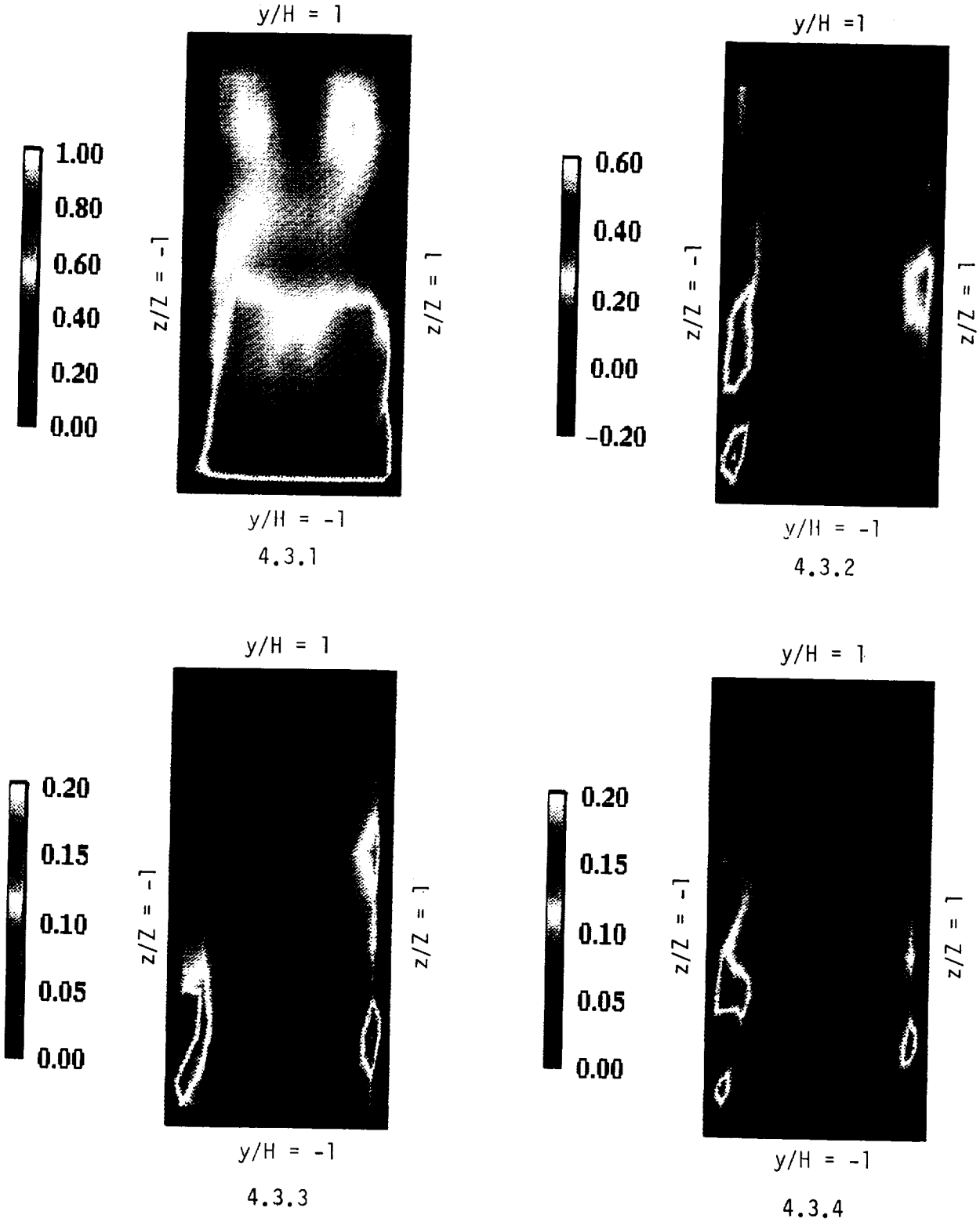

Figure 4.3 - Velocities at location B3, 1 D upstream of the first turn.

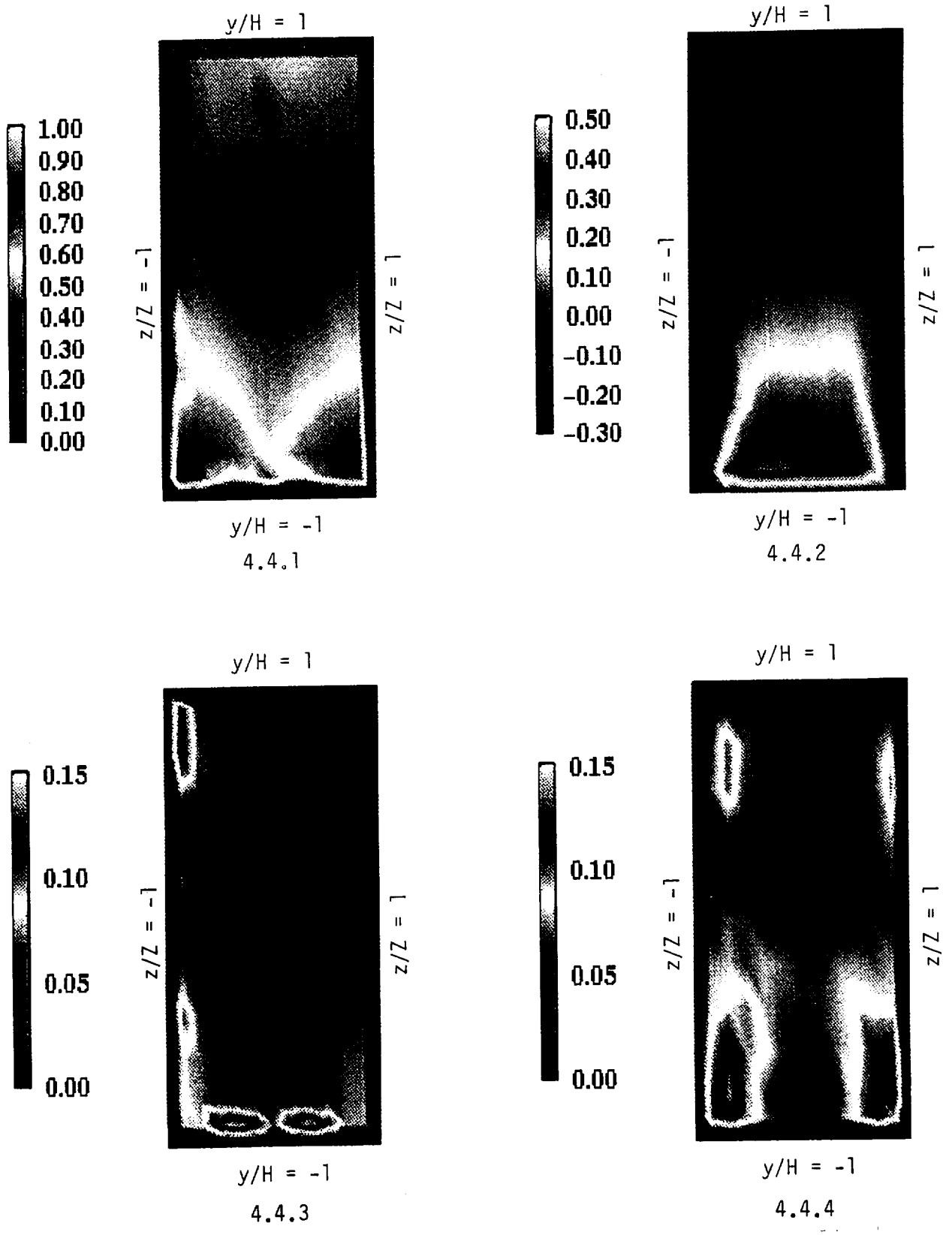

Figure 4.4 - Velocities at location B4, the first turn.

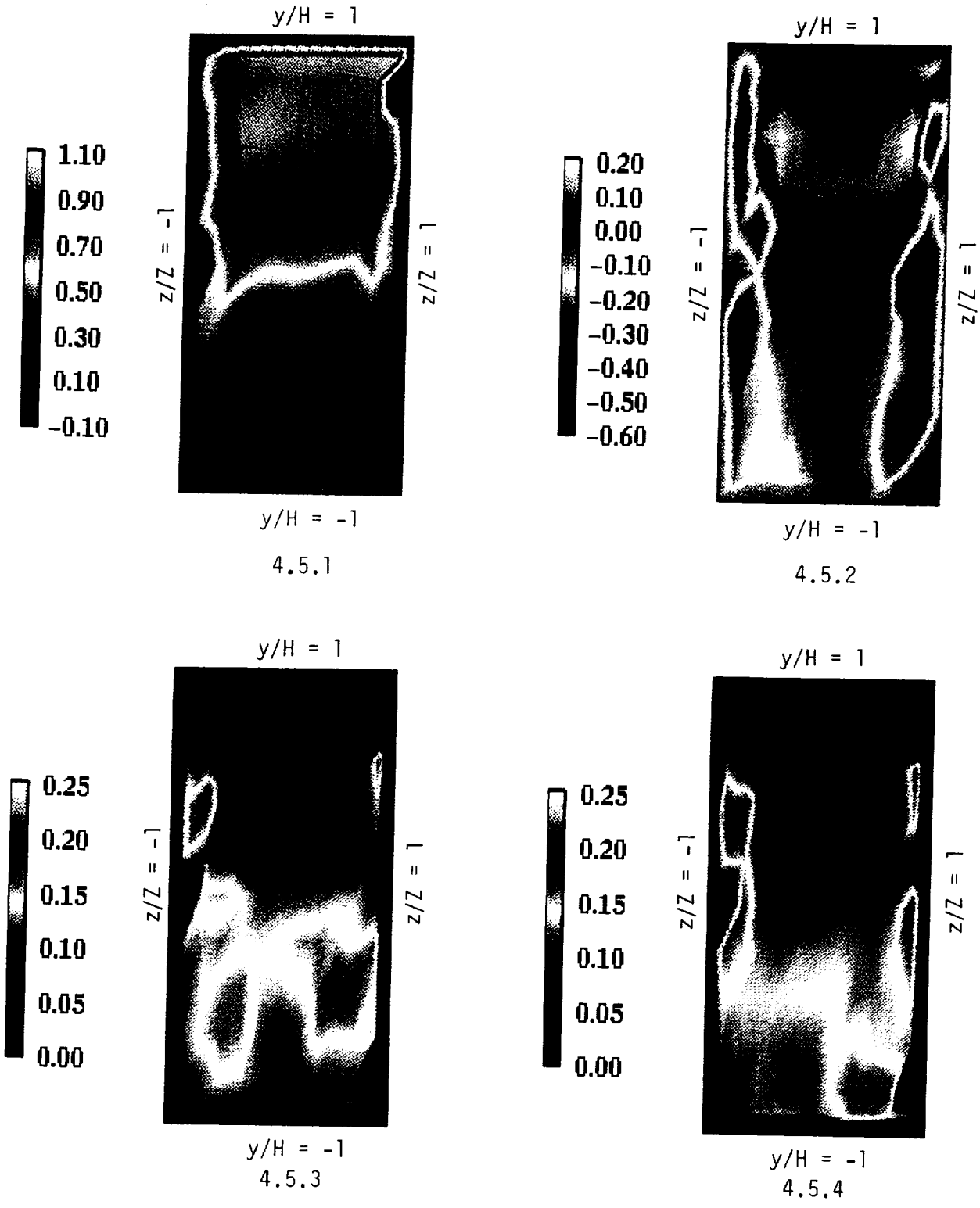

Figure 4.5 - Velocities at location B5, 1 D downstream of the first turn.

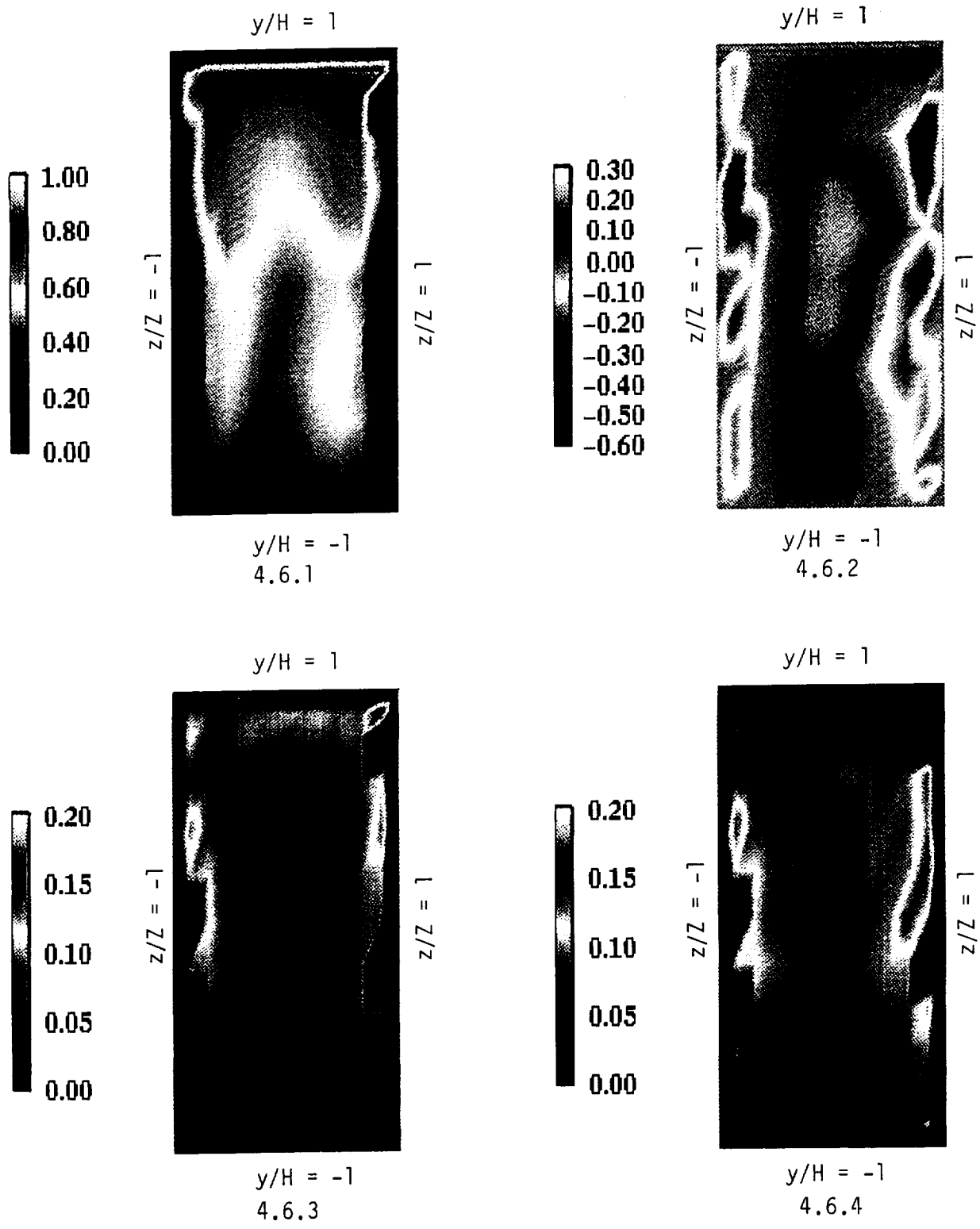

Figure 4.6 - Velocities at location B6, 1 D upstream of the second turn.

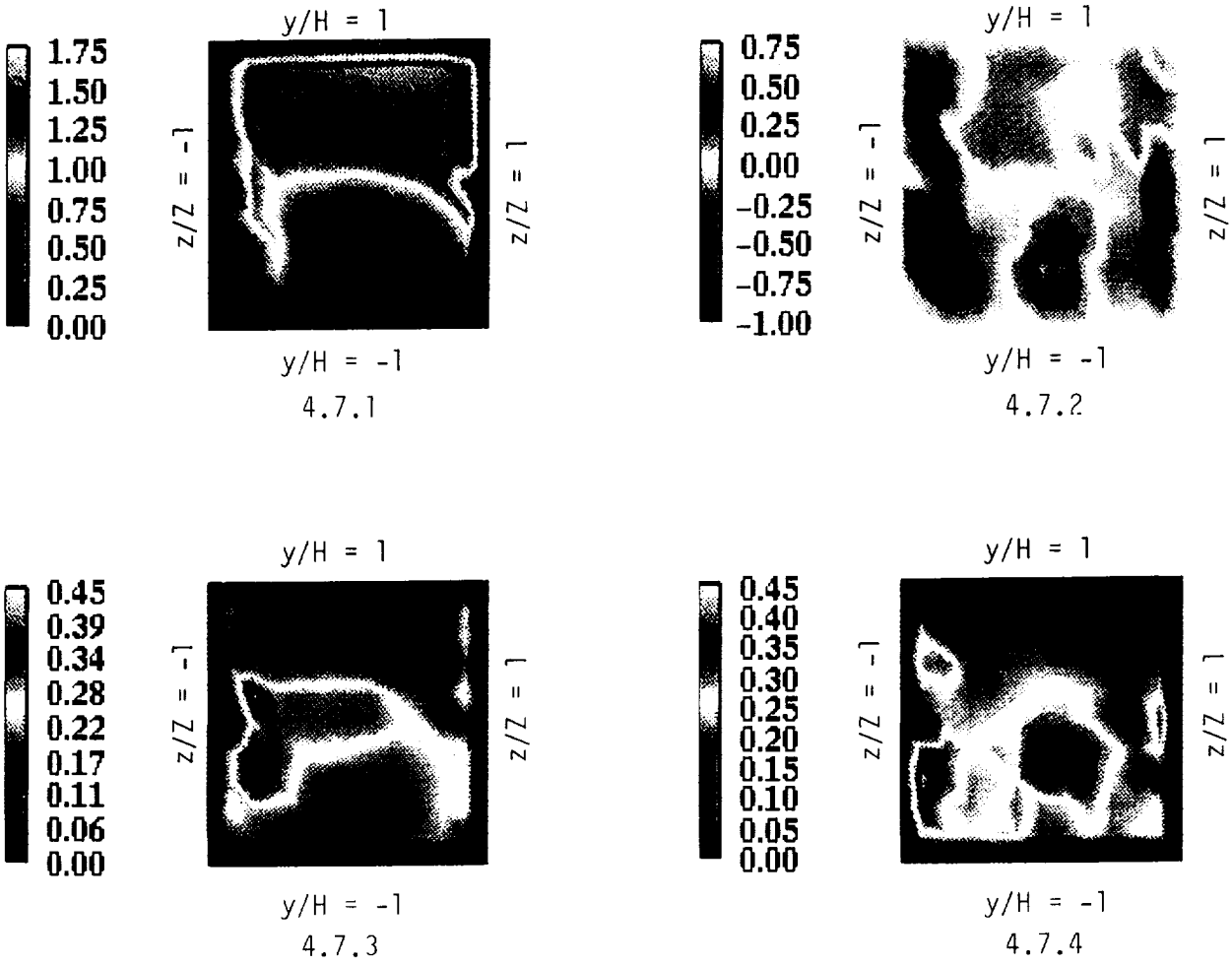

Figure 4.7 - Velocities at location B7, 1 D downstream of the second turn.

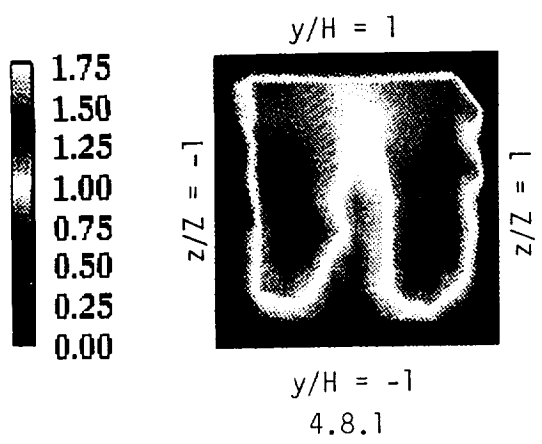

4.8.1

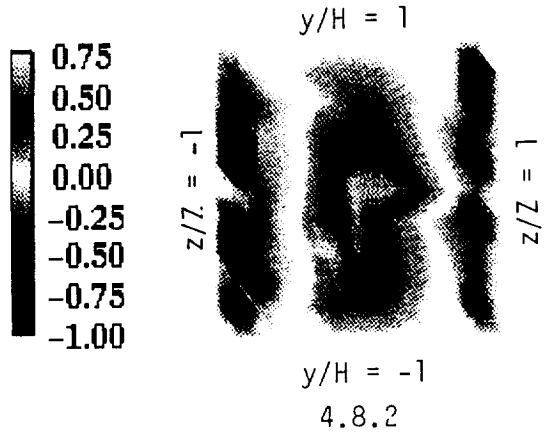

4.8.2

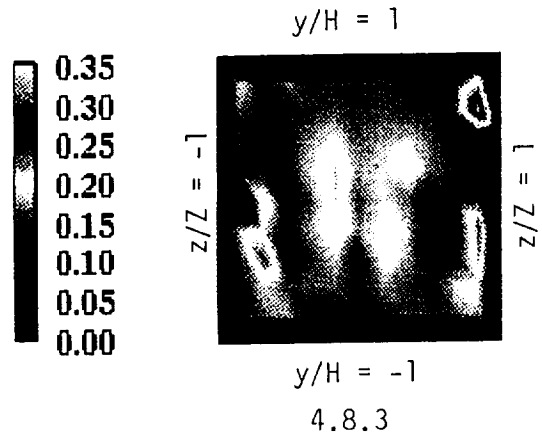

4.8.3

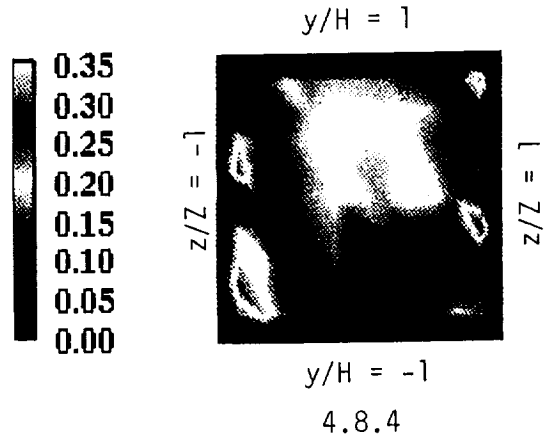

4.8.4

Figure 4.8 - Velocities at location B8, 1 D upstream of the third turn.

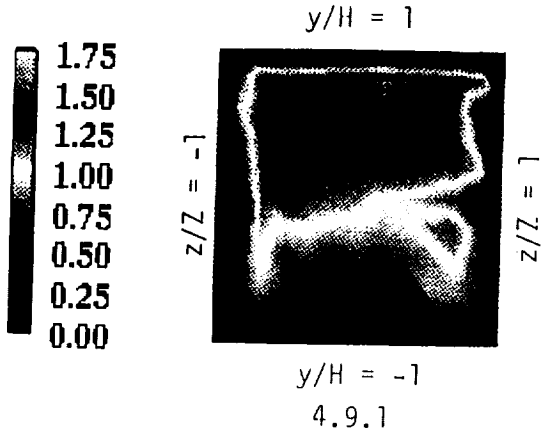

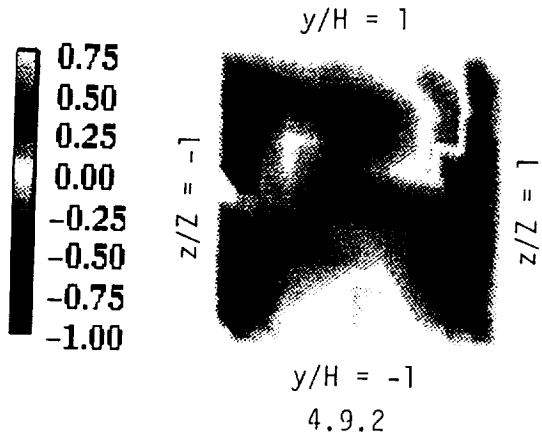

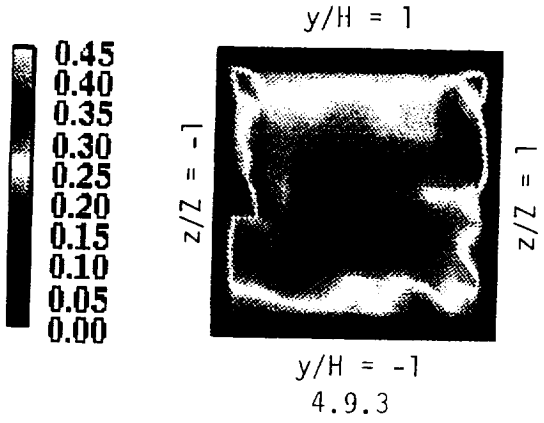

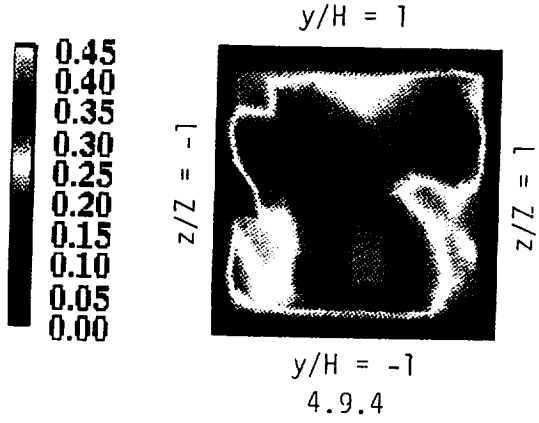

Figure 4.9 - Velocities at location B9, 1 D downstream of the third turn.

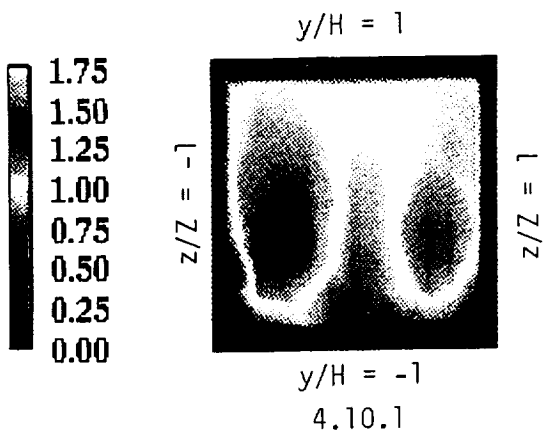

4.10.1

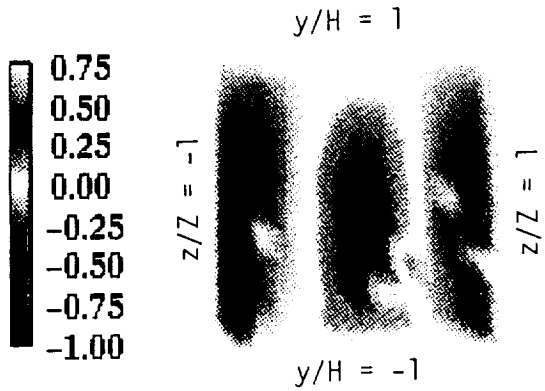

4.10.2

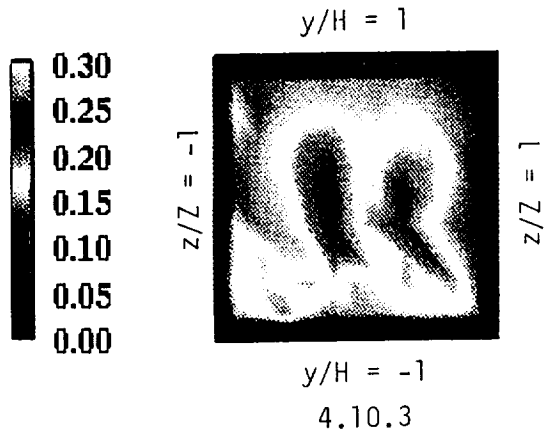

4.10.3

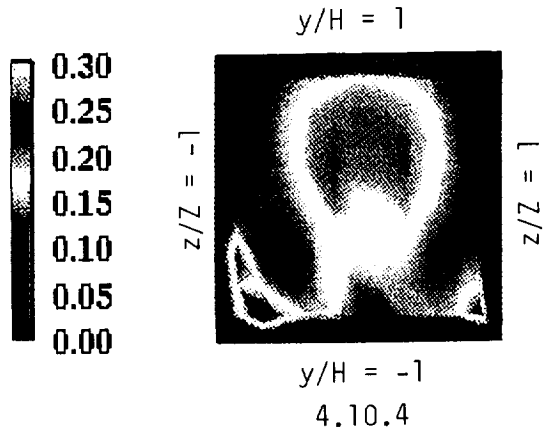

4.10.4

Figure 4.10 - Velocities at location B10, 1 D upstream of the exit.

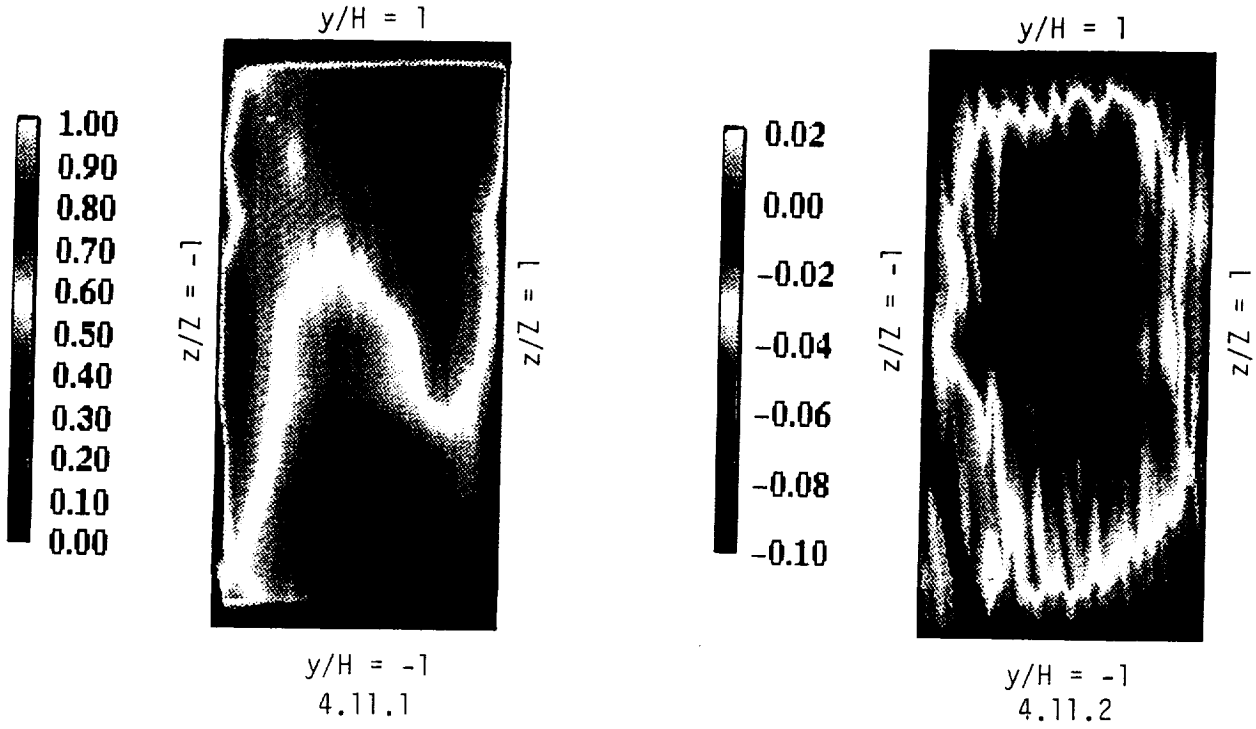

Figure 4.11 - Velocities at location C1, 1 D downstream of the inlet.

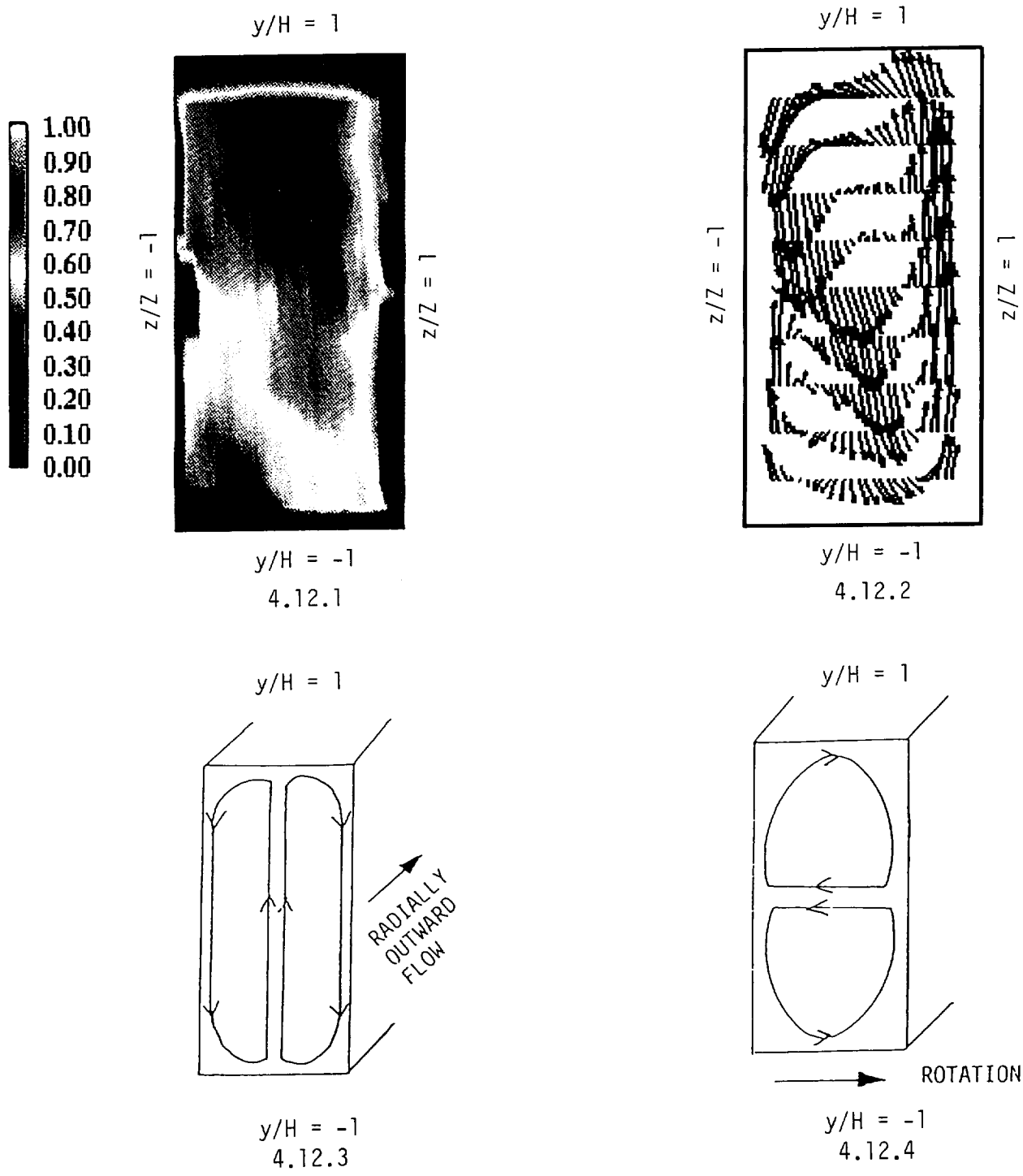

Figure 4.12 - Velocities at location C2 - 4 D downstream of the inlet.

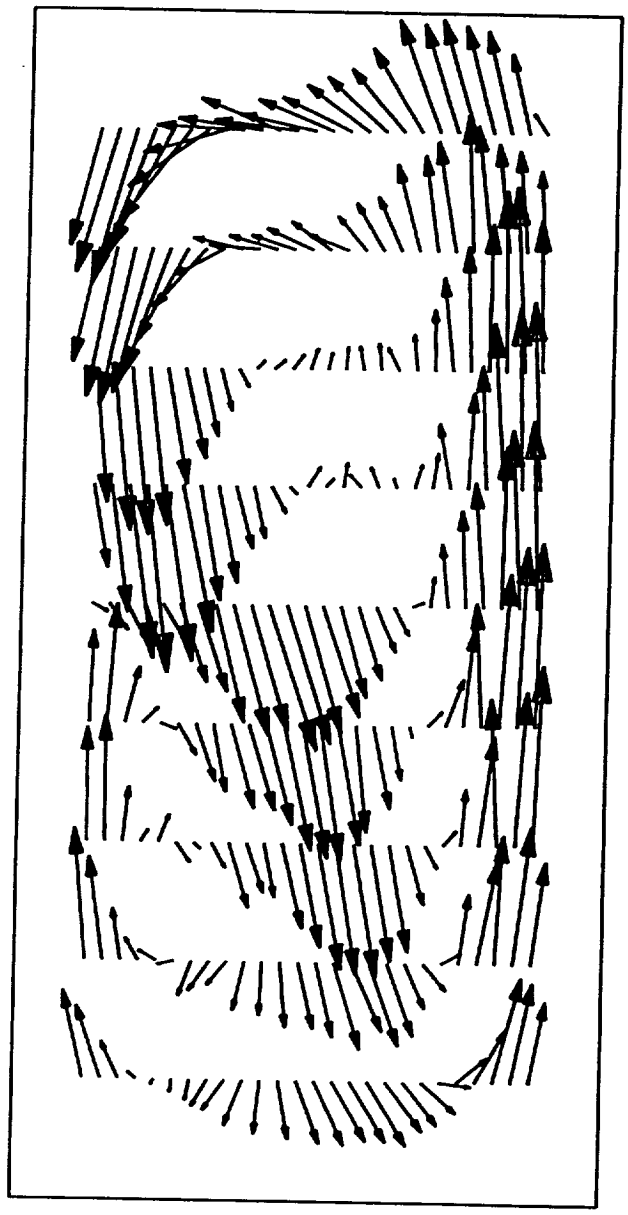

Enlargement of 4.12.2

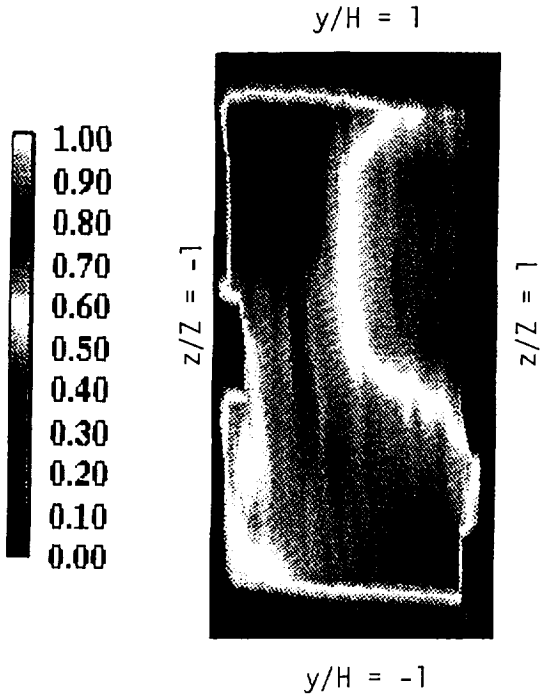

4.13.1

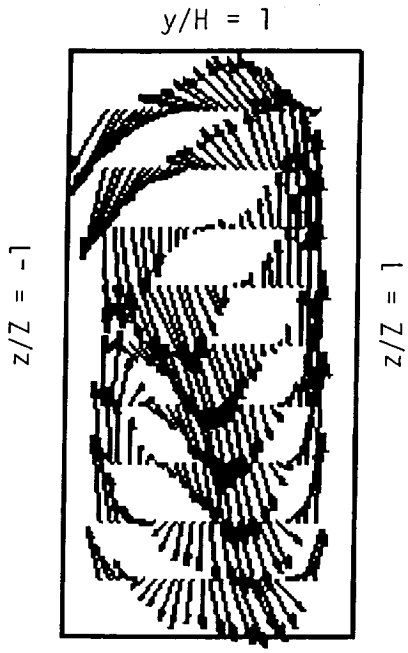

4.13.2

Figure 4.13 - Velocities at location C3, 7 D downstream of the inlet.

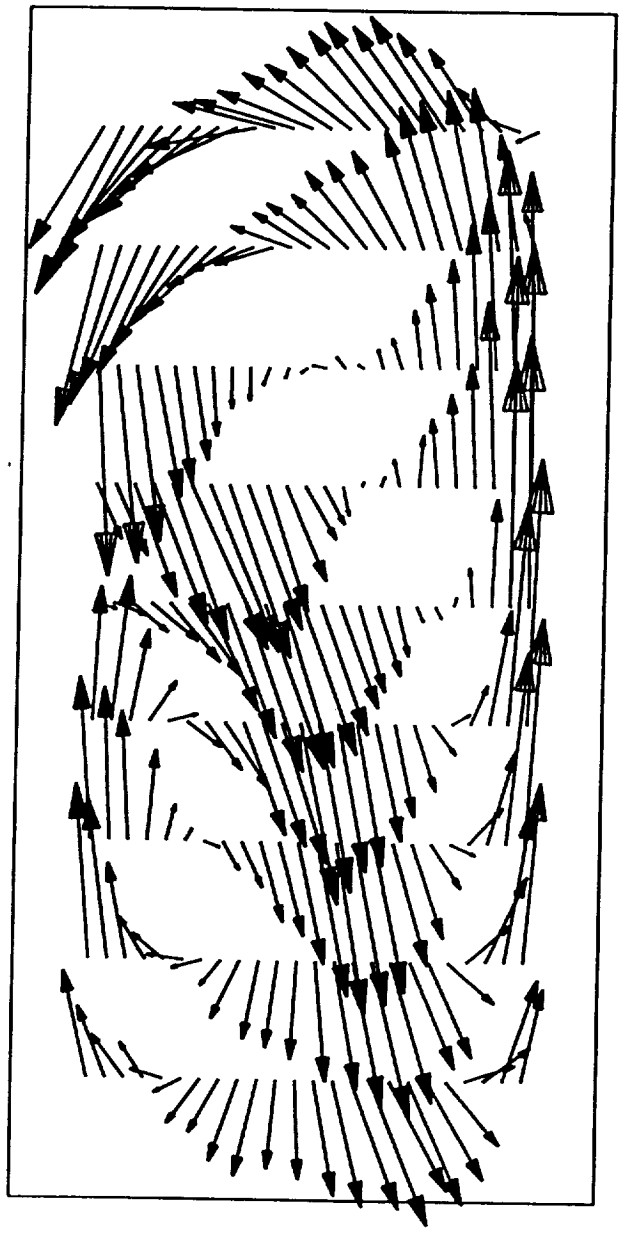

Enlargement of 4.13.2

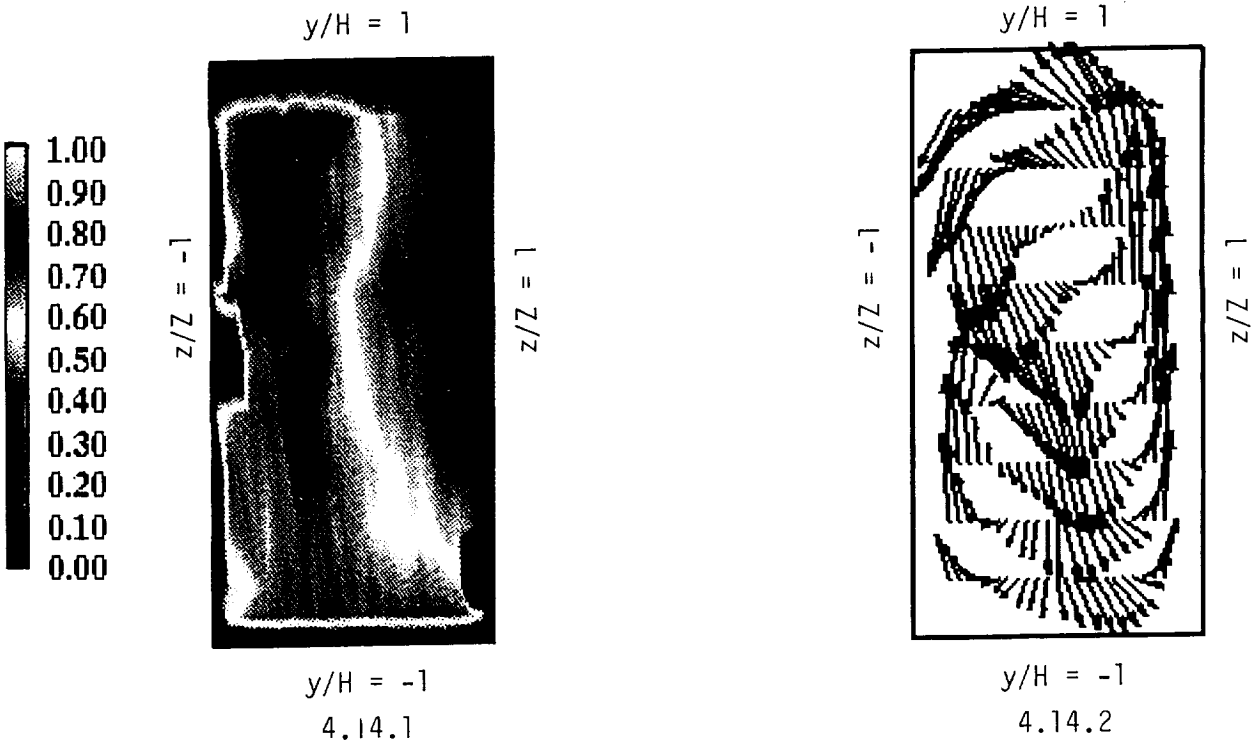

Figure 4.14 - Velocities at location C4, 10 D downstream of the inlet.

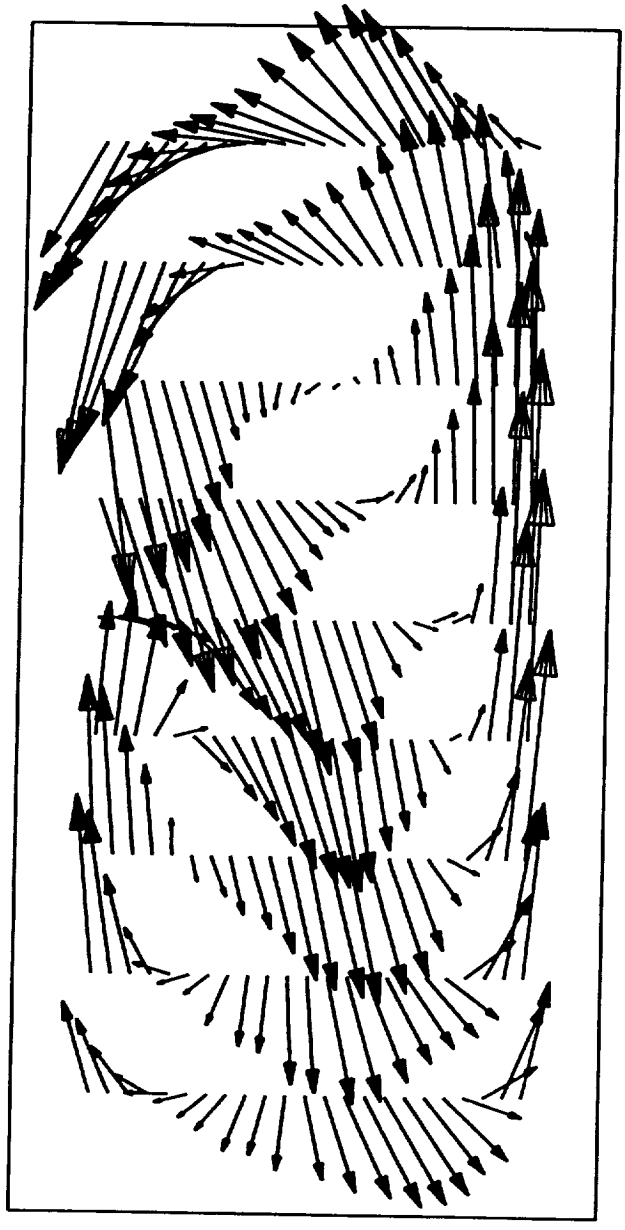

Enlargement of 4.14.2

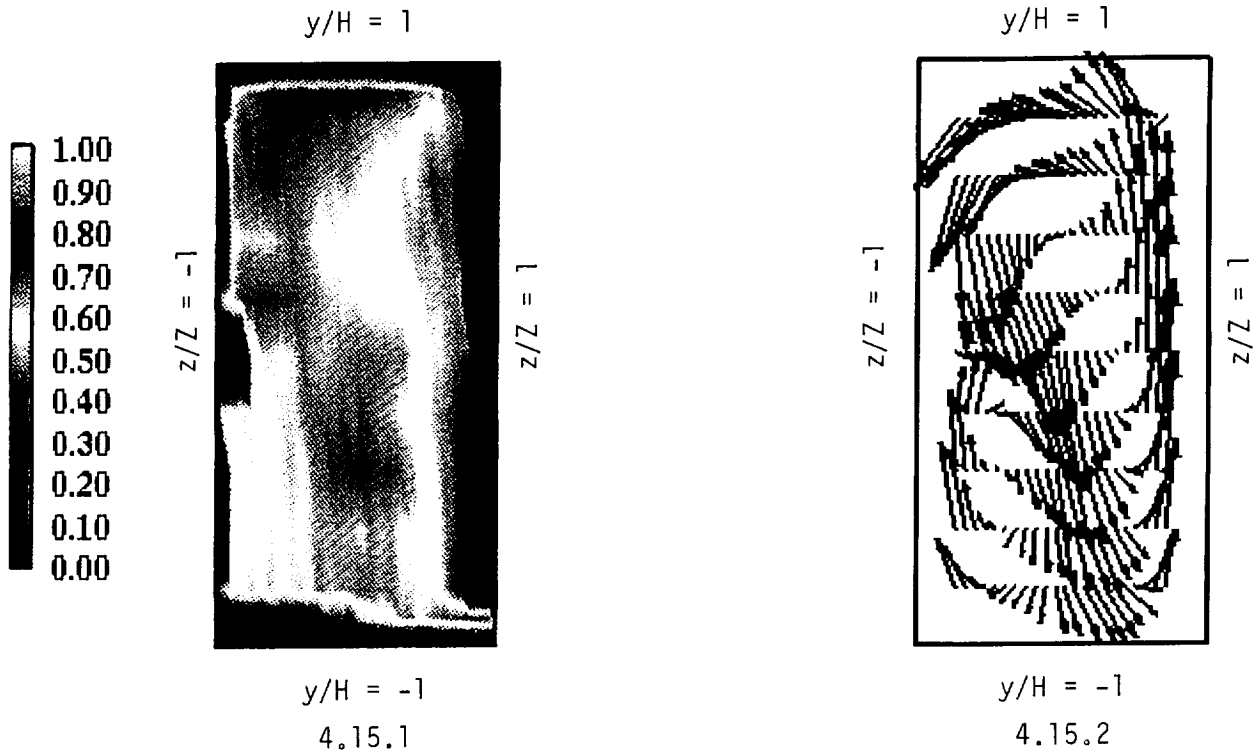

Figure 4.15 - Velocities at location C5, 12 D downstream of the inlet.

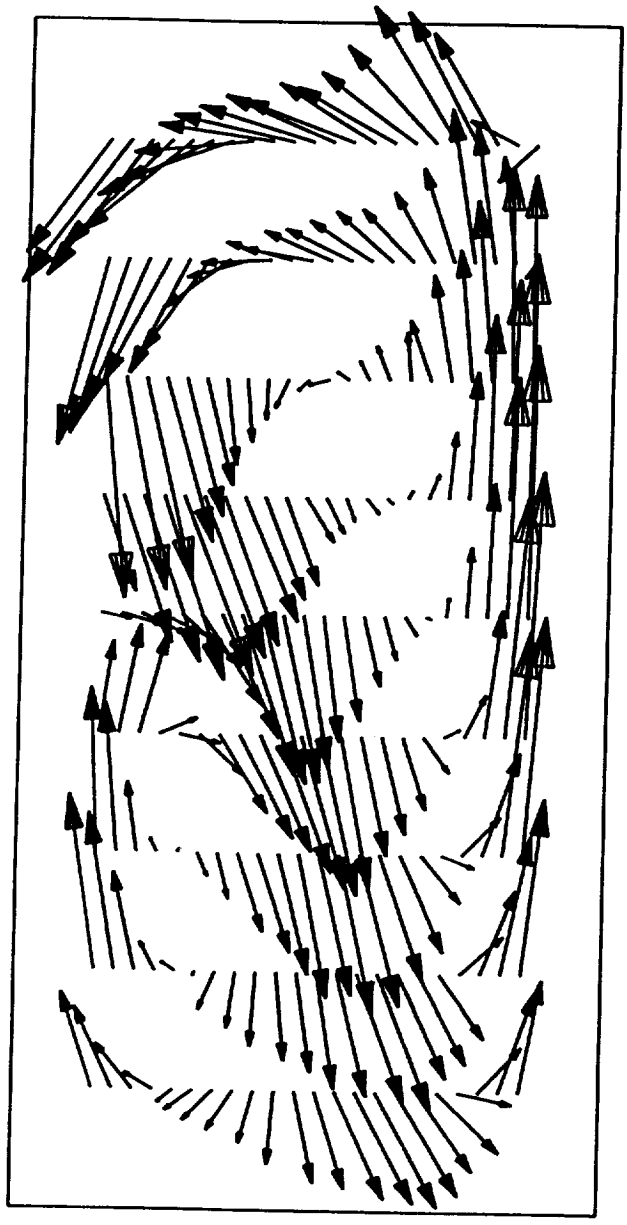

Enlargement of 4.15.2

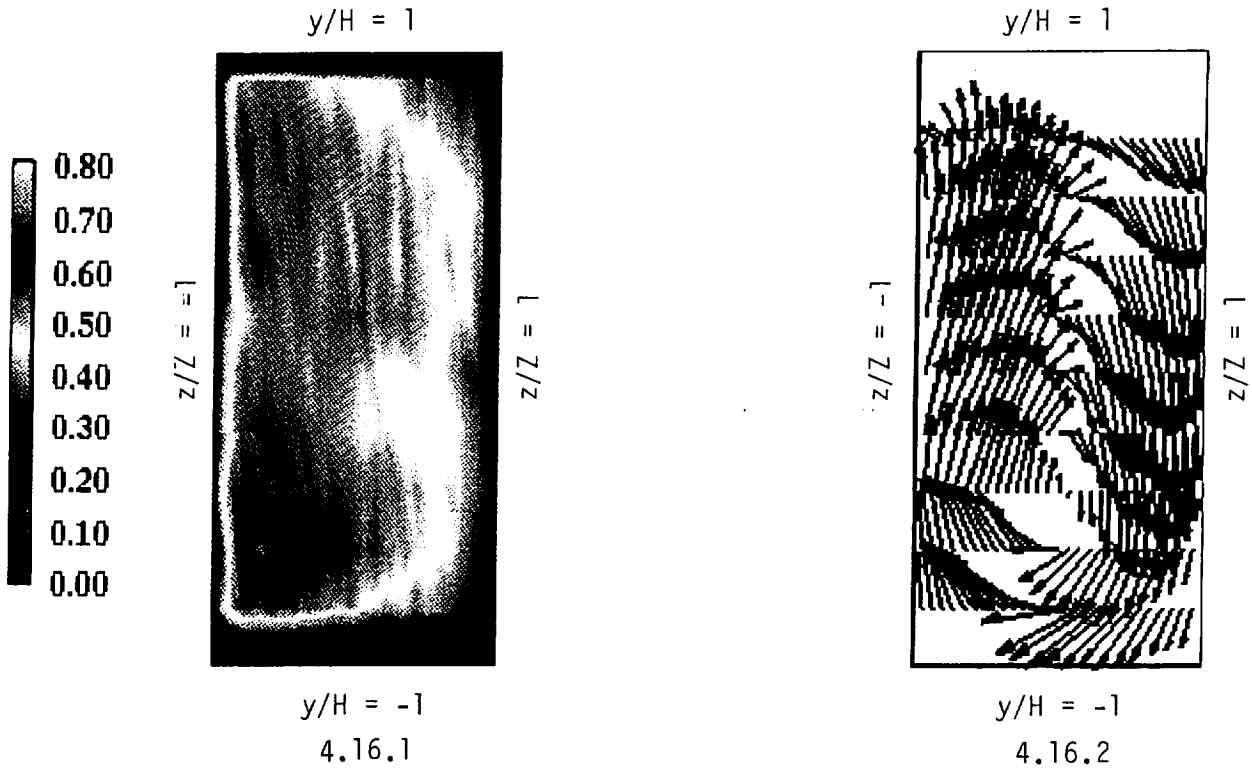

Figure 4.16 - Velocities at location C6, the first turn.

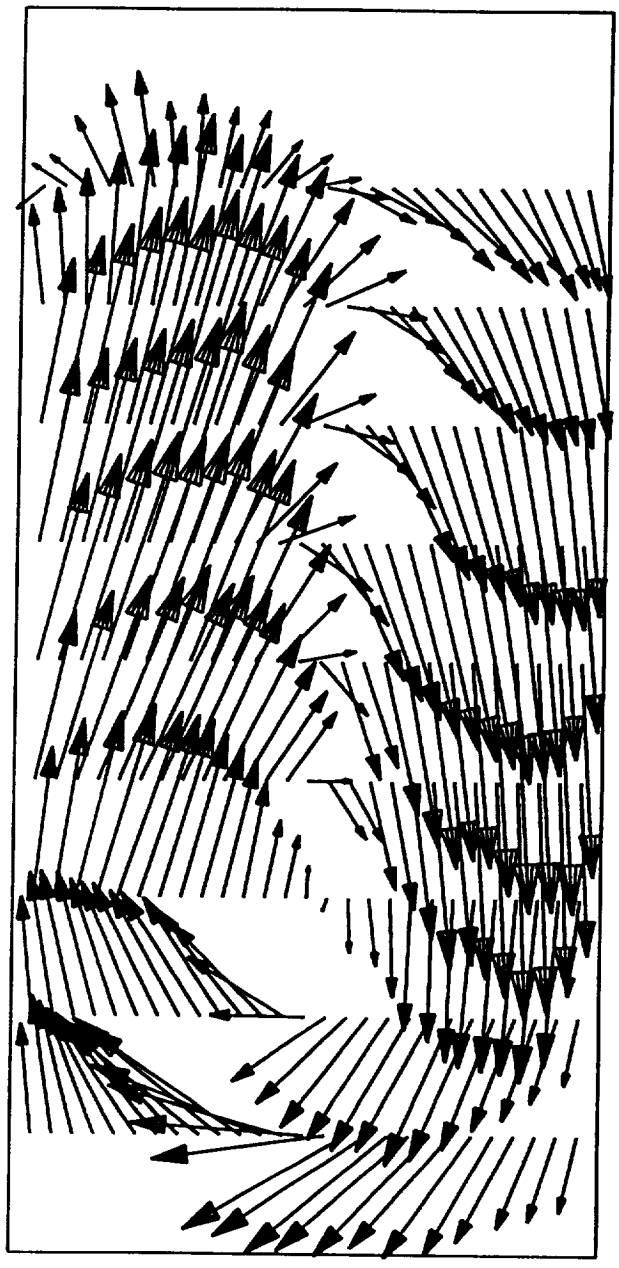

Enlargement of 4.16.2

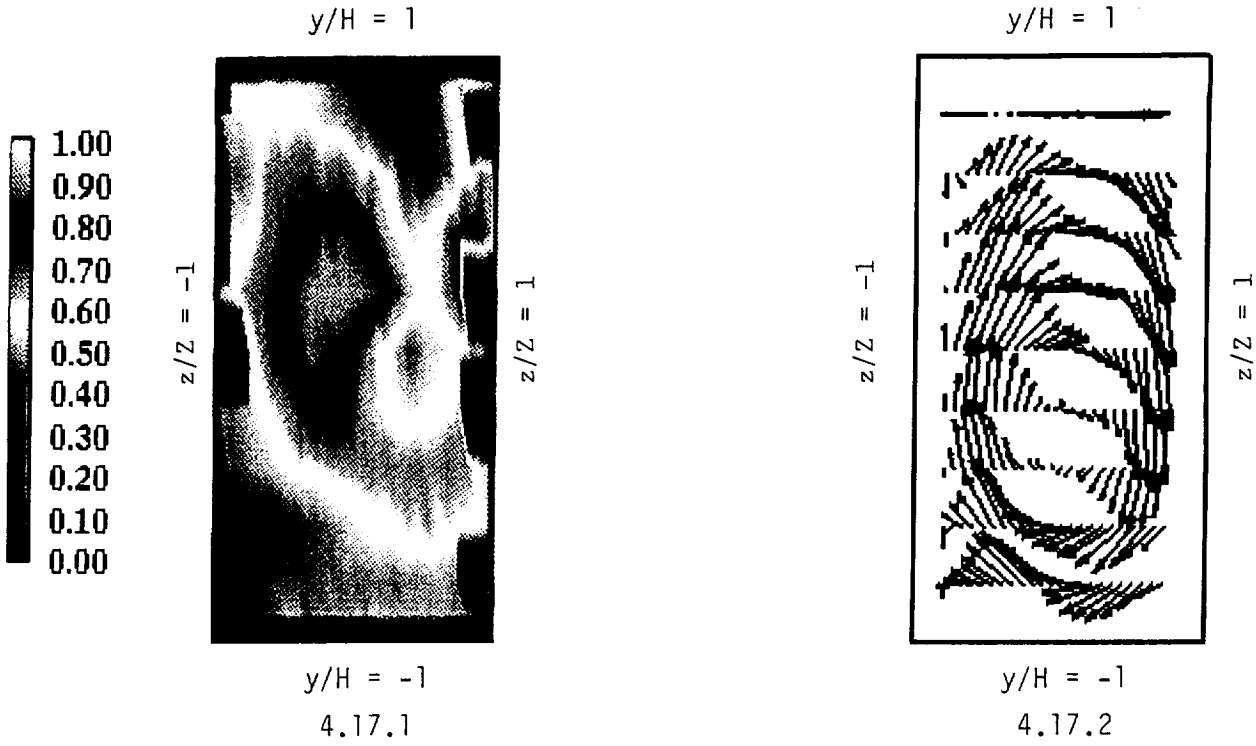

Figure 4.17 - Velocities at location C7, 1 D downstream of the first turn.

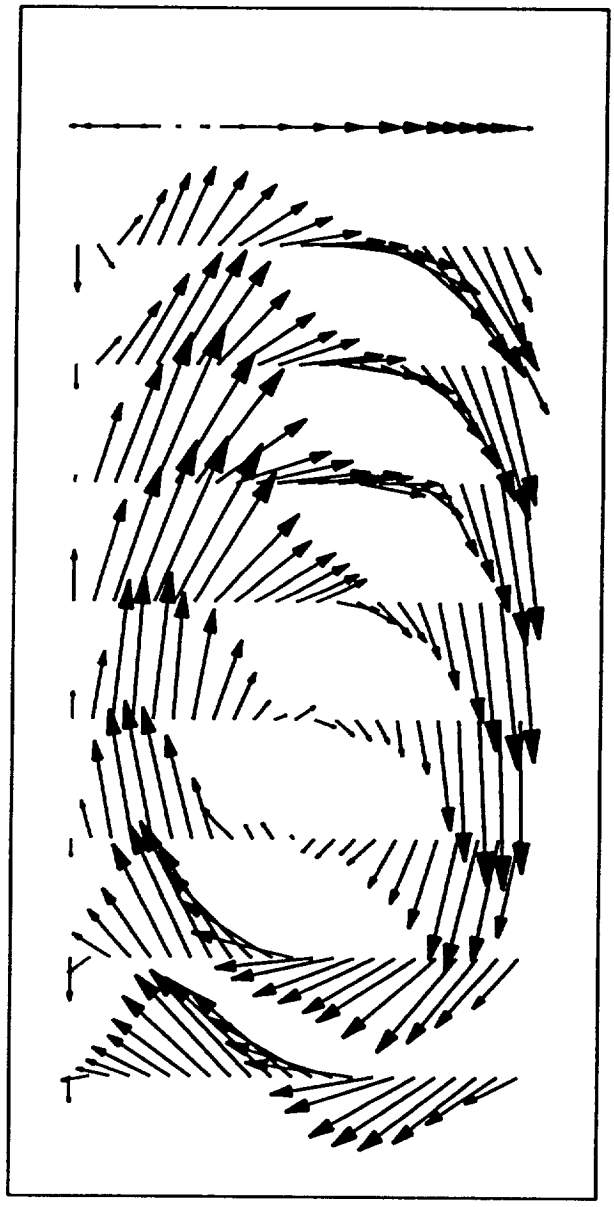

Enlargement of 4.17.2

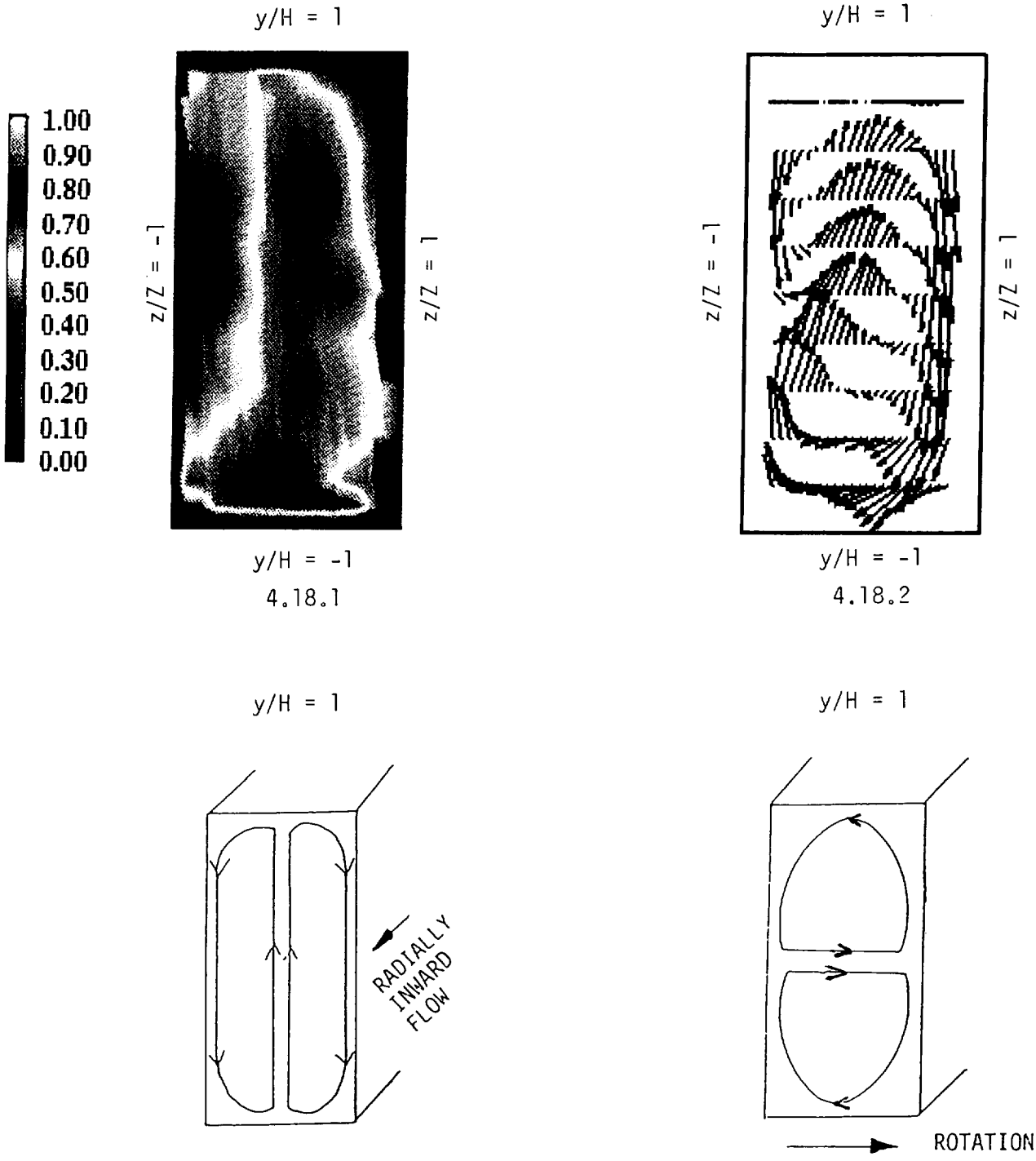

Figure 4.18 - Velocities at location C8, 3 D downstream of the first turn.

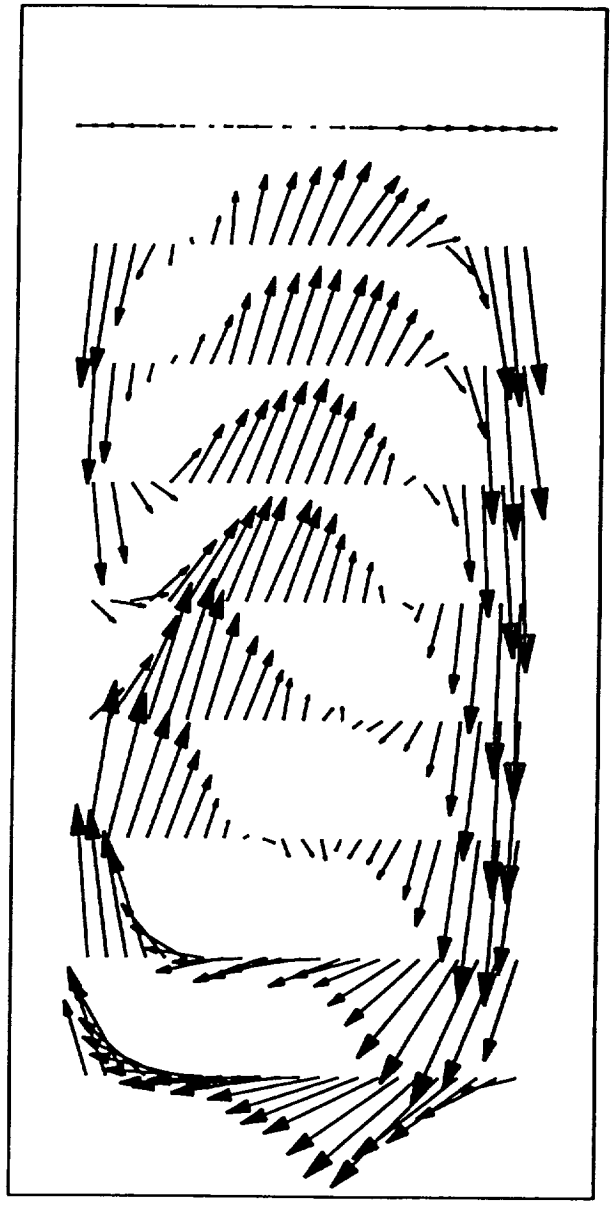

Enlargement of 4.18.2

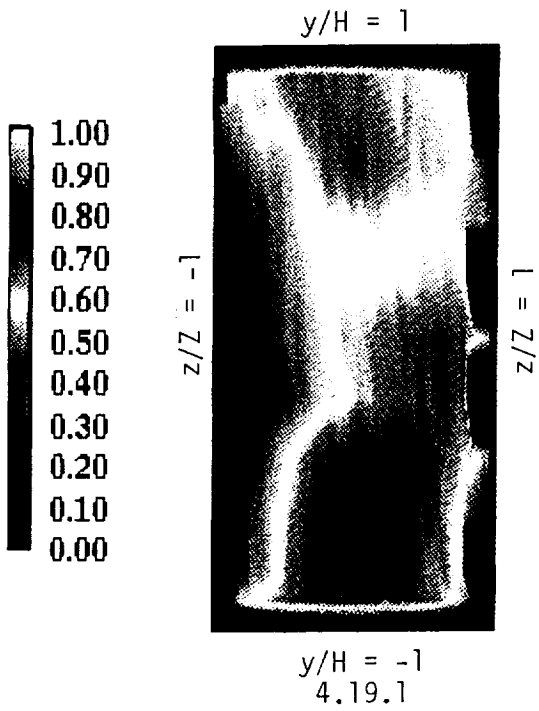

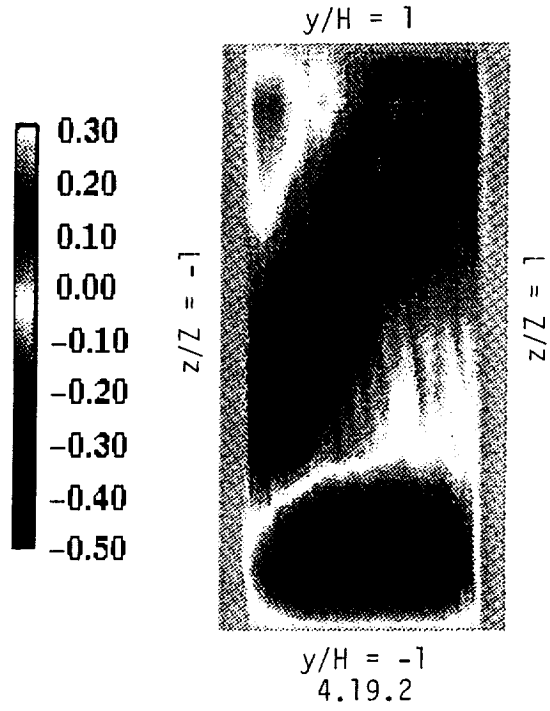

Figure 4.19 - Velocities at location C9, 8.5 D downstream of the first turn.

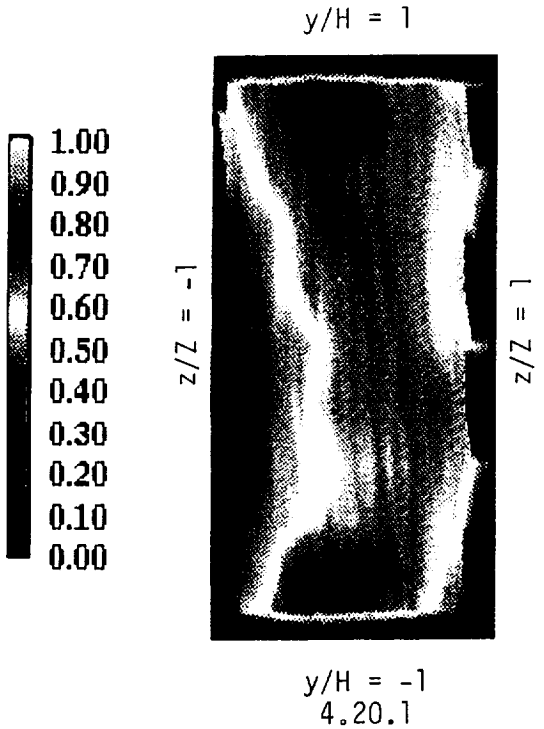

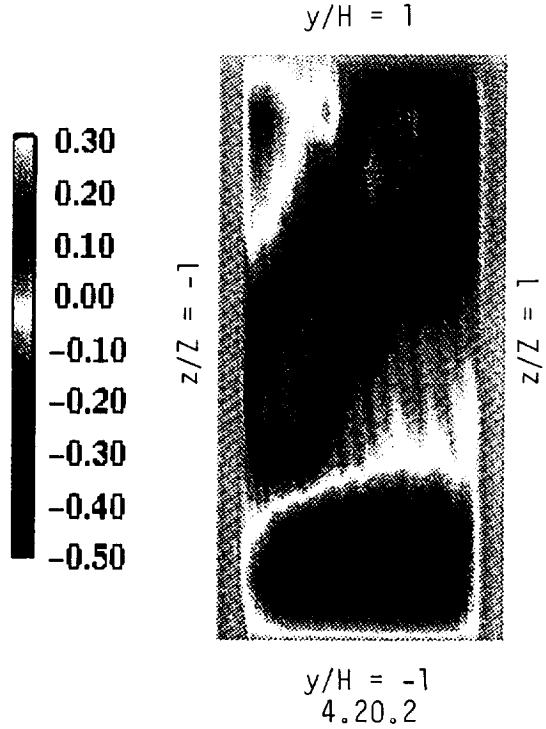

Figure 4.20 - Velocities at location C10, 10.5 D downstream of the first turn.

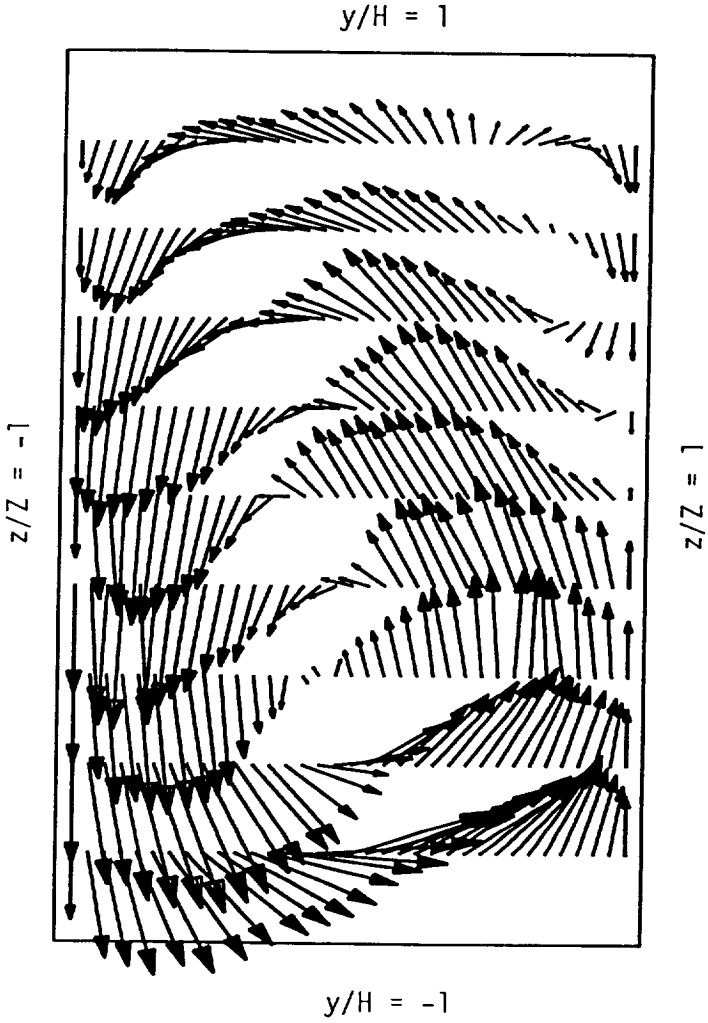

Figure 4.21 - Velocities at location C11, the second turn.

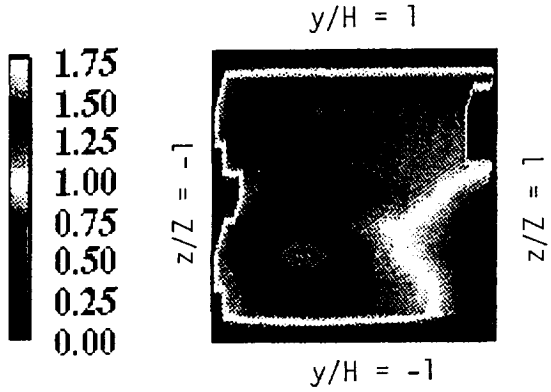

Figure 4.22 - Velocities at location C12, 1 D downstream of the second turn.

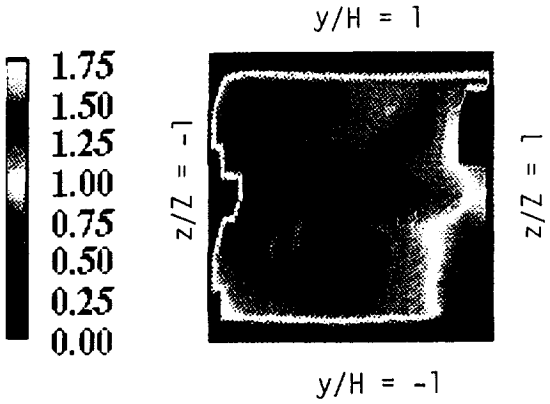

Figure 4.23 - Velocities at location C13, 6 D downstream of the second turn.

UTRC Rig Drawings View from outside of model "looking in"

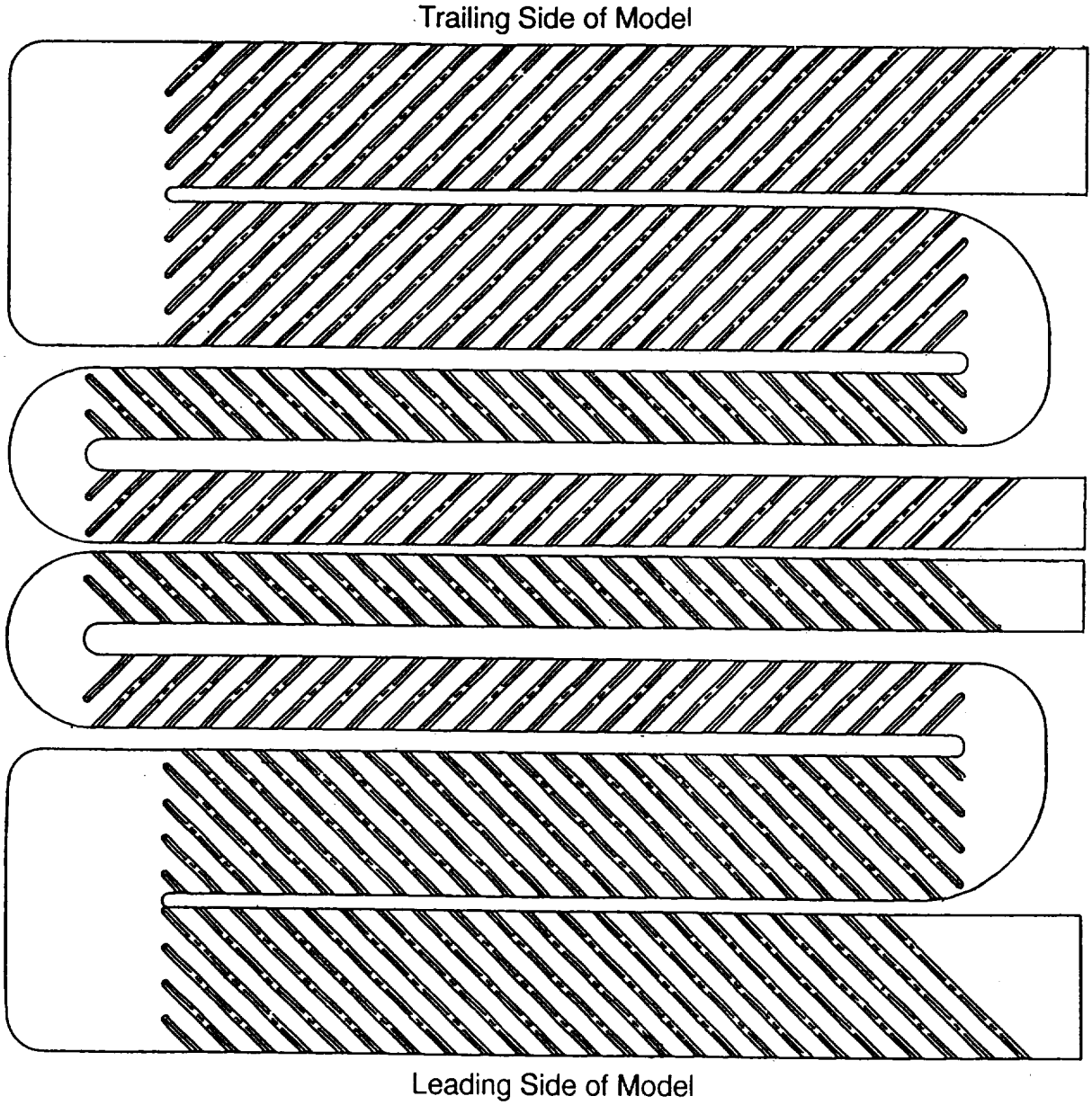

Figure 5.1 Original Rig Drawings from UTRC

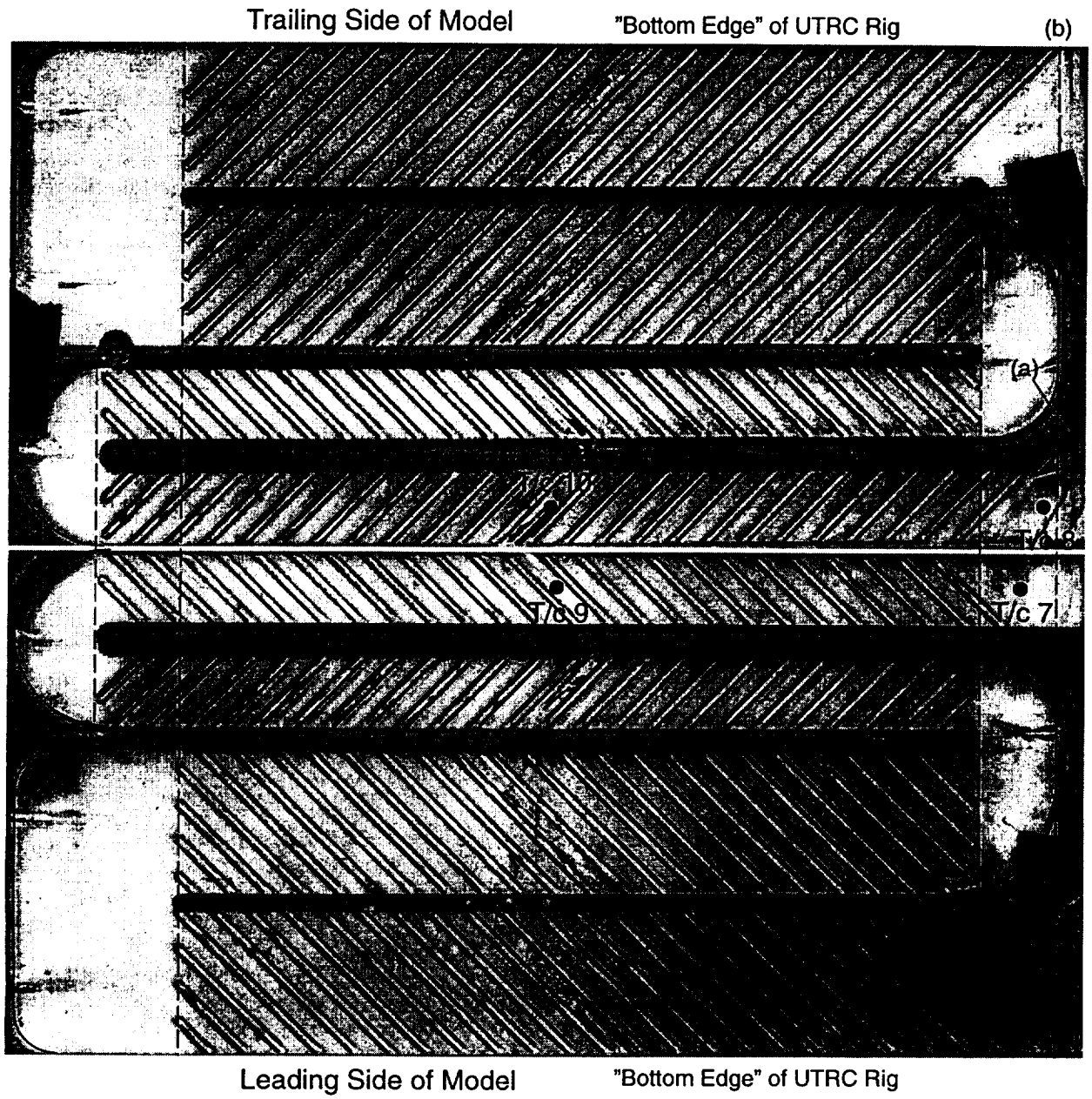

– First (a) and last (b) flowpath tripstrips on SRA rig trailing side

Figure 5.2 UTRC Experimental Heat Transfer Rig

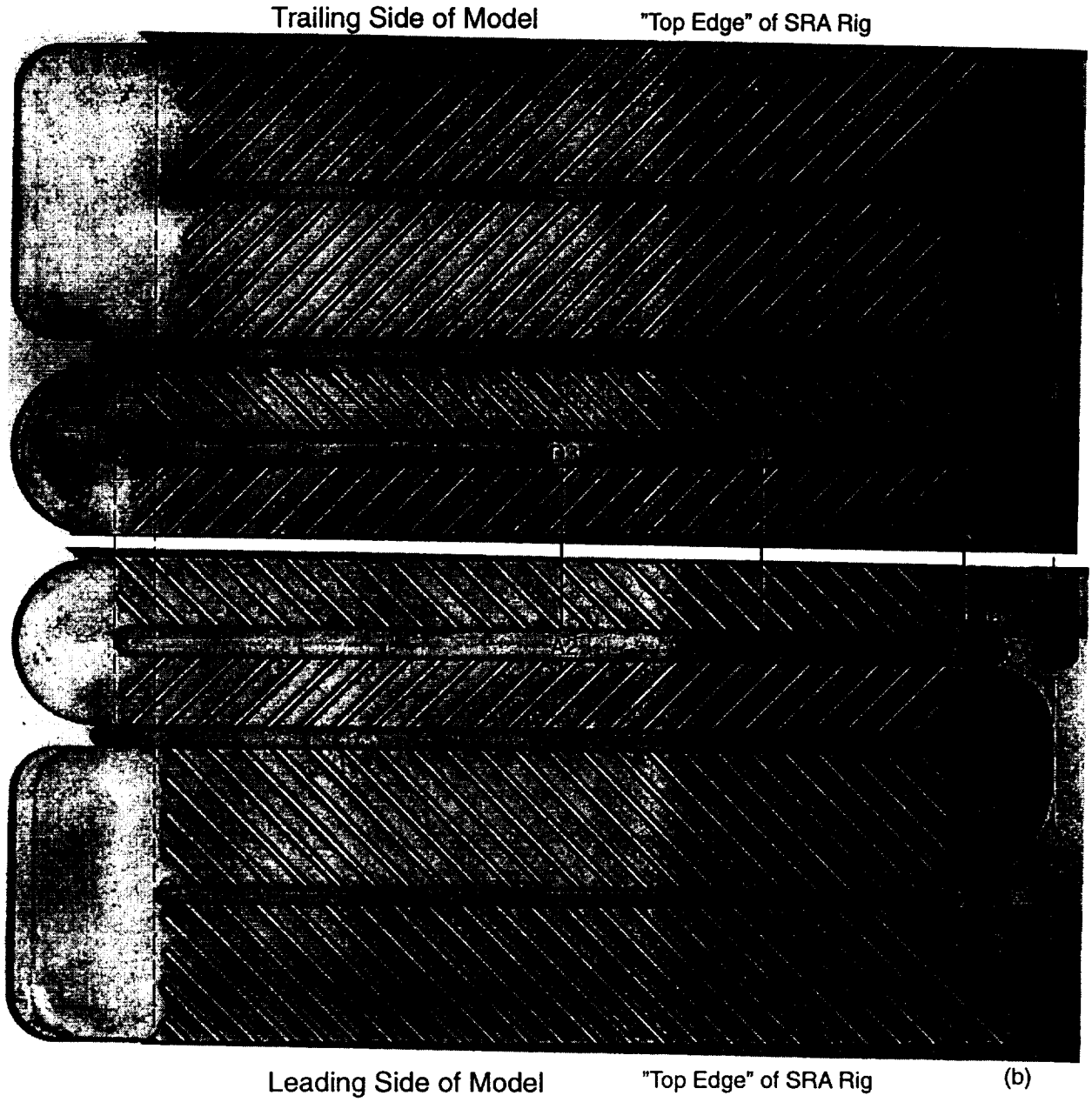

– First (a) and last (b) flowpath tripstrips on SRA rig leading side

Figure 5.3 SRA Experimental Velocity Field Rig

SRA Rig View from outside of model "looking in"

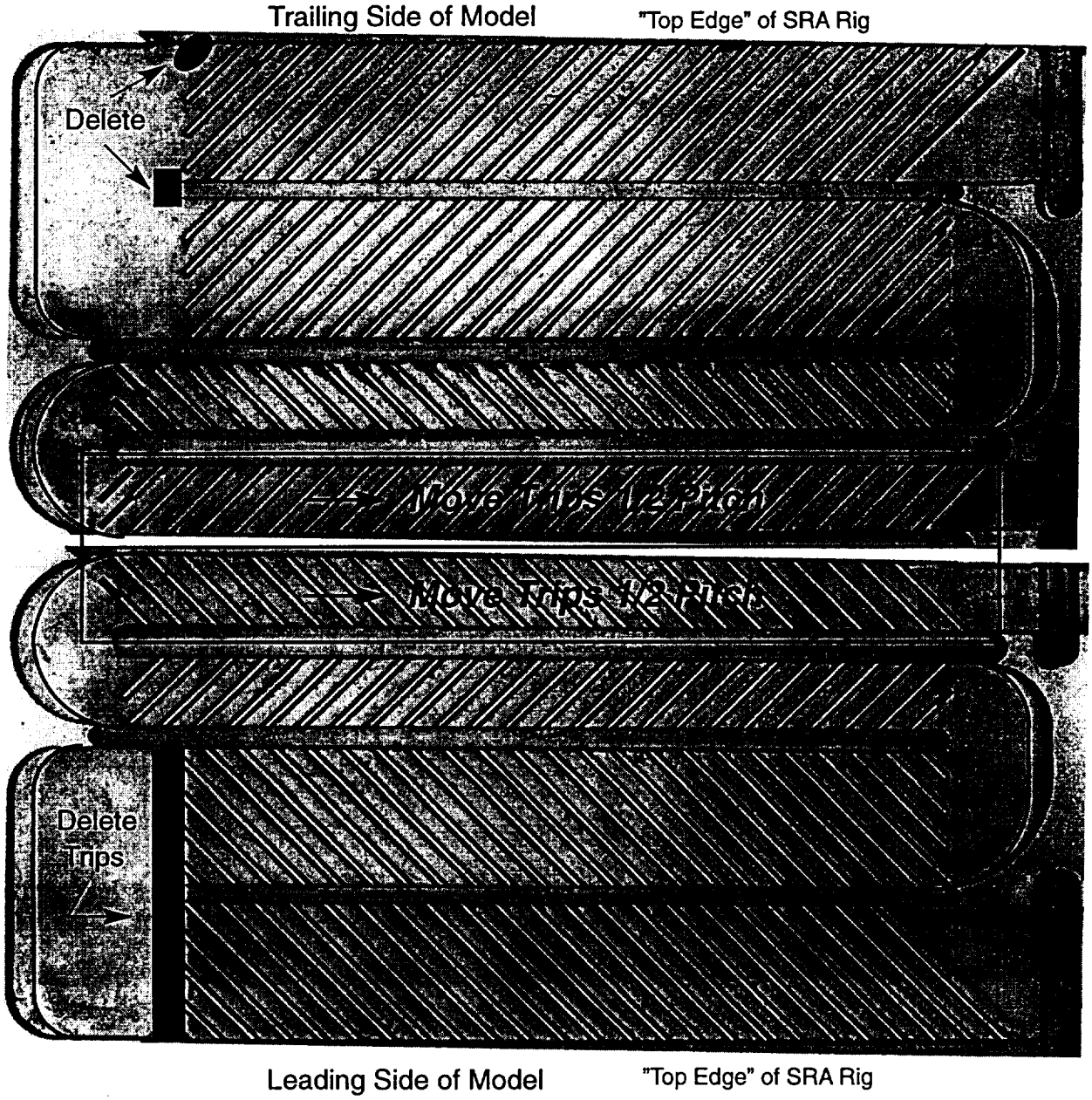

Figure 5.4 Differences Between the UTRC and SRA Experimental Rigs

(a) Trip Strip Channel 0.5" x 3.5" (1.27 cm x 8.89 cm)

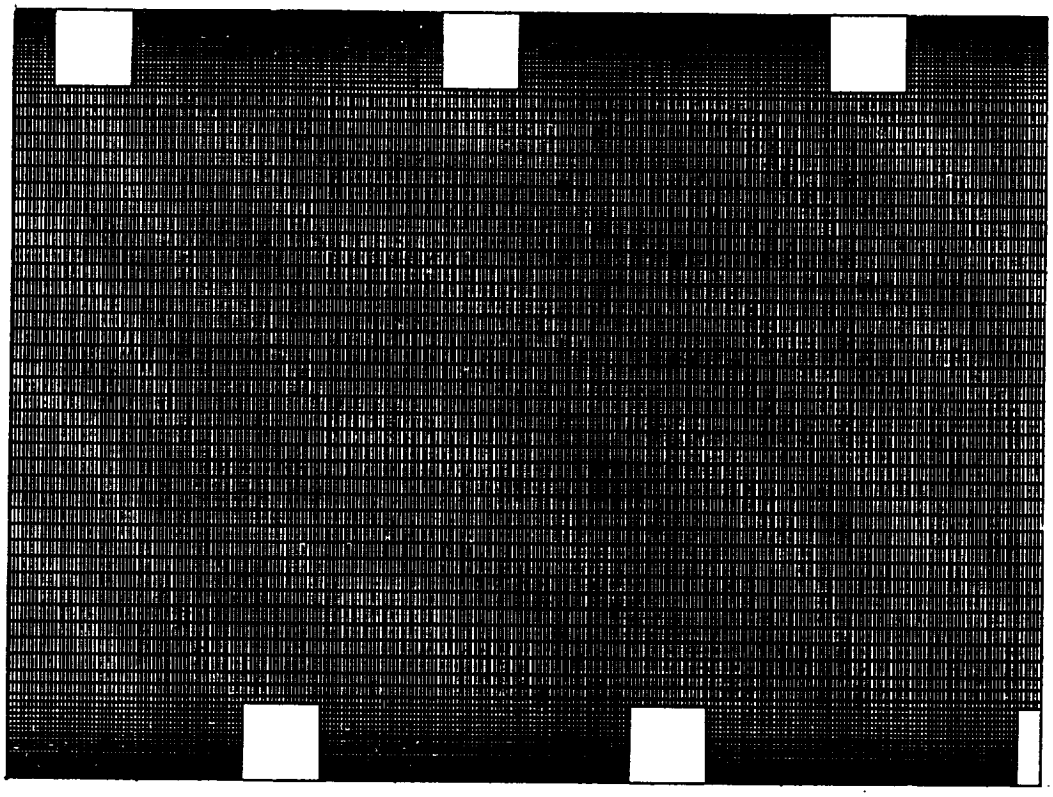

(a) Close Up View of the Grid

Figure 5.5 2−d Channel Computational Grid for the "Conveyor−belt" BC Evaluation Study

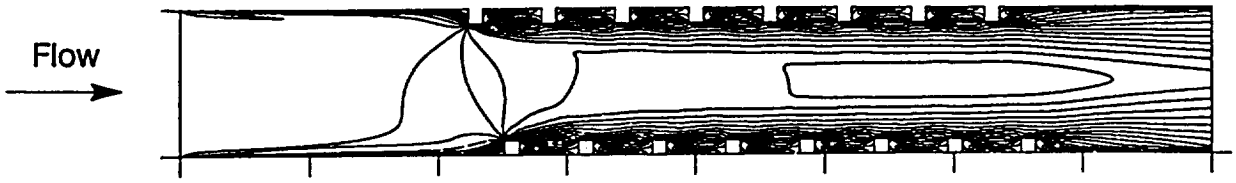

Figure 5.6a 2−d Channel Streamwise Component Velocity Contours

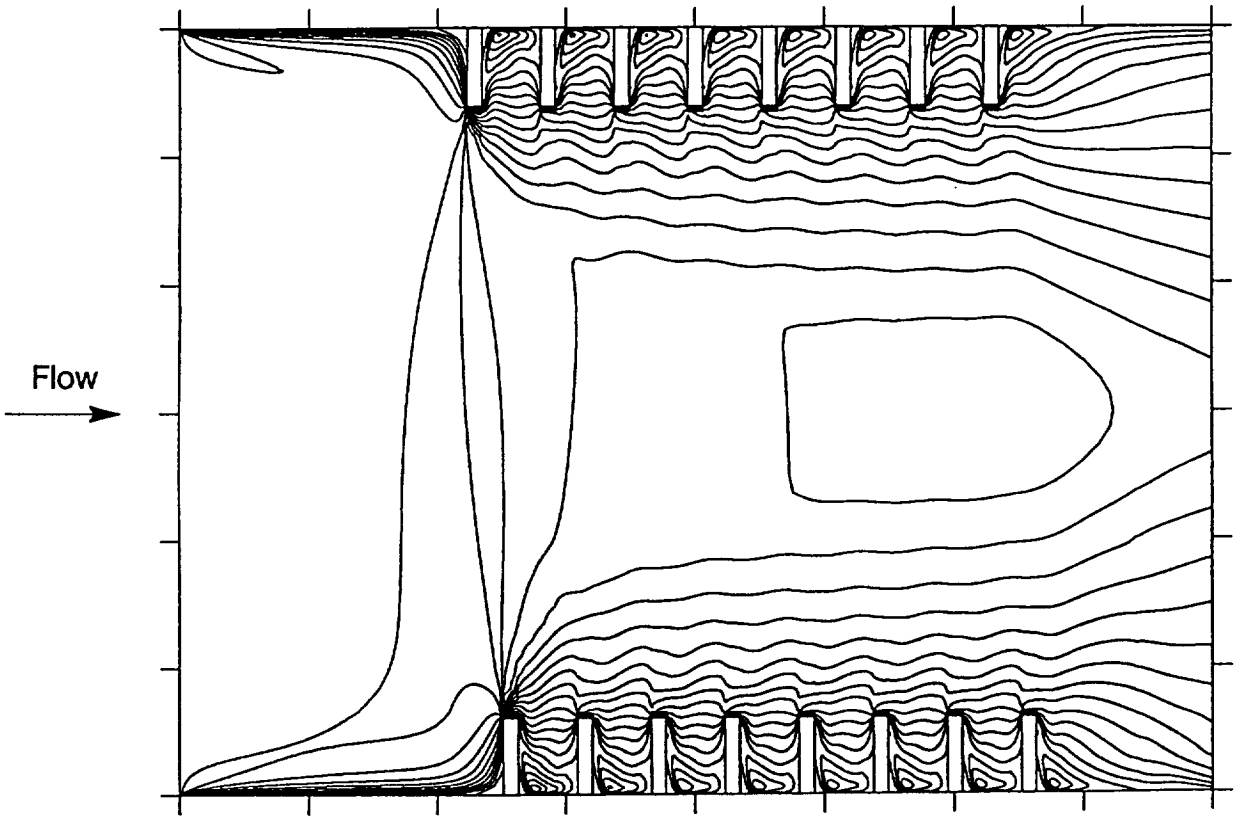

Figure 5.6b Velocity Contours with Channel Height Expanded

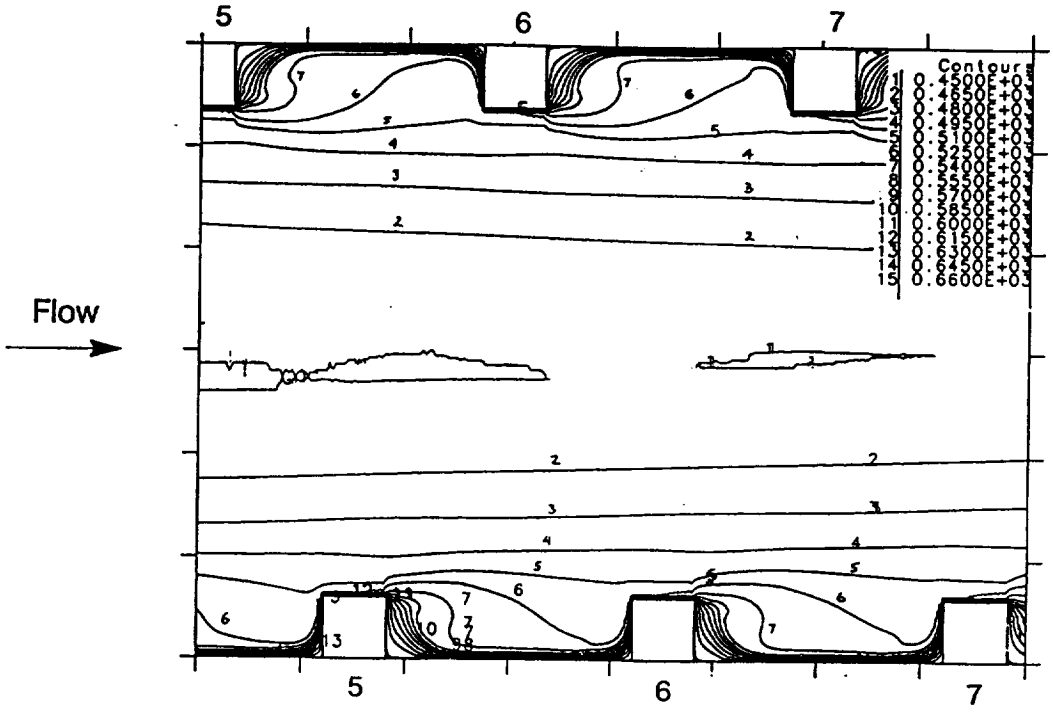

2–d Channel Simulation, 8 Trip Strips Top & Bottom with Smooth Inlet & Exit

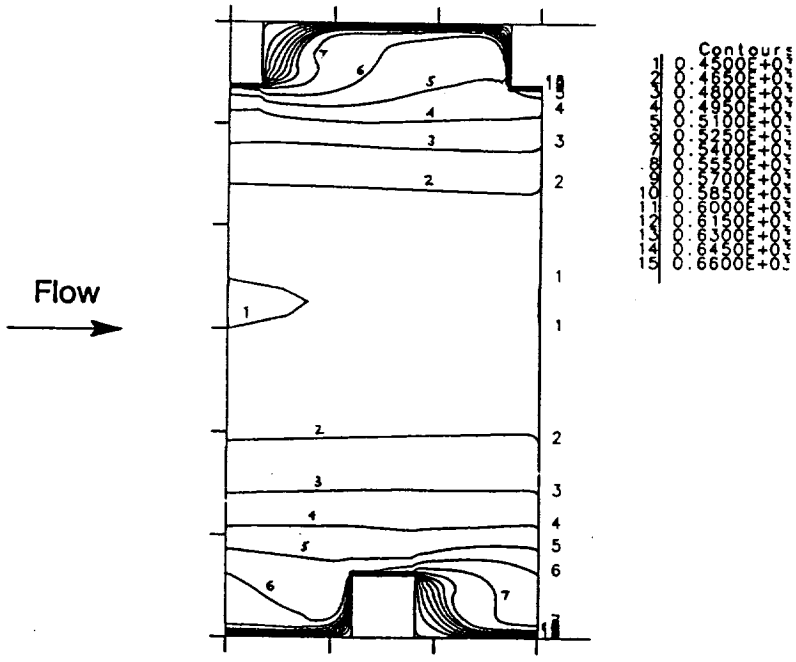

3–d "Conveyor–belt" Simulation

Figure 5.9 Comparison of Static Temperature Contours

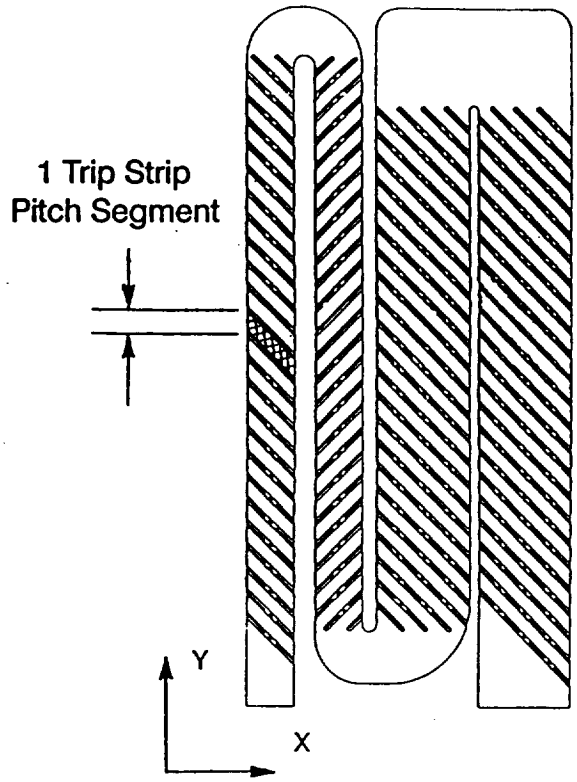

4–Leg Rig Geometry

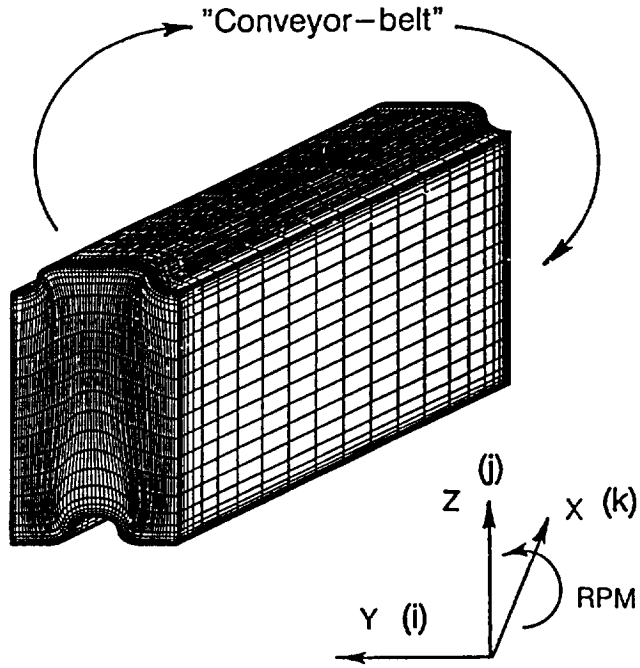

3–d Channel Segment Grid

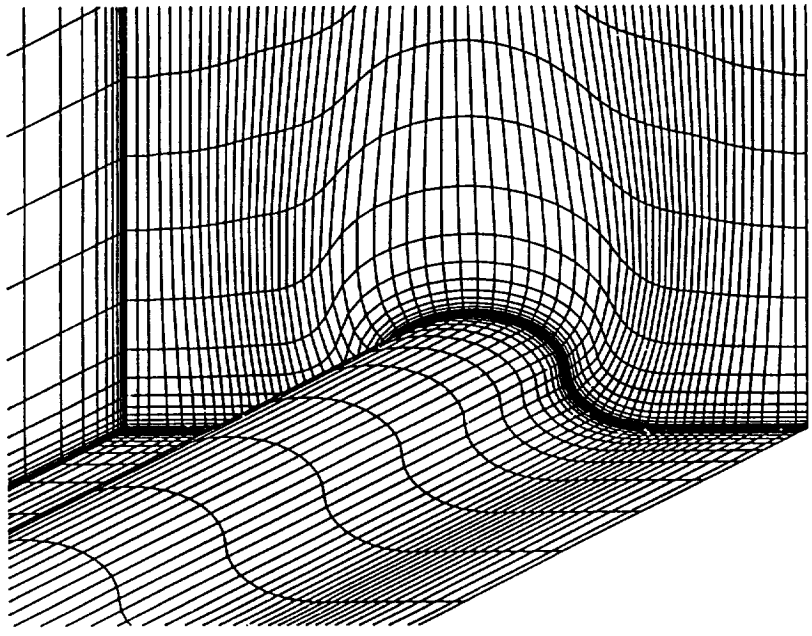

View of Grid Near the Trip Strip

Figure 5.10 3–d Skewed Trip Strip "Conveyor–belt" Channel Segment Grid

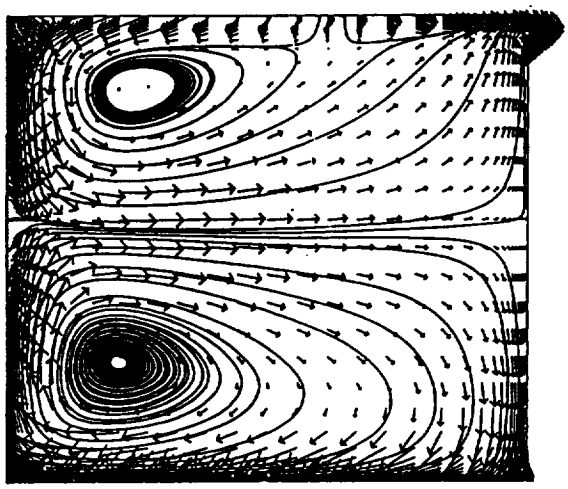

(a) Stationary Channel Segment
Wall Integration, Grid (92x49x49)

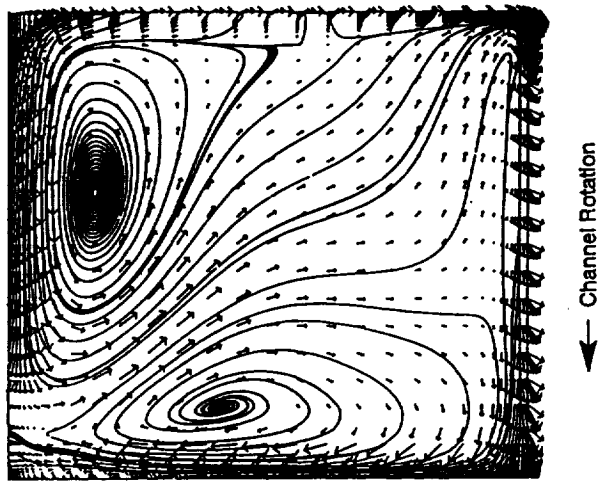

(b) Rotating Channel Segment, −555 rpm
Wall Integration, Grid (92x49x49)

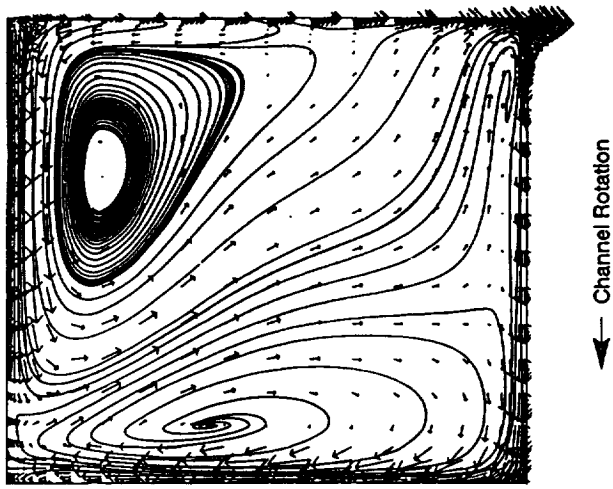

(c) Rotating Channel Segment, −555 rpm
Wall Integration, Grid (66x39x39)

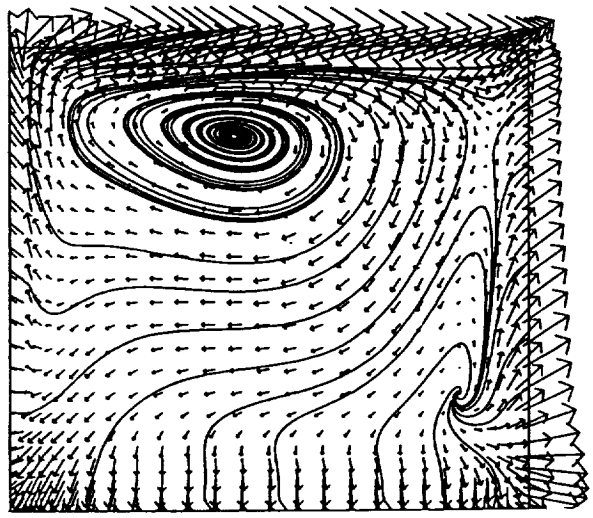

(d) Rotating Channel Segment, −555 rpm
Wall Functions, Grid (67x31x31)

Figure 5.11 Secondary Flow Velocity Field Results from the 3−d Skewed Trip Strip Channel Segment "Conveyor−belt" Grid Study Simulations

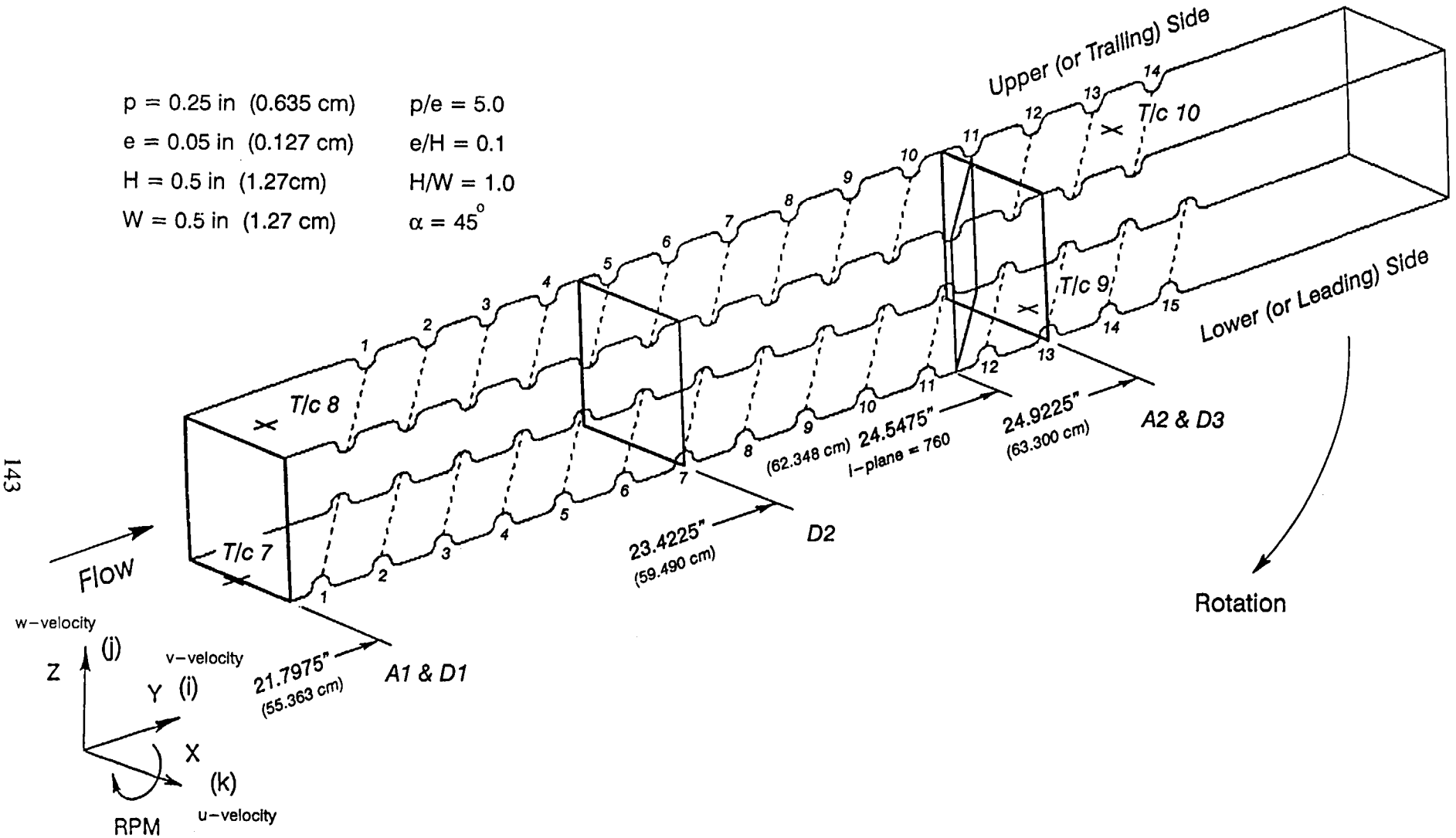

Figure 5.12 Skewed Trip Strip Channel – SRA Data Plane & UTRC Thermocouple Locations

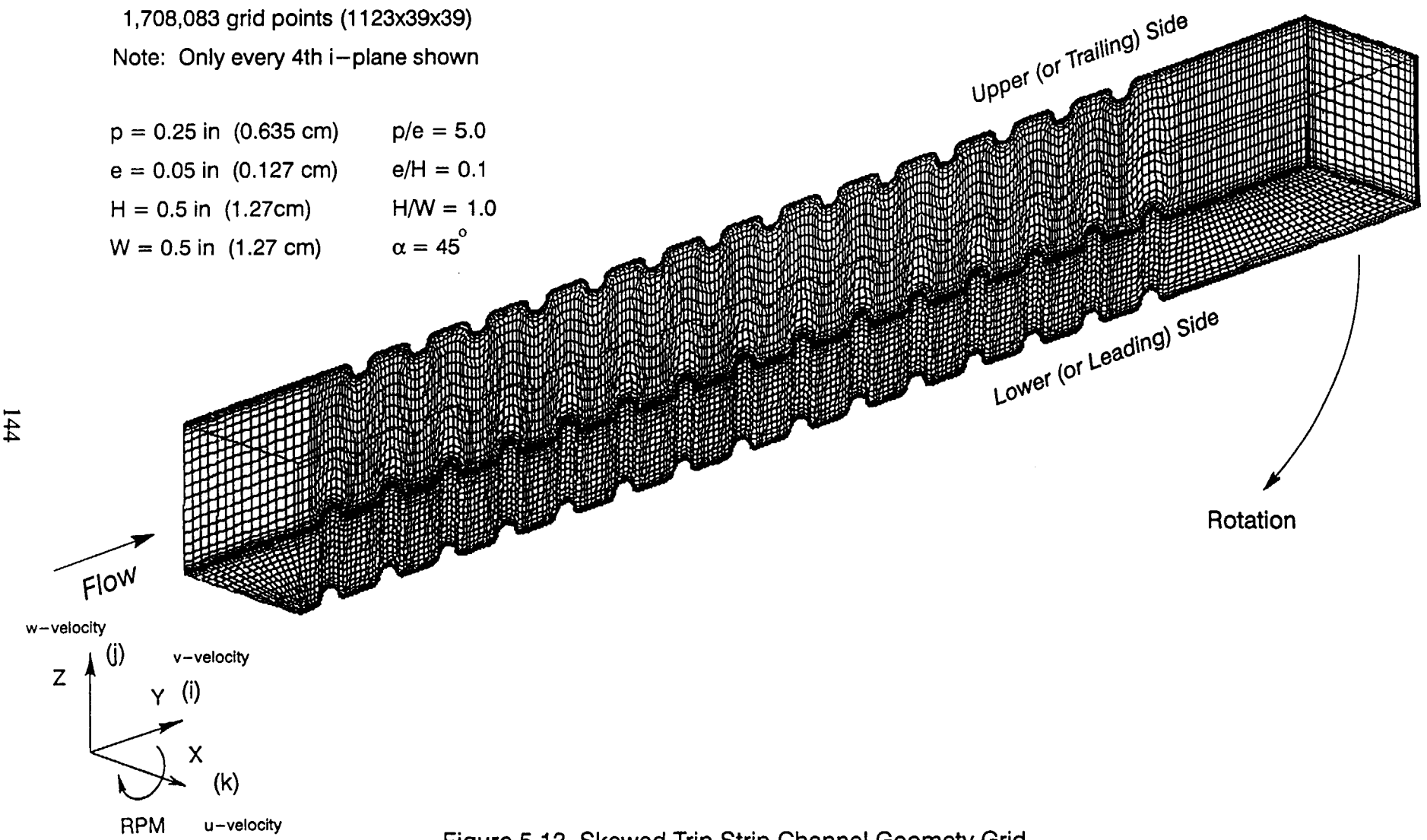

Figure 5.13 Skewed Trip Strip Channel Geomety Grid

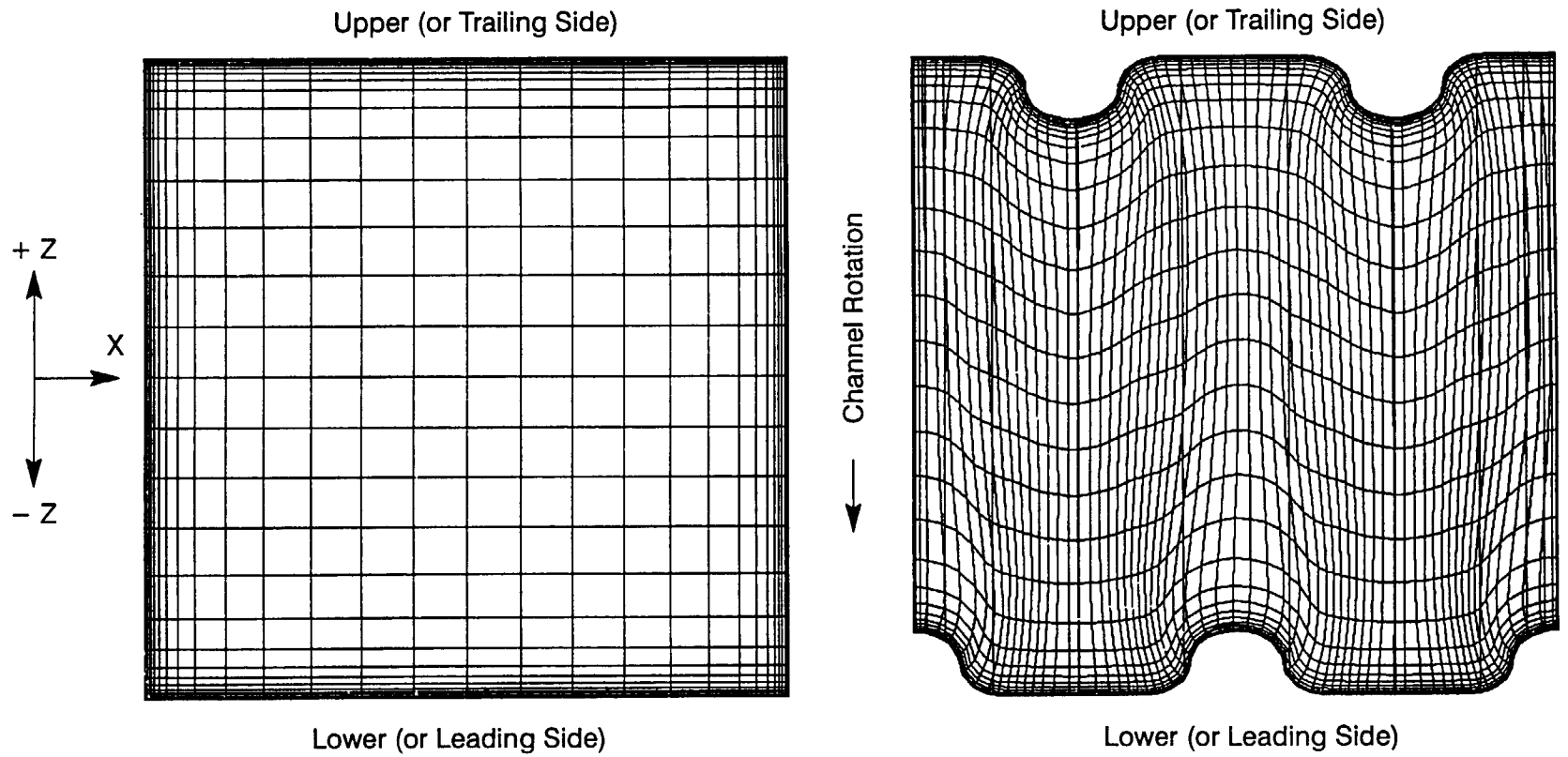

(a) Channel Inlet Plane Locations (A1 & D1)

(b) SRA Data Comparison Plane Locations (A2, D2, & D3). Selected I and K–Plane Grid Locations Removed for the Sake of Clarity

Figure 5.14 Trip Strip Channel Computational Grid – Looking Along the Streamwise Positive Y–Axis

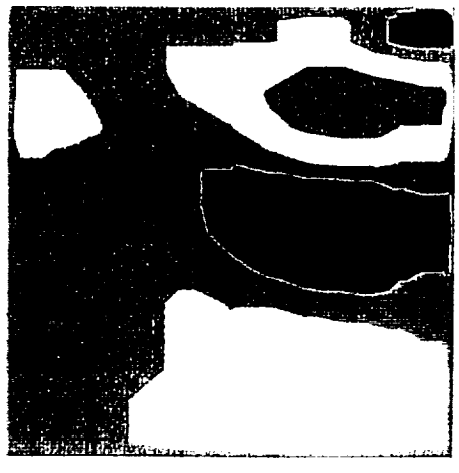

(SRA Data) U−Velocity Component (ft/sec)

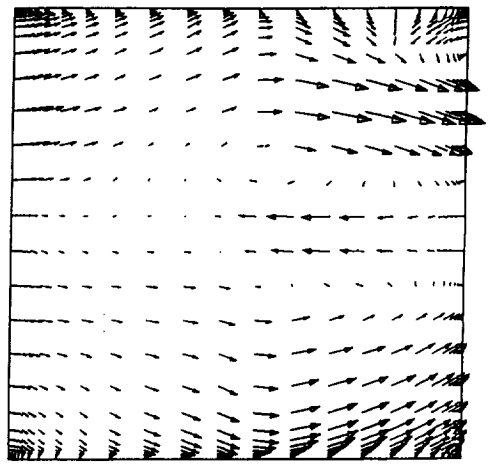

(SRA Data) Velocity Vector Field

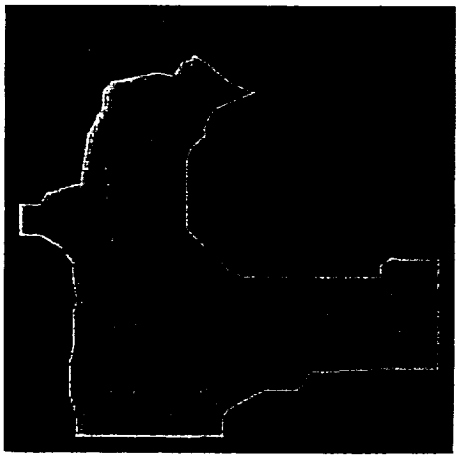

(SRA Data) V−Velocity Component (ft/sec)

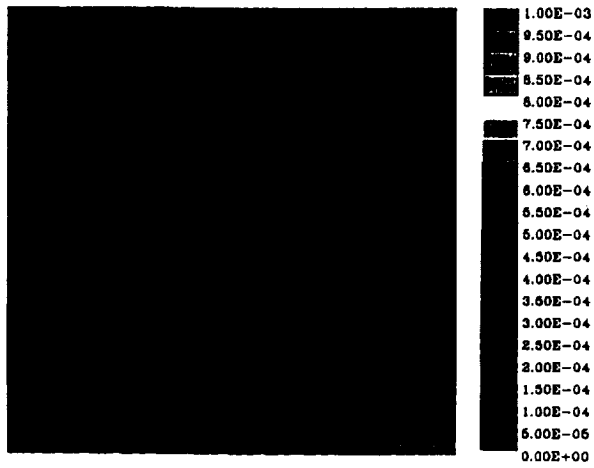

(SRA Data) TKE

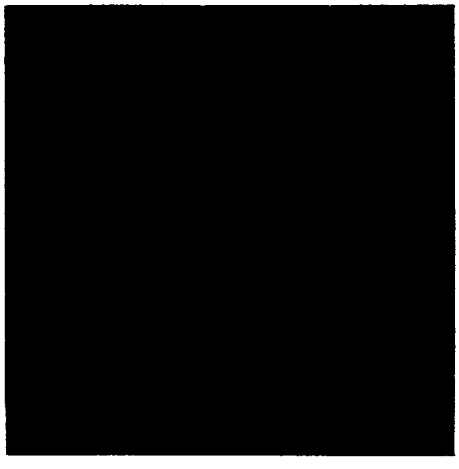

(SRA Data) W−Velocity Component (ft/sec)

m/s = ft/sec / 3.281

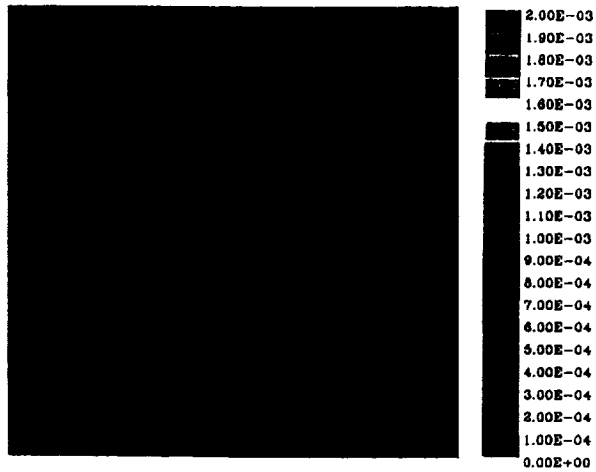

(SRA Data) TDS

Figure 5.15 SRA Data (and CFD Inlet Plane BC's) at Stationary Channel Location A1

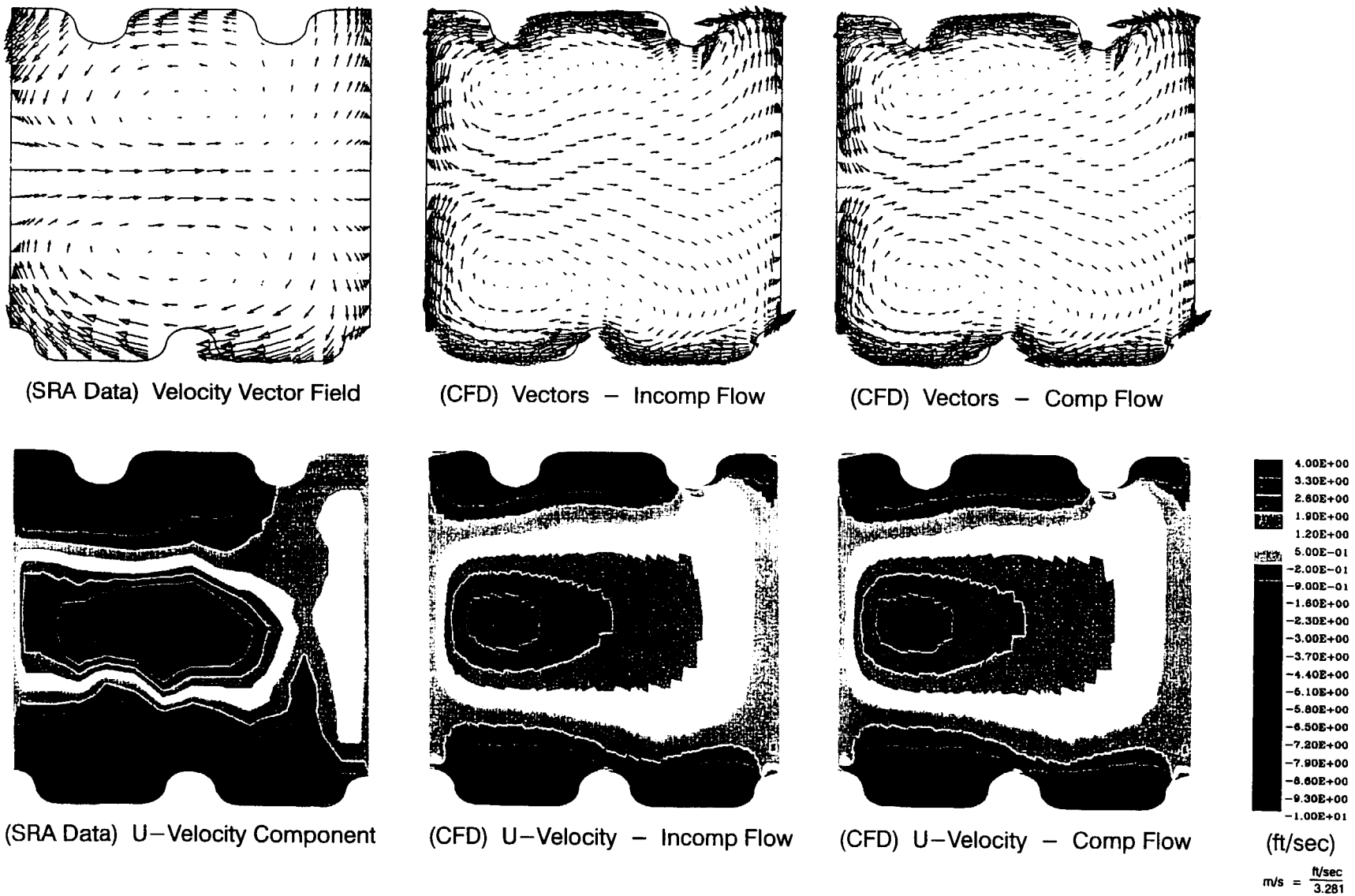

Figure 5.16 Velocity Vector Field and U–Component Velocity Contours – Stationary Channel Location A2

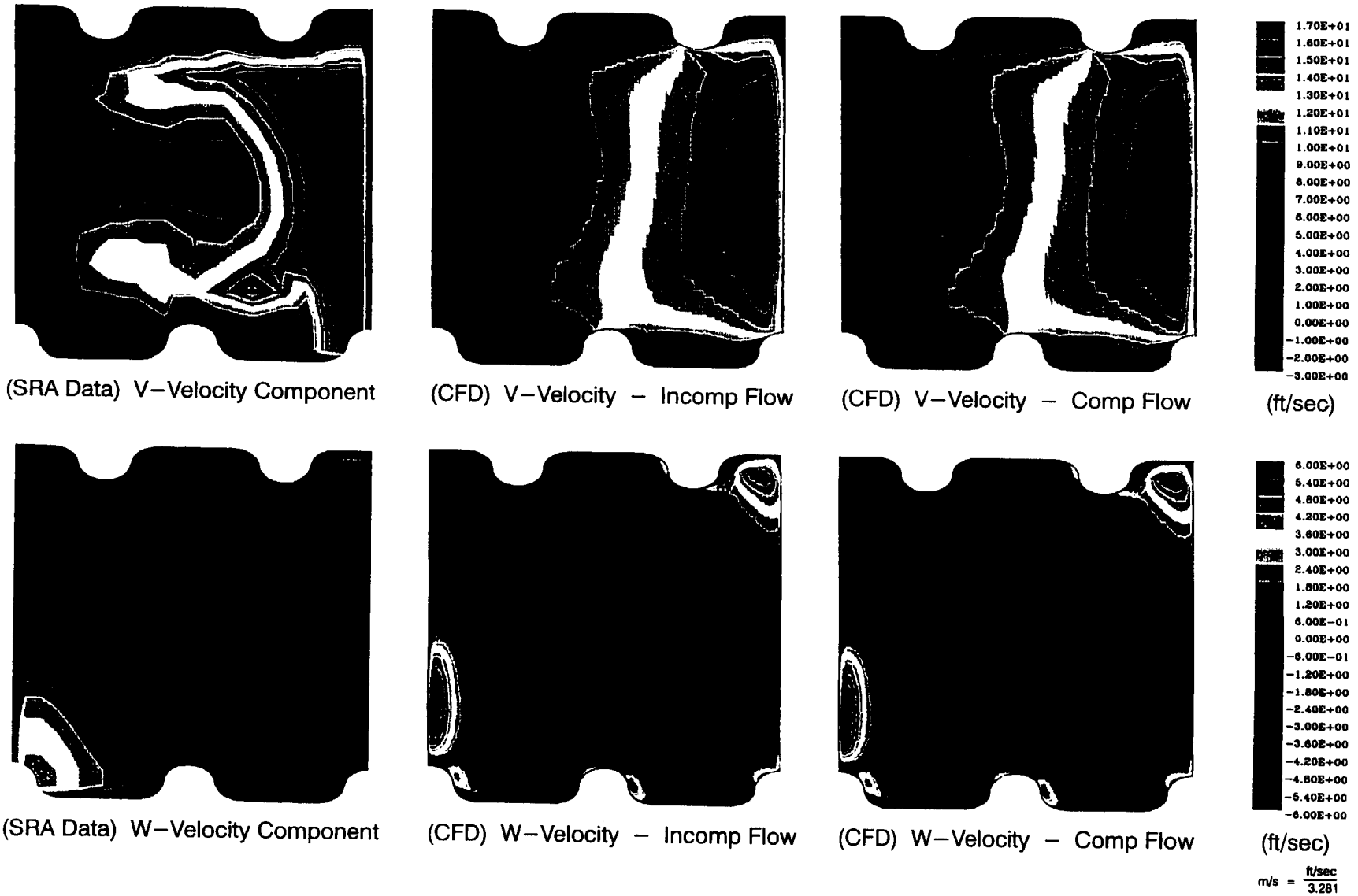

Figure 5.17 V–Component and W–Component Velocity Contours – Stationary Channel Location A2

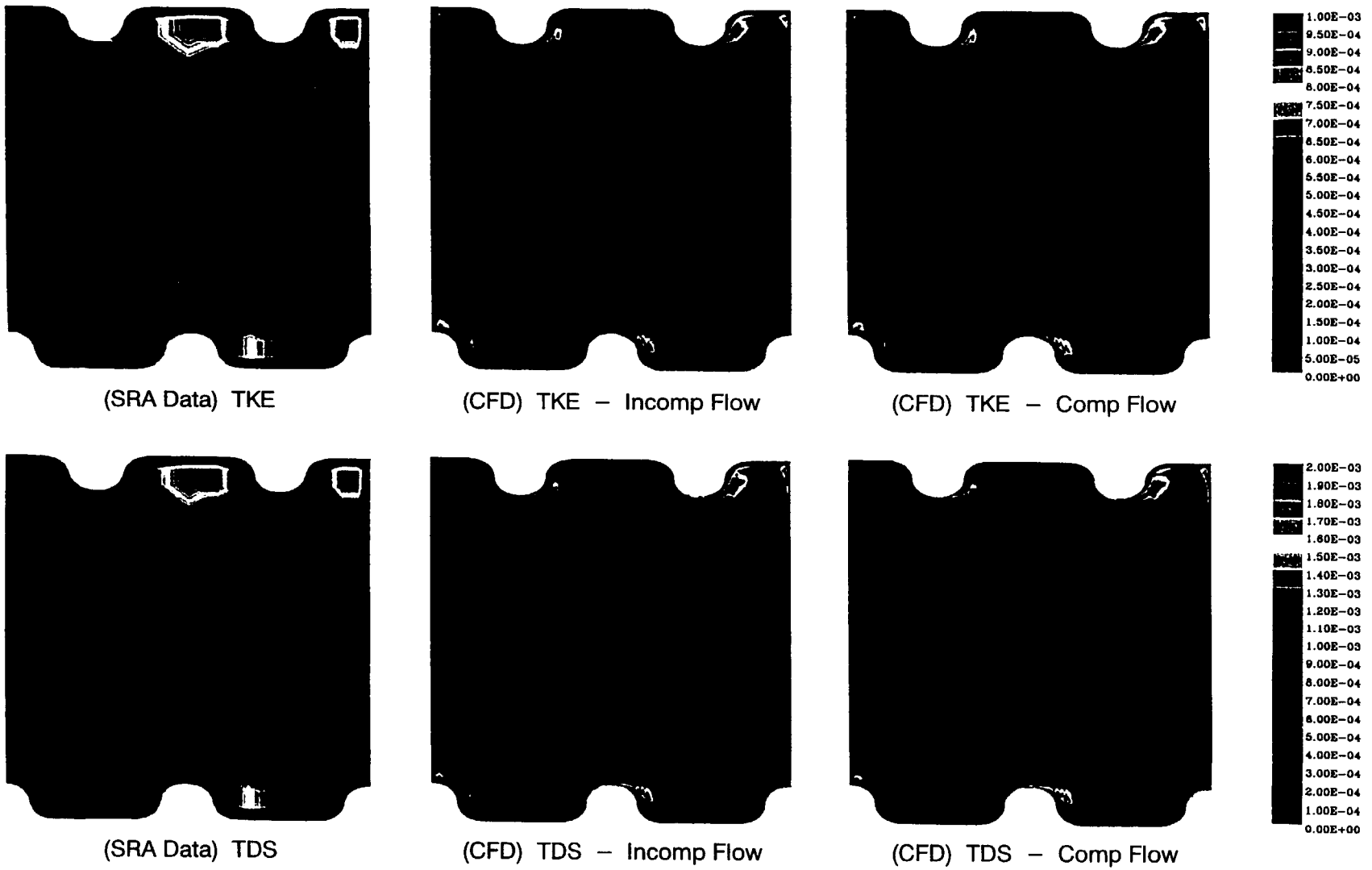

Figure 5.18 Turbulent Kinetic Energy (TKE) and Turbulent Energy Dissipation (TDS) – Stationary Channel Location A2

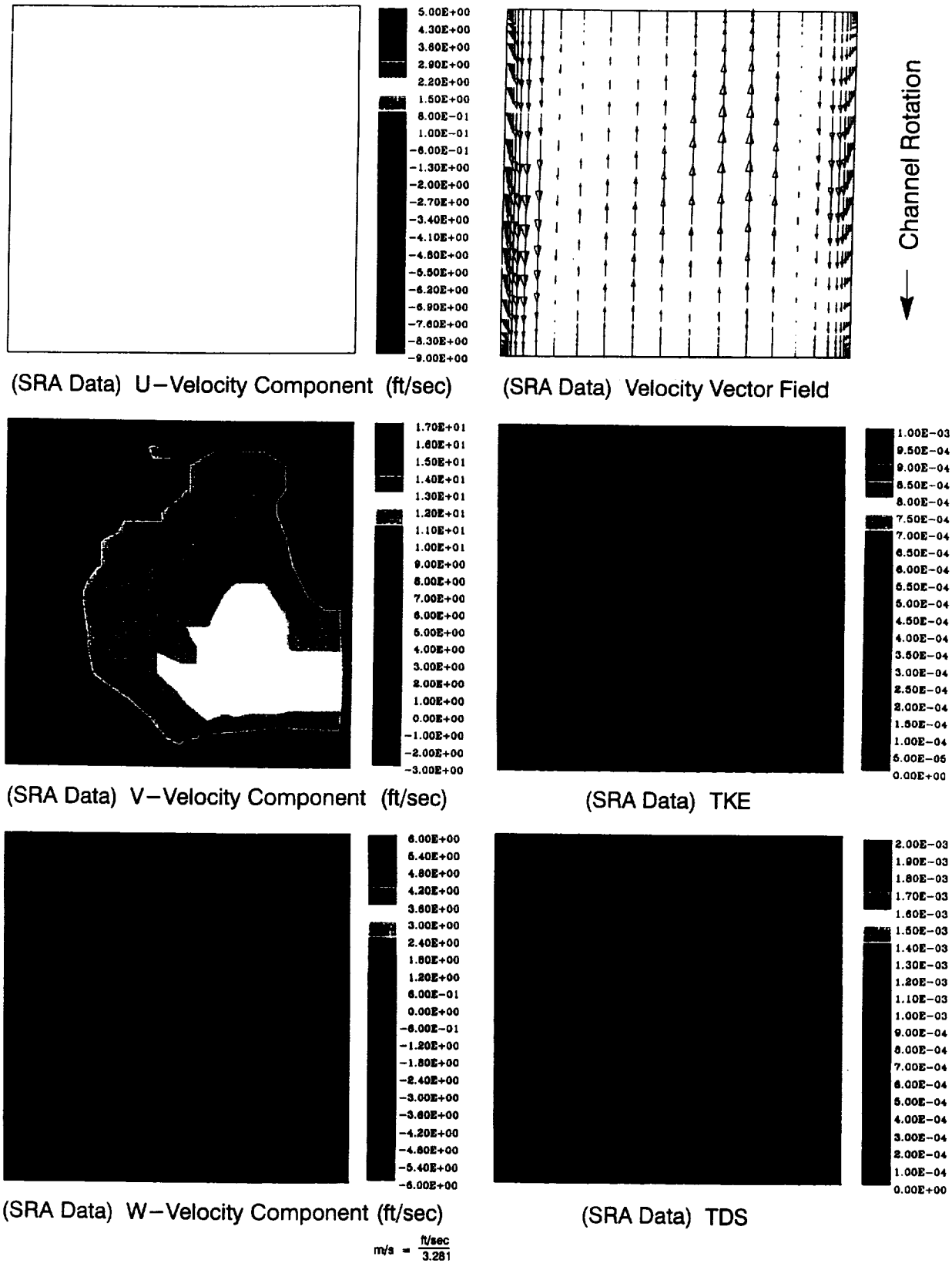

Figure 5.19 SRA Data (and CFD Inlet Plane BC's) at Rotating Channel Location D1

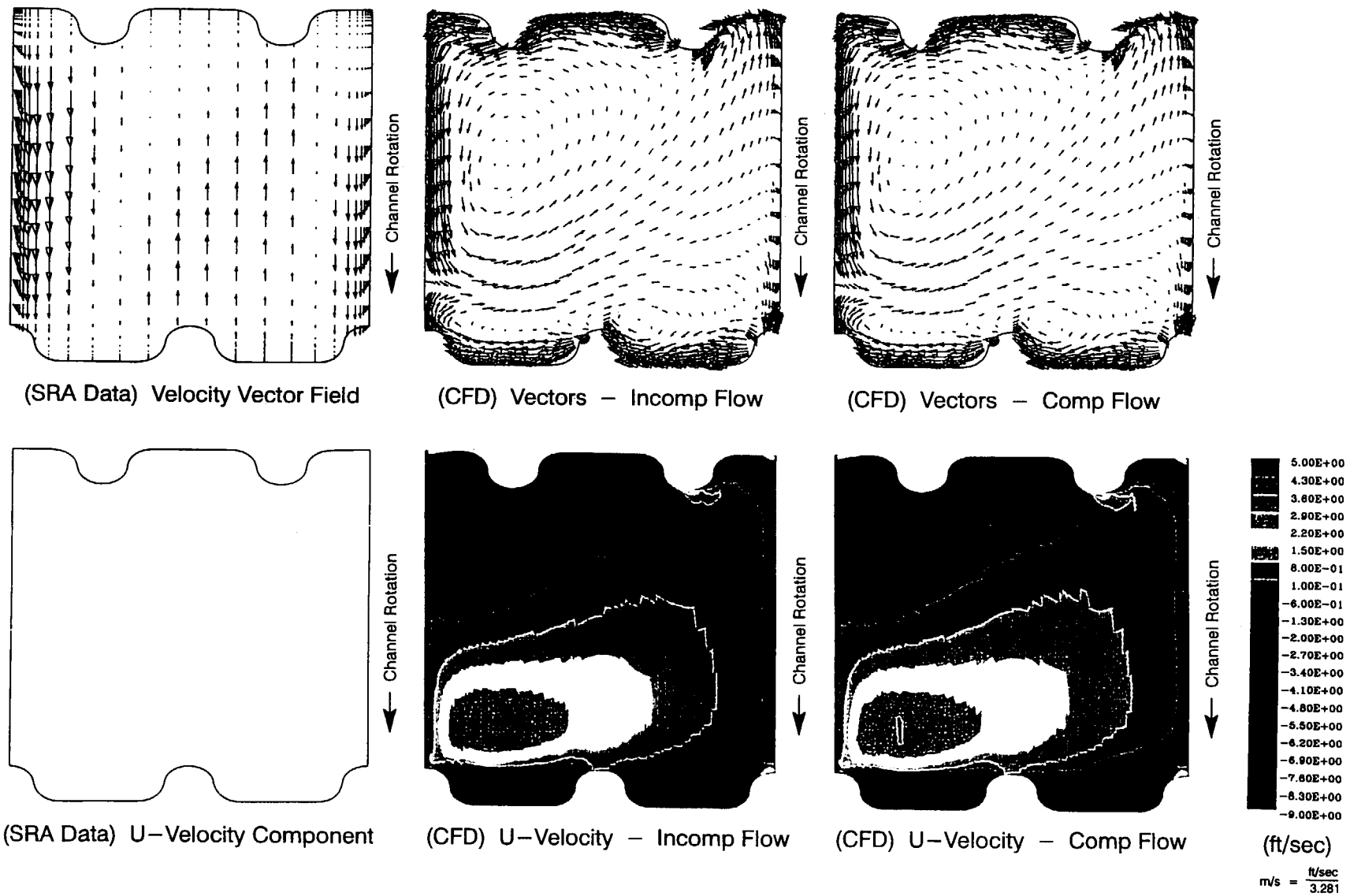

Figure 5.20 Velocity Vector Field and U–Component Velocity Contours – Rotating Channel Location D2

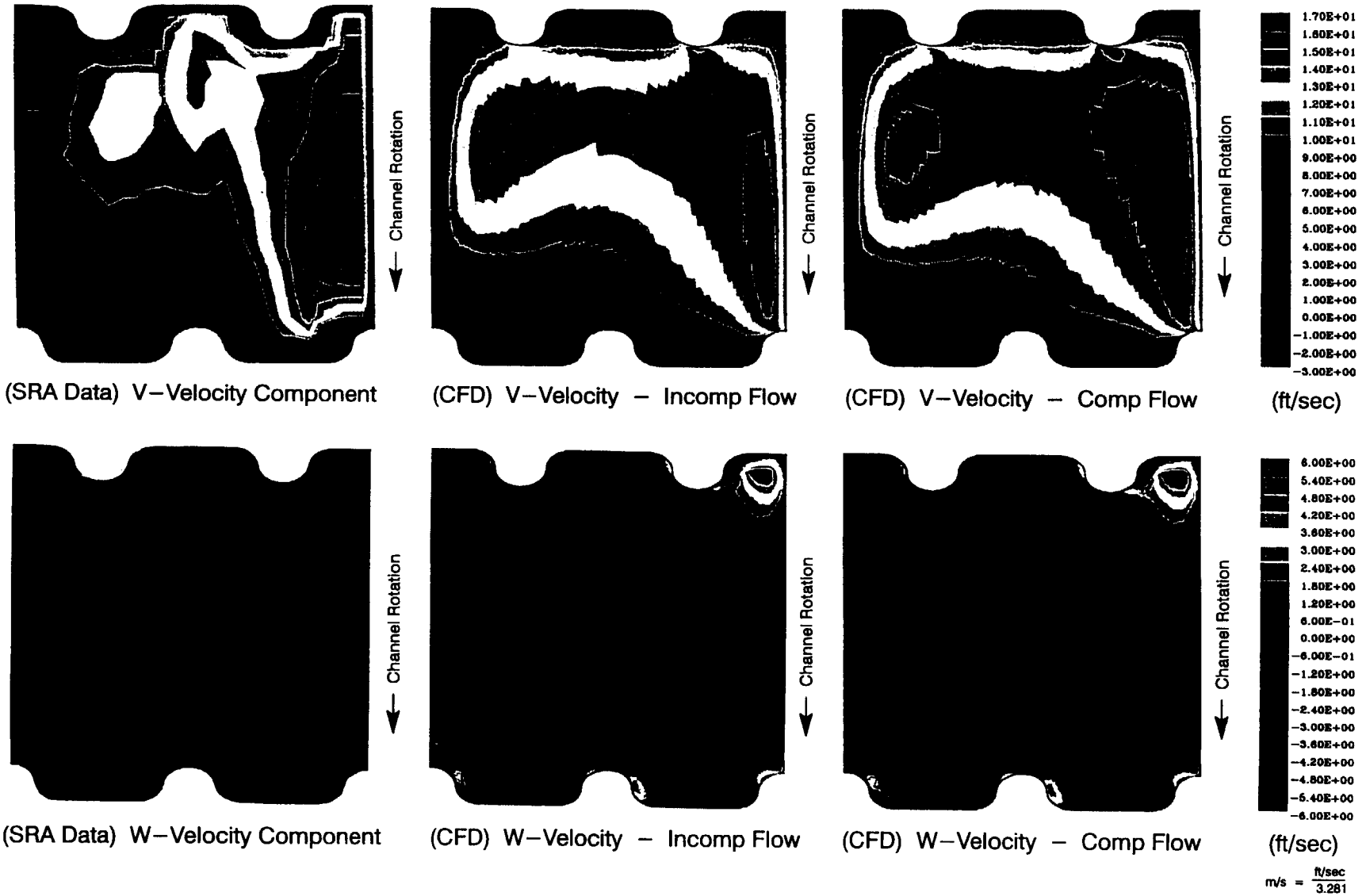

Figure 5.21 V-Component and W-Component Velocity Contours - Rotating Channel Location D2

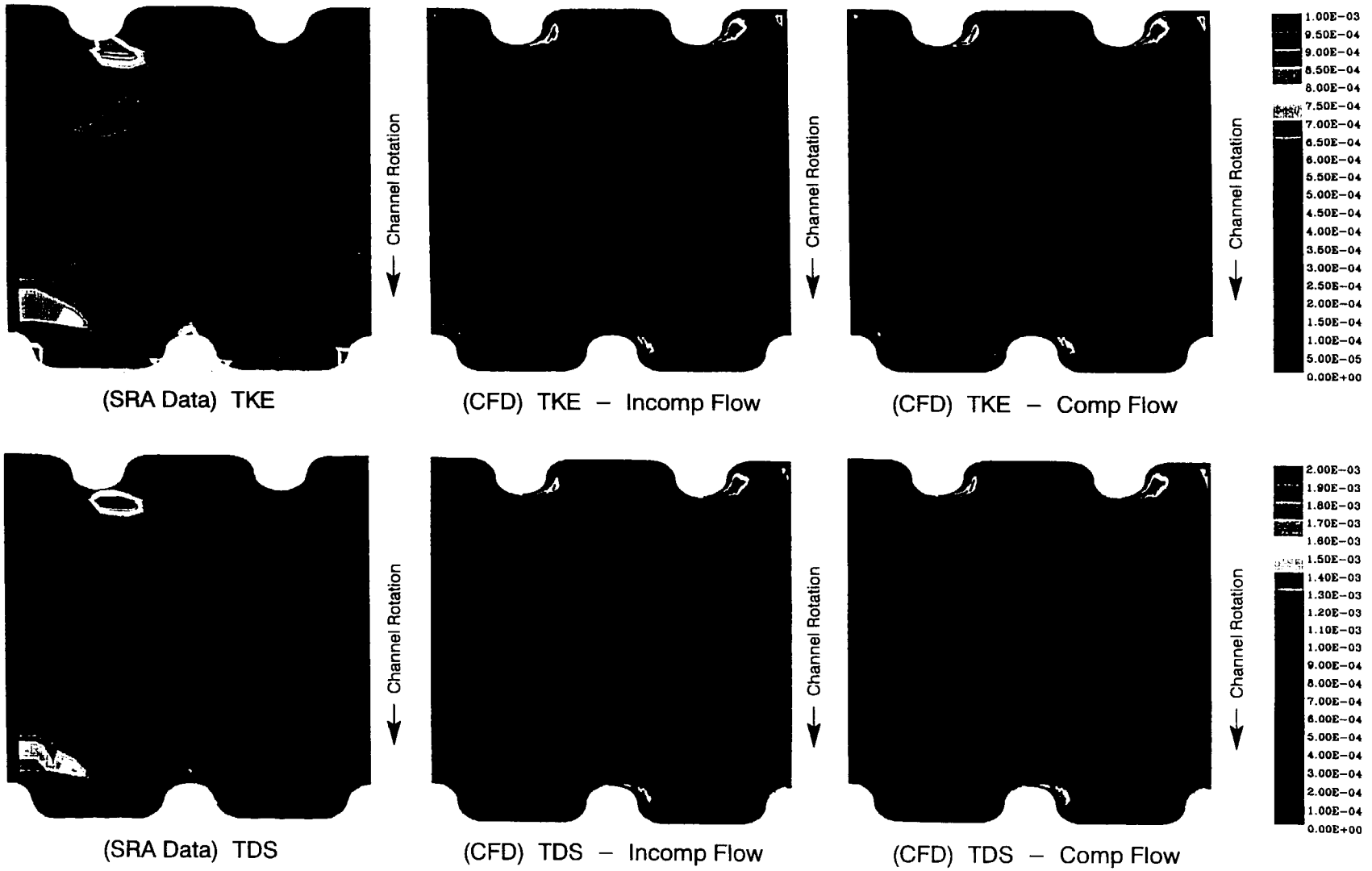

Figure 5.22 Turbulent Kinetic Energy (TKE) and Turbulent Energy Dissipation (TDS) – Rotating Channel Location D2

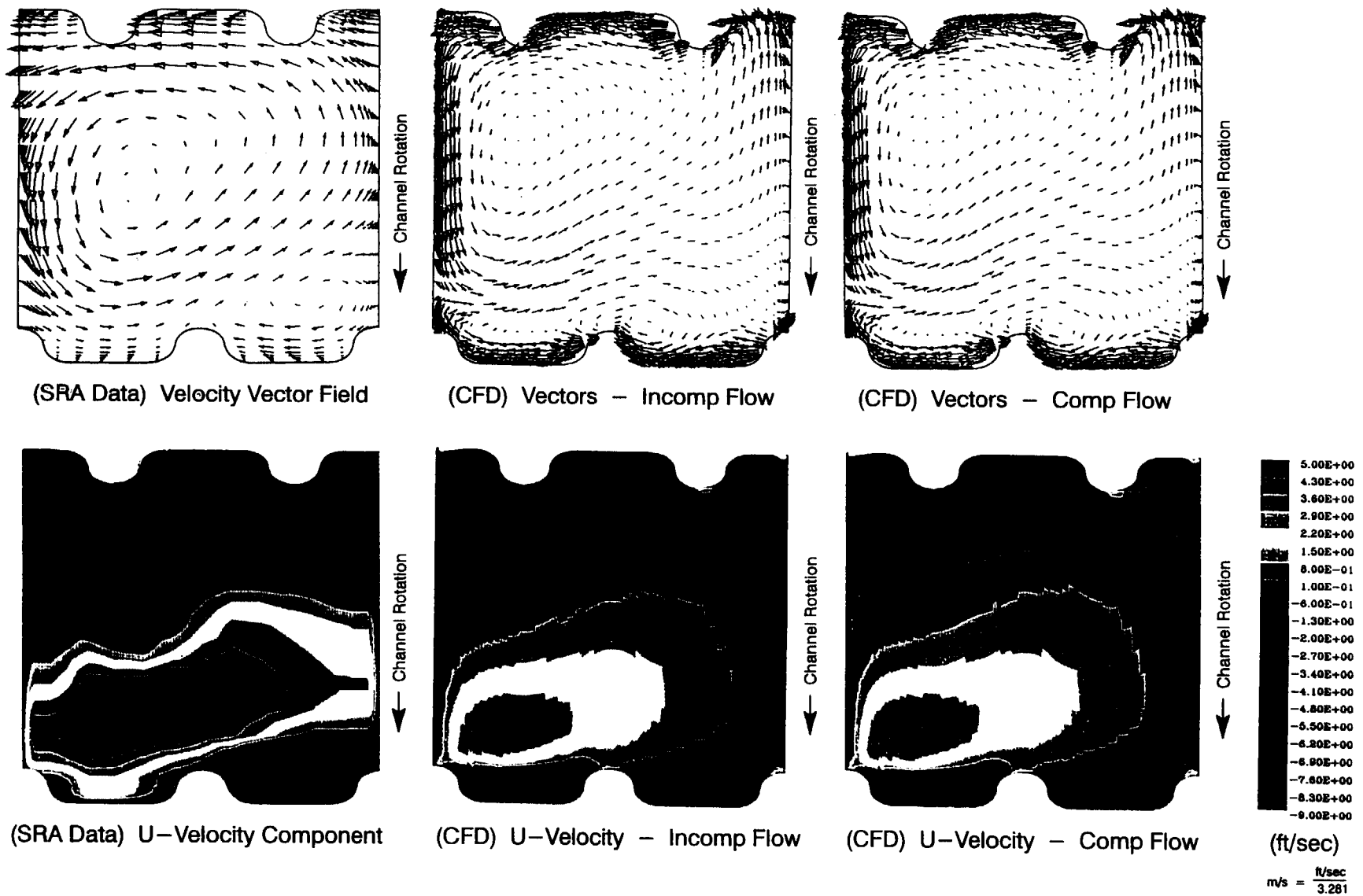

Figure 5.23 Velocity Vector Field and U–Component Velocity Contours – Rotating Channel Location D3

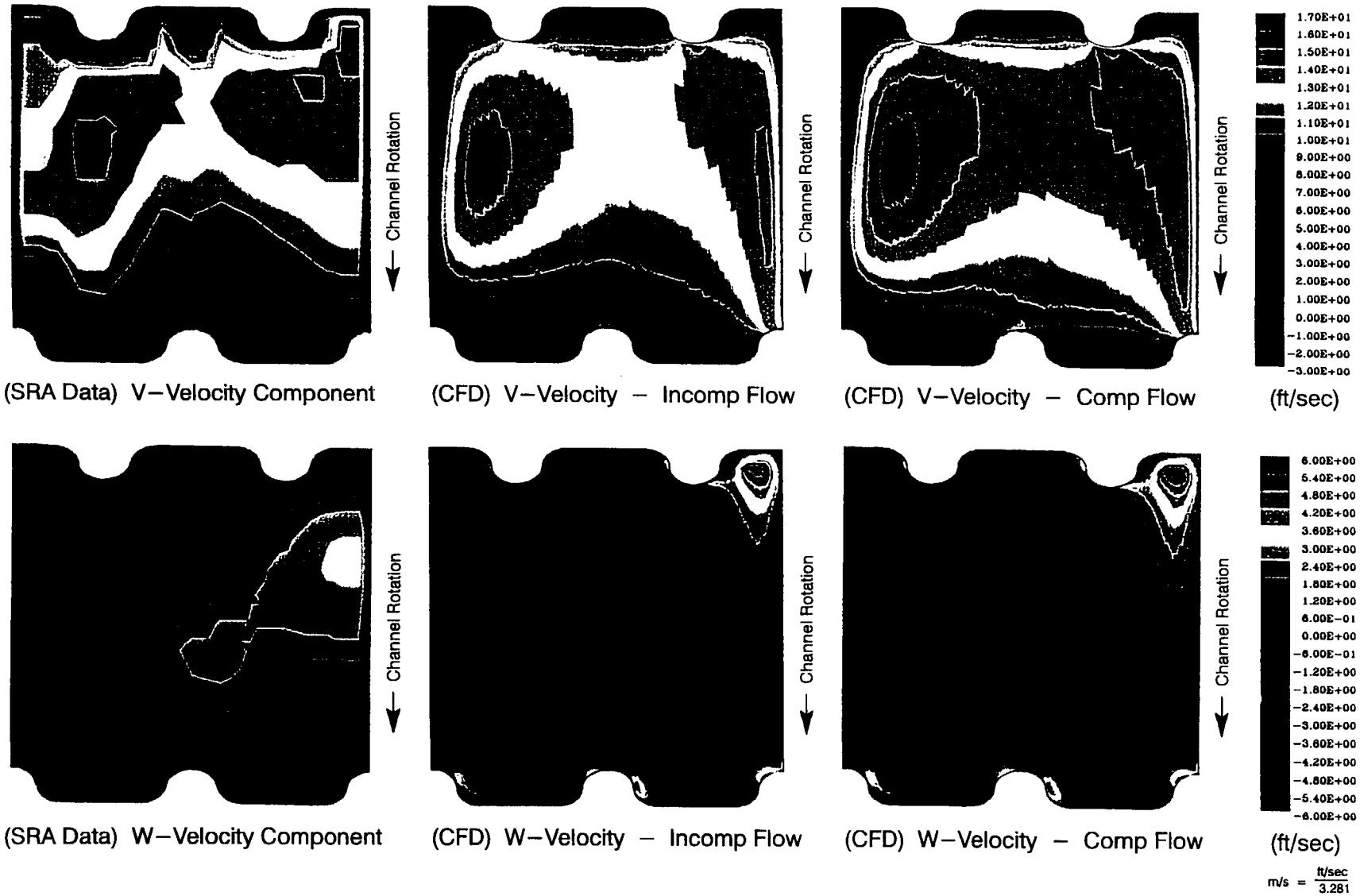

Figure 5.24 V–Component and W–Component Velocity Contours – Rotating Channel Location D3

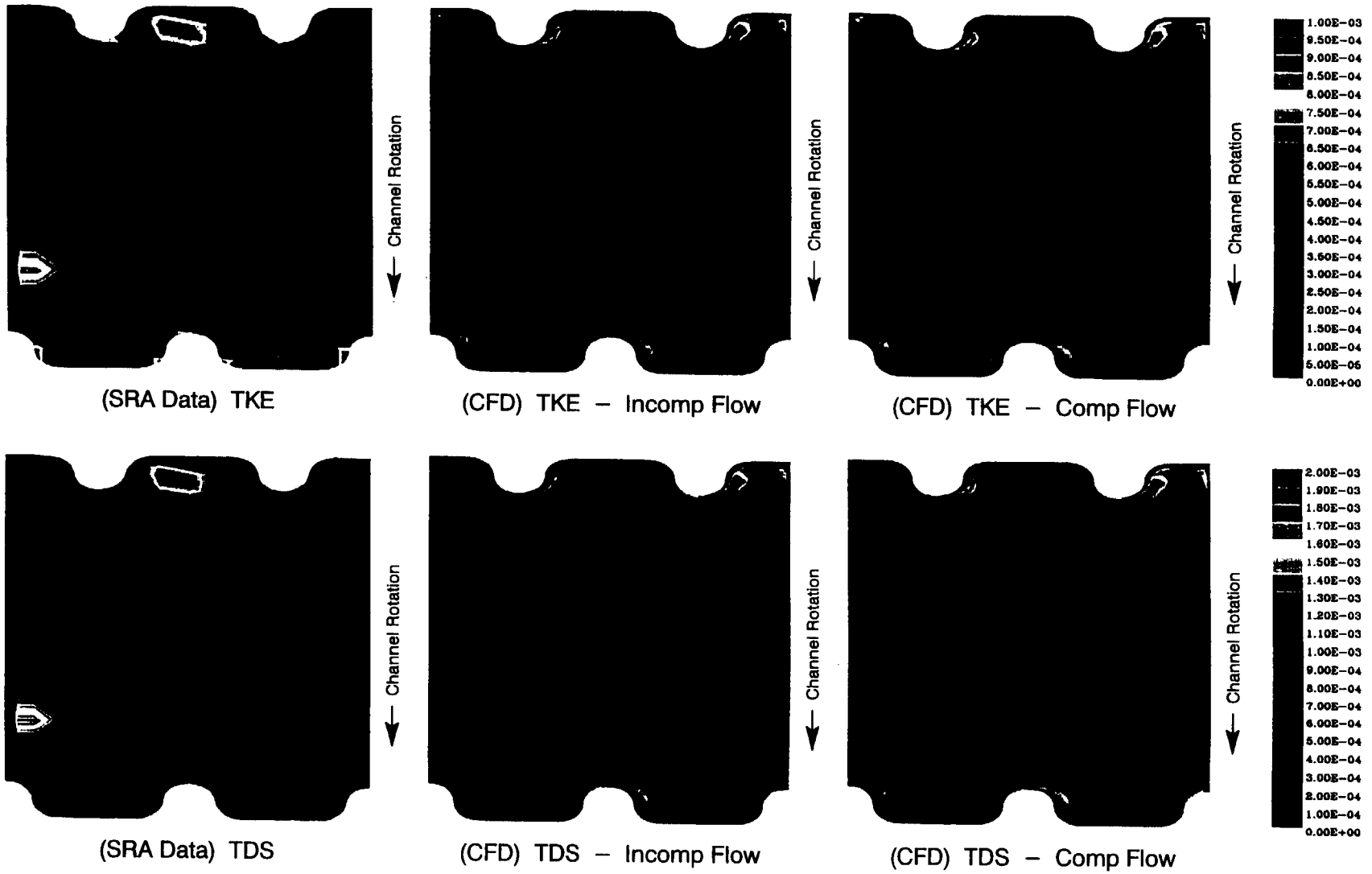

Figure 5.25 Turbulent Kinetic Energy (TKE) and Turbulent Energy Dissipation (TDS) – Rotating Channel Location D3

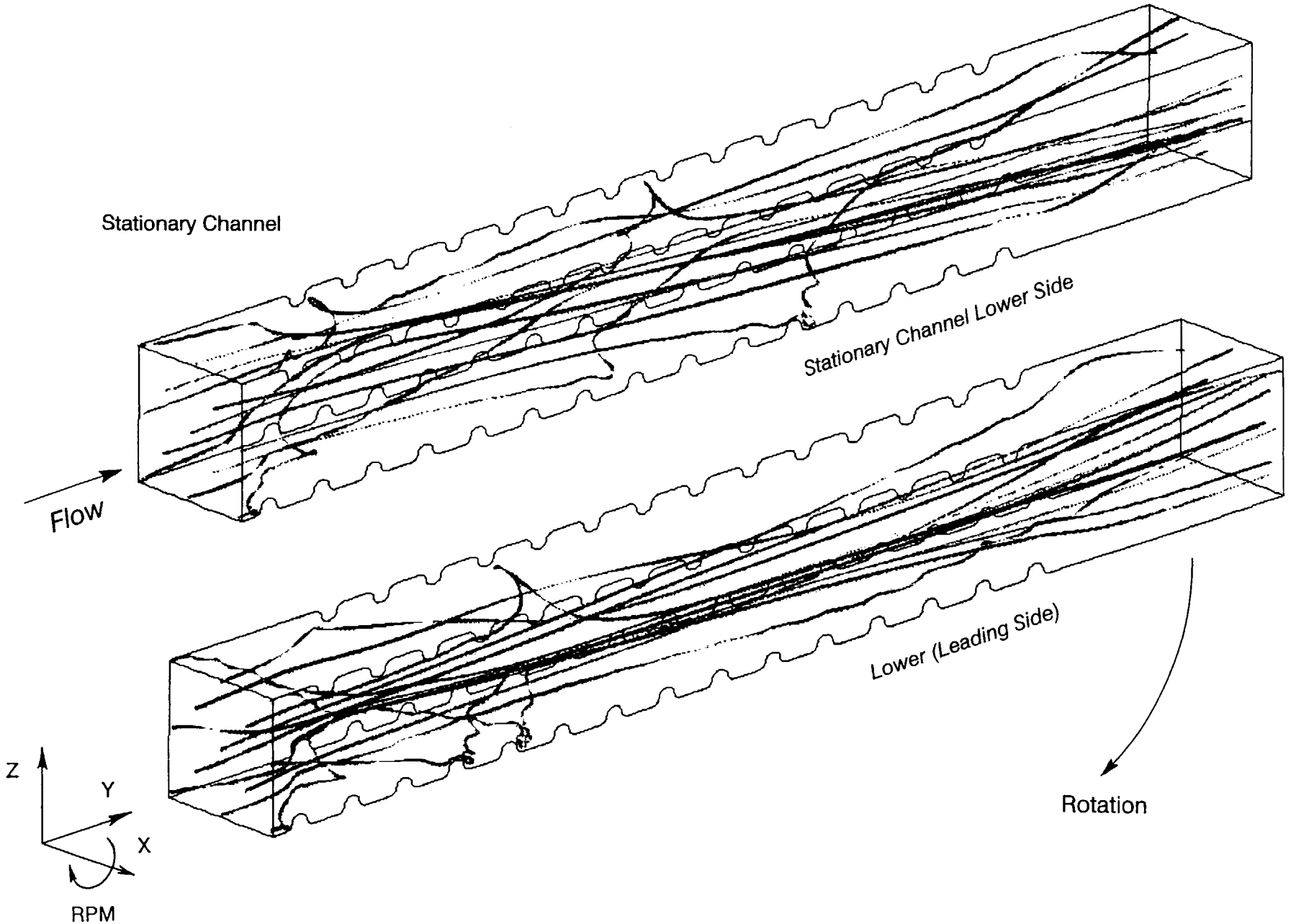

Figure 5.26 Streakiline Particle Trace Comparisons – Stationary vs Rotating Channel Simulations

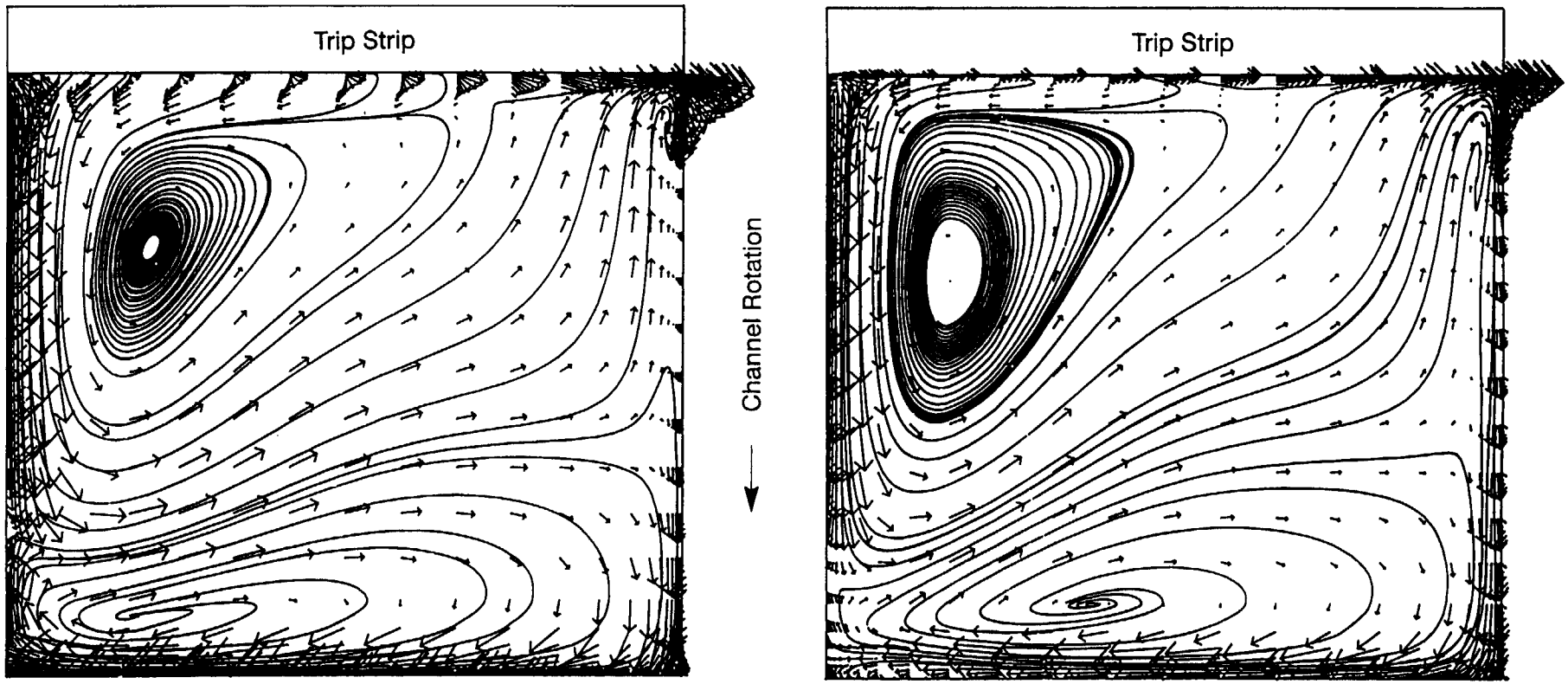

(a) Compressible Flow Channel Simulation
Rotating Channel (at i−Plane = 760)

(b) Compressible Flow "Conveyor−belt" Simulation
Rotating Channel Segment

Figure 5.27 Comparison of Seconday Flow Velocity Vector Fields − Channel vs "Conveyor−Belt" Simulation

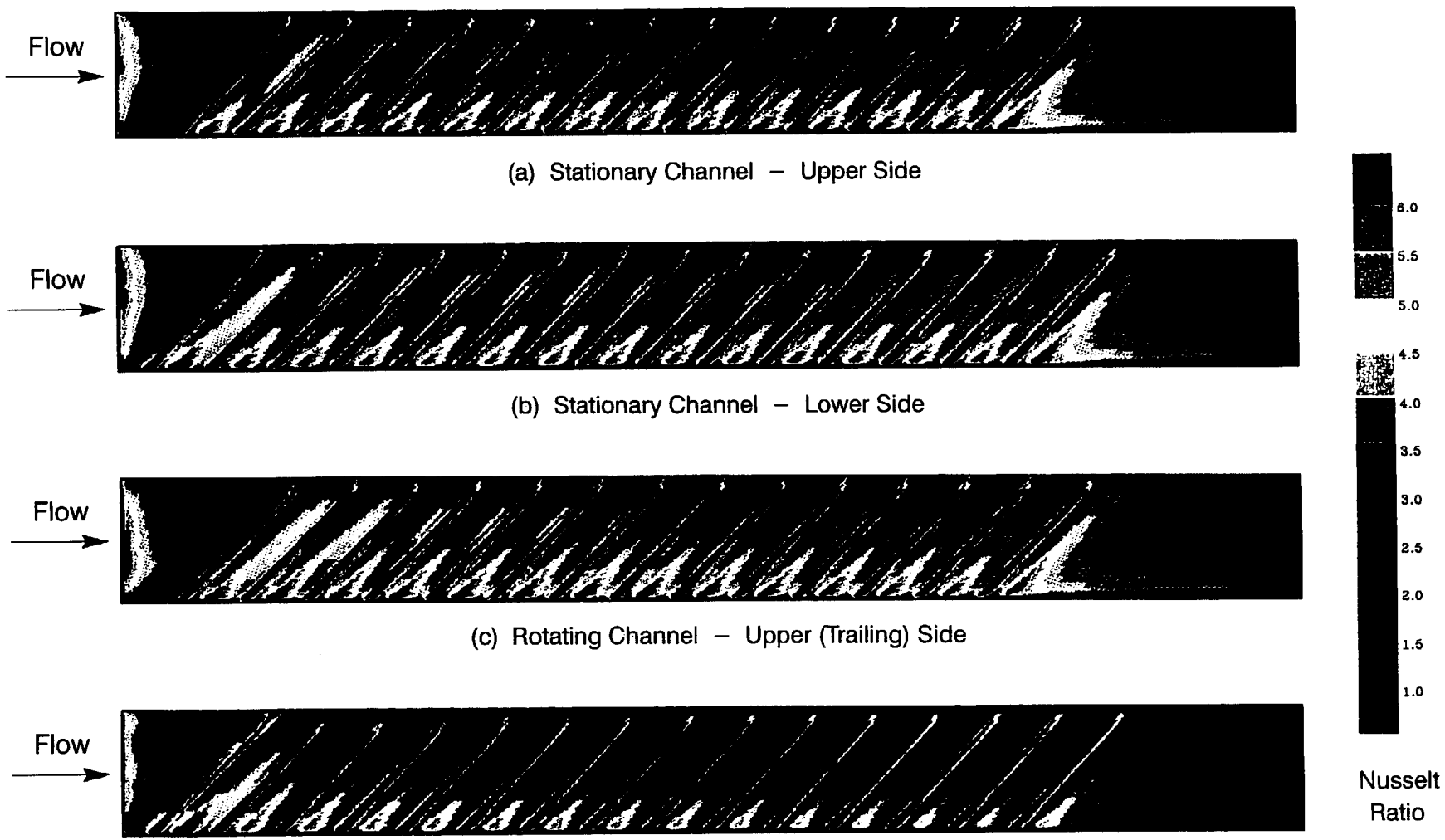

Figure 5.28 Trip Strip Channel Nusselt Number Ratio – Incompressible Flow Simulations

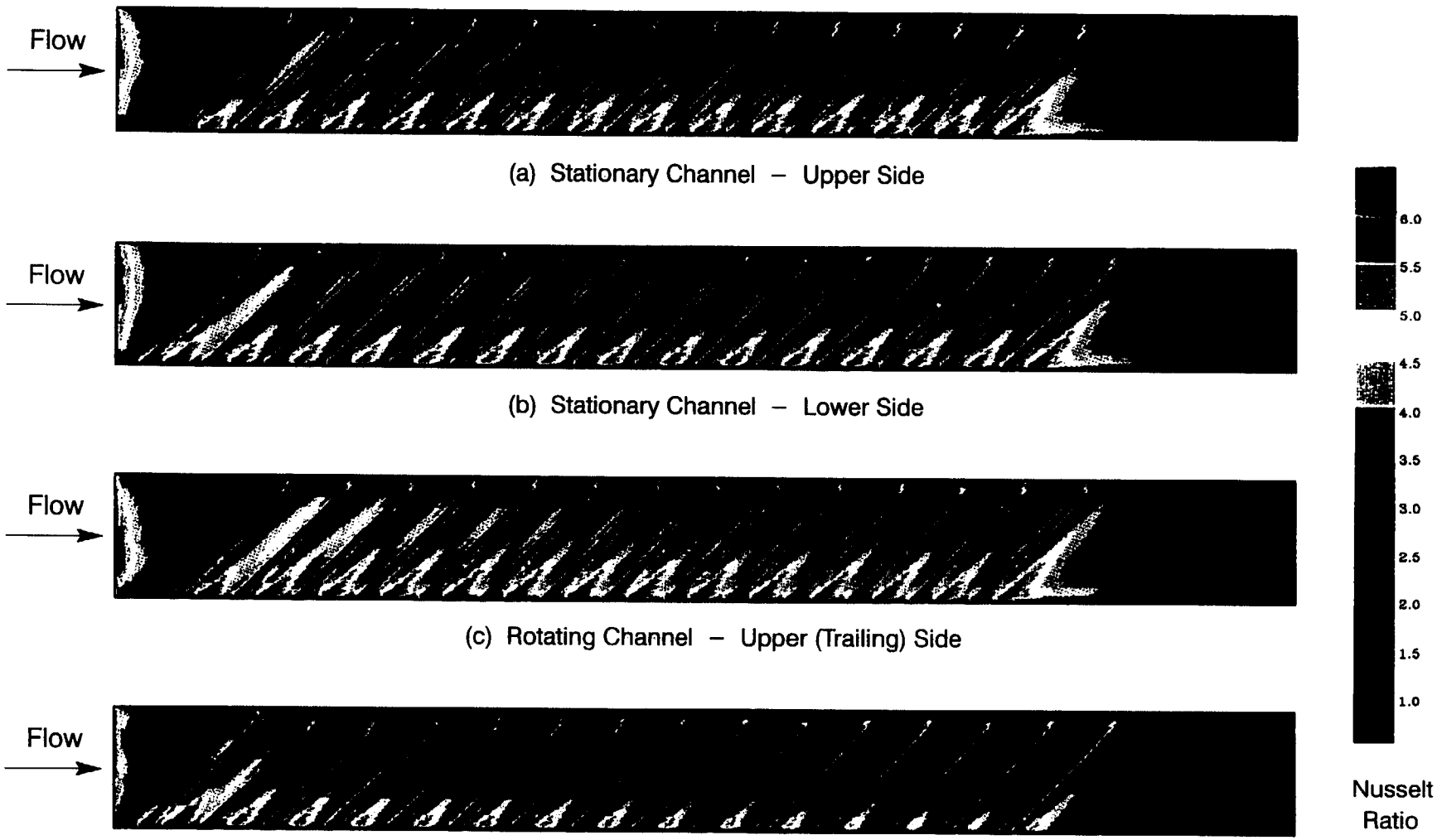

Figure 5.29 Trip Strip Channel Nusselt Number Ratio – Compressible Flow Simulations

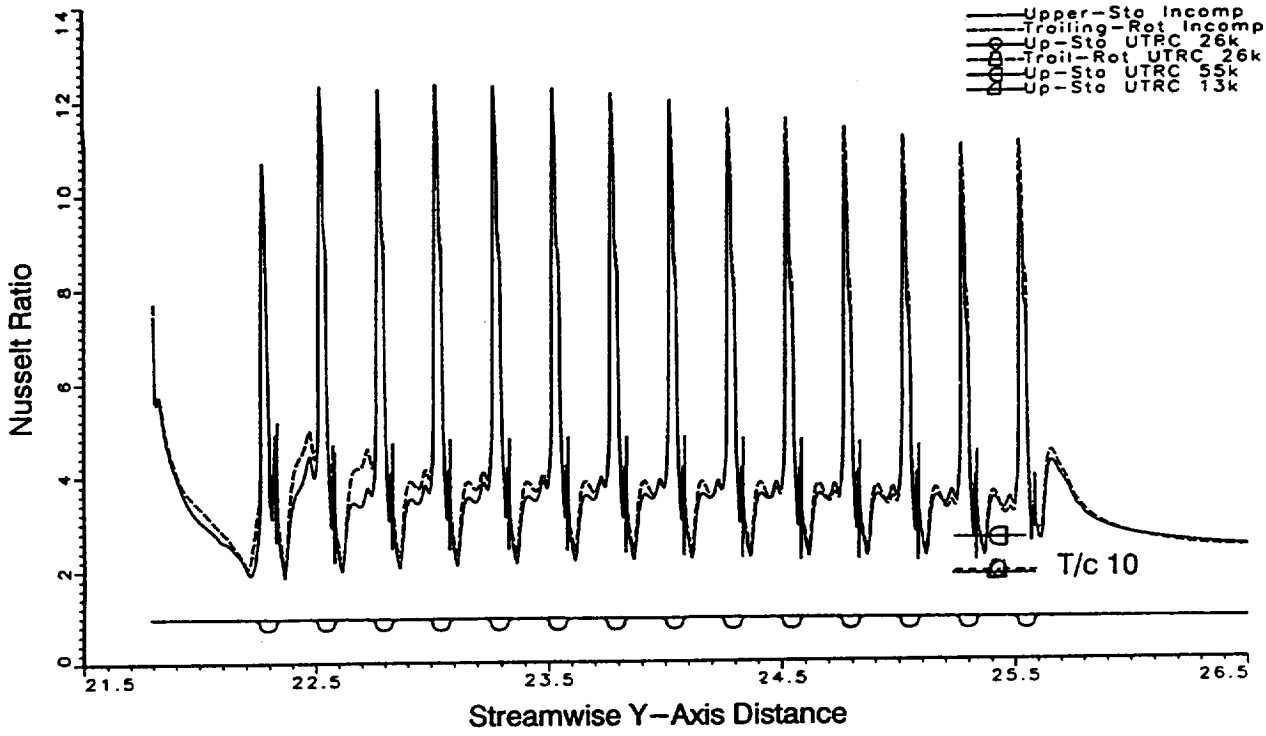

(a) Stationary Channel Upper Side vs Rotating Channel (Trailing Side) Surface

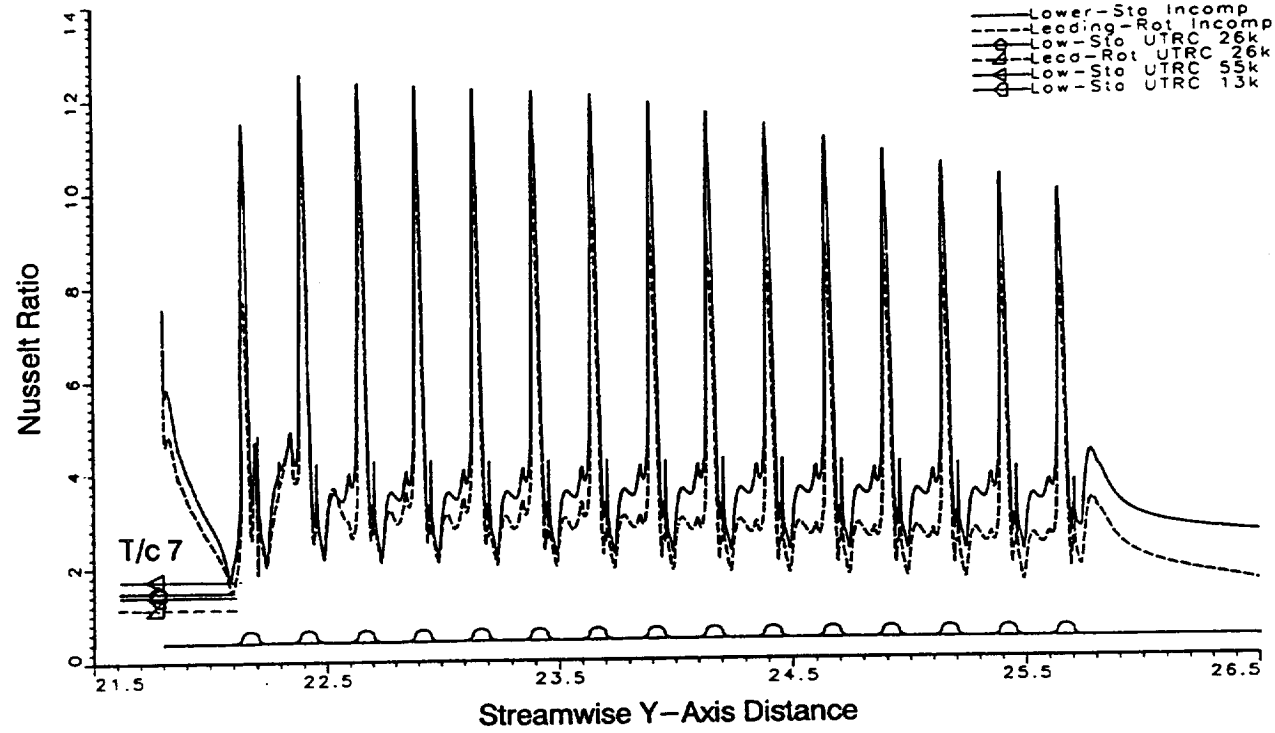

(b) Stationary Channel Lower Side vs Rotating Channel (Leading Side) Surface

Figure 5.30 Channel Centerline Nusselt Ratio – Incompressible Flow Simulations

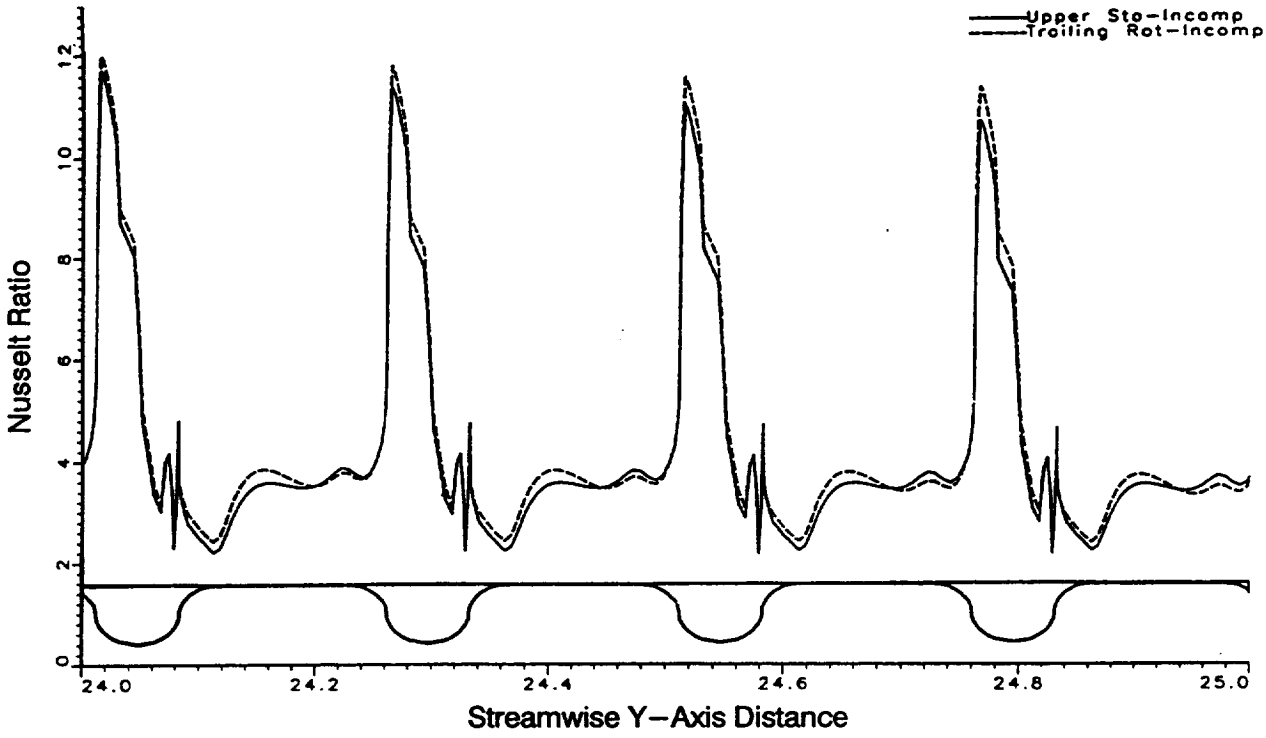

(a) Stationary Channel Upper Side vs Rotating Channel (Trailing Side) Surface

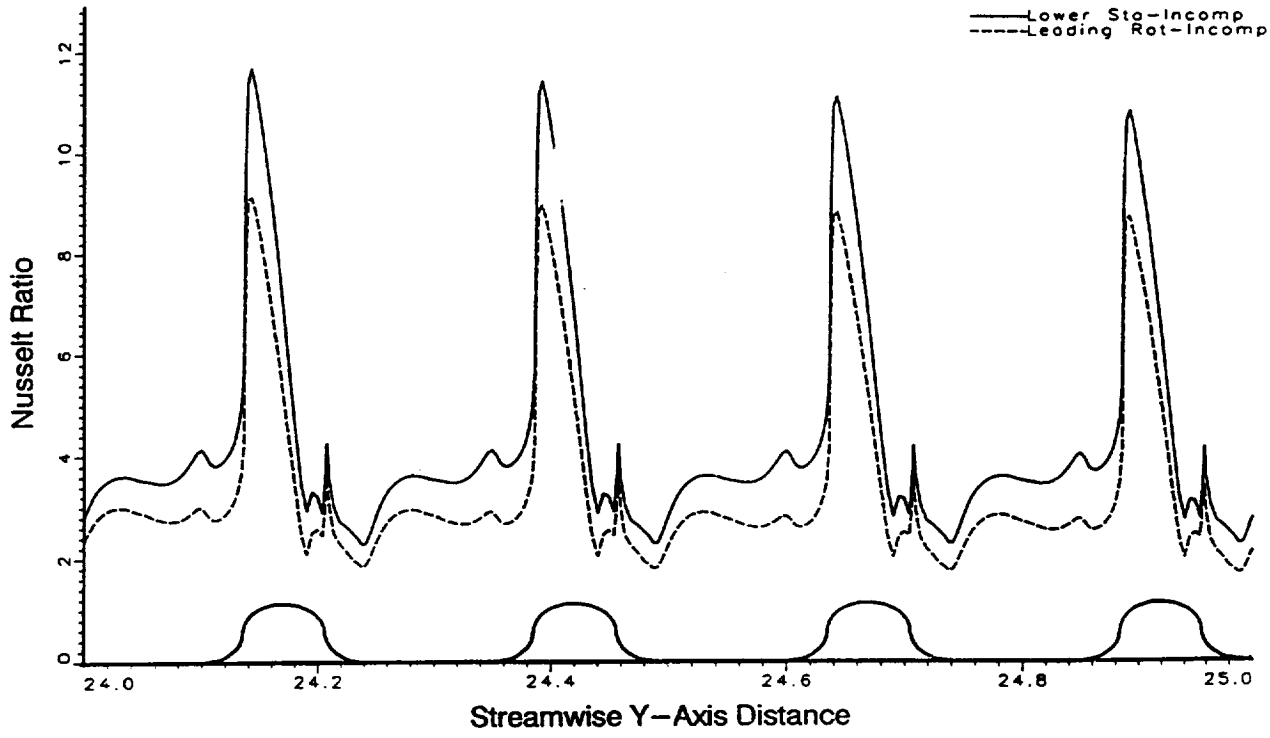

(b) Stationary Channei Lower Side vs Rotating Channel (Leading Side) Surface

Figure 5.31 Channel Centerline Nusselt Ratio – Incompressible Flow Simulations

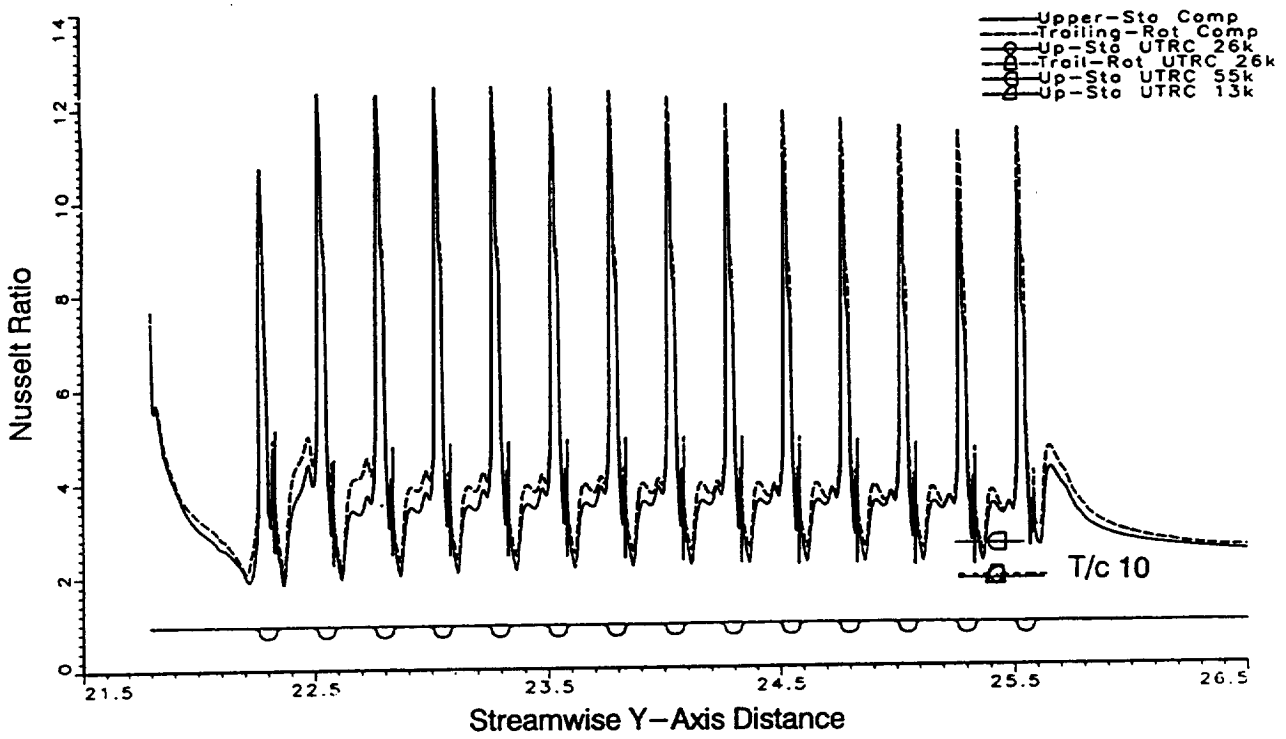

(a) Stationary Channel Upper Side vs Rotating Channel (Trailing Side) Surface

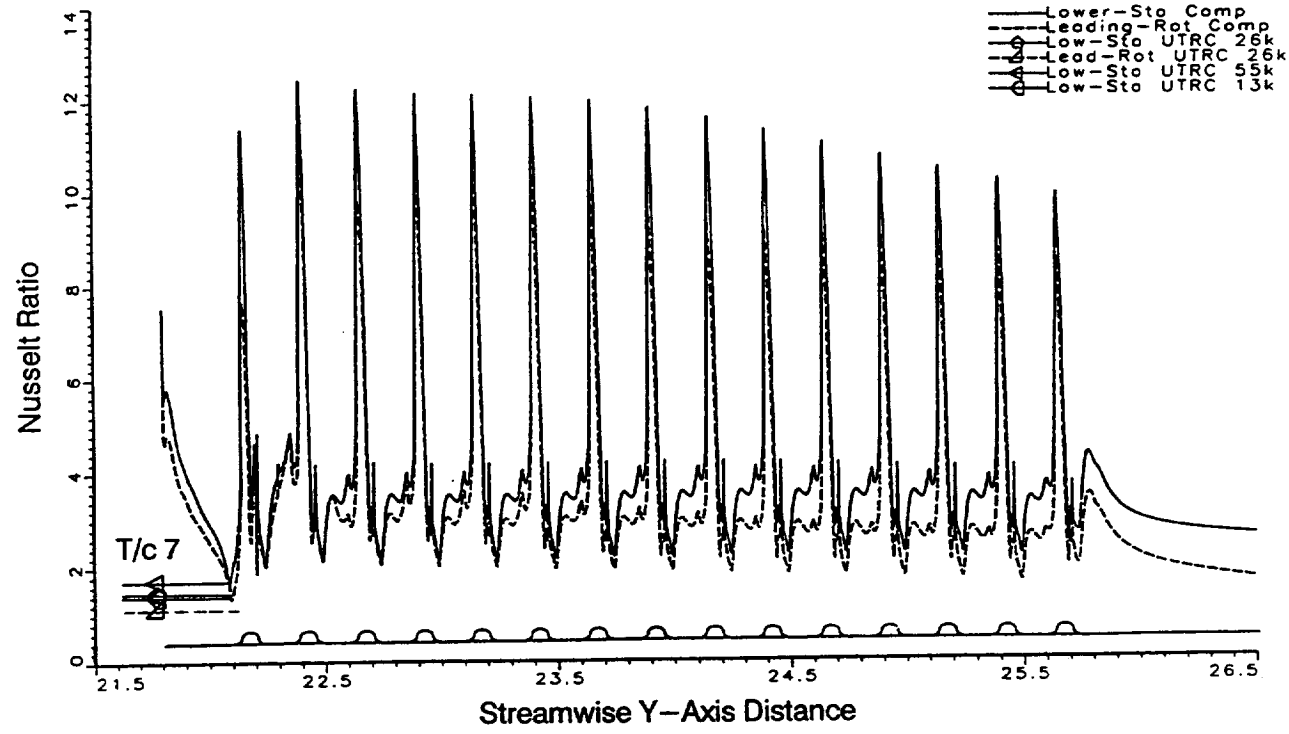

(b) Stationary Channel Lower Side vs Rotating Channel (Leading Side) Surface

Figure 5.32 Channel Centerline Nusselt Ratio – Compressible Flow Simulations

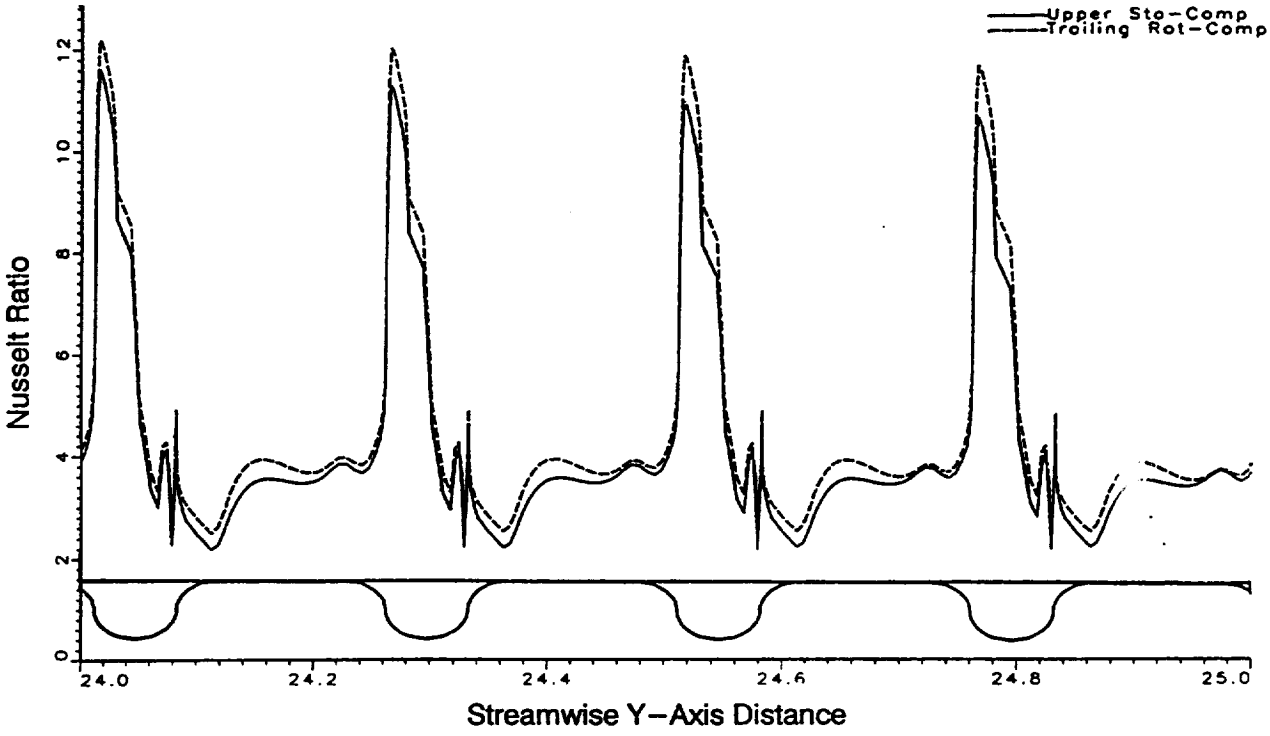

(a) Stationary Channel Upper Side vs Rotating Channel (Trailing Side) Surface

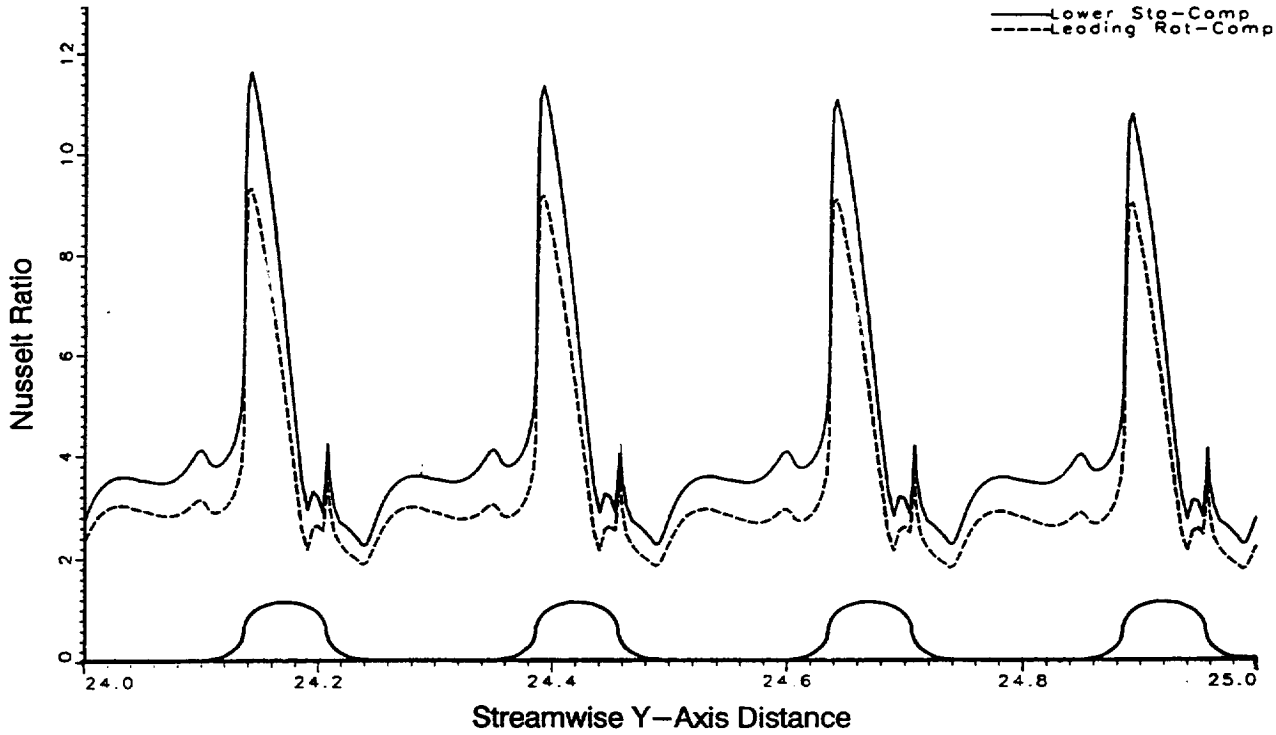

(b) Stationary Channel Lower Side vs Rotating Channel (Leading Side) Surface

Figure 5.33 Channel Centerline Nusselt Ratio – Compressible Flow Simulations

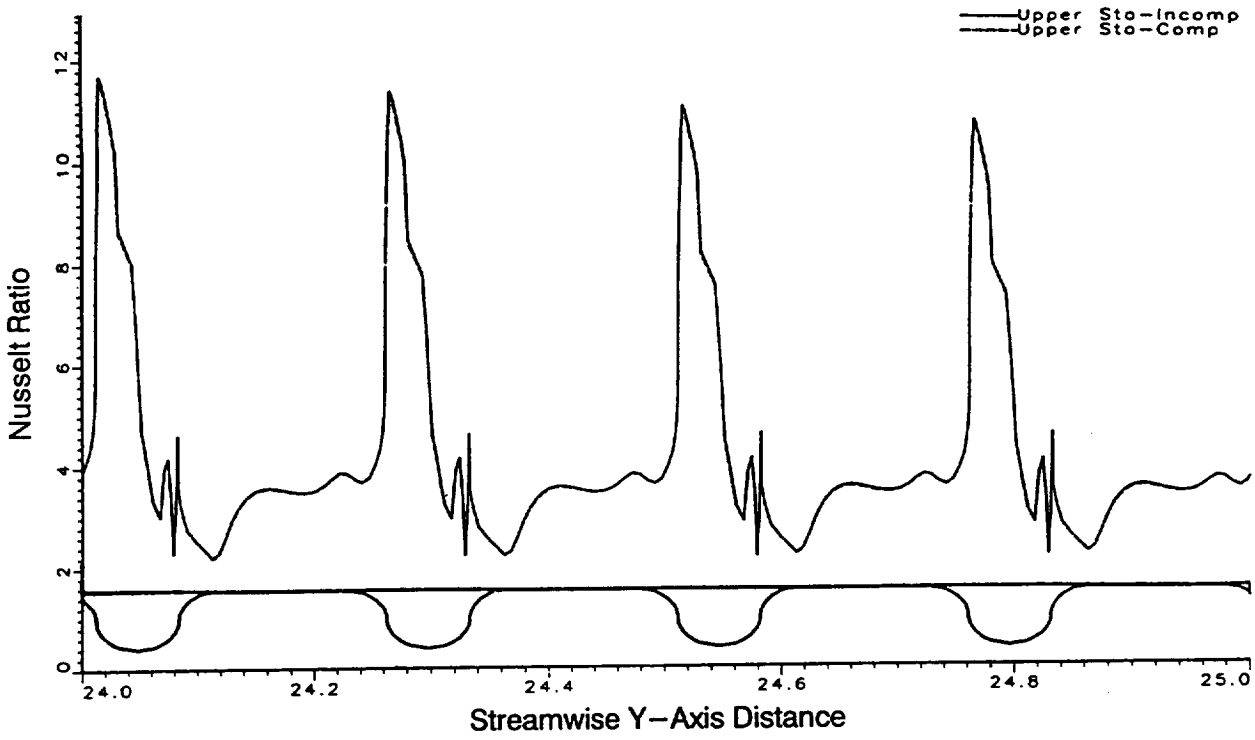

(a) Channel Upper Side Incompressible vs Compressible Flow Simulations

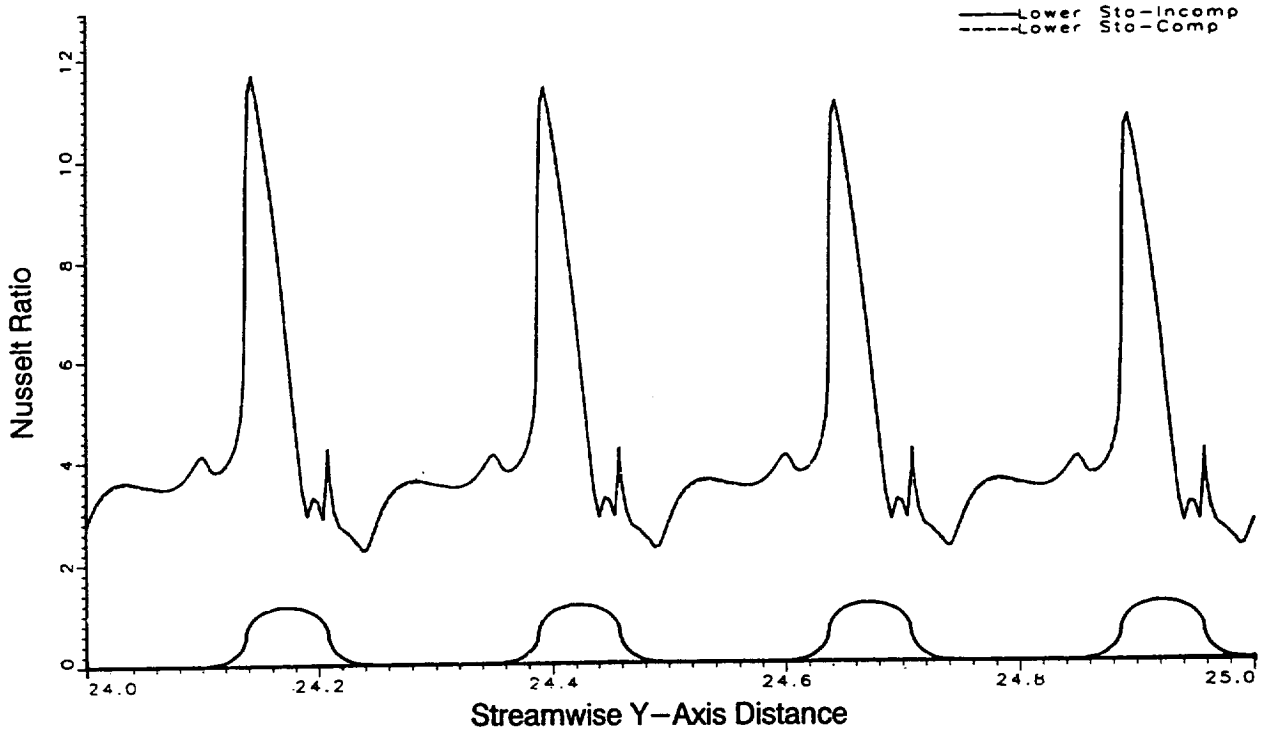

(b) Channel Lower Side Incompressible vs Compressible Flow Simulations

Figure 5.34 Channel Centerline Nusselt Ratio – Stationary Channel Simulations

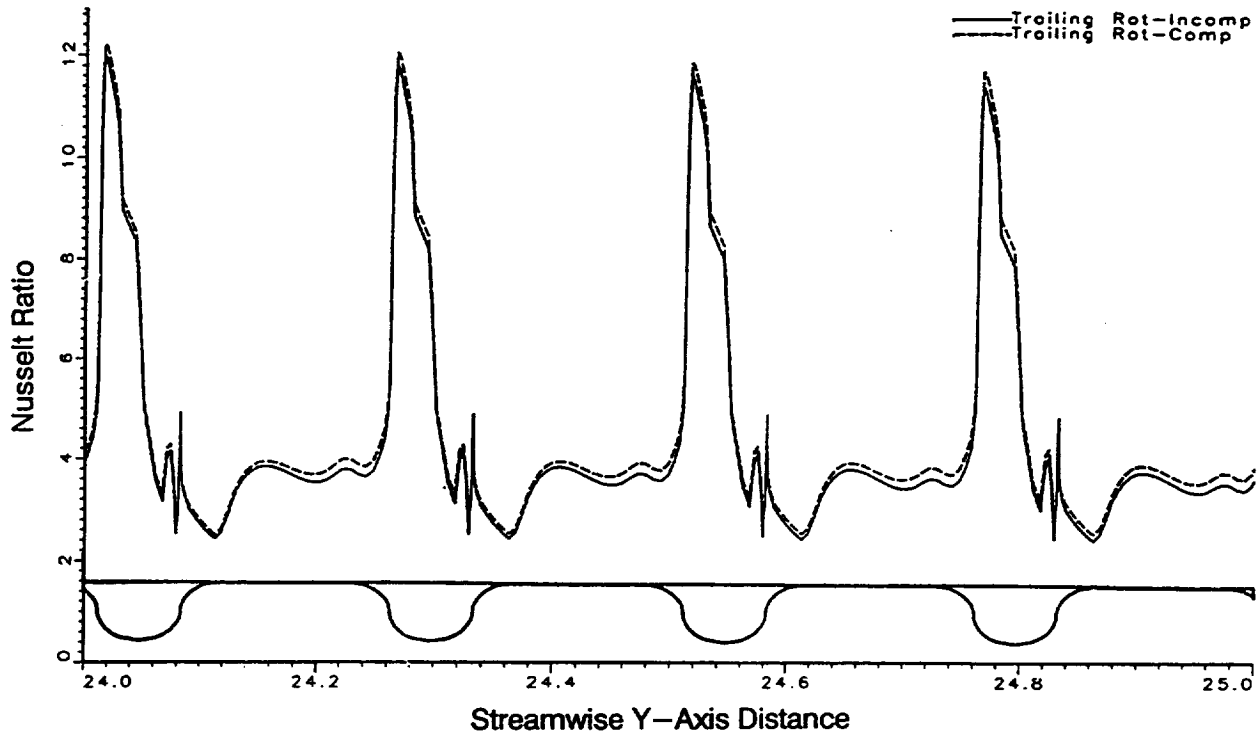

(a) Channel Trailing Side Incompressible vs Compressible Flow Simulations

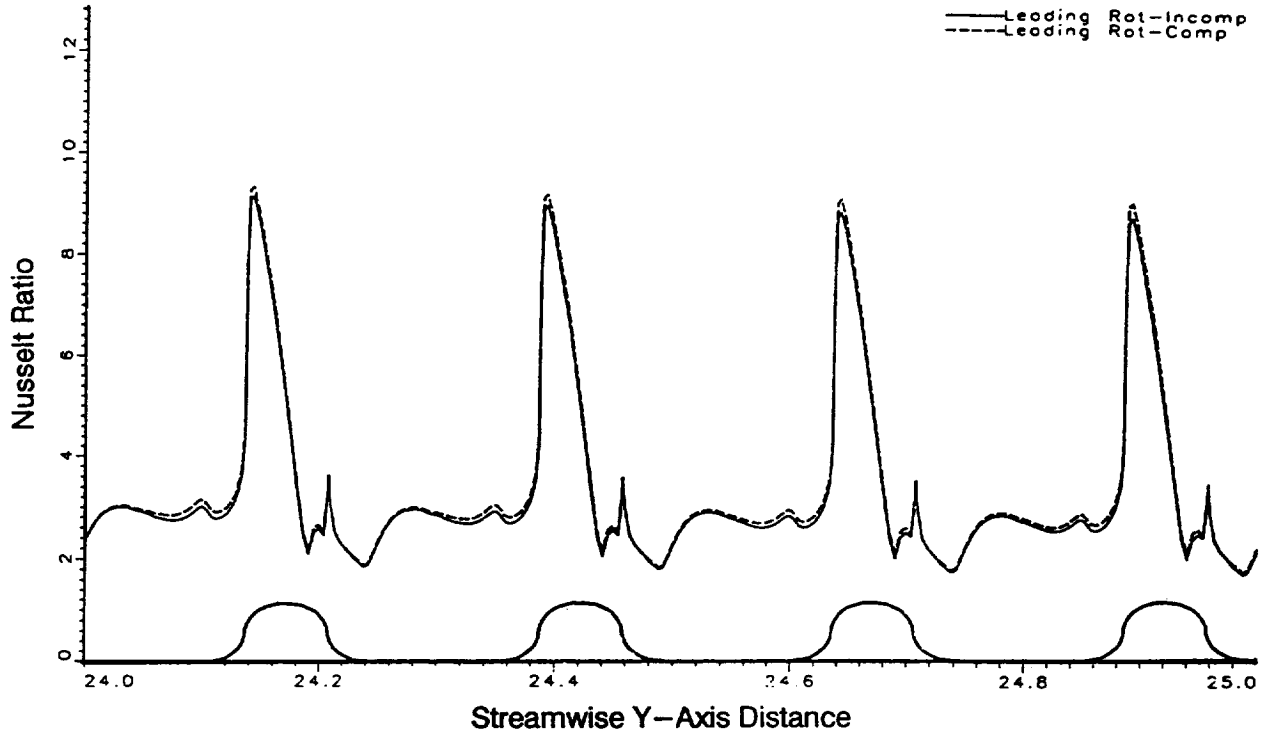

(b) Channel Leading Side Incompressible vs Compressible Flow Simulations

Figure 5.35 Channel Centerline Nusselt Ratio – Rotating Channel Simulations

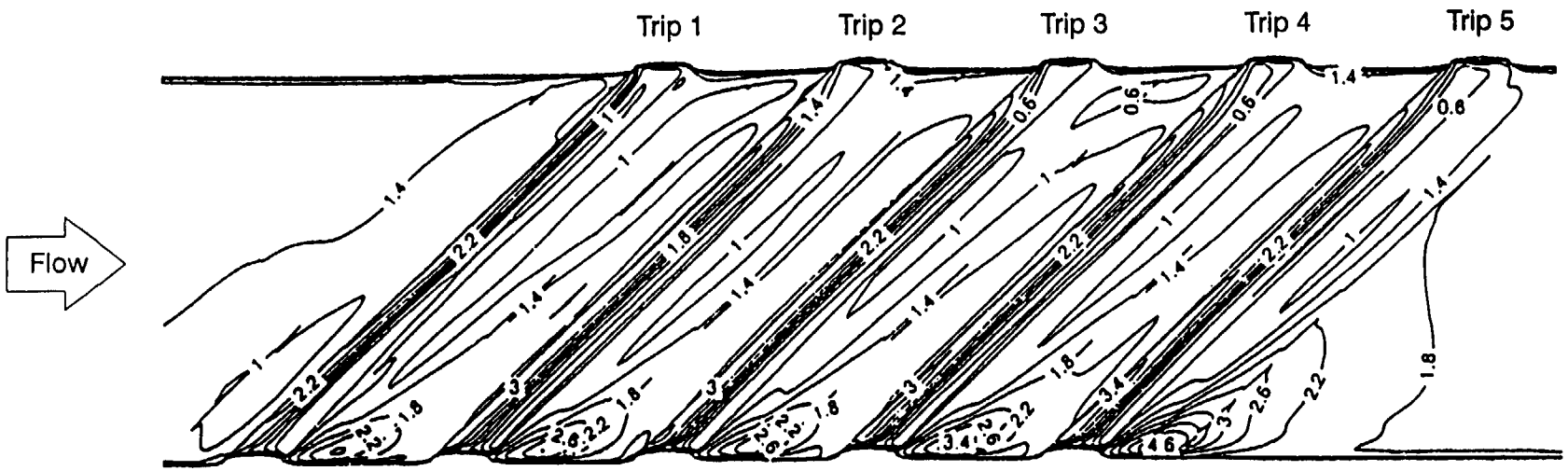

(a) Stationary Channel – Case 1 from Stephens et al. 1995

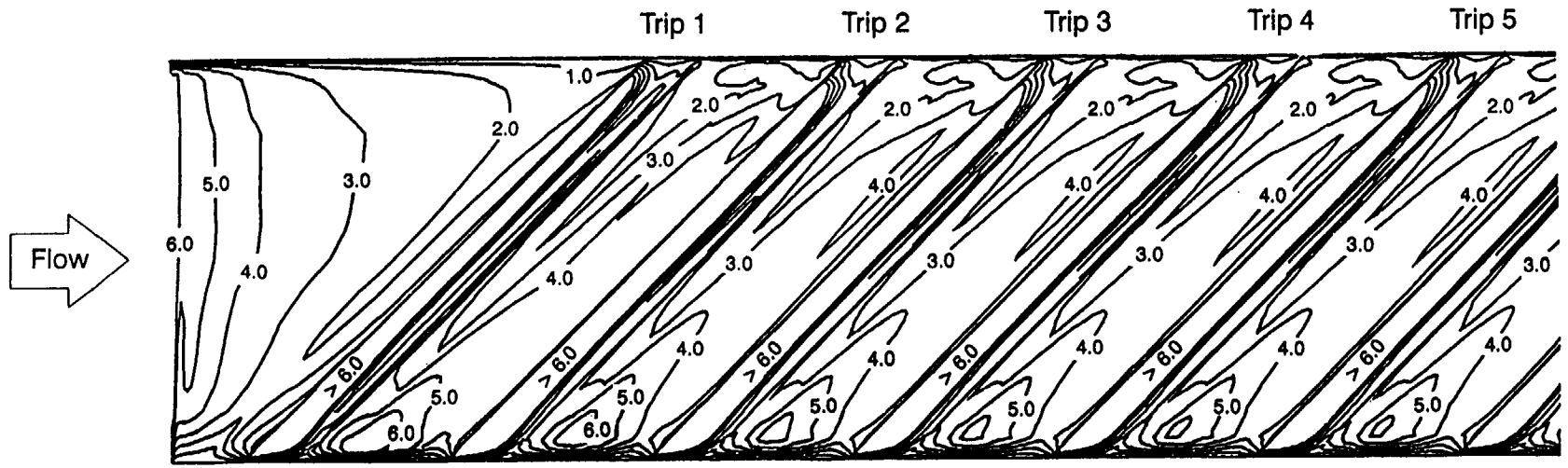

(b) Stationary Channel Compressible Flow Simulation

Figure 5.36 Nusselt Ratio Comparison – Stephens et al. 1995, vs Stationary Channel Compressible Flow Simulation

REPORT DOCUMENTATION PAGE

Form Approved
OMB No. 0704-0188

Public reporting burden for this collection of information is estimated to average 1 hour per response, including the time for reviewing instructions, searching existing data sources, gathering and maintaining the data needed, and completing and reviewing the collection of information. Send comments regarding this burden estimate or any other aspect of this collection of information, including suggestions for reducing this burden, to Washington Headquarters Services, Directorate for Information Operations and Reports, 1215 Jefferson Davis Highway, Suite 1204, Arlington, VA 22202-4302, and to the Office of Management and Budget, Paperwork Reduction Project (0704-0188), Washington, DC 20503.

1. AGENCY USE ONLY (*Leave blank*)	2. REPORT DATE	3. REPORT TYPE AND DATES COVERED
	October 1996	Final Contractor Report

4. TITLE AND SUBTITLE

Flow in Rotating Serpentine Coolant Passages With Skewed Trip Strips

5. FUNDING NUMBERS

WU–538–06–14
C–NAS3–27378 SBIR

6. AUTHOR(S)

David G.N. Tse and Gary Steuber

7. PERFORMING ORGANIZATION NAME(S) AND ADDRESS(ES)

Scientific Research Associates, Inc.
50 Nye Road, P.O. Box 1058
Glastonbury, Connecticut 06033

8. PERFORMING ORGANIZATION REPORT NUMBER

E–10429

9. SPONSORING/MONITORING AGENCY NAME(S) AND ADDRESS(ES)

National Aeronautics and Space Administration
Lewis Research Center
Cleveland, OH 44135–3191

10. SPONSORING/MONITORING AGENCY REPORT NUMBER

NASA CR–198530

11. SUPPLEMENTARY NOTES

David G.N. Tse, Scientific Research Associates, Inc., 50 Nye Road, P.O. Box 1058, Glastonbury, Connecticut 06033; Gary Steuber, Pratt and Whitney, 415 Washington Avenue, Mail Stop 201–09, North Haven, Connecticut 06473, Project Manager, Philip E. Poinsatte, Internal Fluid Mechanics Division, NASA Lewis Research Center, organization code 2630, (216) 433–5898.

12a. DISTRIBUTION/AVAILABILITY STATEMENT

Unclassified - Unlimited
Released as Publicly Available September 1996
Subject Category 34

This publication is available from the NASA Center for AeroSpace Information, (301) 621–0390.

12b. DISTRIBUTION CODE

13. ABSTRACT (*Maximum 200 words*)

Laser velocimetry was utilized to map the velocity field in serpentine turbine blade cooling passages with skewed trip strips. The measurements were obtained at Reynolds and Rotation numbers of 25,000 and 0.24 to assess the influence of trips, passage curvature and Coriolis force on the flow field. The interaction of the secondary flows induced by skewed trips with the passage rotation produces a swirling vortex and a corner recirculation zone. With trips skewed at +45°, the secondary flows remain unaltered as the cross-flow proceeds from the passage to the turn. However, the flow characteristics at these locations differ when trips are skewed at –45°. Changes in the flow structure are expected to augment heat transfer, in agreement with the heat transfer measurements of Johnson, et al. (1994). The present results show that trips skewed at –45° in the outward flow passage and trips skewed at +45° in the inward flow passage maximize heat transfer. Details of the present measurements were related to the heat transfer measurements of Johnson, et al. to relate fluid flow and heat transfer measurements.

14. SUBJECT TERMS

Channel flow; Rotating fluids; Turbine blade cooling; Heat transfer; Serpentine coolant passage

15. NUMBER OF PAGES

169

16. PRICE CODE

A09

17. SECURITY CLASSIFICATION OF REPORT	18. SECURITY CLASSIFICATION OF THIS PAGE	19. SECURITY CLASSIFICATION OF ABSTRACT	20. LIMITATION OF ABSTRACT
Unclassified	Unclassified	Unclassified	